UNIVERSIDAD NACIONAL AUTÓNOMA DE MÉXICO

Posgrado en Ciencia e Ingeniería de Materiales
Instituto de Investigaciones en Materiales

HYDRODYNAMICS OF DEFORMABLE OBJECTS IN CREEPING FLOWS

Tesis
que para obtener el grado de
Doctor en Ciencia e Ingeniería
de Materiales
presenta:

Marco Antonio Reyes Huesca

Director de Tesis
Dr. Enrique Geffroy Aguilar

UNAM
POSGRADO
Ciencia e Ingeniería
de Materiales

México, 2005

Autorizo a la Dirección General de Bibliotecas de la UNAM a difundir en formato electrónico e impreso el contenido de mi trabajo recepcional.

NOMBRE: Marco Antonio Reyes Huesca

FECHA: 15 - Febrero - 2005

FIRMA:

A mi Gabita

A Silviano, Edith y Ale

A mis papás y mis hermanos

A Mami y Rosi

Reconocimientos

Esta tesis fue desarrollada en el Laboratorio de Reología Óptica del Instituto de Investigaciones en Materiales de la Universidad Nacional Autónoma de México, bajo la supervisión del Dr. Enrique Geffroy Aguilar, al cual le agradezco la dirección, revisión y corrección de esta tesis y todo el apoyo recibido durante el desarrollo del proyecto doctoral. También quiero agradecer a los otros miembros de mi comité tutoral, los Drs. Baltasar Mena Iniesta y César Treviño Treviño, y a los miembros del jurado, los Drs. Fermín Viniegra Heberlein, Federico Méndez Lavielle, Gary Leal, Roberto Zenit Camacho, Francisco Solorio Ordaz y Eduardo Ramos Mora, por las observaciones y correcciones hechas a este trabajo.

Agradezco al Ing. Gerardo Guevara Flores por la asesoría y soporte técnico en cómputo. También agradezco a la Lic. Teresa Vázquez y a la Sra. Sara Jiménez por los servicios prestados en la biblioteca del IIM, y a Cristina González del Departamento de Reología y Mecánica Aplicada.

Agradezco la beca para estudios de posgrado otorgada por la DGEP-UNAM, la beca para tesis del proyecto NC-204 del CONACyT y la beca del Programa para Finalizar Estudios de Posgrado del IIM.

Finalmente, quiero agradecer todo el apoyo recibido de mis papás, Gabita, Ale, Edith A., Silviano, Edith, Lalo, Cristina, Sofía, Adrián, Mami y Rosi, de mis amigos y compañeros Jacinto, Eréndira, Ernesto, Marco, Said, Gerardo, Carlos, Panchito, Gil, Juan y Roberto.

Abstract

This Thesis presents a study of the hydrodynamics of deformable objects (viscous drops) in creeping flows generated by co-rotating Two-Roll Mills (TRMs). This work contains analytical and numerical studies of the properties of creeping flow fields generated by TRMs and comprises numerical simulations of the dynamics of drops placed at the stagnation point that these fields present. The aim of these studies is to improve our current understanding of the effects of vorticity on drop dynamics in well characterized two-dimensional strong flow fields, about the modification of the flow field properties due to the presence of the drop and build a framework to a diversity of experimental studies.

The flow field generated by TRMs can be used as benchmarks for studies of non-linear viscoelasticity and for studies of the dynamics of rupture and coalescence of droplets. When these flows are used for studies of drop dynamics, the solutions obtained prescribe the most relevant parameters that determine the external flow conditions imposed on viscous droplets. The TRM flow fields should be useful for studies of complex fluids and dynamics of drops under conditions of relevance to a large set of applications. Indeed, the TRM device is a supplement to the flow fields that can be generated by the most frequently used flow cells: simple shear flow cells and four-roll mills.

The First Part presents (unbounded) analytical and (bounded) numerical solutions for Stokes flows generated by TRMs geometries. These fields are determined basically by the geometrical characteristics of the mills and rates of rotation of the cylinders; with this information all relevant parameters of the flows can be calculated. In addition, it is given the behavior of these parameters as functions of the geometry and cylinders speeds, and are calculated the effects due to the proximity of the boundary domain and the differences of the unbounded analytical and bounded numerical solutions. Also, it is proposed an experimental set up useful for studies of drop dynamics with all relevant flow cell design characteristics calculated using the analytical and numerical results; besides, it is described the control scheme with restrained flow conditions, necessary to maintain a drop at the unstable stagnation point.

The Second Part presents numerical simulations of the dynamics of two-dimensional viscous drops immersed in unbounded linear strong flows and flow fields generated in TRMs, both started impulsively from rest. The simulations were doing using boundary element methods (BEM). These simulations were performed for different ratios of deformation to vorticity (flow-type parameter, λ) and some Capillary number values, with emphasis given to the transient evolution of the drop from its initial shape until its stationary shape. The simulations show that the external and internal flow fields present a significant richness of features and some of those are presented for the equilibrium –long time– shape and for several stages during the transient evolution of the drop. Inside the interval of the flow-type parameter used, it is observed the transition from a damped periodic oscillatory behavior to a free-oscillation behavior, for all Capillary number values studied.

Abstract

Esta Tesis presenta un estudio de la hidrodinámica de objetos deformables (gotas viscosas) en flujos lentos generados por molinos de dos rodillos. Este trabajo contiene estudios analíticos y numéricos de las propiedades de campos de flujos lentos generados por molinos de dos rodillos e incluye simulaciones numéricas de la dinámica de gotas colocadas en el punto de estancamiento que esos campos presentan. La motivación de estos estudios es incrementar nuestro actual entendimiento de los efectos de la vorticidad en la dinámica de gotas de campos de flujo fuerte bidimensionales, de la modificación de las propiedades del campo de flujo debido a la presencia de una gota y sentar la base para una diversidad de estudios experimentales.

Los campos de flujo generados por molinos de dos rodillos pueden ser utilizados como referencias para estudios de viscoelasticidad y para estudios de la dinámica de ruptura y coalescencia de gotas. Cuando estos flujos son utilizados para estudios de dinámica de gotas, las soluciones obtenidas prescriben los parámetros más relevantes que determinan las condiciones del flujo externo impuestas sobre las gotas viscosas. Los campos de flujo generados por molinos de dos rodillos deben ser útiles para estudios de fluidos complejos y de dinámica de gotas bajo condiciones de relevancia para un gran número de aplicaciones. Además, este dispositivo es un complemento para los campos de flujo que pueden generar las celdas de flujo más frecuentemente utilizadas: celdas de flujos simplemente cortantes y molinos de cuatro rodillos.

La Primera Parte presenta las soluciones analítica (no acotada) y la numérica (acotada) para los flujos de Stokes generados por las geometrías de los molinos de dos rodillos. Estos campos están determinados básicamente por las características geométricas de los molinos y de la rapidez de rotación de los cilindros; con esta información, todos los parámetros relevantes de los flujos pueden ser calculados. También es estudiado el comportamiento de estos parámetros como funciones de la geometría y de las velocidades de los cilindros, y son calculados los efectos causados por la proximidad de la frontera del dominio y las diferencias de las soluciones analítica no acotada y numérica acotada. También

se propone un arreglo experimental útil para estudios de dinámica de gotas con todas las características relevantes del diseño de la celda de flujos calculadas con los resultados analítico y numérico; además se describe el algoritmo de control con condiciones de flujo restringidas, necesario para mantener una gota en el punto de estancamiento inestable.

La Segunda Parte contiene las simulaciones numéricas de la dinámica de gotas viscosas bidimensionales inmersas en flujos fuertes lineales y en flujos generados en molinos de dos rodillos, en ambos casos los flujos son iniciados repentinamente. Las simulaciones se hicieron con métodos de elementos de frontera (BEM). Estas simulaciones se hicieron para diferentes razones de deformación entre vorticidad (parámetro del tipo de flujo) y para algunos valores del número capilar, dando énfasis a la evolución transitoria de la gota de su forma inicial hasta su forma estacionaria. Las simulaciones muestran que los campos de flujo interno y externo presentan una gran riqueza de características interesantes. Dentro del intervalo de valores del parámetro del tipo de flujo utilizado, se observa la transición de un comportamiento oscilatorio periódico amortiguado a un comportamiento no oscilatorio, para todos los valores del número capilar estudiados.

Resumen

Hidrodinámica de objetos deformables en flujos lentos

En la naturaleza y en procesos científicos y tecnológicos, se llevan a cabo flujos de sustancias que están constituidas por partículas y una fase fluida, como son las suspensiones, las emulsiones, la sangre, spray, tintas, espumas, polímeros, en la extracción y transporte del petróleo en tuberías, en el proceso y transporte de pinturas, reactivos farmacéuticos, alimentos procesados, entre otros. Particularmente, a este tipo de sustancias se les conoce como fluidos complejos, que se caracterizan por tener una estructura con longitud de escala mesoscópica (10 a 100 nanómetros). Debido a la vasta presencia de estas sustancias, el entendimiento del comportamiento dinámico de los fluidos complejos es de alto interés científico y tecnológico, necesario para el diseño de nuevos productos como dispositivos microfluídicos, sistemas de dosificación de fármacos y procesos de cristalización.

Los fluidos complejos deben la mayoría de sus propiedades y comportamiento a su estructura dinámica. Estas estructuras pueden ser fácilmente modificadas por la presencia de flujos externos como los que se presentan durante el procesamiento de éstos. La riqueza en el comportamiento dinámico de los fluidos complejos surge de la interacción de la rapidez intrínseca de relajación estructural (relajación de cadenas poliméricas, relajación de la forma de gotas, redistribución de surfactantes en una interfaz fluida) y de la rapidez extrínseca de a la que se encuentra sometido, como la magnitud de la rapidez de corte o la frecuencia de oscilación. Es por ello que para lograr una optimización en las aplicaciones de fluidos complejos se requiere desarrollar la capacidad de predicción y control del comportamiento viscoelástico dinámico.

Debido a que un fluido complejo modifica su estructura cuando es sometido a condiciones de flujos externos, la caracterización éstos campos es necesaria para su estudio, y asimismo se requiere para cuantificar el grado de afectación del campo mismo. Entonces se tienen unas condiciones que se pueden llamar globales, que son las condiciones que se

varied, although with less flexibility than in Four-Roll Mills (see Bentley [7]). Compared to Four-Roll Mills, the Two-Roll Mill requires changes of geometry to obtain different values of rate of deformation to vorticity. In contrast and for a given geometry, the shear rate is a simple function of the speed of the cylinders. Also, the effects of the walls can be systematically taken into account both theoretically (analytically and numerically) as well as experimentally. The wall effects are evaluated introducing changes of the geometry of the Two-Roll Mill flow-device, while maintaining fixed all flow field parameters at the stagnation point. That is, for an object located at the center of the flow, wall effects are modified by closing or opening the gap between the cylinders but maintaining identical kinematics. Finally, by choosing the set of liquids appropriately, the material properties can be varied at will.

This work long-term objective is to model drop dynamics through a converging-expanding channel under well characterized conditions. In particular, Two-Roll Mills provide us with an appropriate tool for modeling the relevant kinematics. The short-term objective is to study the dynamics of drops and physical properties of the two fluids associated to flow-induced changes on the shape of the drop. Furthermore, the flow field characteristics can be systematically proved, varying the ratio of stretching to vorticity (similar to flows encountered through pore channel structures). Varying the cylinders speeds in time, different time-histories can be applied to a drop, proving phenomena with different time-scales. Surface tension effects can also be studied, and used to elucidate effects of additives and modifiers of surface phenomena associated to surfactants. This combination of devices, analytical techniques and materials has not been reported in the scientific literature.

This analytical solution is a series solution of Stokes' problem (flows with small Reynolds numbers) of a two-dimensional unbounded strong flow. This solution is an extension of the one presented earlier by Reyes and Geffroy [16]. It is especially useful for a variety of problems in fluid mechanics, and is easily modeled in the laboratory using corotating Two-Roll Mills [17]. Because of the two dimensional flow field it is possible to measure optical and mechanical properties of the fluids, as well as all properties of the velocities field. In particular, it provides an expression for the potential function over the entire domain, as well as a particular solution for the region between the cylinders [17]. The theoretical predictions have a good correlation with published numerical results [18] and experimental observations [19]. This solution is thus of direct relevance to studies of viscoelastic fluids, because it permits knowledge of the applied deformation histories to fluids with structure. This point is crucial for studies of viscoelasticity and rheology of complex fluids. Also, it can provide important information about the dynamics of fluids typical in secondary methods for oil production.

The analytical solution previously reported is valid for Stokes flows generated by Two-Roll Mills when both cylinders rotate at the same speed and direction of rotation [17]. This Chapter presents a more general solution, which considers different speeds and all possible geometries amenable to Two-Roll Mills. All of these solutions imply significant amounts of vorticity in elongational flows, all the way up to the limit corresponding to vorticities of simple shear flows. In this way, Two-Roll Mill flows may represent a true option for studies of non-linear phenomena not presently available when using Four-Roll Mill or simple shear flow geometries. In particular, this flow cell may be useful when the orientation, shape and stresses are affected by the strong vorticity of the flows. Hence, these flows represent the supplementary kinematics to previous studies reported by Acrivos [4], Stone [3] and others, which are based mainly upon the use of Four-Roll Mill flow fields.

The following Figures show some of the features that exist in creeping flow fields generated by Two-Roll Mills, obtained from the previous solution. Figure 1.1 shows stream lines for symmetric corotating Two-Roll Mills for several ratios between the cylinders' radii and their axes distance, r_g. The ratio of deformation rates to vorticity (associated to the flow-type parameter, $0 < \lambda = \tan^2\theta \leq 1$) is a function of the geometry of the Two-Roll Mill, and is independent of the angular velocity of the cylinders. A stagnation point always exists along the line between the cylinders. θ is the angle of the incoming and outgoing stream line that cross the stagnation point.

Figure 1.2 presents a few flow parameters for a given symmetric Two-Roll Mill. This analytical solution is the basis for determining the stress fields imposed upon viscous drops suspended in this flow field. Among the parameters that can be varied for TRM flows in conjunction with drops are the strength of the vorticity, the rate of deformation (shear con la solución analítica muestra que se pueden obtener campos de flujo complejos que no han sido estudiados y que presentan nuevas opciones para realizar experimentos sobre gotas colocadas en el punto de estancamiento en campos de flujo bien caracterizados.

En el Capítulo 2 se presenta la solución numérica al flujo generado por un molino de dos rodillos acotado. La solución numérica se obtuvo utilizando el método de elementos de frontera. Esta solución considera la presencia de la frontera exterior del dispositivo o celda de flujos. Con base en esta solución, se calcula la influencia que tiene la frontera sobre el campo de flujo, haciendo énfasis en los efectos sobre la región central del campo. Esta herramienta permitió evaluar la validez de utilizar la solución analítica no acotada para modelar la región central del campo de flujo.

Para realizar comparaciones de la solución analítica con la numérica, se modelaron dos geometrías externas de las celdas de flujo y una geometría no acotada. La geometría no acotada se utilizó con el fin de calcular el error numérico de forma que se pueda discernir de la contribución de las fronteras externas. En general, el error numérico fue menor del 0.05 % en el punto de estancamiento, siendo mayor cuando el factor geométrico g/de es menor, debido probablemente a la cercanía de las fronteras y a una mayor longitud de los segmentos. Cuando se considera la presencia de las fronteras exteriores, la geometría etiquetada como TRM-B presenta mayor influencia de la frontera exterior a las propiedades del campo de flujo central, siendo la diferencia en el peor de los casos de menos del 1.2 %.

En el Capítulo 3, se propone un arreglo experimental basado en las la geometría de dos rodillos y se presenta un esquema de control para mantener gotas en el punto de estancamiento que presenta el flujo generado por los molinos de dos rodillos. Con base en las soluciones analítica y numérica, se diseñaron dos celdas de flujo. Con base en la solución analítica para molinos de dos rodillos de geometría generalizada y diferentes velocidades angulares se propone un esquema de control para gotas localizadas en el punto de estancamiento. Al variar el radio o la velocidad angular de alguno de los rodillos, el punto de estancamiento de desplaza de su posición, y es por medio del conocimiento del desplazamiento del punto de estancamiento, que se propone un esquema para poder arrastrar la gota cuando se ha alejado del punto de estancamiento cierta distancia permitida y regresar el centroide de ésta lo más cercano posible al punto de estancamiento; o igualmente se puede dejar el objeto en la trayectoria entrante del flujo. Con la solución analítica es posible calcular cada uno de los parámetros de interés (la rapidez de corte y el parámetro del tipo de flujo) que afectan a la deformación de la gota a través de toda la trayectoria recorrida por ésta.

El sistema de control debe de modificar el flujo lo menos posible, debido a que la respuesta de la gota depende fuertemente de las características del flujo. Este tipo de sistema de control pertenece al los denominados "determinísticos"

El sistema de control consta de los siguientes dispositivos: La celda de flujos que contiene a los dos rodillos, dos motores y sus fuentes de poder., dos cámaras para visualizar la posición y deformación de la gota, y una computadora para realizar la captura y procesamiento de las imágenes y calcular las velocidades angulares de los motores. Los factores que hay que controlar para poder llevar a cabo un control eficiente sobre la posición del centroide de la gota son los maquinados de alta precisión, la resolución del sistema óptico y la rapidez en la respuesta del sistema de control

Los parámetros a definir son la "tolerancia" o el área de control. Es una región alrededor del punto de estancamiento de interés en la cual el centroide de la gota está sujeto a las condiciones a estudiar. Cuando el centroide de la gota alcanza la orilla de esta región, el sistema de control se activa para regresar el centroide ya sea lo más cercano al punto de estancamiento o a un eje "entrante" del flujo. La tolerancia es función de la resolución de sistema óptico y de la precisión de los maquinados, y entre más pequeña se defina, el campo en esa región presenta un comportamiento más lineal, lo cual simplifica el problema y lo hace más estable.

Otro parámetro es el tiempo de respuesta del fluido a los cambios de velocidades angulares en los rodillos que depende de la viscosidad del sistema.

El algoritmo del sistema de control está basado en la capacidad de mover el punto de estancamiento a lo largo de la línea entre los ejes de los rodillos, por medio del cambio en la razón entre las velocidades angulares de éstos. El sistema de control aplica las condiciones experimentales cuando el centroide de la gota se encuentra dentro de un intervalo definido por la máxima variación permisible en los parámetros del flujo, y cuando el centroide de la gota alcanza los límites de ese intervalos el sistema de control calcula la razón de velocidades angulares que llevan al centroide nuevamente a la posición deseada para el experimento.

Las aproximaciones que se utilizaron en el sistema de control son que se trata de un flujo a bajo número de Reynolds, que el campo de flujo no se ve afectado por la presencia de la gota (supone por lo tanto gotas pequeñas en comparación con la separación entre las superficies de los rodillos), y que la variación temporal de las velocidades angulares de los rodillos se suponen los suficientemente lentas, además de que la variación de las velocidades angulares es pequeña, por lo que utilizamos la ecuación de Stokes.

Este tipo de dispositivos, al igual que el molino de cuatro rodillos permite el uso de técnicas ópticas para la adquisición de datos, lo cual hace que este tipo de dispositivos sean ideales para estudios de efectos de Marangoni, etc.

Los campos generados por el molino de dos rodillos pueden variarse de diferentes formas, se pueden escoger diferentes puntos de estancamiento para una misma geometría, no necesariamente el que se encuentra en la región central cuando el tamaño de los rodillos y sus velocidades angulares son iguales. En este caso se tienen condiciones de flujo que son asimétricas, donde se tienen además gradientes en los campos del parámetro del tipo de flujo y la rapidez de cortante igualmente asimétricos y cuyos máximos y mínimos ya no coinciden con el punto de estancamiento como en el caso simétrico. En el caso de flujo de emulsiones dentro de tuberías que se expanden y contraen, cuando una partícula se encuentra en el eje de la tubería, se haya sometida a condiciones semejantes a experimentos en el molino de dos rodillos donde la gota se mantiene en el punto de estancamiento que cambia de posición a lo largo del eje y. Se pueden realizar también experimentos periódicos y toda una gama de experimentos.

En la Parte II se estudia numéricamente la dinámica de gotas por medio de la técnica de elemento de frontera. En el Capítulo 4 da una introducción a la física de gotas y al método de elementos de frontera aplicado a gotas en flujos. En el Capítulo 5, se utiliza la técnica descrita en el Capítulo 4 para estudiar la dinámica de gotas viscosas bidimensionales inmersas en flujos lineales no acotados y en flujos generados por molinos de dos rodillos (acotados), dando énfasis a la clase de flujos que no han sido incluidos en la mayoría de los estudios publicados. Las simulaciones fueron realizadas para varios valores del parámetro del tipo de flujo (0, 0.03, 0.1, 0.15, 0.2 y 0.3) y para algunos valores del número capilar (0.23, 0.5, 1, 1.5 y 2). También se estudia la evolución transitoria de la forma inicial de la gota hasta su forma estacionaria. Las simulaciones muestran que los campos de flujo externo e interno presentan una gran riqueza de características cuando el parámetro del tipo de flujo y el número capilar son variados.

Para los casos en donde los campos de flujo llevan a formas estacionarias en las gotas, se presenta una transición en el comportamiento que es función de la relación entre vorticidad y deformación. En los casos en donde el número capilar es mayor que el capilar crítico, se da énfasis al entendimiento de la transición que ocurre en el flujo interior de la gota, de un flujo dominado por la vorticidad a un flujo dominado por la deformación.

Las simulaciones de la dinámica de gotas realizadas en esta tesis fueron bidimensionales, sin embargo, la información obtenida de ellas es útil cuando se trata de números capilares pequeños. A pesar de estas limitaciones, los estudios muestran una riqueza de fenómenos que generan una oportunidad de realizar estudios experimentales que ampliarán el entendimiento de estos fenómenos y complementan los estudios realizados en molinos de cuatro rodillos y dispositivos de flujo cortante simple.

Contents

Part I

Flows generated by Two-Roll Mills

Introduction to Part I

Complex fluids are present in many common products. Usually, these are soft condensed materials such as emulsions, foams, polymers, colloidal suspensions, and liquid crystals. They are involved in the processing and transport of paints, inks, coatings, lubricants, detergents, polymers, polymer blends, pharmaceutical reagents, and processed foods. Enhanced oil recovery and soil and groundwater remediation often involve the use of complex fluids. An understanding of complex fluid dynamics is also needed for the design of new technological products such as microfluidic devices, drug delivery systems, and protein separation and crystallization processes.

Complex fluids owe most of their properties and behavior to a dynamic *microstructure.* These microstructures can be easily modified or disrupted by the presence of external fields such as those encountered during processing. In particular, equilibrium microstructures of complex fluids are readily distorted by an imposed flow or stress field. The rich dynamic behavior of complex fluids arises from the interplay of intrinsic microstructural relaxation rates (e.g., recoiling of polymer chains, relaxation of drop-shapes, redistribution of surfactant on a fluid interface) and comparable extrinsic rates, such as an imposed shear rate, or oscillation frequency. Hence, engineering applications of complex fluids require developing the capacity of prediction and control of its viscoelastic dynamic behavior. That is, its rheology must be based upon the knowledge of its microstructure evolution and stability. For example, the control of a coating flow may require a material that flows when subjected to a sufficient high shearing stress, but not to a moderate buoyancy stress. In other applications, high viscosity fluids are efficiently transported by dispersing them in a low viscosity fluid.

Drops and bubbles are present in a large number of natural as well as man-made complex fluids. In nearly every situation, these simpler fluid particles, which may lie within a continuum of another fluid or another state of the same fluid, have an important bearing on the physical behavior of the system. For most cases, the global response of the two-phase system is dominated by non-linear effects. That is, the response of a fluid drop to stresses generated by a second liquid is frequently determined by whether dispersion of drops occurs, or whether only deformation of the drop exists. Thus, knowledge of the bubbles, drops, or particles' behaviors is very important in a variety of applications and chemical processes. Most importantly, the physics associated to interfaces among two-fluid systems are of great relevance for many of the processes that involve nanosciences or processes in nanotechnology. In this manner, drops and bubbles give us a useful starting point for understanding of more realistic multi-particle systems such as those found in complex fluids [1].

The response of a viscous drop embedded in a second fluid depends on four factors: (1) on its intrinsic properties, such as its viscosity and density, as well as the viscosity of the environment; (2) on the surface tension that exists between both liquids; (3) on the flow characteristics applied by the surrounding liquid; and (4) on the flow history and geometry of the flow device.

In particular there are several flow geometries, mainly those associated to so-called strong flows, which are most relevant for these studies. Strong flows are extensional flows, capable of significant deformation histories. Until now, the bulk of theoretical and experimental studies with strong flows have addressed the fluid dynamics of pure extensional flows, without any vorticity, elongational flows with small amounts of vorticity, or shear flows [2, 3]. This is a well developed field, with experimental devices that include robust controls of all flow parameters. With this setup, drop deformations can be studied under varied and well characterized kinematic conditions. However for most industrial applications of interest, knowledge of the hydrodynamics of drops is required, especially when mixed effects due to elongation and vorticity in the flow are concurrently present.

Earlier studies of the dynamics of drops have been summarized in excellent reviews by Acrivos [4], Rallison [2], Stone [3] and by Briscoe and coworkers [5]. The current understanding of drop dynamics in linear flows *with a strong degree of elongation* is quite comprehensive, especially in relation to effects caused by variation of flow parameters. Among the most important parameters that determine the response of the drop to the deformation rates studied thus far are the surface tension of the drop, the viscosity ratio of the fluids, the shear rate of the flow, and the ratio of deformation rate to vorticity. When the flow is confined by walls, the drop diameter to channel gap ratio and initial drop position and shape [6] are also important. Briscoe et al., [5] present as well a review of effects of surfactants upon immiscible fluid mixing. However, the observed phenomena due to surface tension effects, the presence of nearby boundaries, and those effects due to the presence of electromagnetic forces has had a less complete review, and a more precarious degree of understanding exists until now.

In this Thesis, two different but complementary methodologies will be presented for study the dynamic of drops. That is, besides taking into account stresses generated by a linear flow at the immiscible interface of the drop, this work introduces a new experimental device and a new theoretical tool. Firstly, it is possible to construct a computer-controlled Two-Roll Mill flow device, conceptually similar to that of Bentley and Leal [7]. This new flow cell is capable of providing detailed experimental information about drop dynamics under conditions that include the effects of elongation with significant vorticity, nearby walls, and the presence of surfactants or other polymeric additives. Secondly, for this flow cell geometry it is also possible to apply pure analytical techniques capable of considering finite flow domains, surface tension effects, and other long-range forces. Albeit the experimental device requiring a control scheme with less degrees of freedom than that previously reported by Bentley and Leal [7], the new control appears to be equally robust but slower because it uses a more complex control trajectory. Conversely, the advantage provided by the analytical solution is a better predictive capacity of flow dynamics using these mills. In this manner, drop phenomena analyzed with this experimental setup are similar kinematically, from the point of view of the applicable boundary conditions, as well as dynamically to the hydrodynamics of two-phase flows through pores and fractures.

Chapter 1 presents a mathematical model useful for determination of all properties of flows generated by Two-Roll Mills. In this manner, a simple device with known kinematics is used. In Chapter 2, numerical studies are presented evaluating Two-Roll Mill flows in a bounded domain such as those used in experimental devices. These numerical studies are the basis to address the hydrodynamics of deformation of drops under conditions accessible to experimental studies with two roll mills. Chapter 3 presents an experimental device with all associated components, required for studies of drop dynamics.

Chapter 1

Analytical solution for flows generated by Two-Roll Mills

For studies in fluid mechanics of non-Newtonian fluids [8, 9], chaotic advection [10, 11], drop and bubble dynamics [3, 12], and many industrial applications (e.g., see Stone [3]), the use of laminar flows capable of inducing significant deformation on the fluid microstructure on embedded objects is an essential tool. In general, these flows have proven advantageous for studies of fluid systems that show a marked nonlinear, hysteretic behavior due to its dynamic *microstructure*. Simple viscometric flows and purely extensional flows (see for example [13]) are among the two most frequently used flow fields that are kinematically different. However, on one hand, viscometric flows have significant amounts of vorticity, and are not expected to produce large deformations on an embedded object; thus, they are classified as *weak flows*. The observed behavior in viscometric steady flows is understood by parcels of fluid that at any given time separate linearly in time; i. e., at most the separation can only grow algebraically. Hence, these flows produce only a moderate change on the fluid structure. On the other hand, for steady extensional flows there is no vorticity and two neighboring elements of fluid separate in time exponentially; given enough time, the flow induces significant changes on the microstructure of the fluid regardless of its relaxation mechanisms; therefore, these are *strong flows* [14, 15].

In a Two-Roll Mill, the strength of vorticity and the shear rate can be easily varied, although with less flexibility than in Four-Roll Mills (see Bentley [7]). Compared to Four-Roll Mills, the Two-Roll Mill requires changes of geometry to obtain different values of rate of deformation to vorticity. In contrast and for a given geometry, the shear rate is a simple function of the speed of the cylinders. Also, the effects of the walls can be systematically taken into account both theoretically (analytically and numerically) as well as experimentally. The wall effects are evaluated introducing changes of the geometry of the Two-Roll Mill flow-device, while maintaining fixed all flow field parameters at the stagnation point. That is, for an object located at the center of the flow, wall effects are modified by closing or opening the gap between the cylinders but maintaining identical kinematics. Finally, by choosing the set of liquids appropriately, the material properties can be varied at will.

This work long-term objective is to model drop dynamics through a converging-expanding channel under well characterized conditions. In particular, Two-Roll Mills provide us with an appropriate tool for modeling the relevant kinematics. The short-term objective is to study the dynamics of drops and physical properties of the two fluids associated to flow-induced changes on the shape of the drop. Furthermore, the flow field characteristics can be systematically proved, varying the ratio of stretching to vorticity (similar to flows encountered through pore channel structures). Varying the cylinders speeds in time, different time-histories can be applied to a drop, proving phenomena with different time-scales. Surface tension effects can also be studied, and used to elucidate effects of additives and modifiers of surface phenomena associated to surfactants. This combination of devices, analytical techniques and materials has not been reported in the scientific literature.

This analytical solution is a series solution of Stokes' problem (flows with small Reynolds numbers) of a two-dimensional unbounded strong flow. This solution is an extension of the one presented earlier by Reyes and Geffroy [16]. It is especially useful for a variety of problems in fluid mechanics, and is easily modeled in the laboratory using corotating Two-Roll Mills [17]. Because of the two dimensional flow field it is possible to measure optical and mechanical properties of the fluids, as well as all properties of the velocities field. In particular, it provides an expression for the potential function over the entire domain, as well as a particular solution for the region between the cylinders [17]. The theoretical predictions have a good correlation with published numerical results [18] and experimental observations [19]. This solution is thus of direct relevance to studies of viscoelastic fluids, because it permits knowledge of the applied deformation histories to fluids with structure. This point is crucial for studies of viscoelasticity and rheology of complex fluids. Also, it can provide important information about the dynamics of fluids typical in secondary methods for oil production.

The analytical solution previously reported is valid for Stokes flows generated by Two-Roll Mills when both cylinders rotate at the same speed and direction of rotation [17]. This Chapter presents a more general solution, which considers different speeds and all possible geometries amenable to Two-Roll Mills. All of these solutions imply significant amounts of vorticity in elongational flows, all the way up to the limit corresponding to vorticities of simple shear flows. In this way, Two-Roll Mill flows may represent a true option for studies of non-linear phenomena not presently available when using Four-Roll Mill or simple shear flow geometries. In particular, this flow cell may be useful when the orientation, shape and stresses are affected by the strong vorticity of the flows. Hence, these flows represent the supplementary kinematics to previous studies reported by Acrivos [4], Stone [3] and others, which are based mainly upon the use of Four-Roll Mill flow fields.

The following Figures show some of the features that exist in creeping flow fields generated by Two-Roll Mills, obtained from the previous solution. Figure 1.1 shows stream lines for symmetric corotating Two-Roll Mills for several ratios between the cylinders' radii and their axes distance, r_g. The ratio of deformation rates to vorticity (associated to the flow-type parameter, $0 < \lambda = \tan^2\theta \leq 1$) is a function of the geometry of the Two-Roll Mill, and is independent of the angular velocity of the cylinders. A stagnation point always exists along the line between the cylinders. θ is the angle of the incoming and outgoing stream line that cross the stagnation point.

Figure 1.2 presents a few flow parameters for a given symmetric Two-Roll Mill. This analytical solution is the basis for determining the stress fields imposed upon viscous drops suspended in this flow field. Among the parameters that can be varied for TRM flows in conjunction with drops are the strength of the vorticity, the rate of deformation (shear

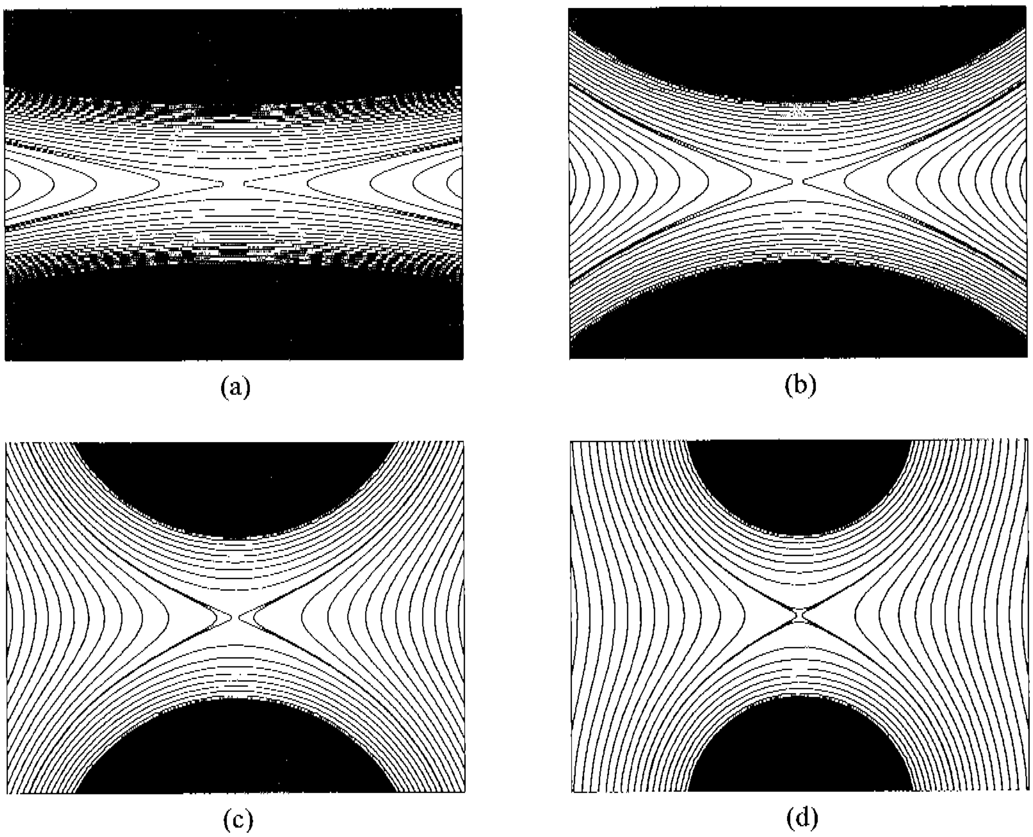
(a) (b) (c) (d)

FIGURE 1.1. Stream lines for symmetric corotating Two-Roll Mills for several ratios between the cylinders' radii and their axes distance, r_g. Their associated ratios of deformation rate to vorticity (flow-type parameter), λ, are also given. (a) $r_g = 0.057$, $\lambda = 0.03$; (b) $r_g = 0.176$, $\lambda = 0.1$; (c) $r_g = 0.303$, $\lambda = 0.2$; and (d) $r_g = 0.412$, $\lambda = 0.3$.

rate), the ratio of viscosities between the liquids, the interfacial tension, the kinematics of surfactants at the interface of the liquids, etc.

Ottino and coworkers [10] have presented a numerical solution for a *bounded* Two-Roll Mill, with variations of the speed and direction of rotation of cylinders, size of cylinders, etc. These results show rich phenomena when the latter parameters are changed. Ottino's results are important for studies of chaotic advection, and the lack of exact solutions is a significant drawback for detailed comparisons of different advection models and chaotic dynamics techniques. Therefore, it is also of interest to investigate possible exact solutions for Stokes flows induced by more general Two-Roll Mill conditions, in particular, asymmetric

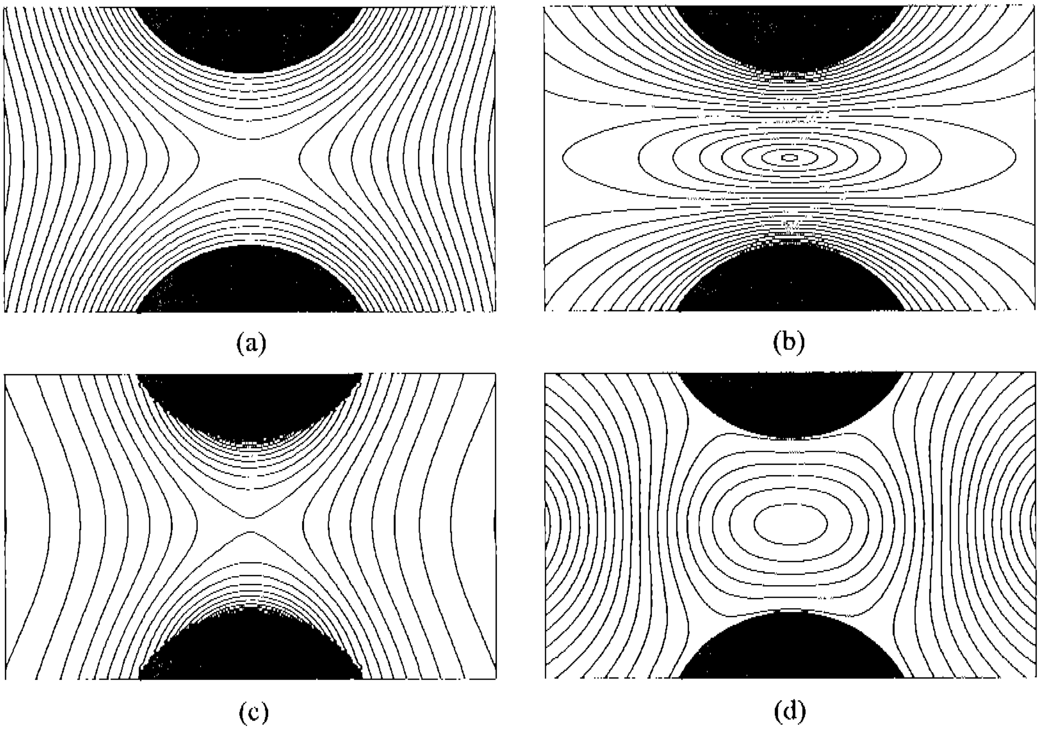

FIGURE 1.2. Several properties of the flow field generated by a Two-Roll Mill with cylinders of equal radii and same angular velocities. Graph (a) shows the streamlines; (b) isopleths for the magnitude of the velocity field $\|\mathbf{u}\|$, with the stagnation point located at the center between the cylinders; (c) isopleths for the magnitude of the gradient of the velocity field $\dot{\gamma}$, with maximum values at the cylinders surfaces; and (d) isopleths for the flow-type parameter λ, the ratio of deformation rates to vorticity, with its larger values of at the center of the flow field.

asynchronous mills. Furthermore, Ballal and Rivlin [20] have obtained an exact solution for the linearized inertia flow in eccentric annular flow. This methodology may also serve as a model to consider the effects of inertia for flows generated with the Two-Roll Mill geometry. The objective of a "linearized inertia" solution is the capacity to model strong flows with finite Reynolds numbers up to order one.

1.1 Solution for TRMs with different size cylinders and angular velocities

The presently available solution assumes equal radii and equal values for the stream function on the cylinders, implying equal constant angular speed for each one. In general, the constraint of equal radii and angular speed should be relaxed, and it is also desirable a solution capable of evaluating *non-steady* flow conditions. In order to reach these goals, a solution should be sought with fewer constraints regarding steadiness and symmetry of the flow. This solution may be useful for cases in which asymmetric vorticity fields may exist due to components of the velocity gradient about the stagnation point which may be significantly different from flow fields generated with Four-Roll Mills. This point will be addressed in Figures 1.13-1.16. Mills with cylinders of different size, different angular speeds in corotational sense of direction will be referred now as asymmetric Two-Roll Mills.

The solution for an asymmetric Two-Roll Mill assumes a steady, two-dimensional flow as if generated by cylinders of infinite length and rotating with different angular velocities. Inertial terms are considered negligible. For corotating Two-Roll Mills, there always exists a stagnation point on the line between the cylinders' axes. At the stagnation point, local kinematic conditions are characteristic of an elongational flow with some vorticity. Also in the more general geometry, the kinematics is defined only by the angular velocity of the cylinders, and by their geometric aspect, i.e., each cylinder's diameter and the separation between them. Thus, one of the interesting features of the strong flow field generated by these mills is the fact that the solution takes into account, firstly, the presence of the cylinders at a finite distance, and secondly, that all flow parameters are defined by the mill's geometry.

Given that bipolar cylindrical coordinates are the natural reference frame for systems composed of two cylinders (see Appendix A), an important set of flow devices have already been theoretically and experimentally studied. In 1922, G. B. Jeffery [21] presented a solution for the Stokes flow generated *inside the annular region* of eccentric cylinders. The solution prescribes the boundary of the cylinders by constant values of one of the bipolar coordinates [1, 22]. The stream function satisfies the biharmonic equation, and Jeffery exploited the well known relationship between Stokes flow and the analytical solution for the applied stresses on a plate that he previously had obtained [23].

In this Section, an analytical solution for the asymmetric Two-Roll Mill is presented, based on the general solution proposed by Jeffery [21]. With the appropriate boundary conditions, a set of equations is obtained for evaluating all coefficients of the stream function ψ. This solution prescribes the position of the stagnation point for variations in the angular velocity on the cylinders, and all flow field properties [17]. The general solution is expressed in bipolar coordinates, providing models for two-dimensional mills without an external boundary (infinite domain). Based on this solution, it is possible to build experimental devices that generate flows with properties close to those prescribed by the analytical solution for an ample region that includes the stagnation point. This solution is the basis for experimental mills as well as for developing a control scheme essential for studies of deformation of drops during long times.

1.1.1 Stream function for an unbounded Two-Roll Mill

Two-dimensional creeping flows are described by the biharmonic equation $\nabla^4\psi = 0$, plus the appropriate boundary conditions. The general solution that Jeffery [23] obtained, in bipolar coordinates, for the stream function is

$$\begin{aligned}\frac{\psi}{h} &= A_0\cosh\alpha + B_0\,\alpha\,(\cosh\alpha - \cos\beta) + C_0\sinh\alpha \\ &\quad + D_0\,\alpha\sinh\alpha + K\,(\cosh\alpha - \cos\beta)\ln(\cosh\alpha - \cos\beta) \\ &\quad + (A_1\cosh 2\alpha + B_1 + C_1\sinh 2\alpha)\cos\beta \\ &\quad + \left(A_1'\cosh 2\alpha + C_1'\sinh 2\alpha\right)\sin\beta \\ &\quad + \sum_{n=2}^{\infty}\left(\phi_n(\alpha)\cos n\beta + \phi_n'(\alpha)\sin n\beta\right) \\ &\quad + (E\cos\beta + F\sin\beta + G\cosh\alpha + H\sinh\alpha)\,\beta, \end{aligned} \tag{1.1}$$

where h is the metric factor

$$h = \frac{a}{(\cosh\alpha - \cos\beta)}, \tag{1.2}$$

and the functions $\phi_n(\alpha)$ and $\phi_n^{'}(\alpha)$ are

$$\begin{aligned}\phi_n(\alpha) &= A_n\cosh(n+1)\alpha + B_n\cosh(n-1)\alpha\\ &\quad + C_n\sinh(n+1)\alpha + D_n\sinh(n-1)\alpha,\end{aligned}\tag{1.3}$$

and

$$\begin{aligned}\phi_n^{'}(\alpha) &= A_n^{'}\cosh(n+1)\alpha + B_n^{'}\cosh(n-1)\alpha\\ &\quad + C_n^{'}\sinh(n+1)\alpha + D_n^{'}\sinh(n-1)\alpha.\end{aligned}\tag{1.4}$$

Given a geometry, i. e., the values of the gap between the cylinders, g (or the distance between the axes of the cylinders, $de = g + R_1 + R_2$), and the cylinders radii R_1 and R_2, the geometric parameter a is given by

$$a = \frac{\sqrt{g\,(g+2R_1)\,(g+2R_2)\,(g+2R_1+2R_2)}}{2\,(g+R_1+R_2)}.\tag{1.5}$$

With this calculated value of a, the values of the coordinate α at each cylinder can be computed using the following equation

$$\alpha_R = \operatorname{arcsinh}\left(\frac{a}{R}\right).\tag{1.6}$$

The stream function is simplified by using the symmetric and antisymmetric conditions of the velocity field (see Fig. 1.3), which are obtained by mean of the velocity vector

$$\mathbf{u} = \nabla\times\boldsymbol{\psi} = \frac{1}{h^2}\begin{vmatrix} h\mathbf{e}_1 & h\mathbf{e}_2 & \mathbf{e}_3\\ \frac{\partial}{\partial\alpha} & \frac{\partial}{\partial\beta} & \frac{\partial}{\partial z}\\ 0 & 0 & \psi\end{vmatrix} = \frac{1}{h}\frac{\partial\psi}{\partial\beta}\mathbf{e}_1 - \frac{1}{h}\frac{\partial\psi}{\partial\alpha}\mathbf{e}_2.\tag{1.7}$$

Thus, the velocity components are

$$u_\alpha = \frac{1}{h}\frac{\partial\psi}{\partial\beta} = \frac{\partial(\psi/h)}{\partial\beta} - \left(\frac{\psi}{h}\right)\left(h\frac{\partial(1/h)}{\partial\beta}\right),\tag{1.8}$$

and

$$u_\beta = -\frac{1}{h}\frac{\partial\psi}{\partial\alpha} = -\frac{\partial(\psi/h)}{\partial\alpha} + \left(\frac{\psi}{h}\right)\left(h\frac{\partial(1/h)}{\partial\alpha}\right).\tag{1.9}$$

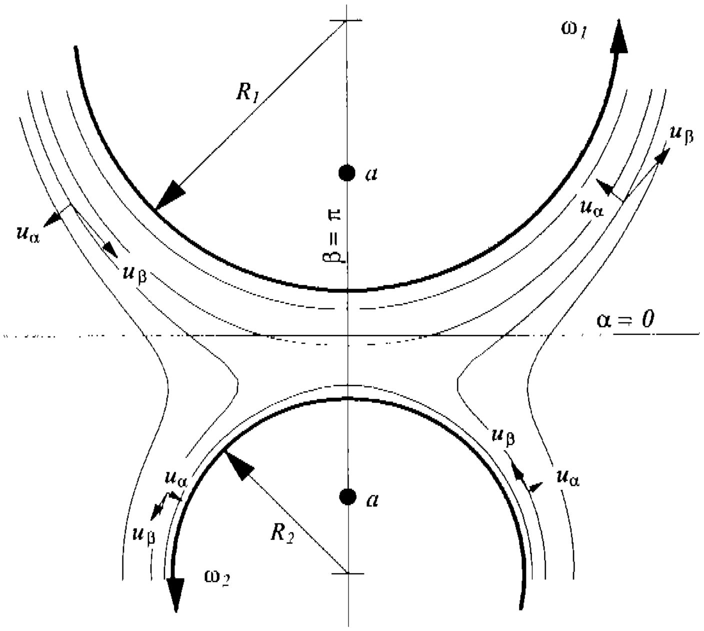

FIGURE 1.3. Symmetry of the flow generated by a Two-Roll Mill. Paths for several stream lines and the direction of velocity's components at a few points are also shown.

In an expanded form, the velocity components become

$$\begin{aligned}
u_\alpha = \sin\beta\,&\Big(B_0\,\alpha + K\left(\ln\left(\cosh\alpha - \cos\beta\right) + 1\right) - A_1\cosh 2\alpha + B_1 + C_1\sinh 2\alpha\Big)\\
&+ \cos\beta\,\Big(A_1^{'}\cosh 2\alpha + C_1^{'}\sinh 2\alpha\Big)\\
&+ \sum_{n=2}^{\infty}\Big[-n\sin n\beta\,\Big(A_n\cosh\left(n+1\right)\alpha + B_n\cosh\left(n-1\right)\alpha\\
&\qquad\qquad\qquad + C_n\sinh\left(n+1\right)\alpha + D_n\sinh\left(n-1\right)\alpha\Big)\\
&\qquad + n\cos n\beta\,\Big(A_n^{'}\cosh\left(n+1\right)\alpha + B_n^{'}\cosh\left(n-1\right)\alpha\\
&\qquad\qquad\qquad + C_n^{'}\sinh\left(n+1\right)\alpha + D_n^{'}\sinh\left(n-1\right)\alpha\Big)\Big]\\
&- \frac{\psi}{h}\frac{\sin\beta}{\cosh\alpha - \cos\beta},
\end{aligned} \tag{1.10}$$

and

$$\begin{aligned}
u_\beta = &-A_0\ \sinh\alpha - B_0\left((\cosh\alpha-\cos\beta)+\alpha\sinh\alpha\right) - C_0\cosh\alpha \\
&- D_0\left(\alpha\cosh\alpha+\sinh\alpha\right) - K\sinh\alpha\left(1+\ln\left(\cosh\alpha-\cos\beta\right)\right) \\
&- \cos\beta\left(2A_1\sinh 2\alpha + 2C_1\cosh 2\alpha\right) - \sin\beta\left(2A_1'\sinh 2\alpha + 2C_1'\cosh 2\alpha\right) \\
&- \sum_{n=2}^{\infty}\Big[\cos n\beta\Big(\left(n+1\right)A_n\sinh\left(n+1\right)\alpha + \left(n-1\right)B_n\sinh\left(n-1\right)\alpha \\
&\qquad\qquad + \left(n+1\right)C_n\cosh\left(n+1\right)\alpha + \left(n-1\right)D_n\cosh\left(n-1\right)\alpha\Big) \\
&\qquad + \sin n\beta\Big(\left(n+1\right)A_n'\sinh\left(n+1\right)\alpha + \left(n-1\right)B_n'\sinh\left(n-1\right)\alpha \\
&\qquad\qquad + \left(n+1\right)C_n'\cosh\left(n+1\right)\alpha + \left(n-1\right)D_n'\cosh\left(n-1\right)\alpha\Big)\Big] \\
&+ \frac{\psi}{h}\frac{\sinh\alpha}{\cosh\alpha-\cos\beta}.
\end{aligned} \tag{1.11}$$

For corotating cylinders of different size, the flow field is symmetric with respect to the line described by the y axis in the xy plane: the vertical axis passing through the centers of the cylinders (i.e., $\beta = \pi$ in the region between the cylinders, and $\beta = 0$ for outside this region). Imposing this symmetry condition upon the flow field geometry and antisymmetric conditions upon the velocities, the stream function reduces to

$$\begin{aligned}
\frac{\psi}{h} = &A_0\cosh\alpha + B_0\,\alpha\ \left(\cosh\alpha-\cos\beta\right) + C_0\sinh\alpha \\
&+ D_0\,\alpha\ \sinh\alpha + K\ \left(\cosh\alpha-\cos\beta\right)\ln\left(\cosh\alpha-\cos\beta\right) \\
&+ \left(A_1\cosh 2\alpha + B_1 + C_1\sinh 2\alpha\right)\cos\beta \\
&+ \sum_{n=2}^{\infty}\Big(A_n\cosh\left(n+1\right)\alpha + B_n\cosh\left(n-1\right)\alpha \\
&\qquad + C_n\sinh\left(n+1\right)\alpha + D_n\sinh\left(n-1\right)\alpha\Big)\cos n\beta.
\end{aligned} \tag{1.12}$$

The stream function should also be supplemented with the appropriate boundary conditions. The first boundary condition prescribing the impenetrability of the cylinders' surfaces implies that the velocity component normal to the these surfaces is zero; that is,

$$u_\alpha\left(\alpha_R\right) = \left.\frac{1}{h}\frac{\partial\psi}{\partial\beta}\right|_{\alpha_R} = 0 \qquad \text{or} \qquad \psi\left(\alpha_R,\ \beta\right) = M_R, \tag{1.13}$$

where α_R is the bipolar coordinate that represent the cylinder perimeter and M_R is the value of the stream function at the cylinders' surface. The dynamic no-slip boundary condition is

$$u_\beta\left(\alpha_R\right) = -\frac{1}{h}\frac{\partial \psi}{\partial \alpha}\bigg|_{\alpha_R} = \omega\, R = \frac{a\,\omega}{\sinh \alpha_R}, \tag{1.14}$$

with ω being the angular velocity in $\mathrm{rad\,s^{-1}}$, and R is the cylinder's radius. These conditions apply to each one of the cylinders, specifying the radius and angular velocity. Finally, at infinity, the fluid must remain at rest, then

$$\mathbf{u}\left(\alpha = 0,\ \beta = 0\right) = \mathbf{0}. \tag{1.15}$$

Thus,

$$\lim_{\substack{\alpha\longrightarrow 0,\\ \beta\longrightarrow 0}} u_\alpha = A_0 + \sum_{n=1}^{\infty}\left(A_n + B_n\right) = 0, \tag{1.16}$$

$$\lim_{\substack{\alpha\longrightarrow 0,\\ \beta\longrightarrow 0}} u_\beta = -C_0 - 2C_1 - \sum_{n=2}^{\infty}\left(\left(n+1\right)C_n + \left(n-1\right)D_n\right) = 0. \tag{1.17}$$

With these boundary conditions (as prescribed by Eqs. 1.13 – 1.15) and using the expansion for the logarithmic term presented at the Appendix C, a system of equations is obtained, which can be solved for each one of the unknown coefficients.

Then, replacing Eq. C.24 into the stream function, Eq. 1.12, this can be recast as

$$\begin{aligned}\frac{\psi}{h} &= A_0\cosh\alpha + B_0\,\alpha\left(\cosh\alpha - \cos\beta\right) + C_0\sinh\alpha + D_0\,\alpha\sinh\alpha\\ &\quad + K\left(\mathrm{b}_0 + \mathrm{b}_1\cos\beta + \sum_{n=2}^{\infty}\mathrm{b}_n\cos n\beta\right)\\ &\quad + \left(A_1\cosh 2\alpha + B_1 + C_1\sinh 2\alpha\right)\cos\beta\\ &\quad + \sum_{n=2}^{\infty}\Big(A_n\cosh\left(n+1\right)\alpha + B_n\cosh\left(n-1\right)\alpha\\ &\qquad + C_n\sinh\left(n+1\right)\alpha + D_n\sinh\left(n-1\right)\alpha\Big)\cos n\beta.\end{aligned} \tag{1.18}$$

Applying the boundary condition given by Eq. 1.13 into Eq. 1.18, the following equation is obtained

$$\begin{aligned}\frac{1}{h}\psi(\alpha_R,\beta) = \left(\frac{\cosh\alpha}{a} - \frac{\cos\beta}{a}\right)\; M_R = \\ A_0\cosh\alpha_R + B_0\,\alpha_R\,(\cosh\alpha_R - \cos\beta) + C_0\sinh\alpha_R \\ + D_0\,\alpha_R\,\sinh\alpha_R + K\left(\mathrm{b}_0 + \mathrm{b}_1\cos\beta + \sum_{n=2}^{\infty}\mathrm{b}_n\cos n\beta\right) \\ + (A_1\cosh 2\alpha_R + B_1 + C_1\sinh 2\alpha_R)\cos\beta \\ + \sum_{n=2}^{\infty}\Big(A_n\cosh(n+1)\,\alpha_R + B_n\cosh(n-1)\,\alpha_R \\ + C_n\sinh(n+1)\,\alpha_R + D_n\sinh(n-1)\,\alpha_R\Big)\cos n\beta.\end{aligned} \tag{1.19}$$

Arranging all terms of the same order of $\cos n\beta$, a system of $n+2$ equations is obtained for each one of the cylinders

$$\begin{aligned}A_0\cosh\alpha_{R_{1,2}} + B_0\,\alpha_{R_{1,2}}\cosh\alpha_{R_{1,2}} + D_0\,\alpha_{R_{1,2}}\sinh\alpha_{R_{1,2}} \\ + C_0\sinh\alpha_{R_{1,2}} + K\;\mathrm{b}_0\left(\alpha_{R_{1,2}}\right) - \frac{M_{R_{1,2}}}{a}\cosh\alpha_{R_{1,2}} = 0,\end{aligned} \tag{1.20}$$

$$-B_0\,\alpha_{R_{1,2}} + A_1\cosh 2\alpha_{R_{1,2}} + B_1 + C_1\sinh 2\alpha_{R_{1,2}} + K\;\mathrm{b}_1\left(\alpha_{R_{1,2}}\right) + \frac{M_{R_{1,2}}}{a} = 0. \tag{1.21}$$

And for $n \geq 2$

$$\begin{aligned}A_n\cosh(n+1)\,\alpha_{R_{1,2}} + B_n\cosh(n-1)\,\alpha_{R_{1,2}} + C_n\sinh(n+1)\,\alpha_{R_{1,2}} \\ + D_n\sinh(n-1)\,\alpha_{R_{1,2}} + K\;\mathrm{b}_n\left(\alpha_{R_{1,2}}\right) = 0,\end{aligned} \tag{1.22}$$

where $\alpha_{R_{1,2}}$ represents the α coordinate for cylinder one (R_1) or cylinder two (R_2).

Now, applying boundary condition given by Eq. 1.14 into Eq. 1.18, the following equation is obtained

$$
\begin{aligned}
\frac{a\,\omega_R}{\sinh\alpha_R} = & -A_0\sinh\alpha_R - B_0\left(\alpha_R\sinh\alpha_R+\cosh\alpha_R\right) \\
& - C_0\cosh\alpha_R - D_0\left(\alpha_R\cosh\alpha_R+\sinh\alpha_R\right) \\
& + \left(B_0 - 2A_1\sinh 2\alpha_R - 2\,C_1\cosh 2\alpha_R\right)\cos\beta \\
& - K\,\sinh\alpha_R\left(1+\mathrm{a}_0+\sum_{n=1}^{\infty}\mathrm{a}_n\cos n\beta\right)+\frac{M_R}{a}\sinh\alpha_R \\
& - \sum_{n=2}^{\infty}\cos n\beta\Big((n+1)\,A_n\sinh(n+1)\,\alpha_R \\
& \qquad + (n-1)\,B_n\sinh(n-1)\,\alpha_R \\
& \qquad + (n+1)\,C_n\cosh(n+1)\,\alpha_R \\
& \qquad + (n-1)\,D_n\cosh(n-1)\,\alpha_R\Big)\,. \qquad (1.23)
\end{aligned}
$$

And again, arranging the terms of the same order of $\cos n\beta$, another system of $n{+}2$ equations is obtained for each one of the cylinders

$$
\begin{aligned}
& A_0\sinh\alpha_{R_{1,2}} + B_0\left(\alpha_{R_{1,2}}\sinh\alpha_{R_{1,2}}+\cosh\alpha_{R_{1,2}}\right)+C_0\cosh\alpha_{R_{1,2}} \\
& \quad + D_0\left(\alpha_{R_{1,2}}\cosh\alpha_{R_{1,2}}+\sinh\alpha_{R_{1,2}}\right)+K\,\sinh\alpha_{R_{1,2}}\left(1+\mathrm{a}_0\left(\alpha_{R_{1,2}}\right)\right) \\
& \qquad -\frac{M_{R_{1,2}}}{a}\sinh\alpha_{R_{1,2}}+\omega_{R_{1,2}}\left(\frac{a}{\sinh\alpha_{R_{1,2}}}\right)=0, \qquad (1.24)
\end{aligned}
$$

$$
-B_0 + 2A_1\sinh 2\alpha_{R_{1,2}} + 2\,C_1\cosh 2\alpha_{R_{1,2}} + K\,\mathrm{a}_1\left(\alpha_{R_{1,2}}\right)\sinh\alpha_{R_{1,2}} = 0. \qquad (1.25)
$$

And for $n \geq 2$

$$
\begin{aligned}
& (n+1)\,A_n\sinh(n+1)\,\alpha_{R_{1,2}} + (n-1)\,B_n\sinh(n-1)\,\alpha_{R_{1,2}} \\
& \quad + (n+1)\,C_n\cosh(n+1)\,\alpha_{R_{1,2}} + (n-1)\,D_n\cosh(n-1)\,\alpha_{R_{1,2}} \\
& \qquad + K\,\mathrm{a}_n\left(\alpha_{R_{1,2}}\right)\sinh\alpha_{R_{1,2}} = 0. \qquad (1.26)
\end{aligned}
$$

There are $4n+10$ equations, $4n+8$ unknowns corresponding to coefficients A_0, A_1, A_n, B_0, B_1, B_n, C_0, C_1, C_n, D_0, D_n and K, plus the two values of the stream function on the surface of the cylinders M_{R_1} and M_{R_2}. Solving Eqs. 1.22 and 1.26 for a given geometry, the A_n, B_n, C_n and D_n coefficients are obtained as functions of K. In the same form, solving Eqs. 1.20, 1.21, 1.24, and 1.25, coefficients A_0, A_1, B_0, B_1, C_0, C_1, D_0 and M_{R_2}, can be obtained as functions of K, ω_1, and ω_2. Only coefficients A_0 and A_1, and M_{R_2} have an explicit dependence on M_{R_1}, with the following relations:

$$A_0 = F_1(K) + G_1(\omega_1) + H_1(\omega_2) + \frac{M_{R_1}}{a}, \tag{1.27a}$$

$$B_1 = F_2(K) + G_2(\omega_1) + H_2(\omega_2) - \frac{M_{R_1}}{a}, \tag{1.27b}$$

$$M_{R_2} = F_3(K) + G_3(\omega_1) + H_3(\omega_2) + M_{R_1}. \tag{1.27c}$$

Now, using Eq. 1.16, the K coefficient can be evaluated. In this case, K is only a function of ω_1 and ω_2, in agreement with Eqs. 1.16 and 1.27. Thus,

$$K = K(\omega_1, \omega_2). \tag{1.28}$$

Finally, only Eq. 1.17 remains to be satisfied. After substituting the corresponding expressions of all coefficients, an equation is obtained that depends only of the angular velocities, ω_1 and ω_2. This result means that there is not a general closed-form solution for the TRM geometry; there is only a closed-form solution for certain values of ω_2/ω_1 that satisfy the far field condition. In spite of this fact there is, in general, nonsteady motion of the fluid for which the velocity of the fluid vanishes at infinity. For those cases that a closed solution does not exist, the approximation of the creeping motion ceases to be accurate far from the cylinders. This condition is to be expected far away from the cylinders, because Stokes paradox implies that the inertia dominates the flow field region at infinity. However, a solution that can be valid in the region near the cylinders is sought; hence, this solution can be useful for this work purposes. The shaded area in Fig. 1.4 shows values of the ratio between the magnitude of the velocity at infinity and the maximum velocity in the flow (which occurs at the cylinder surface), u_∞/U_{Max}. This Graph is valid for a Two-Roll Mill with equal cylinders' radii. The maximum value for this ratio is obtained when one of the cylinders is stationary. A closed-form solution exists when the angular velocities are equal. For any mill with different cylinders' radii, a closed solution always exists for particular values of the ratio between the angular velocities of the cylinders.

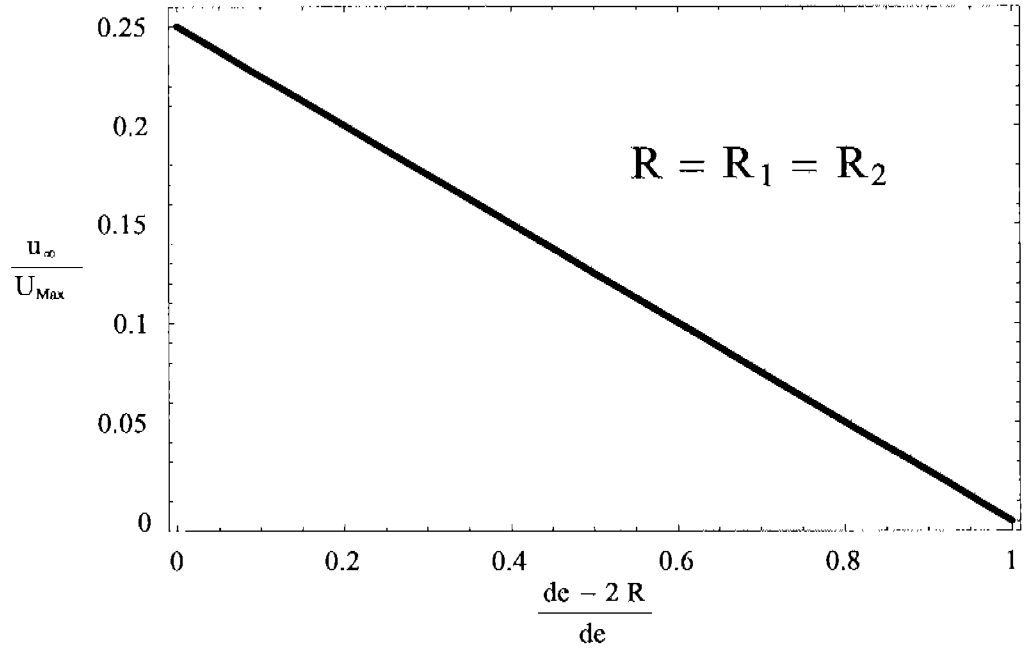

FIGURE 1.4. The gray area corresponds to possible ratios of the magnitude of the velocity at infinity between the maximum velocity in the flow, u_∞/U_{Max}, versus the TRM geometry factor, $(dc - 2R)/dc = g/dc$. The maximum value (continuous line) is obtained when one of the cylinders is stationary. The abscissa covers the full range of possible geometries; simple shear flow corresponds to a value of $g/dc = 0$.

1.2 Properties of the flow field generated by Two-Roll Mills

Figure 1.5 shows the streamlines for flows generated in a TRM geometry, with different angular velocities for each cylinder. The main stagnation point is located at the dot between the cylinders. In this Figure, the first graph corresponds to the angular velocity ratio ω_2/ω_1 valid for the closed solution (r_{cs}). In the following cases, $\omega_2/\omega_1 \neq r_{cs}$, and there is a nonzero velocity component at infinity, generating a secondary stagnation point far from the origin. Regardless of the value of ω_2/ω_1, the main stagnation point position moves away from the cylinder rotating faster along the y−axis.

Using TRMs for studies of particles immersed in strong flows requires knowledge of all properties over the complete flow field, in order to predict the trajectory of the particle on a given streamline. Among the most relevant properties are the velocity gradient tensor, the rate of deformation tensor, the vorticity tensor and the flow-type parameter. In this

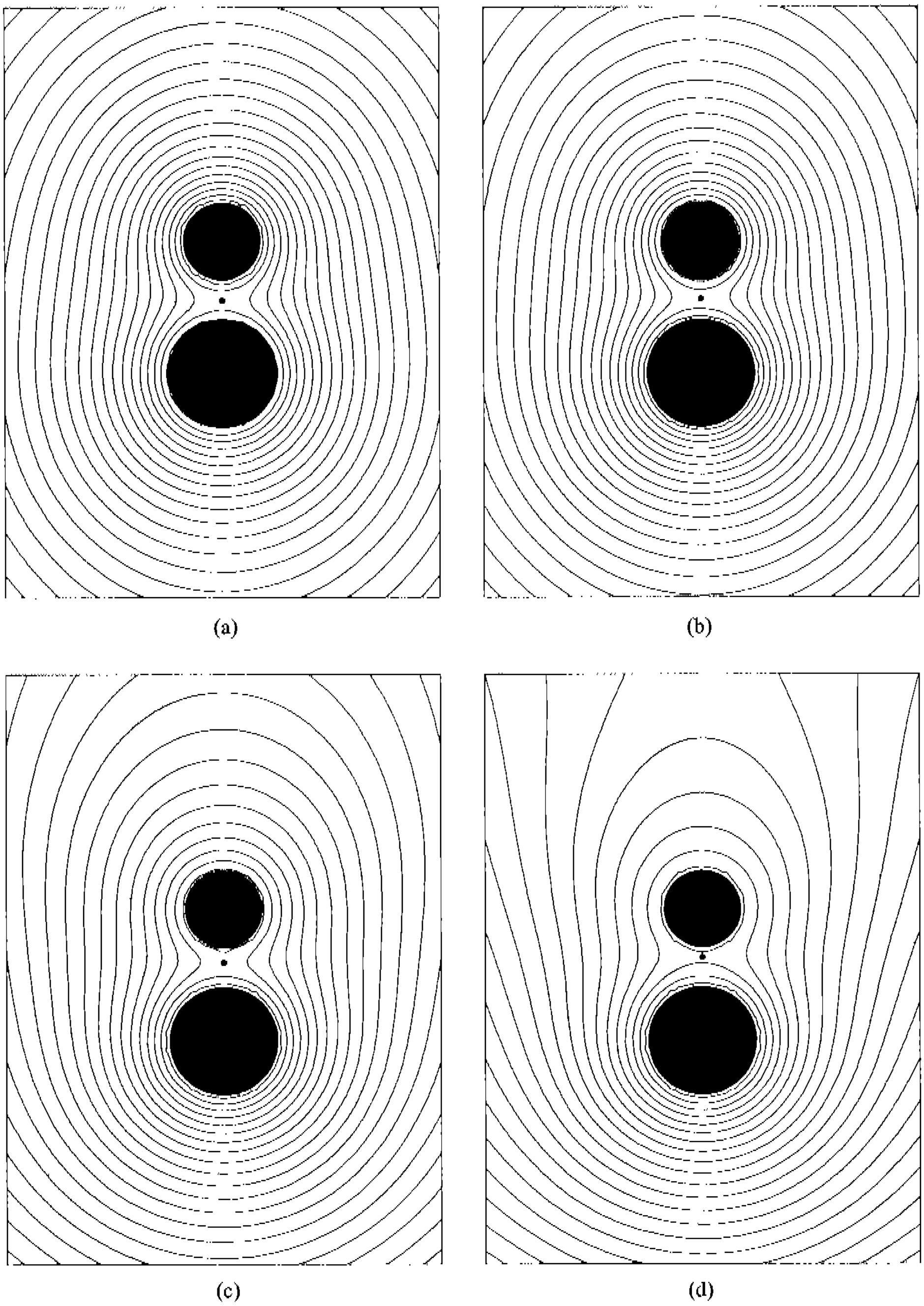

(a) (b)

(c) (d)

FIGURE 1.5. Streamlines for a TRM with $R_1 = 10.00\,\mathrm{mm}$, $R_2 = 14.00\,\mathrm{mm}$ and $de = 34.00\,\mathrm{mm}$. The ratio of the angular velocities on the rollers are: (a) Closed solution: $\omega_2/\omega_1 = 0.621658$, (b) Equal tangential velocity, $\omega_2/\omega_1 = R_1/R_2$, (c) Equal angular velocities, $\omega_2/\omega_1 = 1$, (d) $\omega_2/\omega_1 = 5/3$. The dot is the stagnation point at the center of the flow field, close to the slower rotating cylinder.

Section these relations are obtained.

The two-dimensional velocity field for the Two-Roll Mill in bipolar coordinates system (See Appendix A) is

$$\mathbf{u} = u_\alpha\, \mathbf{e}_1 + u_\beta\, \mathbf{e}_2 + 0\, \mathbf{e}_3,$$

with the velocity gradient tensor given by

$$\boldsymbol{\nabla}\mathbf{u} = \begin{bmatrix} \dfrac{1}{h}\dfrac{\partial u_\alpha}{\partial \alpha} - \dfrac{\sin\beta}{a} u_\beta & \dfrac{1}{h}\dfrac{\partial u_\beta}{\partial \alpha} + \dfrac{\sin\beta}{a} u_\alpha & 0 \\ \dfrac{1}{h}\dfrac{\partial u_\alpha}{\partial \beta} + \dfrac{\sinh\alpha}{a} u_\beta & \dfrac{1}{h}\dfrac{\partial u_\beta}{\partial \beta} - \dfrac{\sinh\alpha}{a} u_\alpha & 0 \\ 0 & 0 & 0 \end{bmatrix}. \tag{1.29}$$

Its magnitude is $\|\boldsymbol{\nabla}\mathbf{u}\| = \sqrt{\mathrm{Tr}\left(\boldsymbol{\nabla}\mathbf{u} \cdot \boldsymbol{\nabla}\mathbf{u}^T\right)}$, which is the *magnitude of the velocity gradient tensor* or *shear rate*

$$\|\boldsymbol{\nabla}\mathbf{u}\| = \dot{\gamma} = \Bigg(\left(\frac{1}{h}\frac{\partial u_\alpha}{\partial \alpha} - \frac{\sin\beta}{a} u_\beta\right)^2 + \left(\frac{1}{h}\frac{\partial u_\alpha}{\partial \beta} + \frac{\sinh\alpha}{a} u_\beta\right)^2 + \left(\frac{1}{h}\frac{\partial u_\beta}{\partial \alpha} + \frac{\sin\beta}{a} u_\alpha\right)^2 + \left(\frac{1}{h}\frac{\partial u_\beta}{\partial \beta} - \frac{\sinh\alpha}{a} u_\alpha\right)^2\Bigg)^{\frac{1}{2}}. \tag{1.30}$$

The velocity gradient tensor can be decomposed into a symmetric part (**D**) and an antisymmetric part (**W**). This symmetric part corresponds to the tensor of *deformation rate* or *rate of strain tensor*. Thus,

$$\mathbf{D} = \tfrac{1}{2}\left(\boldsymbol{\nabla}\mathbf{u} + \boldsymbol{\nabla}\mathbf{u}^T\right), \tag{1.31}$$

i.e.,

$$\mathbf{D} = \begin{bmatrix} \dfrac{1}{h}\dfrac{\partial u_\alpha}{\partial \alpha} - \dfrac{\sin\beta}{a} u_\beta & \begin{array}{c} \dfrac{1}{2h}\left(\dfrac{\partial u_\alpha}{\partial \beta} + \dfrac{\partial u_\beta}{\partial \alpha}\right) + \\ \dfrac{1}{2a}\left(\sinh\alpha\; u_\beta + \sin\beta\; u_\alpha\right) \end{array} \\ \begin{array}{c} \dfrac{1}{2h}\left(\dfrac{\partial u_\alpha}{\partial \beta} + \dfrac{\partial u_\beta}{\partial \alpha}\right) + \\ \dfrac{1}{2a}\left(\sinh\alpha\; u_\beta + \sin\beta\; u_\alpha\right) \end{array} & \dfrac{1}{h}\dfrac{\partial u_\beta}{\partial \beta} - \dfrac{\sinh\alpha}{a} u_\alpha \end{bmatrix}. \tag{1.32}$$

From the equation of continuity,

$$\boldsymbol{\nabla} \cdot \mathbf{u} = 0 = \mathbf{Tr}(\boldsymbol{\nabla}\mathbf{u}) = \mathbf{Tr}(\mathbf{D}) = \frac{1}{h}\frac{\partial u_\alpha}{\partial \alpha} - \frac{\sin\beta}{a} u_\beta + \frac{1}{h}\frac{\partial u_\beta}{\partial \beta} - \frac{\sinh\alpha}{a} u_\alpha = 0, \tag{1.33}$$

thus,

$$\frac{1}{h}\frac{\partial u_\alpha}{\partial \alpha} - \frac{\sin\beta}{a} u_\beta = -\left(\frac{1}{h}\frac{\partial u_\beta}{\partial \beta} - \frac{\sinh\alpha}{a} u_\alpha\right), \tag{1.34}$$

and

$$\mathbf{D} = \begin{bmatrix} \frac{1}{h}\frac{\partial u_\alpha}{\partial \alpha} - \frac{\sin\beta}{a} u_\beta & \frac{1}{2h}\left(\frac{\partial u_\alpha}{\partial \beta} + \frac{\partial u_\beta}{\partial \alpha}\right) + \frac{1}{2a}\left(\sinh\alpha\ u_\beta + \sin\beta\ u_\alpha\right) \\ \frac{1}{2h}\left(\frac{\partial u_\alpha}{\partial \beta} + \frac{\partial u_\beta}{\partial \alpha}\right) + \frac{1}{2a}\left(\sinh\alpha\ u_\beta + \sin\beta\ u_\alpha\right) & -\frac{1}{h}\frac{\partial u_\alpha}{\partial \alpha} + \frac{\sin\beta}{a} u_\beta \end{bmatrix}. \tag{1.35}$$

The antisymmetric part is the tensor of vorticity or rate of rotation tensor, which is

$$\mathbf{W} = \tfrac{1}{2}\left(\boldsymbol{\nabla}\mathbf{u} - \boldsymbol{\nabla}\mathbf{u}^T\right), \tag{1.36}$$

and can be rewritten as

$$\mathbf{W} = \begin{bmatrix} 0 & \frac{1}{2h}\left(\frac{\partial u_\beta}{\partial \alpha} - \frac{\partial u_\alpha}{\partial \beta}\right) + \frac{1}{2a}\left(\sin\beta\ u_\alpha - \sinh\alpha\ u_\beta\right) \\ -\frac{1}{2h}\left(\frac{\partial u_\beta}{\partial \alpha} - \frac{\partial u_\alpha}{\partial \beta}\right) - \frac{1}{2a}\left(\sin\beta\ u_\alpha - \sinh\alpha\ u_\beta\right) & 0 \end{bmatrix}. \tag{1.37a}$$

Using the following relations for a further simplification:

$$p = 2D_{11} = 2\left(\boldsymbol{\nabla}\mathbf{u}\right)_{11} = \frac{2}{h}\frac{\partial u_\alpha}{\partial \alpha} - \frac{2}{a}\sin\beta\, u_\beta, \tag{1.38}$$

$$q = D_{12} = \left(\boldsymbol{\nabla}\mathbf{u}\right)_{12} + \left(\boldsymbol{\nabla}\mathbf{u}\right)_{21} = \frac{1}{h}\left(\frac{\partial u_\alpha}{\partial \beta} + \frac{\partial u_\beta}{\partial \alpha}\right) + \frac{1}{a}\left(\sinh\alpha\, u_\beta + \sin\beta\, u_\alpha\right), \tag{1.39}$$

and

$$\operatorname{sign}[q] = \frac{q}{\sqrt{q^2}}. \tag{1.40}$$

Thus, the magnitude of $\mathbf{D}$ is given by

$$\|\mathbf{D}\| = \sqrt{\operatorname{Tr}\left(\mathbf{D}\cdot\mathbf{D}^T\right)} = \frac{\sqrt{p^2+q^2}}{2}, \tag{1.41}$$

with eigenvectors

$$\mathbf{N}_{\pm} = \left\{ \frac{(D_{11} - D_{22}) \mp \sqrt{(D_{11} - D_{22})^2 + 4D_{12}^2}}{2\,D_{12}},\ 1 \right\}. \tag{1.42}$$

The normalized eigenvectors are given by

$$\mathbf{n}_{\pm} = \frac{\mathbf{N}_{\pm}}{\|\mathbf{N}_{+}\|}. \tag{1.43}$$

The magnitudes of these eigenvectors are

$$\|\mathbf{N}_{\pm}\| = \sqrt{2}\sqrt{(p^2 + q^2)\left(1 \mp \frac{p}{\sqrt{p^2 + q^2}}\right)}, \tag{1.44}$$

with $\mathbf{n}_{\pm}$ expressed as

$$\mathbf{n}_{\pm} = \frac{1}{\sqrt{2}} \left\{ \mp\ \mathrm{sign}[q]\sqrt{1 \mp \frac{p}{\sqrt{p^2 + q^2}}},\ \sqrt{1 \pm \frac{p}{\sqrt{p^2 + q^2}}} \right\}. \tag{1.45}$$

From Astarita [24], the kinematic tensor $\mathbf{\Omega}$ is the rate of rotation of the tensor $\mathbf{D}$ on a particle. Astarita's definition of $\mathbf{\Omega}$ is

$$\frac{D\mathbf{n}}{Dt} = \frac{\partial \mathbf{n}}{\partial t} + \mathbf{u} \cdot \mathbf{\nabla}\mathbf{n} = \mathbf{\Omega} \cdot \mathbf{n}, \tag{1.46}$$

where $\mathbf{u} \cdot \mathbf{\nabla n}$ is given by

$$(\mathbf{u} \cdot \mathbf{\nabla})\,\mathbf{n} = \begin{bmatrix} u_\alpha \left(\dfrac{1}{h}\dfrac{\partial n_1}{\partial \alpha} - \dfrac{\sin\beta}{a} n_2\right) + u_\beta \left(\dfrac{1}{h}\dfrac{\partial n_1}{\partial \beta} + \dfrac{\sinh\alpha}{a} n_2\right) \\ u_\alpha \left(\dfrac{1}{h}\dfrac{\partial n_2}{\partial \alpha} - \dfrac{\sin\beta}{a} n_1\right) + u_\beta \left(\dfrac{1}{h}\dfrac{\partial n_2}{\partial \beta} + \dfrac{\sinh\alpha}{a} n_1\right) \end{bmatrix}. \tag{1.47}$$

Due to a steady flow field, then $\dfrac{\partial \mathbf{n}}{\partial t} = 0$.

The derivative of $\mathbf{n}_{\pm}$ is

$$\mathbf{n}'_{\pm} = \frac{q\,(q * p' - p * q')}{\sqrt{8}\,(p^2 + q^2)^{\frac{3}{2}}} \left\{ \mathrm{sign}[q] \left(1 \mp \frac{p}{\sqrt{p^2 + q^2}}\right)^{-\frac{1}{2}},\ \pm\left(1 \pm \frac{p}{\sqrt{p^2 + q^2}}\right)^{-\frac{1}{2}} \right\}, \tag{1.48}$$

where

$$\frac{\partial p}{\partial \alpha} = \frac{2\sinh\alpha}{a}\frac{\partial u_\alpha}{\partial \alpha} + \frac{2}{h}\frac{\partial^2 u_\alpha}{\partial \alpha^2} - \frac{2\sin\beta}{a}\frac{\partial u_\beta}{\partial \alpha}, \tag{1.49}$$

$$\frac{\partial p}{\partial \beta} = \frac{2\sin\beta}{a}\left(\frac{\partial u_\alpha}{\partial \alpha} - \frac{\partial u_\beta}{\partial \beta}\right) + \frac{2}{h}\frac{\partial^2 u_\alpha}{\partial \beta \partial \alpha} - \frac{2}{a}\cos\beta\, u_\beta; \tag{1.50}$$

and

$$\begin{aligned}\frac{\partial q}{\partial \alpha} &= \frac{\sinh\alpha}{a}\left(\frac{\partial u_\alpha}{\partial \beta}+2\frac{\partial u_\beta}{\partial \alpha}\right)+\frac{1}{h}\left(\frac{\partial^2 u_\alpha}{\partial\alpha\partial\beta}+\frac{\partial^2 u_\beta}{\partial\alpha^2}\right)\\ &\quad+\frac{1}{a}\left(\sin\beta\,\frac{\partial u_\alpha}{\partial\alpha}+\cosh\alpha\, u_\beta\right), \qquad (1.51)\\ \frac{\partial q}{\partial \beta} &= \frac{\sin\beta}{a}\left(2\frac{\partial u_\alpha}{\partial \beta}+\frac{\partial u_\beta}{\partial \alpha}\right)+\frac{1}{h}\left(\frac{\partial^2 u_\alpha}{\partial\beta^2}+\frac{\partial^2 u_\beta}{\partial\beta\partial\alpha}\right)\\ &\quad+\frac{1}{a}\left(\cos\beta\, u_\alpha+\sinh\alpha\,\frac{\partial u_\beta}{\partial\beta}\right). \qquad (1.52)\end{aligned}$$

The right side of the Eq. 1.46 can be expressed as

$$\mathbf{\Omega}\cdot\mathbf{n}=\begin{bmatrix}\Omega_{11} & \Omega_{12}\\ \Omega_{21} & \Omega_{22}\end{bmatrix}\cdot\begin{bmatrix}n_1\\ n_2\end{bmatrix}=\begin{bmatrix}\Omega_{11}\;n_1+\Omega_{12}\;n_2\\ \Omega_{21}\;n_1+\Omega_{22}\;n_2\end{bmatrix}, \qquad (1.53)$$

and together with the Eq. 1.45 and Eq. 1.47, a system of equations useful for calculating the $\mathbf{\Omega}$ tensor is obtained

$$\begin{aligned}\Omega_{11}\;n_{+1}+\Omega_{12}\;n_{+2} &= (\mathbf{u}\cdot\mathbf{\nabla n})_{(+1)}=A, \qquad (1.54)\\ \Omega_{21}\;n_{+1}+\Omega_{22}\;n_{+2} &= (\mathbf{u}\cdot\mathbf{\nabla n})_{(+2)}=B, \qquad (1.55)\\ \Omega_{11}\;n_{-1}+\Omega_{12}\;n_{-2} &= (\mathbf{u}\cdot\mathbf{\nabla n})_{(-1)}=C, \qquad (1.56)\\ \Omega_{21}\;n_{-1}+\Omega_{22}\;n_{-2} &= (\mathbf{u}\cdot\mathbf{\nabla n})_{(-2)}=D. \qquad (1.57)\end{aligned}$$

Solving this system, elements for $\mathbf{\Omega}$ are:

$$\begin{aligned}\Omega_{11} &= \frac{n_{-2}\;A-n_{+2}\;C}{n_{+1}\;n_{-2}-n_{-1}\;n_{+2}}=\mathrm{sign}[q]\;\left(n_{+2}\;C-n_{-2}\;A\right), \qquad (1.58)\\ \Omega_{12} &= \frac{n_{+1}\;C-n_{-1}\;A}{n_{+1}\;n_{-2}-n_{-1}\;n_{+2}}=\mathrm{sign}[q]\;\left(n_{-1}\;A-n_{+1}\;C\right), \qquad (1.59)\\ \Omega_{21} &= \frac{n_{-2}\;B-n_{+2}\;D}{n_{+1}\;n_{-2}-n_{-1}\;n_{+2}}=\mathrm{sign}[q]\;\left(n_{+2}\;D-n_{-2}\;B\right), \qquad (1.60)\\ \Omega_{22} &= \frac{n_{+1}\;D-n_{-1}\;B}{n_{+1}\;n_{-2}-n_{-1}\;n_{+2}}=\mathrm{sign}[q]\;\left(n_{-1}\;B-n_{+1}\;D\right). \qquad (1.61)\end{aligned}$$

Substituting Eqs. 1.45, 1.47 and 1.48 in the above equation and simplifying,

$$\Omega_{11} = \Omega_{22}=0, \qquad (1.62)$$

$$\begin{aligned}\Omega_{12} &= -\Omega_{21}=\\ &= \frac{u_\alpha\left(q\,\dfrac{\partial p}{\partial\alpha}-p\,\dfrac{\partial q}{\partial\alpha}\right)+u_\beta\left(q\,\dfrac{\partial p}{\partial\beta}-p\,\dfrac{\partial q}{\partial\beta}\right)}{2h\,(p^2+q^2)}+\frac{\sinh\alpha}{a}\,u_\beta-\frac{\sin\beta}{a}\,u_\alpha. \qquad (1.63)\end{aligned}$$

The kinematic tensor $\bar{\mathbf{W}}$, defined by

$$\bar{\mathbf{W}} = -(\mathbf{W} + \mathbf{\Omega}), \tag{1.64}$$

measures the rate of rotation of a particle with respect to the rate of strain's principal axes at that particle, and $\bar{\mathbf{W}}$ is *objective*. From the definition of the *flow-type parameter*, λ,

$$\frac{1+\lambda}{1-\lambda} = \frac{\|\mathbf{D}\|}{\|\bar{\mathbf{W}}\|}, \tag{1.65}$$

thus, λ is given by

$$\lambda = \frac{\|\mathbf{D}\| - \|\bar{\mathbf{W}}\|}{\|\mathbf{D}\| + \|\bar{\mathbf{W}}\|}. \tag{1.66}$$

1.3 Characteristics of flow fields generated by Two-Roll Mills

For geometries with equal radii, the flow-type parameter at the stagnation point has a maximum value when the angular velocity is the same on each cylinder, as shown in Fig. 1.6. In this Figure, the gray area represents the domain of possible flow-type parameter values accessible experimentally when using TRMs. This criterion is based on reasonable values for λ and $\dot{\gamma}$. At large λ values, $\lambda > 0.4$, the maximum shear rate accessible is comparatively small, requiring a high rotational speed of the cylinders in order to achieve moderate shear rates at the stagnation region. Under this condition, a high shear rate always exists around the cylinders, a poor condition for a low Reynolds number flow field. Most likely, this is the main limitation for generating strong flows using devices based on Two-Roll Mill geometries. When using Four-Roll Mills, the smaller values of the flow field parameter are achieved by rotating a set of two cylinders very slowly compared to the other two. Thus, Four-Roll Mill flow fields with small λ values are intrinsically unstable, and the control scheme becomes less reliable, contrary to what is expected for flows generated by TRMs. Consequently, Two-Roll and Four-Roll Mills are adequate flow field complements to each other.

Figure 1.7 presents the flow-type parameter field for a symmetric mill. The central region is dominated by the elongational character of the flow field: i. e., positive values of the flow-type parameter. This Figure shows that two vortices exist to the right and left of

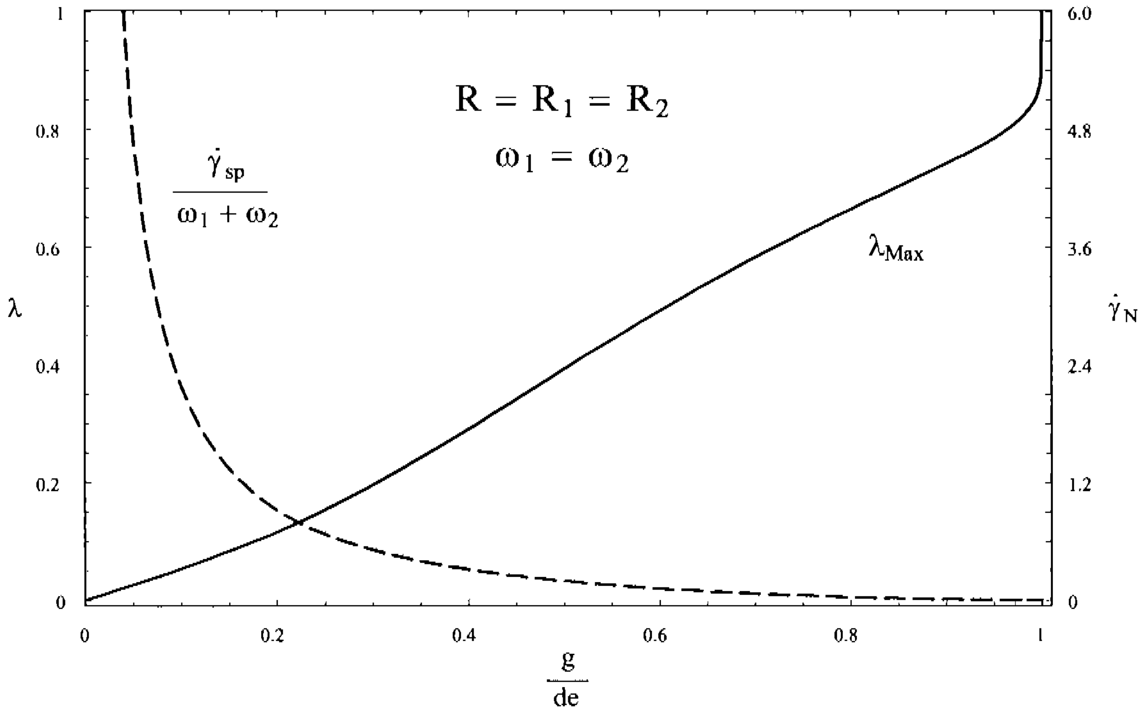

FIGURE 1.6. Values for the flow-type parameter λ and the normalized shear rate $\dot{\gamma}_N$ in a TRM with equal rollers' radii at the stagnation point in the flow. The maximum value for λ is obtained when the angular velocities of the rollers are equal. The shaded area represents experimentally accessible λ values obtained with the TRM geometries proposed in this work.

the cylinders along the horizontal symmetry line. In such regions, the velocity field is weak, but the flow-type parameter value is very close to -1. Towards the exterior regions, the horseshoe-shape areas correspond to λ values close to one; that is, almost pure elongational flow.

In Figure 1.8, cylinders have different radii. Comparing this Figure with Fig. 1.7, general features are preserved, but the two symmetric vortices located to the right and left of the cylinders are displaced away from the largest cylinder. The central region maintains a value of the flow-type parameter that is quite homogeneous. Within the central region, observed values of λ are always close to the value observed at the stagnation point. However, because of a faster tangential speed of the larger cylinder, the stagnation point is neither longer located at the center of the coordinate system nor at the center of the gap.

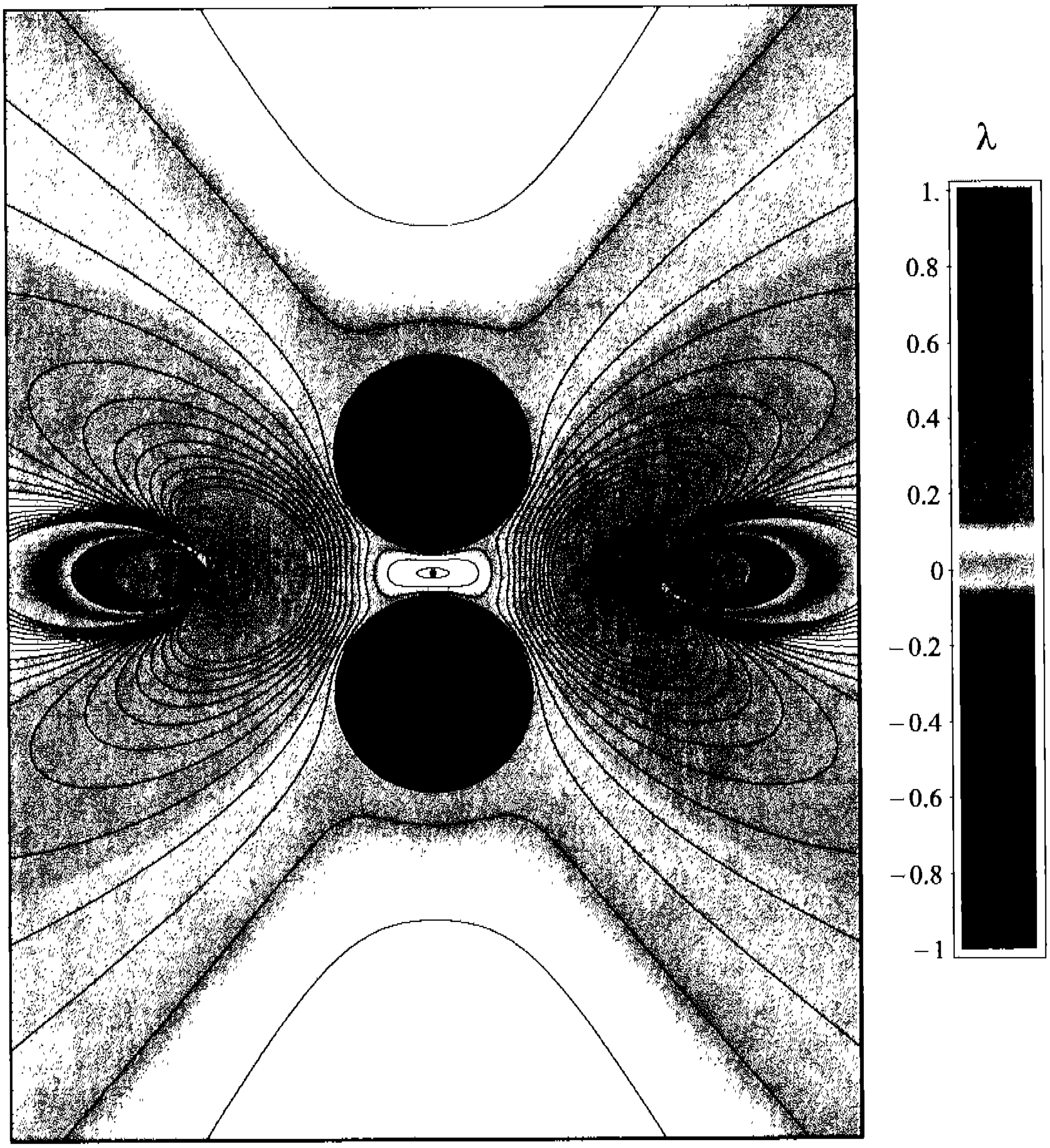

FIGURE 1.7. Field of the flow-type parameter λ for the case of rollers' radii and angular velocities being equal. $R_1 = R_2 = 14.00$ mm and $\omega_1/\omega_2 = 1.0$. The flow field is symmetric with respect to horizontal axis. The heart-shaped regions to the right and left are regions of strong vorticity, λ close to -1; and the external horseshoe regions, of high rates of deformation, λ close to 1.

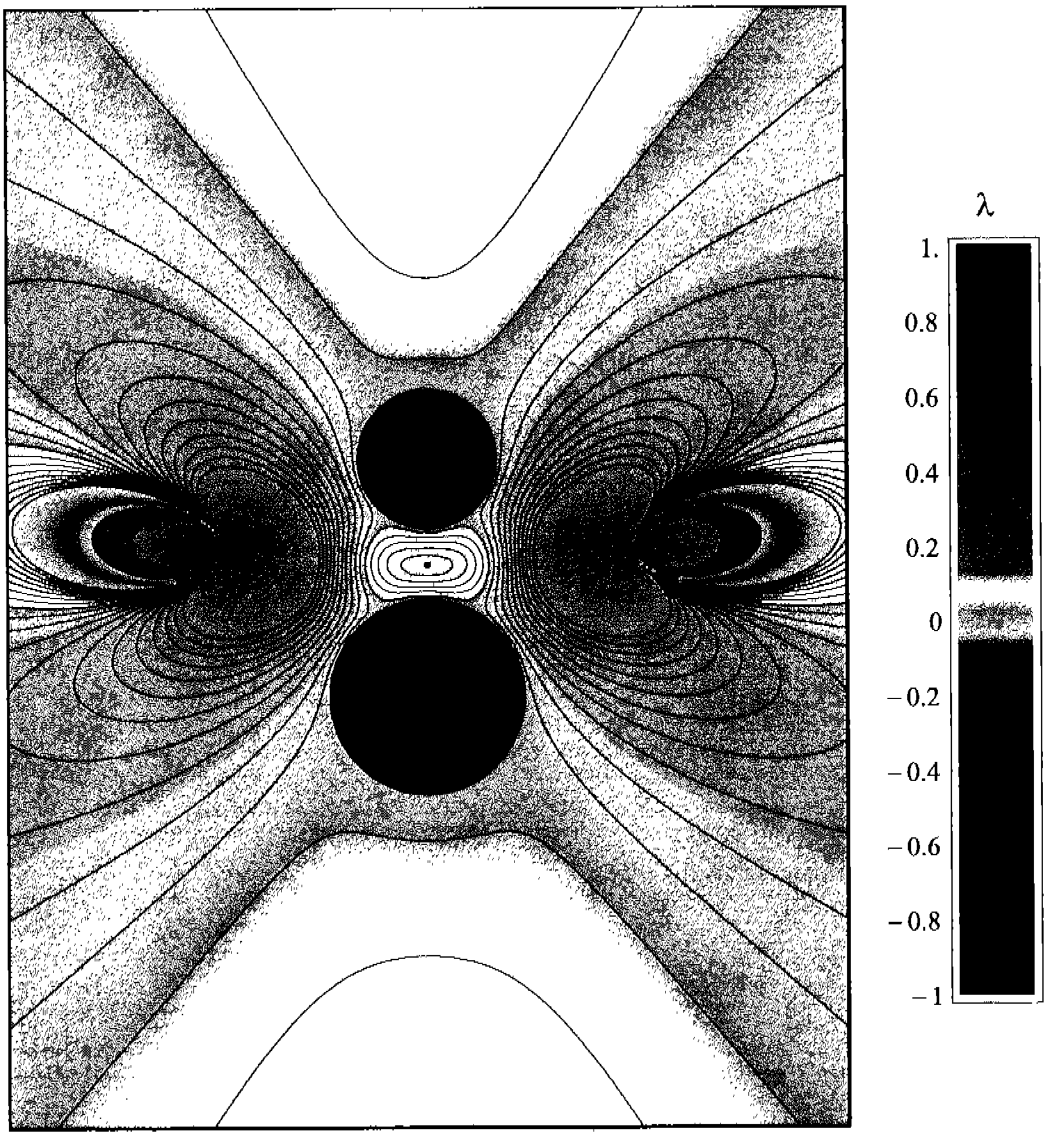

FIGURE 1.8. Field of the flow-type parameter λ. The radii are $R_1 = 10.00$ mm and $R_2 = 14.00$ mm, and the angular velocity ratio is $\omega_1/\omega_2 = 0.6216$. In this case, the solution is exact for the full domain. Left and right virtual vortices are displaced away from x–axis towards the smaller cylinder.

The stagnation point is displaced closer to the cylinder rotating at the lower speed while maintaining a finite positive value for λ within the full range of speed ratios.

Figures 1.9 1.11 show several properties of the flow field generated by different Two-Roll Mill configurations. Graphs (a) correspond to streamlines; (b) to isopleths for the magnitude of the velocity field $\|\mathbf{u}\|$; (c) to isopleths for the magnitude of the gradient of the velocity field $\dot{\gamma}$; and (d) to isopleths for the flow-type parameter λ. In order to cover a wide range of λ values, the optimum experimental arrangement is achieved with a set of rollers and by selecting more than one separation of the axes of cylinders. Figures 1.9 and 1.11 correspond to cylinders' axes separation of 34 mm, and Fig. 1.10 to a separation of 52 mm. Figure 1.11 presents a Two-Roll Mill configuration that is asymmetric, while Figs. 1.9 and 1.10 show the fields for the principal flow parameters in configurations with flow-type parameter value at the stagnation point of 0.3 for the first, and close to simple shear flow for the last.

For studies of droplets dynamics, effects of closeness of walls are at the present time an open research topic. Usage of equivalent pairs of TRM's configurations allows for studies of similar strong flow conditions but with different scaling ratios for a given droplet size. As can be seen in Fig. 1.12 by using two sets of cylinders it is possible to generate flow fields that essentially have the same values of all parameters, but with notably different boundary effects. That is, although these geometries may have significantly different separations between cylinders -actually, a separation larger than three times- these flow configurations have the same λ value at the stagnation point. This feature is a significant advantage for studies of finite-size droplets embedded in strong type flows.

Table 1.1 shows the data used for the analysis presented in the Figures 1.13–1.16. This Table presents two symmetric configurations of TRMs with five cylinder sizes each one (represented by ratios g/de), and their respective flow-type parameter and normalized shear rate values at the stagnation point when the cylinders rotate at the same angular velocity. The selected geometries shown are those analyzed in detail in Chapter 2.

When the ratio of rotational speeds of the cylinders increases, the position of the stagnation point along the waist of the gap is displaced towards the slower rotating cylinder. This change is accompanied by other relevant features. Especially, this effect is

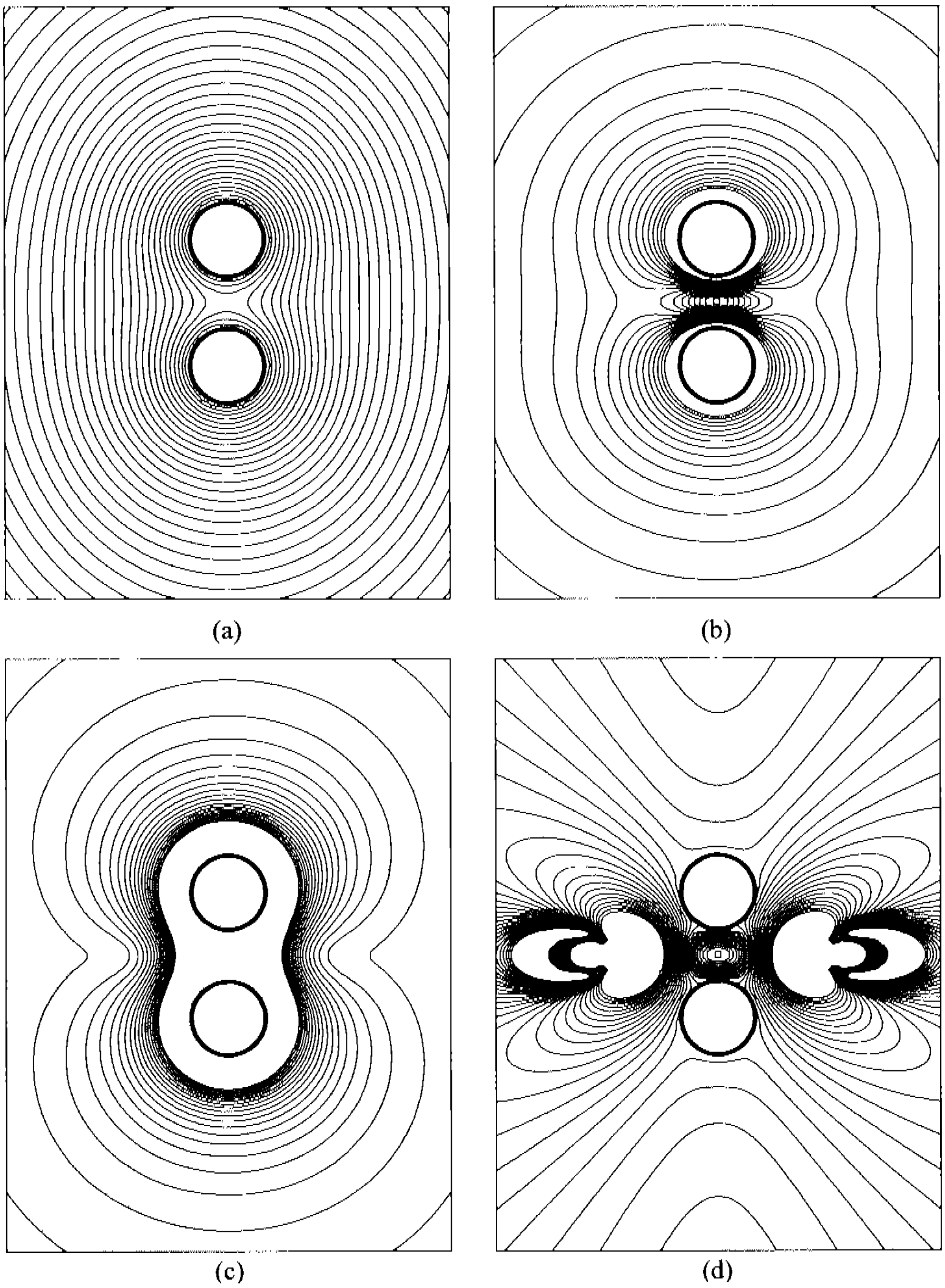
(a) (b) (c) (d)

FIGURE 1.9. Properties of the flow field generated by a Two-Roll Mill with cylinders of equal radii $R = 10.00$ mm, distance between axes $de = 34.00$ mm (the geometric ratio r_g is 0.4118), and the angular velocities are equal. Graph (a) correspond to streamlines; (b) to isopleths for the magnitude of the velocity field $\|\mathbf{u}\|$; (c) to isopleths for the magnitude of the gradient of the velocity field $\dot{\gamma}$; and (d) to isopleths for the flow-type parameter λ.

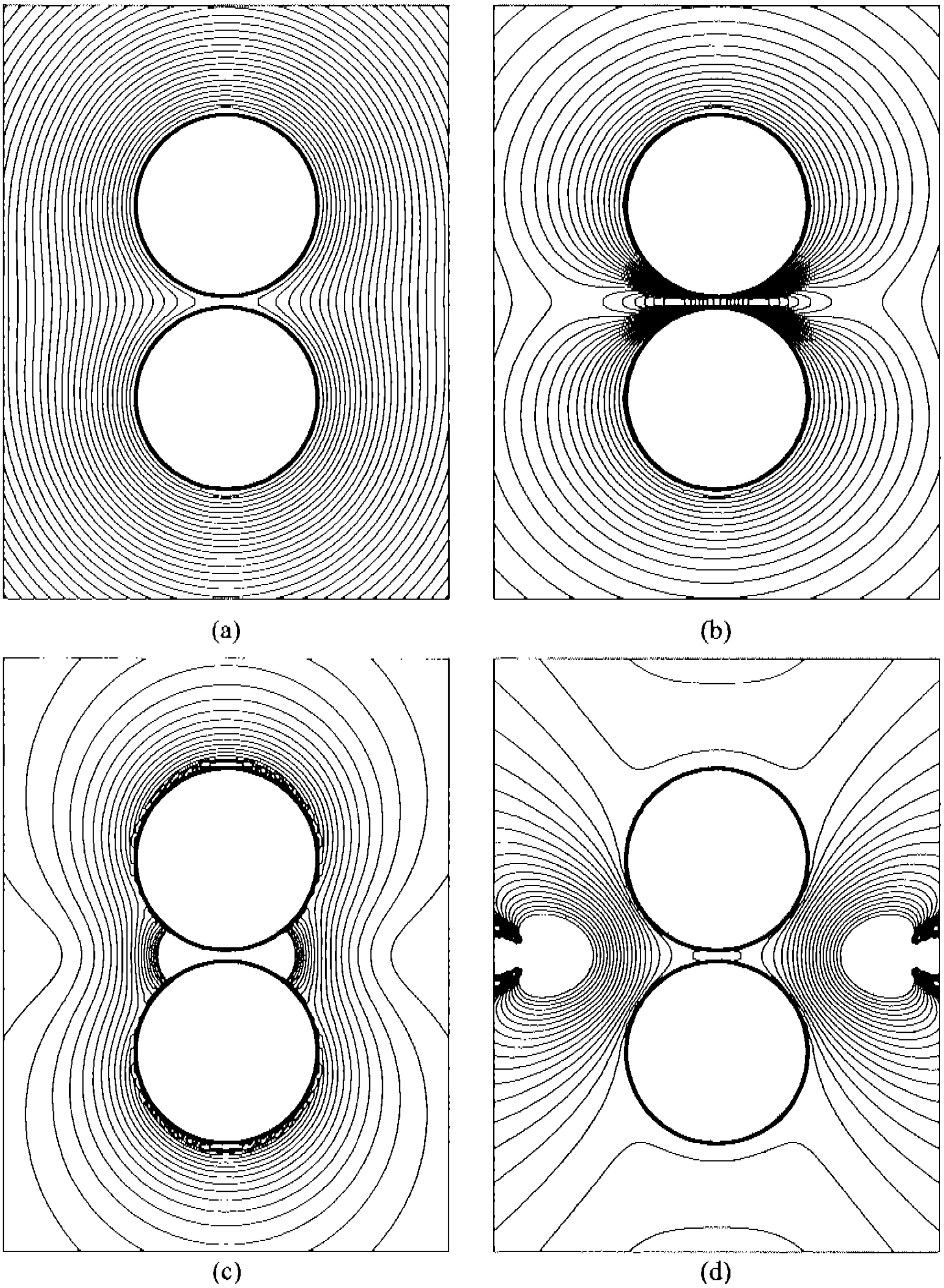

(a)

(b)

(c)

(d)

FIGURE 1.10. Properties of the flow field generated by a Two-Roll Mill with cylinders of equal radii $R = 24.50$ mm, distance between axes $de = 52.00$ mm (the geometric ratio r_g is 0.0577), and the angular velocities are equal. Graph (a) correspond to streamlines; (b) to isopleths for the magnitude of the velocity field $\|\mathbf{u}\|$; (c) to isopleths for the magnitude of the gradient of the velocity field $\dot{\gamma}$; and (d) to isopleths for the flow-type parameter λ.

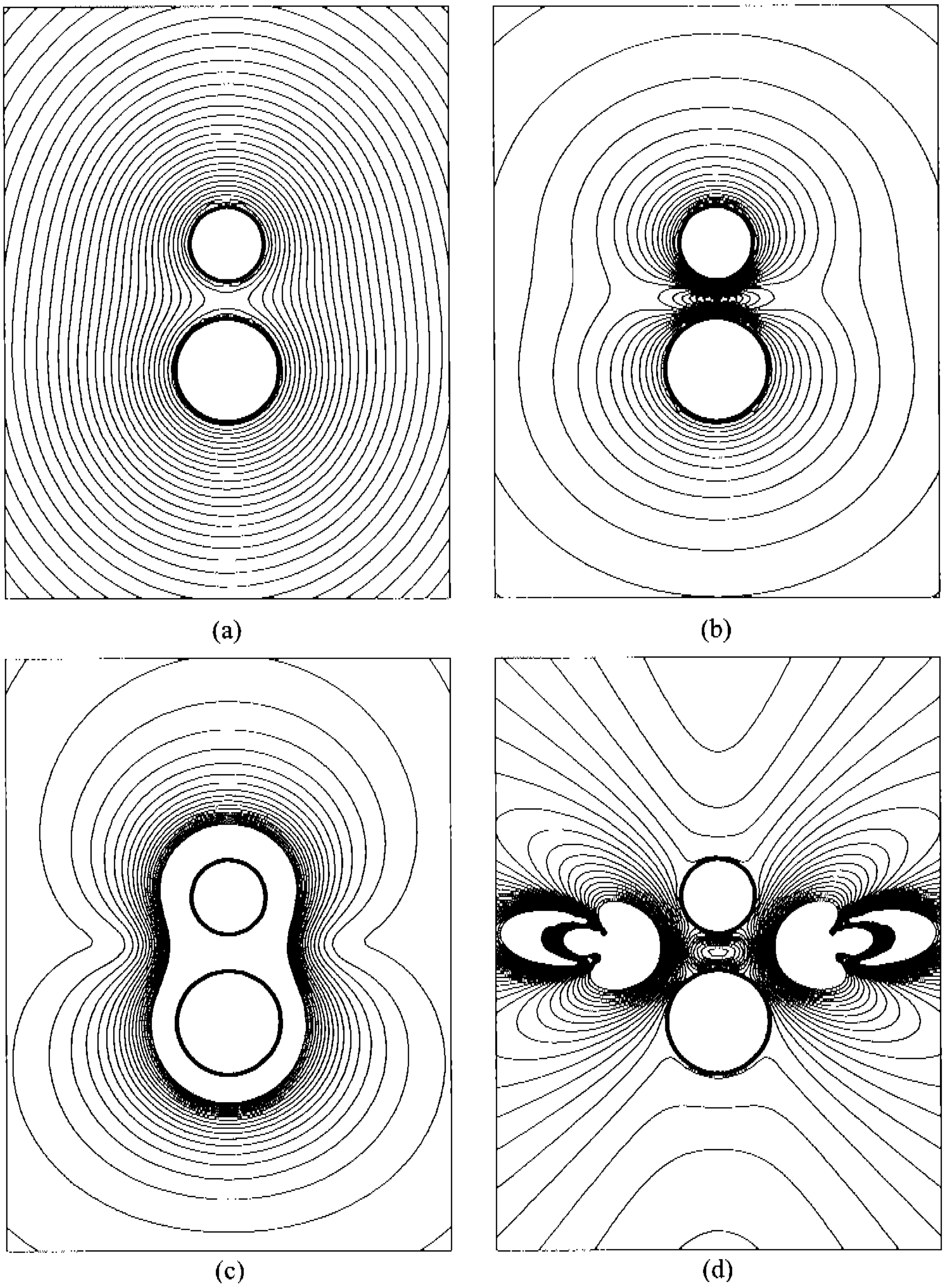

FIGURE 1.11. Properties of the flow field generated by a Two-Roll Mill with cylinders of different radii $R_1 = 10.00$ mm, $R_2 = 14.00$ mm, distance between axes $de = 34.00$ mm. The angular velocities corresponds to the closed solution. Graph (a) correspond to streamlines; (b) to isopleths for the magnitude of the velocity field $\|\mathbf{u}\|$; (c) to isopleths for the magnitude of the gradient of the velocity field $\dot{\gamma}$; and (d) to isopleths for the flow-type parameter λ.

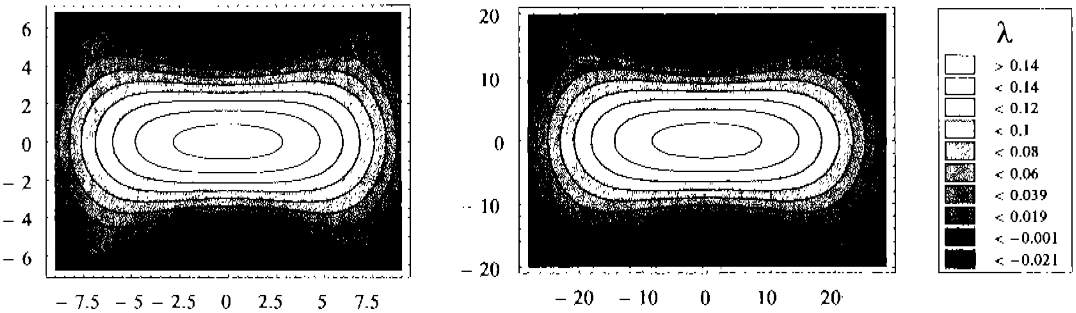

FIGURE 1.12. Fields of flow-type parameter values, but with two different geometries. In both cases the value of λ at the stagnation point is 0.1495. Length scales for these flows are dimensional, showing the same range of values for λ. For the Graph to the left, radii are 12.85 mm, gap is 8.30 mm, and axes separation is 34.00 mm. For the Graph to the right, radii are 38.7 mm, gap is 25.01 mm, and axes separation of 102.41 mm.

accompanied by a change of the value observed for the flow-type parameter. Figure 1.13 presents chances of values for the flow-type parameter at the stagnation point position and as a function of the ratio of rotational speeds. The same behavior exists for all geometries of Two-Roll Mills, depicted by cylinders (a) to (e) see Table 1.1. For example, for the geometry designated by (a), a decrement of about 6% of the λ value is observed when $\omega_1/(\omega_1+\omega_2)=0.6$, with respect to the value of λ calculated at the stagnation point and for equal rotational speed of cylinders. As can be seen in Fig. 1.8, the flow field shows a displacement for the virtual vortices – located at the right and left of the central region – towards the smaller cylinder. The net effect of such global behavior is the presence for an asymmetric gradient of the λ values along the line joining the cylinders axes. In fact, the maximum value for the flow-type parameter in the central region is no longer located at the stagnation point. Thus, positions for $\lambda_{\max}$ are displaced slightly less than the actual position of the stagnation point; these relative displacements $y_{sp}-y(\lambda_{\max})$ are shown in the top graph insert in Fig. 1.13. For a given geometry, $\lambda_{\max}$ is slightly larger than the value of λ at the stagnation point, and the ratio of $\lambda_{\max}/\lambda_{sp}$ increases with increasing values of the ratio of rotational speeds $\omega_1/(\omega_1+\omega_2)$. Please note that Figs. 1.13-1.16 show a range of $\omega_1/(\omega_1+\omega_2)$ values contained within [0.5, 0.6], which is amenable to numerical verification; the latter calculations are presented in Chapter 2.

TRM–A ($de = 34\,\text{mm}$)				TRM–B ($de = 52\,\text{mm}$)			
g/de		λ	$\dot{\gamma}_N$	g/de		λ	$\dot{\gamma}_N$
(*a*)	0.4118	0.302737	0.59079	(*a*)	0.2442	0.149635	1.39614
(*b*)	0.3588	0.250579	0.76059	(*b*)	0.1754	0.099971	2.19313
(*c*)	0.3029	0.198770	1.00797	(*c*)	0.1362	0.075045	3.01222
(*d*)	0.2441	0.149547	1.39707	(*d*)	0.0935	0.049883	4.68753
(*e*)	0.1765	0.100692	2.17566	(*e*)	0.0577	0.030011	8.00265

TABLE 1.1. Symmetric configurations of TRMs with five g/de ratios each one, and their respective flow-type parameter and normalized shear rate values at the stagnation point when the cylinders rotate at the same angular velocity.

Furthermore, and for all geometries and speed ratios, there is a finite gradient for the flow-type parameter at the stagnation point along the direction of the centers of the cylinders, as can be seen in the graph inserted in Fig. 1.13 when the cylinders rotate at different speeds. As the gap reduces, the gradient of the flow type parameter λ increases. Figure 1.14 presents the same behavior for λ values but for a different geometry characterized with a larger separation between the cylinders axes and capable of generating flow fields with kinematics closer to simple shear flows.

Also, values for others parameters of the flow are modified as a function of the ratio of rotational speeds. Of special interest is the magnitude of the velocity gradient across the gap. In this case, and for all configurations, the maximum values of the shear rate are achieved at the surfaces of the cylinders. The minimum value along the gap occurs at the stagnation point for cylinders rotating at equal speeds. When the ratio of rotational speeds is different than one, the values of $\dot{\gamma}$ at the stagnation point increases as the ratio of speeds augments. For the (e) geometry in Fig. 1.15, the shear rate increases up to 3.2% for speed ratios $\omega_1/(\omega_1+\omega_2) = 0.6$. As well as with the λ field, the minimum value in the $\dot{\gamma}$–fields occurs at a different position than the location of the stagnation point or the maximum value of the flow type parameter. The location for the minimum shear rate $y\left(\dot{\gamma}_{\min}\right)$ is always closer to the faster spinning cylinder. The relative distance $y_{sp} - y\left(\dot{\gamma}_{\min}\right)$ increases as a function of the ratio of speeds, as well as with the relative width of the gap.

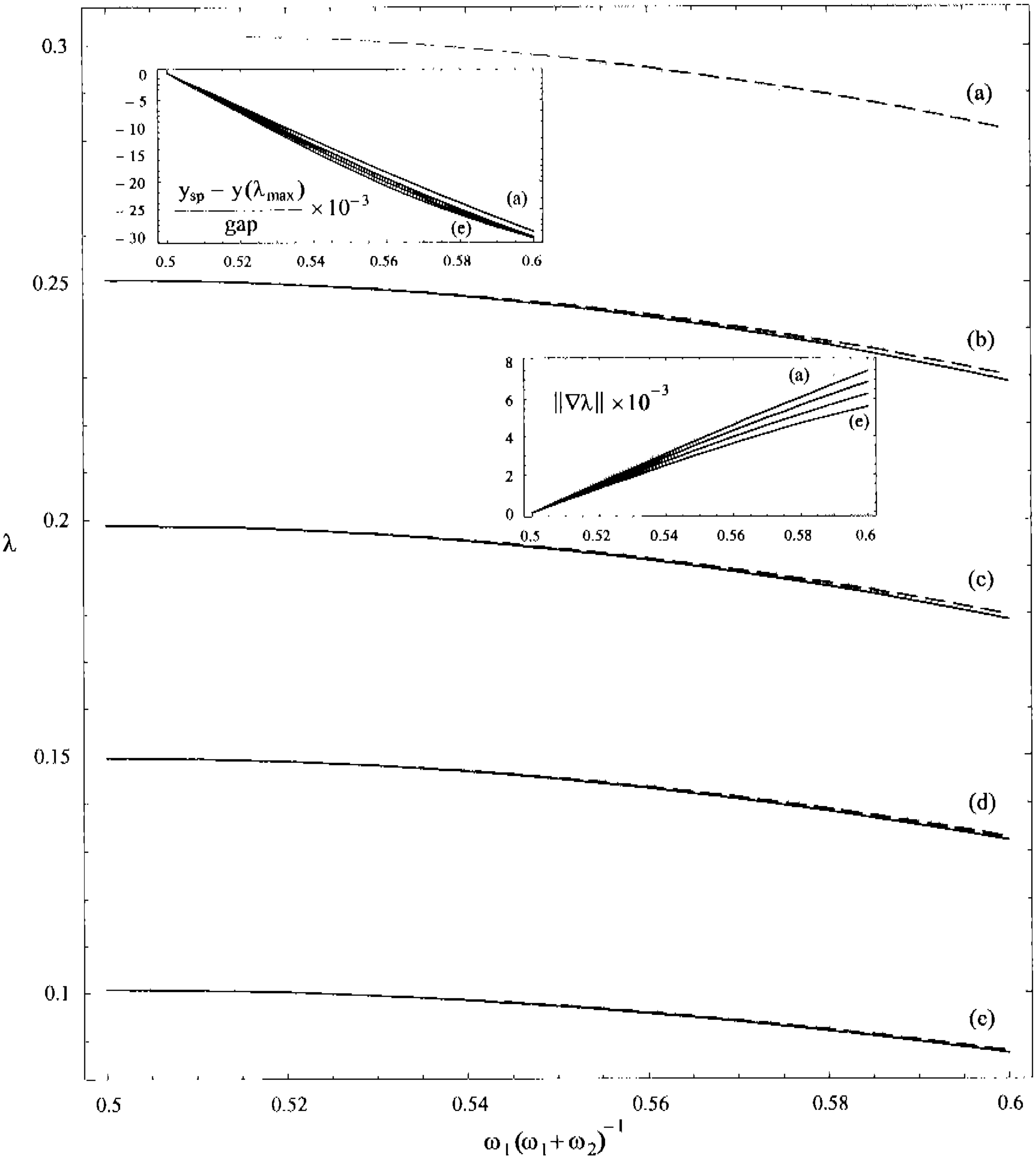

FIGURE 1.13. Flow-type parameter value at the stagnation point as a function of the angular velocity variation for the TRM–A geometries. Continuous lines correspond to the value of λ at the stagnation point for a given angular velocity, and the dashed lines correspond to the maximum value of λ in the central field. Curves (a) to (e) corresponds to 5 different geometries detailed in Table 1.1. In the right-hand inserted Graph, $y_{sp} - y\left(\lambda_{\max}\right)$ corresponds to the distance between the stagnation point and the location of $\lambda_{\max}$. In the left-hand inserted Graph, the magnitude of the flow-type parameter gradient at the stagnation point is shown.

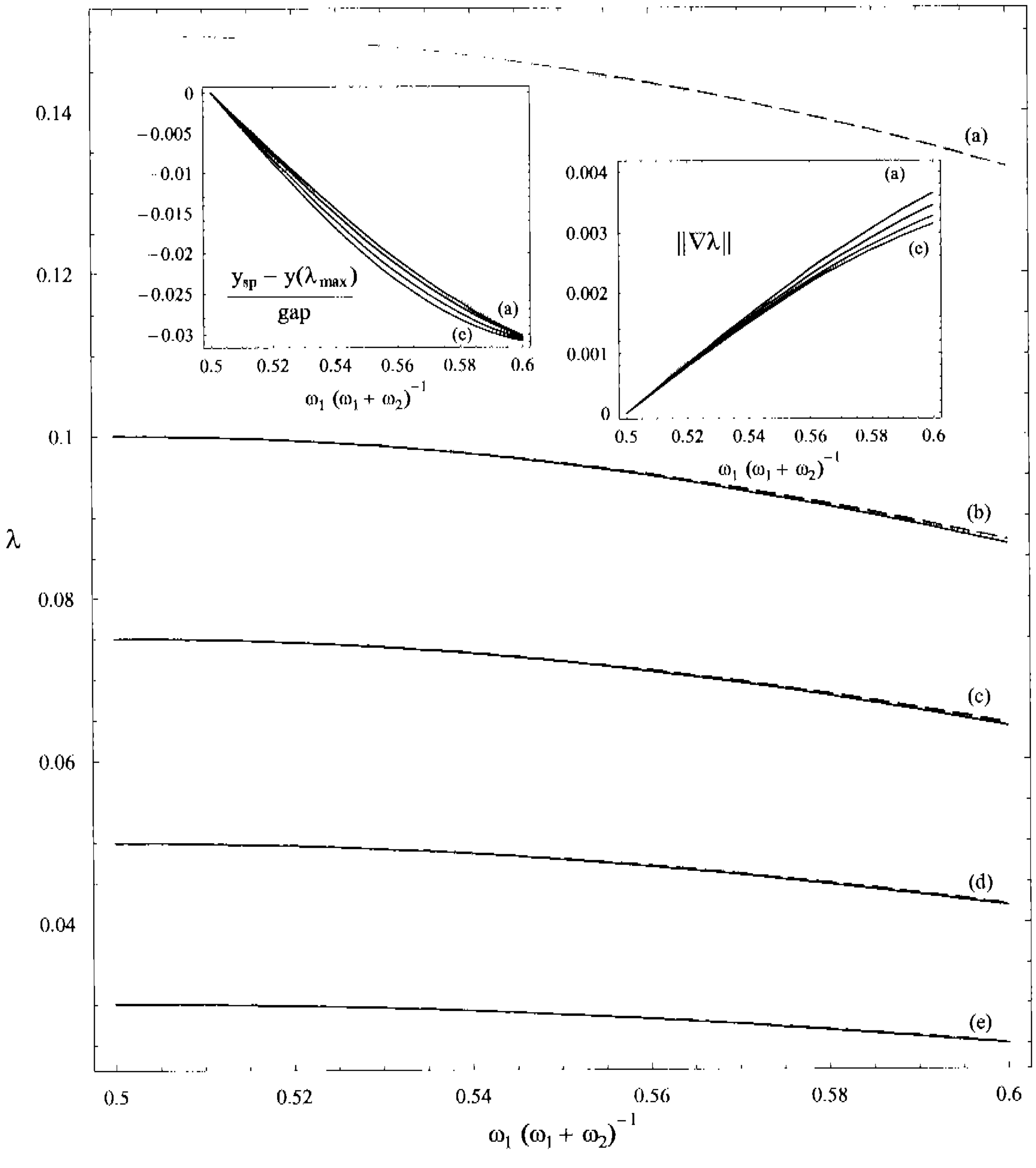

FIGURE 1.14. Flow-type parameter value at the stagnation point as a function of the angular velocity variation for the TRM B geometries. Continuous lines correspond to the value of λ at the stagnation point for a given angular velocity, and the dashed lines correspond to the maximum value of λ in the central field. Curves (a) to (e) corresponds to 5 different geometries detailed in Table 1.1. In the right-hand inserted Graph, $y_{sp} - y(\lambda_{\max})$ corresponds to the distance between the stagnation point and the location of $\lambda_{\max}$. In the left-hand inserted Graph, the magnitude of the flow-type parameter gradient at the stagnation point is shown.

This relative distance $y_{sp} - y\left(\dot{\gamma}_{\min}\right)$ can be as 20% of the gap for the widest separation of cylinders; see insert in Fig. 1.15. For geometries with very small gaps such as those in Fig. 1.16, i. e., corresponding to small values of λ at the stagnation point, then $\dot{\gamma}_{\min}$ has a stepper curvature as evaluated by $\|\nabla\dot{\gamma}\|$, and $y_{sp} - y\left(\dot{\gamma}_{\min}\right)$ can be over one half of the gap. For these geometries, the high values of $\|\nabla\dot{\gamma}\|$ are due to the fact that the highest value of $\dot{\gamma}$ is precisely located at the surface of the fastest spinning cylinder.

1.4 Conclusions

An analytical solution for Two-Roll Mills is presented that should be useful for experimental studies of elongational flows with significant vorticity. With it, three important advantages have been attained: (1) it is a closed form and can be applied to a fully asymmetric geometry of the Two-Roll Mill; (2) it can be used to calculate all flow parameters; and (3) it is valid for an extended central region. The full solution for asymmetric configurations presents rather complex elongational flows. Not only it is possible to generate elongational flows with significant vorticity using symmetric Two-Roll Mills, but by changing to an asymmetric configuration it is possible to generate flows which include gradients of the flow-type parameter as well as gradients of the shear rate at the stagnation point. These results can be the basis for novel studies of droplets deformation in a similar manner to studies reported by Bentley and Leal in a Four-Roll Mill [12].

The experimental setup of Bentley and Leal uses a computer control to maintain drops at the stagnation point for extended periods of time and under specified flow conditions. The control scheme adjusts the speeds of the four cylinders to accomplish these tasks. With the analytical solution presented here, it is possible to envision an equivalent control scheme but based on two cylinders only. The control scheme based on the analytical solution is presented in Chapter 3 of this Thesis. Such possibility opens a significant addition to experimental studies of complex flows, because TRMs are possibly the best option for strong flows with significant vorticity; that is, flows with kinematics much closer to simple shear flows but maintaining the elongational character. Such conditions are not

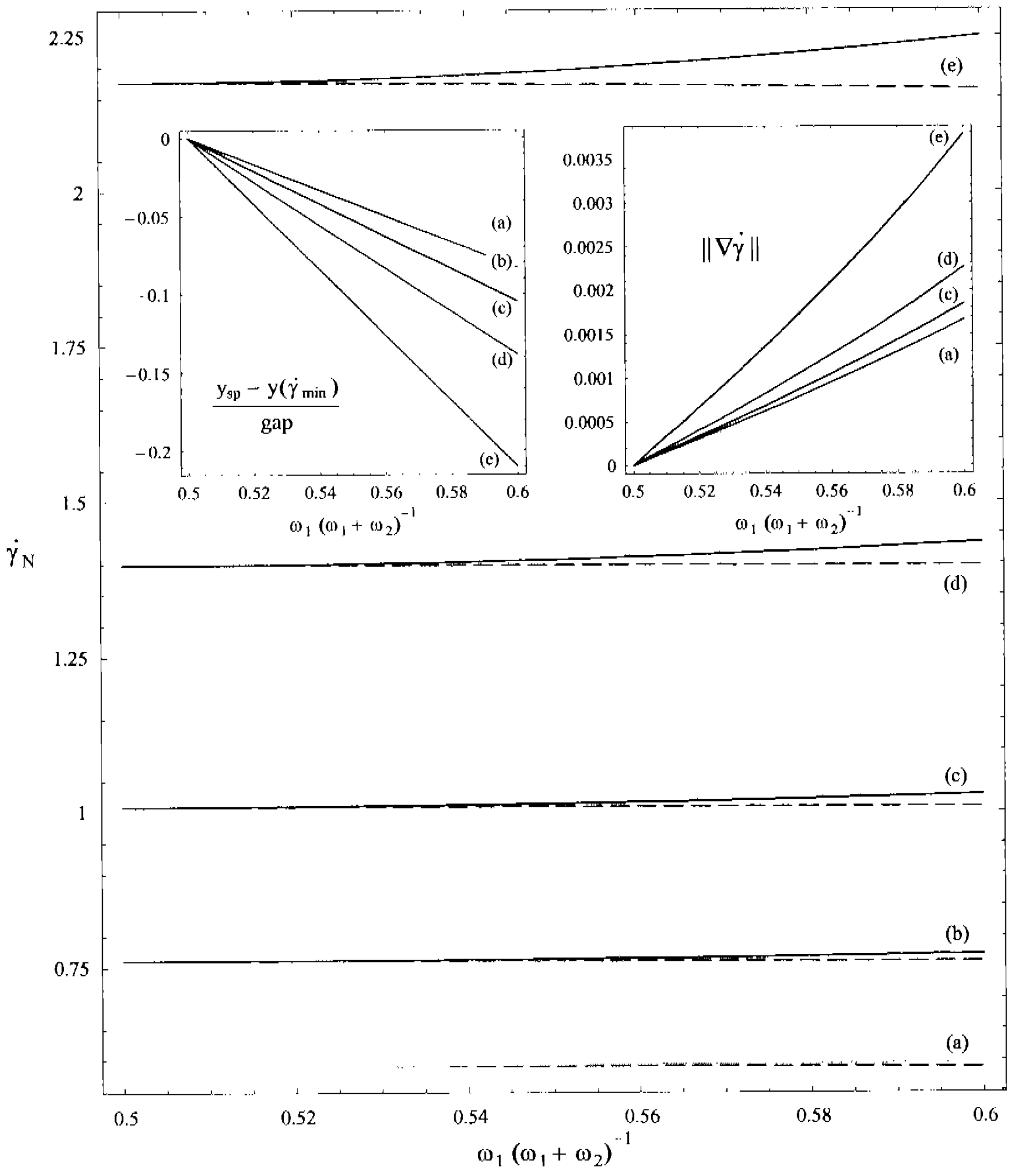

FIGURE 1.15. Normalized shear rate at the stagnation point for the TRM–A geometries. Curves sets (a) to (e) correspond to some geometries as those in Figure 1.13. Continuous curves are values of $\dot{\gamma}_N$ at the stagnation point, and dashed curves to the minimum value observed along the stagnation region. The relative distance $y_{sp} - y\,(\dot{\gamma}_{\min})$ and $\|\nabla\dot{\gamma}\|$ at the stagnation point are given in inserts.

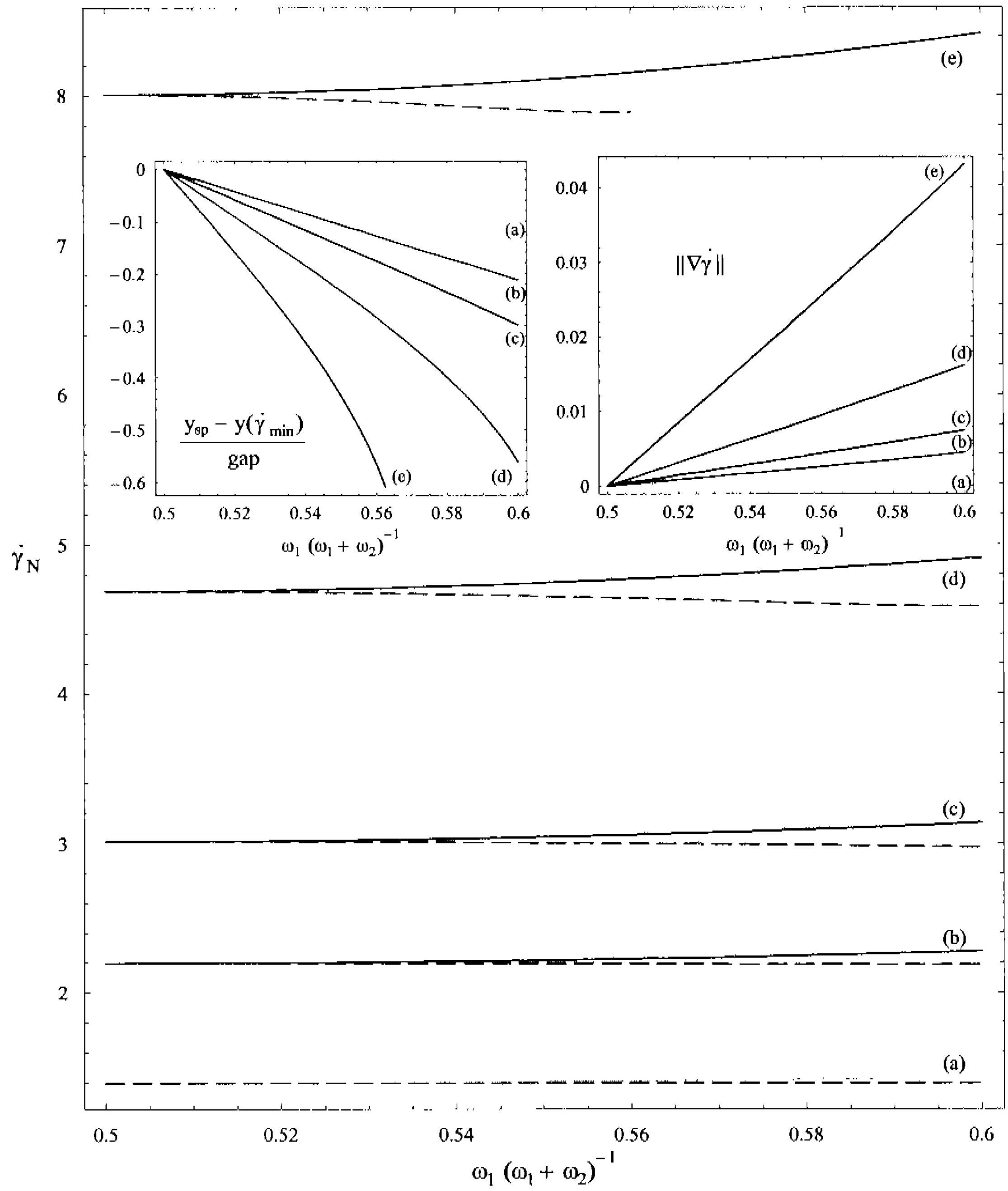

FIGURE 1.16. Normalized shear rate at the stagnation point for the TRM–B geometries. Curves sets (a) to (e) correspond to some geometries as those in Figure 1.14. Continuous curves are values of $\dot{\gamma}_N$ at the stagnation point, and dashed curves to the minimum value observed along the stagnation region. The relative distance $y_{sp} - y\left(\dot{\gamma}_{\min}\right)$ and $\|\nabla\dot{\gamma}\|$ at the stagnation point are given in inserts.

easily accessible with Four-Roll Mills.

When ratios of angular velocities for cylinders are different than one, and the geometry is asymmetric, the flow field is significantly more complex that previously reported for strong flows generated in Four-Roll Mills. In turn, this asymmetric solution presents a rather complex scenario for studies of droplets at the stagnation point that has not been addressed. Concurrently to the strong flow conditions, other asymmetries appear, in particular, asymmetries of the flow-type and shear rate parameters. These asymmetries may represent a controlled scenario for studies of drop deformations of a more complex nature.

Among other asymmetries, the position of the stagnation point is dependent of the relative rotational speed of the cylinders. Given that the flow-type value at the cylinders is zero, then the maximum value occurs at the stagnation point only for the case of equal speed of cylinders. Also, the minimum shear rate exists at the stagnation point. However under flow conditions characterized by ratios of rotational speeds different than one, the stagnation point no longer corresponds neither to the position of the maximum value of the flow-type parameter nor to the position of the minimum shear rate. Furthermore, a gradient for these two parameters exists at the stagnation point.

Finally, the state of the art of the description of the strong flow field generated in a corotating Two-Roll Mill is still limited, and several extensions can be proposed based on the solution here given. A nonsteady solution could be useful for dynamic studies of complex flows or droplets deformations. A similar problem has already been addressed by studying the counter-rotating TRM [25]. Ballal and Rivlin [20] analyzed the case of a finite Reynolds number solution for eccentric concentric cylinders. These ideas will be most useful for complex experiments using corotating TRM's.

Chapter 2

Numerical solution of flows generated by Two-Roll Mills using Boundary Element Methods

Boundary Element Methods (BEM) are numerical techniques for approximate solution of two or three-dimensional boundary value problem which rely on casting the problem onto an integral equation over a bounded domain. By discretization of the boundary into "elements", on each of which a low-degree polynomial approximation is assumed to be valid, the resulting discrete problem is solved numerically. Due to the fact that the problem is cast upon its boundary and the latter is numerically solved, the dimension of the numerical problem is lower when using BEM methods in comparison to using Finite Element Methods (FEM).

The BEM relates velocities at points within the fluid to velocities and stresses on the bounding surfaces. The solution of linear, elliptic, and homogeneous boundary value problems may be represented in terms of boundary integrals involving the boundary values of the unknown function and its derivatives. For the case of Stokes' flow, a boundary integral representation involving the boundary values of the velocity field is obtained.

The analytical solution for Stokes flow of Two-Roll Mills (TRM's) given in the Chapter 1 is valid for an unbounded domain. However when using 2-D strong flows in the laboratory, a constrained, bounded flow field is always used. Thus, the analytical solution is only an approximation to these flows because it does not include the boundary of the actual device; thus, caution must be exercise when it is used. Furthermore, this solutions cannot be used for studies of boundary effects onto the flow field, as for the case of diffusion of vorticity at great distances or the nature of recirculation zones, etc. Thus, BEM predictions can be a useful tool in order to study effects of boundaries over the flow field. In this Chapter, BEM is used for simulating flows generated by *bounded* Two-Roll Mill geometries, and these results are compared with those by the analytical solution. Also, this approximate numerical solution is the basis for studies of drops embedded in a strong flow with flow parameters close to those of simple shear flow, results which are presented in the Second Part of this work.

2.1 Boundary integral equations

Boundary Integral formulation for Stokes flows was theoretically described by Ladyzhenskaya in 1969 [26] within the framework of hydrodynamic potentials, but it was until 1978, when Brebbia [27] formalized the boundary-integral equation methods (BIEM) and introduced the terminology Boundary-Element Method. In this Section, the basic equations necessary for the boundary element method are presented.

2.1.1 Governing equations and boundary conditions with Stokes approximation

In the limit of small Reynolds numbers, incompressible fluid motion is governed by Stokes and continuity equations

$$\boldsymbol{\nabla}\cdot\boldsymbol{\sigma} = \boldsymbol{\nabla}\cdot\boldsymbol{\tau} + \rho\mathbf{b} = -\boldsymbol{\nabla}p + \mu\boldsymbol{\nabla}^2\mathbf{u} + \rho\mathbf{b} = \mathbf{0} \quad \text{and} \tag{2.1}$$

$$\boldsymbol{\nabla}\cdot\mathbf{u} = 0, \tag{2.2}$$

where $\mathbf{u}$ is the velocity, p is the pressure, μ and ρ are the fluid viscosity and density, respectively, $\mathbf{b}$ is the body force, and $\boldsymbol{\sigma}$ is the modified stress tensor given by

$$\boldsymbol{\sigma} = -\left(p - \rho\mathbf{b}\cdot\mathbf{x}\right)\mathbf{I} + \mu(\boldsymbol{\nabla}\mathbf{u} + (\boldsymbol{\nabla}\mathbf{u})^T), \tag{2.3}$$

the laboratory, a constrained, bounded flow field is always used. Thus, the analytical solution is only an approximation to these flows because it does not include the boundary of the actual device; thus, caution must be exercise when it is used. Furthermore, this solutions cannot be used for studies of boundary effects onto the flow field, as for the case of diffusion of vorticity at great distances or the nature of recirculation zones, etc. Thus, BEM predictions can be a useful tool in order to study effects of boundaries over the flow field. In this Chapter, BEM is used for simulating flows generated by *bounded* Two-Roll Mill geometries, and these results are compared with those by the analytical solution. Also, this approximate numerical solution is the basis for studies of drops embedded in a strong flow with flow parameters close to those of simple shear flow, results which are presented in the Second Part of this work.

2.1 Boundary integral equations

Boundary Integral formulation for Stokes flows was theoretically described by Ladyzhenskaya in 1969 [26] within the framework of hydrodynamic potentials, but it was until 1978, when Brebbia [27] formalized the boundary-integral equation methods (BIEM) and introduced the terminology Boundary-Element Method. In this Section, the basic equations necessary for the boundary element method are presented.

2.1.1 Governing equations and boundary conditions with Stokes approximation

In the limit of small Reynolds numbers, incompressible fluid motion is governed by Stokes and continuity equations

$$\boldsymbol{\nabla}\cdot\boldsymbol{\sigma} = \boldsymbol{\nabla}\cdot\boldsymbol{\tau} + \rho\mathbf{b} = -\boldsymbol{\nabla}p + \mu\boldsymbol{\nabla}^2\mathbf{u} + \rho\mathbf{b} = \mathbf{0} \quad \text{and} \tag{2.1}$$

$$\boldsymbol{\nabla}\cdot\mathbf{u} = 0, \tag{2.2}$$

where $\mathbf{u}$ is the velocity, p is the pressure, μ and ρ are the fluid viscosity and density, respectively, $\mathbf{b}$ is the body force, and $\boldsymbol{\sigma}$ is the modified stress tensor given by

$$\boldsymbol{\sigma} = -\left(p - \rho\mathbf{b}\cdot\mathbf{x}\right)\mathbf{I} + \mu(\boldsymbol{\nabla}\mathbf{u} + (\boldsymbol{\nabla}\mathbf{u})^T), \tag{2.3}$$

with τ being the stress tensor excluding body forces. The small Reynolds number assumption requires that $\mathrm{Re} = (\rho u l/\mu) \ll 1$, where u and l are the characteristic velocity and length scales of the fluid motion.

Some properties of the Stokes equation are:

- The Stokes equation states that pressure, viscous, and body forces balance at any instant in time. Quasi-steady time evolution of the flow may occur as a result of boundary motion or varying boundary conditions.
- The instantaneous structure of the flow depends solely on the present boundary configuration and boundary conditions, and is independent of the history of motion.
- There is no intense concentration of vorticity in Stokes flow and furthermore, the magnitude of vorticity attains extreme values only at the boundaries of the flow.

2.1.2 Green's functions

A basic feature of Boundary Element Methods is the application of fundamental solutions, which are analytical free-space solutions of the governing differential equation under the action of point sources. The fact that they are exact solutions accounts for some of the advantages of BEM, viz., the improved accuracy in the calculation of stresses and exterior problems.

The Green's functions of Stokes flow provides the velocity and pressure fields that satisfy the continuity equation, $\boldsymbol{\nabla} \cdot \mathbf{u} = 0$. The singularly forced Stokes equation is

$$-\boldsymbol{\nabla} p + \mu \boldsymbol{\nabla}^2 \mathbf{u} + \mathbf{b}\, \delta_D(\mathbf{x} - \mathbf{x}_0) = \mathbf{0}, \tag{2.4}$$

where $\mathbf{b}$ is a constant vector, the position of the point $\mathbf{x}_0$ is arbitrary, and δ_D is a two-dimensional or three-dimensional delta function [28]. Physically, Green's function expresses the flow due to a point force located at $\mathbf{x}_0$ (named *pole* or *source point*), with the direction and strength of $\mathbf{b}$, in the absence or presence of boundaries. Green's functions are named *fundamental solutions* or *propagators*. The point $\mathbf{x}$ is the *observation* or *field point*.

The solution for the velocity and pressure fields of the Eq. 2.4 is given by

$$\mathbf{u}(\mathbf{x}) = \frac{1}{C_D\, \pi\, \mu} \mathbf{G}(\mathbf{x}, \mathbf{x}_0) \cdot \mathbf{b} \tag{2.5}$$

Equations. 2.13 relate the velocity field $\mathbf{u}(\mathbf{x})$ at any point inside (or outside) a fluid volume, or on the boundary, to the velocity $\mathbf{u}(\mathbf{x}_S)$ and traction $\boldsymbol{\sigma}(\mathbf{x}_S) \cdot \mathbf{n} = \mathbf{f}$ on the bounding surface. For points on the boundary S, this is a Fredholm integral equation of the second kind for the velocity $\mathbf{u}(\mathbf{x}_S)$ and of the first kind for the traction $\boldsymbol{\sigma}(\mathbf{x}_S) \cdot \mathbf{n} = \mathbf{f}$. Finally, Eq. 2.13c is an useful identity for developing integral equations with a minimum number of unknowns.

The kernels $\mathbf{G}$ and $\mathbf{T}$ have integrable singularities (at $\mathbf{x} = \mathbf{x}_S$) and some care is needed carrying out the numerical integration. Common procedures either cut out a region surrounding the singularity and perform the local integration analytically, or subtract the singularity directly in the numerical approximation of the integral.

Equation 2.13b imposes a mathematical constraint between the distributions of boundary velocities and surface forces. Physically, this constraint implies that the boundary velocities and surface forces may not be specified independently in an arbitrary manner, but must be prescribed in such a way that Eq. 2.13b is fulfilled [28]. Here, the boundary velocity $\mathbf{u}_S(\mathbf{x})$ over S is prescribed, and Eq. 2.13b is reduced to a *Fredholm integral equation of the first kind* for the boundary surface forces,

$$\int_S \mathbf{G}(\mathbf{x}, \mathbf{x}_0) \cdot \boldsymbol{\sigma}(\mathbf{x}) \cdot \mathbf{n}(\mathbf{x}) \;\, dS(\mathbf{x}) = -\frac{C_D}{2}\, \pi\, \mu\, \mathbf{u}(\mathbf{x}_0) + \mu\, \mathbf{I}^D(\mathbf{x}_0), \tag{2.14}$$

where $\mathbf{I}^D(\mathbf{x}_0)$ represents the known double-layer potential, that is

$$\mathbf{I}^D(\mathbf{x}_0) = \int_S^{PV} \mathbf{u}(\mathbf{x}) \cdot \mathbf{T}(\mathbf{x}, \mathbf{x}_0) \cdot \mathbf{n}(\mathbf{x}) \;\, dS(\mathbf{x}), \tag{2.15}$$

where the superscript PV indicates the principal value of the double-layer potential, defined as the value of the improper double-layer integral when the point $\mathbf{x}_0$ is right on S [28].

2.2 Numerical implementation of BEM

Because BEM are very susceptible to round-off errors when not using the appropriate mathematical techniques, in this work, Mathematica software was used, maintaining a close relation to the analytical technique; however, the computational time spent carrying out the numerical method is greater as compared to an optimal numerical implementation [29]. Nonetheless, the results here presented are calculated with a fast but standard personal computer.

The steps required for the numerical implementation of BEM are:

1. The domain of the integral equation S is traced with a network of marker points or nodes, which approximate S using a set of N boundary elements defined with respect to the nodes (discretization).

2. The unknown boundary velocity $\mathbf{u}$ (or the surface force $\mathbf{f}$) over each boundary element are approximated using a truncated polynomial expression in terms of properly defined surface variables. In our case, the unknown boundary function is assumed to be constant over each element, therefore, there is a set of M coefficients, equal to the number of elements N.

3. The unknown function is substituted into the integral equation, and all M coefficients are extracted from the single and double layer potentials. In this manner, an integral equation is converted into an algebraic equation involving M coefficients. The factor multiplying these coefficients are integrals of the single and double layer potential over selected boundary elements.

4. The local expansions coefficients are computed using the collocation method. In the collocation method, the discretized integral equation is enforced at M collocation points over the boundary. As a result, a system of M linear algebraic equations for the coefficients of the local expansions is obtained. Using Eq. 2.14 and by setting up a system of equations with as many unknowns, the collocation method allows computation of the unknown boundary data. The principle of collocation imply the location of load points sequentially at all nodes of the discretization such that the domain variable at the load point coincides with the nodal value. Because linear and higher order polynomial shape functions lead to nodes which belong to more than one element, it is worthwhile to introduce a global node numbering ($n = 1, ..., N$) which does not depend on an element.

5. Finally, the system of linear algebraic equations is solved for the M coefficients of the local expansions. In general, this system is dense and non-symmetric.

2.2.1 Spatial discretization of the Fredholm integral equation in 2D

In order to discretize Eq. 2.14, this equation may be rewritten using an index notation (for Cartesian coordinates) and for the two-dimensional case ($j = 1, 2$), the following equation is obtained

$$\int_C f_i(\mathbf{x})\, G_{ij}(\mathbf{x}, \mathbf{x}_0)\, dl(\mathbf{x}) = - 2\pi\mu u_j(\mathbf{x}_0) + \mu \int_C^{PV} u_i(\mathbf{x})\, T_{ijk}(\mathbf{x}, \mathbf{x}_0)\, n_k(\mathbf{x})\, dl(\mathbf{x}), \quad (2.16)$$

where $\mathbf{f} = \boldsymbol{\sigma} \cdot \mathbf{n}$. Then,

$$\sum_{n=1}^{N} \int_{C^n} f_i(\mathbf{x})\, G_{ij}(\mathbf{x}, \mathbf{x}_0)\, dl(\mathbf{x}) = - 2\pi\mu u_j(\mathbf{x}_0) + \mu \sum_{n=1}^{N} \int_{C^n}^{PV} u_i(\mathbf{x})\, T_{ijk}(\mathbf{x}, \mathbf{x}_0)\, n_k(\mathbf{x})\, dl(\mathbf{x}). \quad (2.17)$$

Using a local mean value for f_i and u_i as the approximated value for each element, then the above Equation can be rewritten as

$$\sum_{n=1}^{N} f_i^n \int_{C^n} G_{ij}(\mathbf{x}, \mathbf{x}_0)\, dl(\mathbf{x}) = - 2\pi\mu u_j(\mathbf{x}_0) + \mu \sum_{n=1}^{N} u_i^n \int_{C^n}^{PV} T_{ijk}(\mathbf{x}, \mathbf{x}_0)\, n_k(\mathbf{x})\, dl(\mathbf{x}). \quad (2.18)$$

Gauss-Legendre quadrature methods can be used for the numerical integration of the Eq. 2.18, hence

$$\sum_{n=1}^{N} f_i^n \left(q^n \sum_{m=1}^{M+1} w_m G_{ij}(\mathbf{x}^m, \mathbf{x}_0) \right) = - 2\pi\mu u_j(\mathbf{x}_0) + \mu \sum_{n=1}^{N} \left(u_i^n q^n \sum_{m=1}^{M+1} w_m T_{ijk}(\mathbf{x}^m, \mathbf{x}_0)\, n_k^m \right), \quad (2.19)$$

where M is the degree of the Gauss-Legendre quadrature, q^n is the resultant factor obtained from the transformation of the limits of integration to a canonical form for the segment n,

w_m is the weight for the $\mathbf{x}^m$–th base point, and $\mathbf{G}(\mathbf{x}^m, \mathbf{x}_0)$, $\mathbf{T}(\mathbf{x}^m, \mathbf{x}_0)$ and $\mathbf{n}^m = \mathbf{n}(\mathbf{x}^m)$ are evaluated at the $\mathbf{x}^m$–th base point.

Now, for each one of the collocation points there is an equation of the form 2.19, and then

$$\sum_{l=1}^{N} \left[\sum_{n=1}^{N} f_i^n \left(q^n \sum_{m=1}^{M+1} w_m \, G_{ij} \left(\mathbf{x}^m, \mathbf{x}_0^l \right) \right) + 2\,\pi\,\mu\, u_j \left(\mathbf{x}_0^l \right) - \mu \sum_{n=1}^{N} \left(u_i^n \, q^n \sum_{m=1}^{M+1} w_m \, T_{ijk} \left(\mathbf{x}^m, \mathbf{x}_0^l \right) \, n_k^m \right) \right] = 0. \quad (2.20)$$

Therefore, a $j\ N \times j\ N$ system of linear equations for the components of the surface force $\mathbf{f}$ at each collocation point is obtained. This system is dense and non-symmetric, and a general-purpose numerical method must be used for solving it, such as the Gauss elimination method or by an iterative method as Jacobi's method.

In Equation 2.20 and for $l = n$, integrals become singular (the pole $\mathbf{x}_0^n$ is on the element n), and a method for computing singular integral must be used. For the determination of the flow fields in the TRM, the method of "removal of the singularity" is used. Once the system 2.20 is solved, the velocity field can be obtained at any point by means of the Eq. 2.13a.

2.2.2 Properties of the flow field

The flow field properties are obtained from the transformation of Eqs. 1.29 – 1.66 to Cartesian coordinates. Thus, the shear rate is given now by

$$\|\nabla \mathbf{u}\| = \dot{\gamma} = \sqrt{2\left(\frac{\partial u_x}{\partial x}\right)^2 + \left(\frac{\partial u_x}{\partial y}\right)^2 + \left(\frac{\partial u_y}{\partial x}\right)^2}\,; \quad (2.21)$$

the rate of strain is

$$\|\mathbf{D}\| = \sqrt{2\left(\frac{\partial u_x}{\partial x}\right)^2 + \frac{1}{2}\left(\frac{\partial u_x}{\partial y} + \frac{\partial u_y}{\partial x}\right)^2}\,; \quad (2.22)$$

the objective rate of rotation is

$$\|\bar{\mathbf{W}}\| = \sqrt{2}\left|\frac{1}{2}\left(\frac{\partial u_x}{\partial y} - \frac{\partial u_y}{\partial x}\right) - \Omega_{12}\right|, \quad (2.23)$$

Coefficients c_l for centered differences									
$p\backslash l$	-4	-3	-2	-1	0	1	2	3	4
First derivative									
8	$\frac{1}{280}$	$-\frac{4}{105}$	$\frac{1}{5}$	$-\frac{4}{5}$	0	$\frac{4}{5}$	$-\frac{1}{5}$	$\frac{4}{105}$	$-\frac{1}{280}$
Second derivative									
8	$-\frac{1}{560}$	$\frac{8}{315}$	$-\frac{1}{5}$	$\frac{8}{5}$	$-\frac{205}{72}$	$\frac{8}{5}$	$-\frac{1}{5}$	$\frac{8}{315}$	$-\frac{1}{560}$

TABLE 2.1. Coefficients for the centered finite-difference formula.

where

$$\begin{aligned}\Omega_{12} = \Bigg(&u_x\left(\frac{\partial^2 u_x}{\partial x^2}\left(\frac{\partial u_x}{\partial y}+\frac{\partial u_y}{\partial x}\right)-\frac{\partial u_x}{\partial x}\left(\frac{\partial^2 u_x}{\partial x\partial y}+\frac{\partial^2 u_y}{\partial x^2}\right)\right)+\\ &u_y\left(\frac{\partial^2 u_x}{\partial x\partial y}\left(\frac{\partial u_x}{\partial y}+\frac{\partial u_y}{\partial x}\right)-\frac{\partial u_x}{\partial x}\left(\frac{\partial^2 u_x}{\partial y^2}+\frac{\partial^2 u_y}{\partial x\partial y}\right)\right)\Bigg)*\\ &\left(4\left(\frac{\partial u_x}{\partial x}\right)^2+\left(\frac{\partial u_x}{\partial y}+\frac{\partial u_y}{\partial x}\right)^2\right)^{-1}, \qquad (2.24)\end{aligned}$$

and the flow-type parameter is

$$\lambda = \frac{\|\mathbf{D}\| - \|\bar{\mathbf{W}}\|}{\|\mathbf{D}\| + \|\bar{\mathbf{W}}\|}. \qquad (2.25)$$

All parameters of the flow are functions of derivatives of the velocity field, which are obtained by mean of numerical differentiation. The method used is the centered finite-difference formula [30]. Thus, the k–th derivative of a function $f(x)$, at the data point x_i, in terms of the function's values at a number of evenly spaced data points separated by the distance Δx, is

$$\left(\frac{\partial^k f}{\partial x^k}\right)_{x=x_i} = \frac{1}{\Delta x^k}\sum_{l=-l_1}^{l_2} c_l\, f_{i+l} + O\left(\Delta x^p\right), \qquad (2.26)$$

where p is the order of the approximation, and c_l are the associated coefficients. In this Thesis, the order of approximation used is 8. Table 2.1, presents the values of the coefficients c_l and $p = 8$ for the first and second derivative. Mixed derivatives are obtained first applying the appropriate formula to the function with respect to a variable, and subsequently to the second variable.

In order to apply the formula of differentiation, it is necessary to calculate the velocity field in a grid evenly spaced in each direction (however, Δx can be different of Δy). To calculate the flow parameters at a point in the field it is necessary to calculate the velocities at 81 points. Due to this fact, "memory" functions are used for the velocity field and its derivatives.

2.3 Characteristics of flows generated by Two-Roll Mills

For the experimental work to be carried out, two devices or flow cells are proposed. Each flow cell uses a set of five cylinder-pairs, each pair of a different diameter, but all cylinders separated by a fixed distance. With these devices, it is possible to cover values of the flow-type parameter at the stagnation point with complementary ranges and within the interval of [0.03, 0.3]. The flow cells are named TRM–A and TRM-B, having a distance between axes of the cylinders of 34.00 mm and 52.00 mm, respectively. Other important difference between flow devices is the outer contour of the flow cells, which has a different distance from the center of the device to the wall (wd). The contour is established assuming the best match of shapes for the streamlines of flows generated by all five pairs of cylinders (obtained from the analytical solution); its shapes are shown in Fig. 2.1.

Tables 2.2 and 2.3 list the geometrical characteristics and the flow field properties at the stagnation point for all different sets of cylinders and for each flow cell, when the radius and the angular velocity of the cylinders are equal. In order to compare the analytical values to those determined with the numerical procedure, the subscript A stands for *Analytic*, and the subscript N means *Numeric*; the dimensions are in millimeters. The value of the shear rate is normalized by $(\omega_1 + \omega_2)$.

The discretization of the cylinders' surfaces is performed with arc elements, while the external surface of the TRM is discretized with both arc and linear elements as shown in Fig. 2.1. The collocation points are placed at the middle distance point on each element. Fig. 2.1 also shows the relative distribution of element on the boundaries. With the purpose

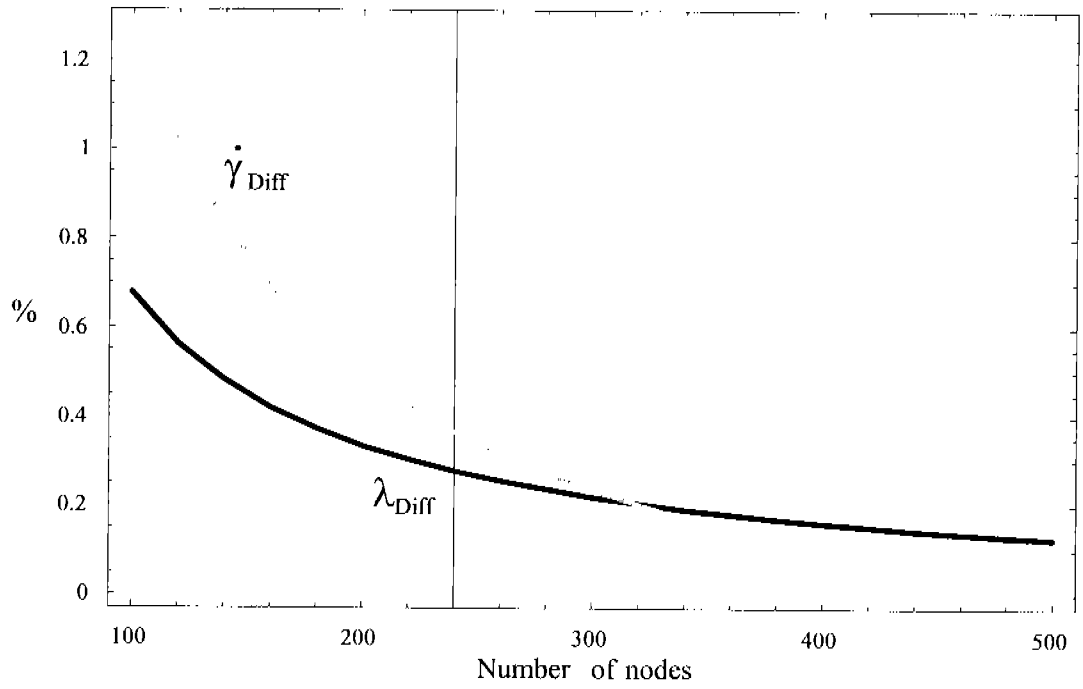

FIGURE 2.2. Convergence of the percentage of difference between the numeric and the analytical values of the flow-type parameter and the shear rate at the stagnation point, with respect to the number of nodes on each roller surface. The data are for the TRM–A geometry with $R_1 = R_2 = 10.00\,\text{mm}$ and $\omega_1 = \omega_2$.

the proximity of the boundaries of the cylinders that are much closer to the stagnation point, and by the fact that discretization elements on the cylinders' surface used are more elongated (due to bigger radii but with a fixed number of elements for all geometries). For the TRM A and TRM B flow devices, the difference of the flow-type parameter values are more accentuated than the unbounded case due to the presence of the outer boundary. However, the difference between the numerical and the theoretical values are always small; for the worst case it is less than 1.2 %. Therefore, the analytical solution with the proposed number of elements is a good approximation to the flow field generated by the Two Roll Mill in the region near the stagnation point, even for bounded TRM geometries. Another feature observed in Fig. 2.3, is the fact that for geometries with larger gaps (TRM–A), effects due to the external boundary diminish the flow-type parameter value (λ at the boundaries is equal to zero), whereas in all other cases, the value of λ_N is greater than the analytical value, λ_A.

The first graph of Figure 2.4 shows the value of the normalized shear rate at the stagnation point for the analytical solution, the TRM–Unbounded, the TRM–A geometry, and the TRM–B geometry. The second graph shows the difference between the numerical value of the shear rate with respect to the analytical value. Opposite to the behavior observed for the flow-type parameter, the shear rate increases for those geometries with larger gaps, because the shear rate is always maximum at the boundaries.

Figures 2.5, 2.6 and 2.7 show properties of the flow field generated by a TRM–A flow device, with $R_1 = R_2 = 10.00$ mm, and $\omega_1 = \omega_2$; a TRM–B, with $R_1 = R_2 = 24.50$ mm, and $\omega_1 = \omega_2$; and a TRM–A, with $R_1 = 10.00\,\mathrm{mm}$, $R_2 = 14.00$ mm, and $\omega_1/\omega_2 = 1.609$, respectively. All Graphs (a) correspond to streamlines; (b) to isopleths for the magnitude of the velocity field $||\mathbf{u}||$; (c) to isopleths for the magnitude of the gradient of the velocity field $\dot{\gamma}$; and (d) to isopleths for the flow-type parameter λ. All fields are obtained using a square grid with length $= 0.5\,\mathrm{mm}$ for the numerical differentiation.

For the flow-type parameter field, Fig. 2.5 Graph (d), the same structure of the fields is obtained with the analytical solution as shown in Fig. 1.9, but in this case the existence of the external boundary displaces the vortices toward the center of the device. This displacement of the vortices, is the cause of the flow-type parameter behavior observed for different geometries as shown in Fig. 2.3. When the cylinders are relatively large, i. e. small λ values, isopleths for λ show a structure quite affected by the presence of the external boundary, as shown in Fig. 2.6, in contrast with the analytical result shown in the Fig. 1.10. Here, the two vortices are present too, but their size are smaller and their shapes quite different.

Other possible variations of the flow field characteristics are those induced by changes of the ratio of angular velocities of the cylinders. For these cases, the position of the stagnation point is displaced towards the slower rotating cylinder. But given the symmetry properties of the flow field, displacement of the stagnation point occurs only along the line of the y-axis. Other important characteristics are modified as well: the values for the observed shear rate and flow-type parameter at the stagnation point are influence accordingly by a stronger source of vorticity on the faster cylinder. Figure 2.7

shows the flow parameters that correspond to those analytical results shown in Fig. 1.11.

Figures 2.8 and 2.9 present a comparison of the numerical solution data with respect to the analytical solution; radii of the cylinders are equal but the angular velocity is varied. These comparisons are among three geometries: the TRM–Unbounded, the TRM–A and the TRM–B. The graphs show the percentages of the differences between the flow-type parameter at the stagnation point, $\Delta\lambda = 100\left(\lambda_N - \lambda_A\right)/\lambda_A$; the shear rate at the stagnation point, $\Delta\dot{\gamma} = 100\left(\dot{\gamma}_N - \dot{\gamma}_A\right)/\dot{\gamma}_A$; and the position of the stagnation point, $\Delta sp = 100\left(y\left(sp\right)_N - y\left(sp\right)_A\right)/g$; where the subscripts A and N implies analytical and numerical, respectively. Continuous lines correspond to the bounded geometries, and dashed lines, to the unbounded geometries. The labels shown to the right of the Graphs, corresponds to the radius size tabulated in Tables 2.2 and 2.3. These Figures show that the flow parameters for the unbounded geometries are slightly different of those of given by the analytical solution. In these cases, when the relation g/de is larger, the differences for $\Delta\lambda$ are greater, being in the worst of the cases less than 0.5%; as for $\Delta\dot{\gamma}$, the difference is negative, but its magnitude is less than 0.25%. This behavior can be explained by the graph of Δsp, where the predicted locations of the stagnation point by the unbounded numerical solution do not coincide with those obtained with the analytical solution for each velocity ratio. When the angular velocities of the cylinders are different, the analytical solution is not closed anymore, this difference in position being greater when angular velocities ratios are larger, and as can be seen from Fig. 1.4, a velocity component at infinity appears, which affects slightly the whole field, including the central region. This behavior is most important for geometries with the largest values of the flow-type parameter.

The discretization of the TRMs' boundaries and the fact that BEMs are based on a fundamental solution that is in essence singular (because is the solution of the singular forced Stokes equation) generate a velocity field (and consequently in its derivatives) with significant noise, especially at the vicinity of the walls, as Fig. 2.10 shows. This lack of accurate information around all surfaces and for all parameter fields of the TRM geometries is shown in Figs. 2.5 2.7.

For the flow-type parameter field given in Figs. 2.5 - 2.7, there are two regions, one close to the cylinders and the other to the external boundary where low accuracy predictions

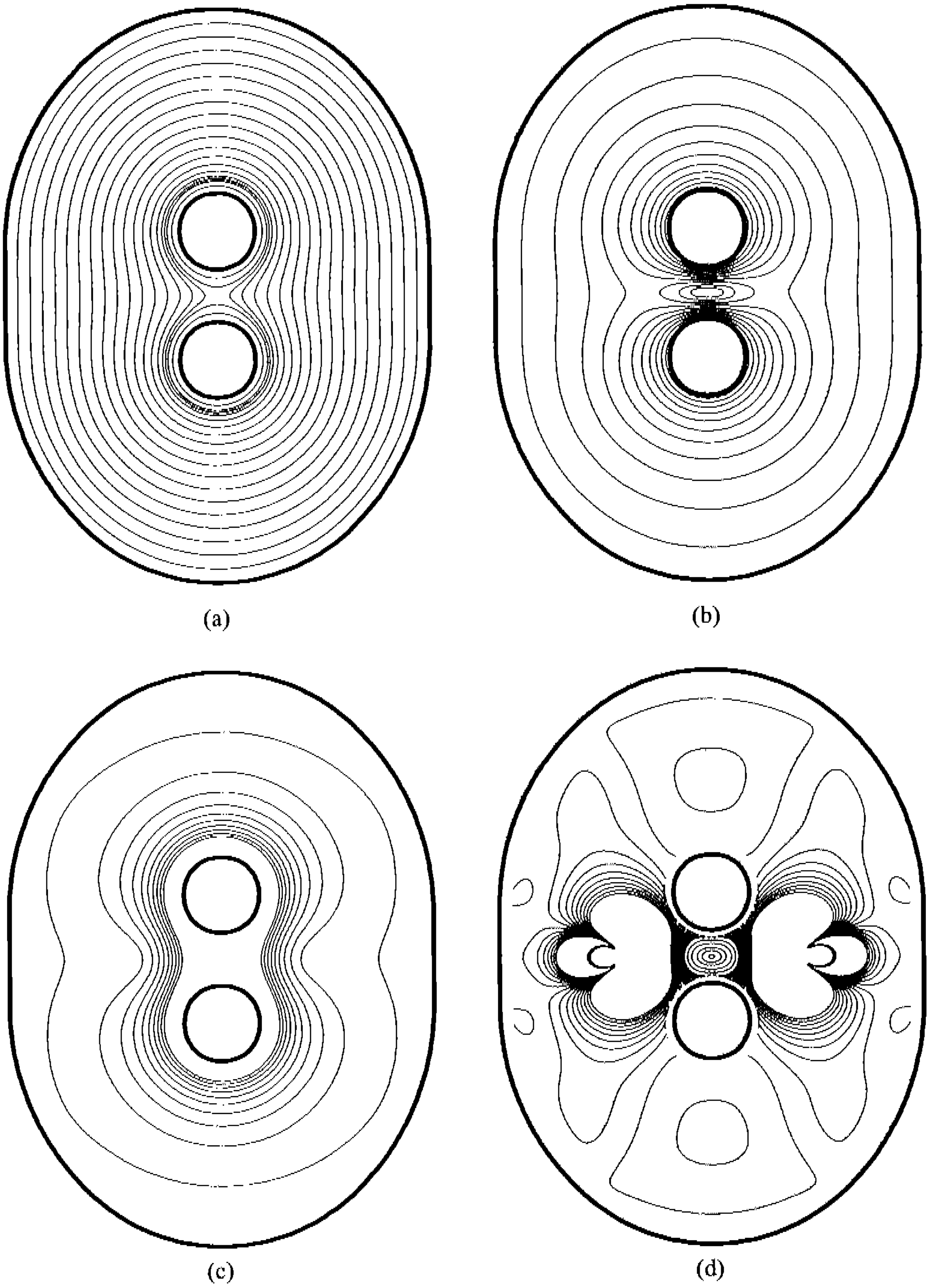

FIGURE 2.5. Properties of the flow field generated by a TRM–A flow cell, with $R_1 = R_2 = 10.00$ mm, and $\omega_1 = \omega_2$. Graph (a) correspond to streamlines; (b) to isopleths for the magnitude of the velocity field $\|\mathbf{u}\|$; (c) to isopleths for the magnitude of the gradient of the velocity field $\dot{\gamma}$; and (d) to isopleths for the flow-type parameter λ.

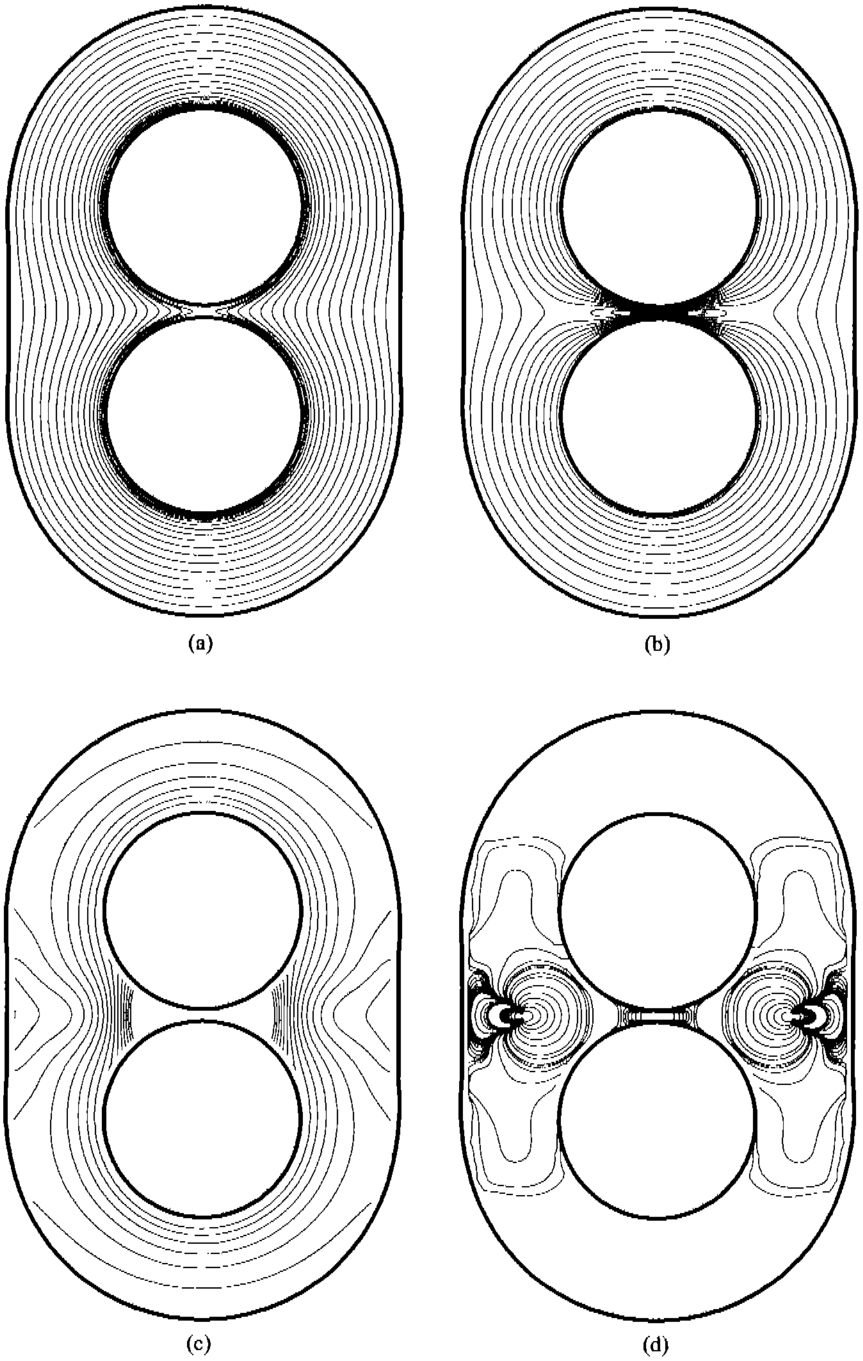

FIGURE 2.6. Properties of the flow field generated by a TRM–B flow cell, with $R_1 = R_2 = 24.50$ mm, and $\omega_1 = \omega_2$. Graph (a) correspond to streamlines; (b) to isopleths for the magnitude of the velocity field $\|\mathbf{u}\|$; (c) to isopleths for the magnitude of the gradient of the velocity field $\dot{\gamma}$; and (d) to isopleths for the flow-type parameter λ.

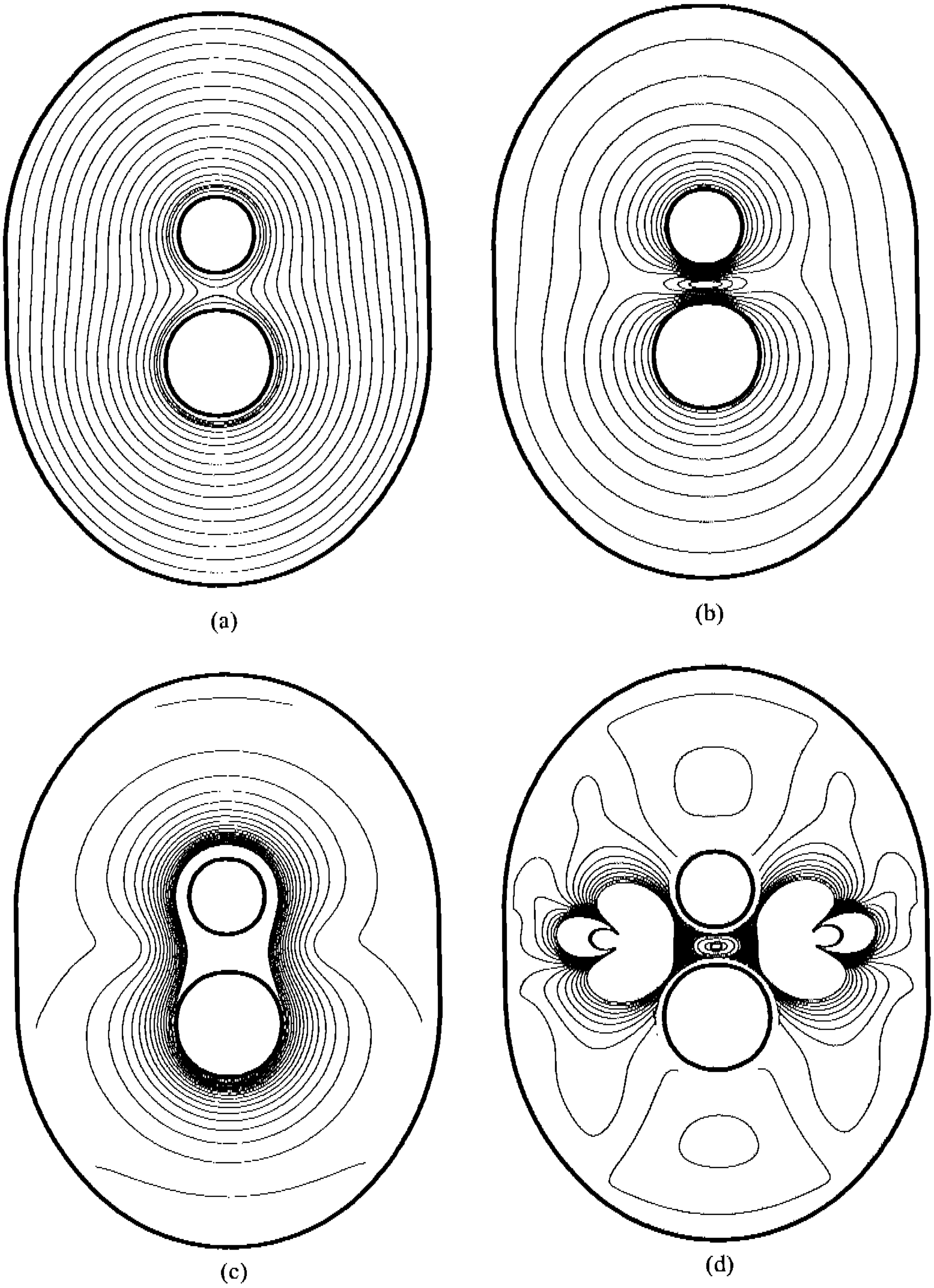
(a) (b) (c) (d)

FIGURE 2.7. Properties of the flow field generated by a TRM–A flow cell, with $R_1 = 10.00$ mm, $R_2 = 10.00$ mm, and $\omega_1/\omega_2 = 1.609$. Graph (a) correspond to streamlines; (b) to isopleths for the magnitude of the velocity field $\|\mathbf{u}\|$; (c) to isopleths for the magnitude of the gradient of the velocity field $\dot{\gamma}$; and (d) to isopleths for the flow-type parameter λ.

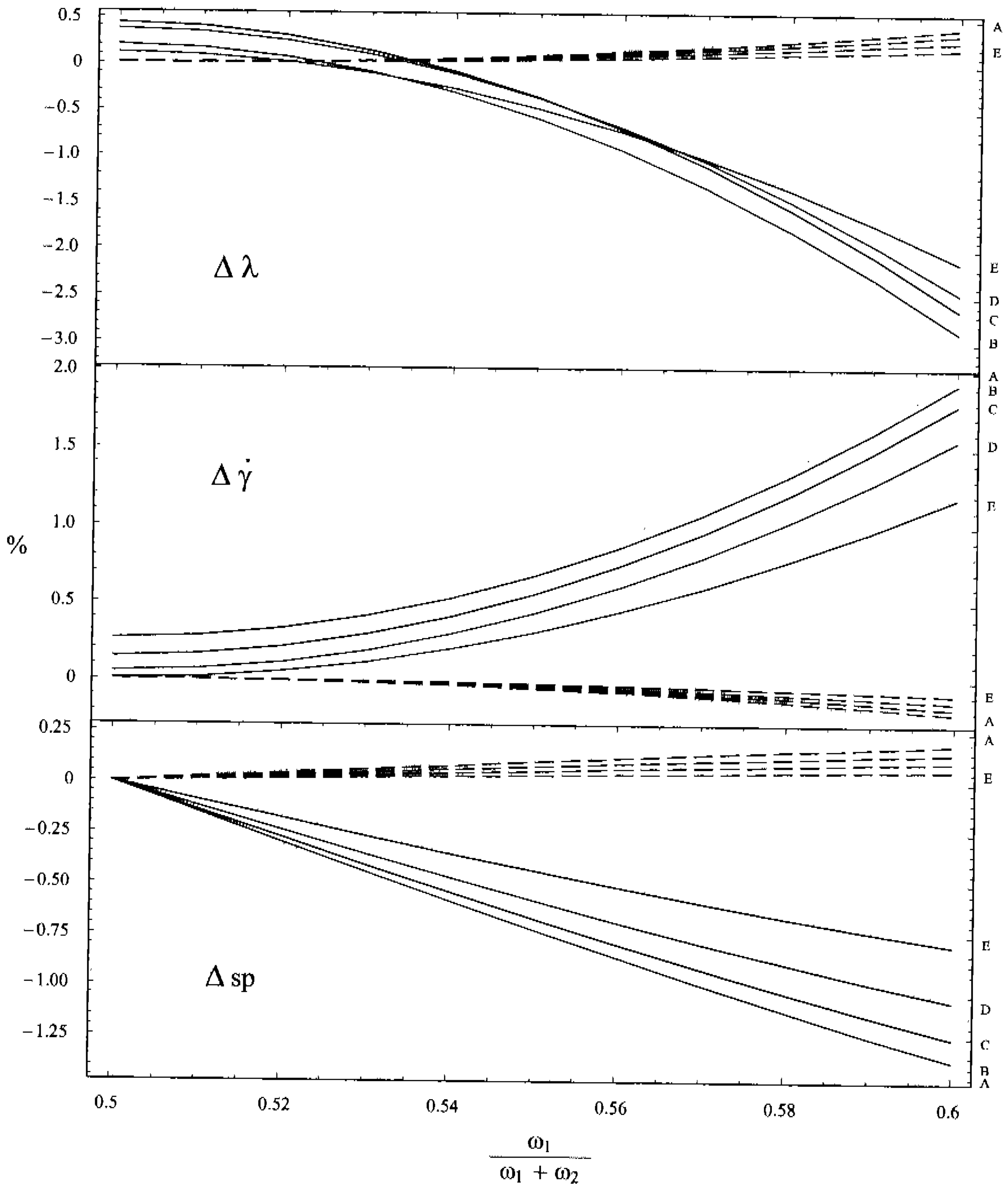

FIGURE 2.8. Graphs of the difference between the numerical data obtained from the TRM A geometry and its respective TRM–Unbounded geometry, with respect to the analytical solution as function of the angular velocity variation. Graphs are for the flow-type parameter, $\Delta\lambda$; the shear rate, $\Delta\dot{\gamma}$; and the position of the stagnation point, Δsp. Continuous lines corresponds to the bounded geometries, whereas dashed lines correspond to the unbounded cases.

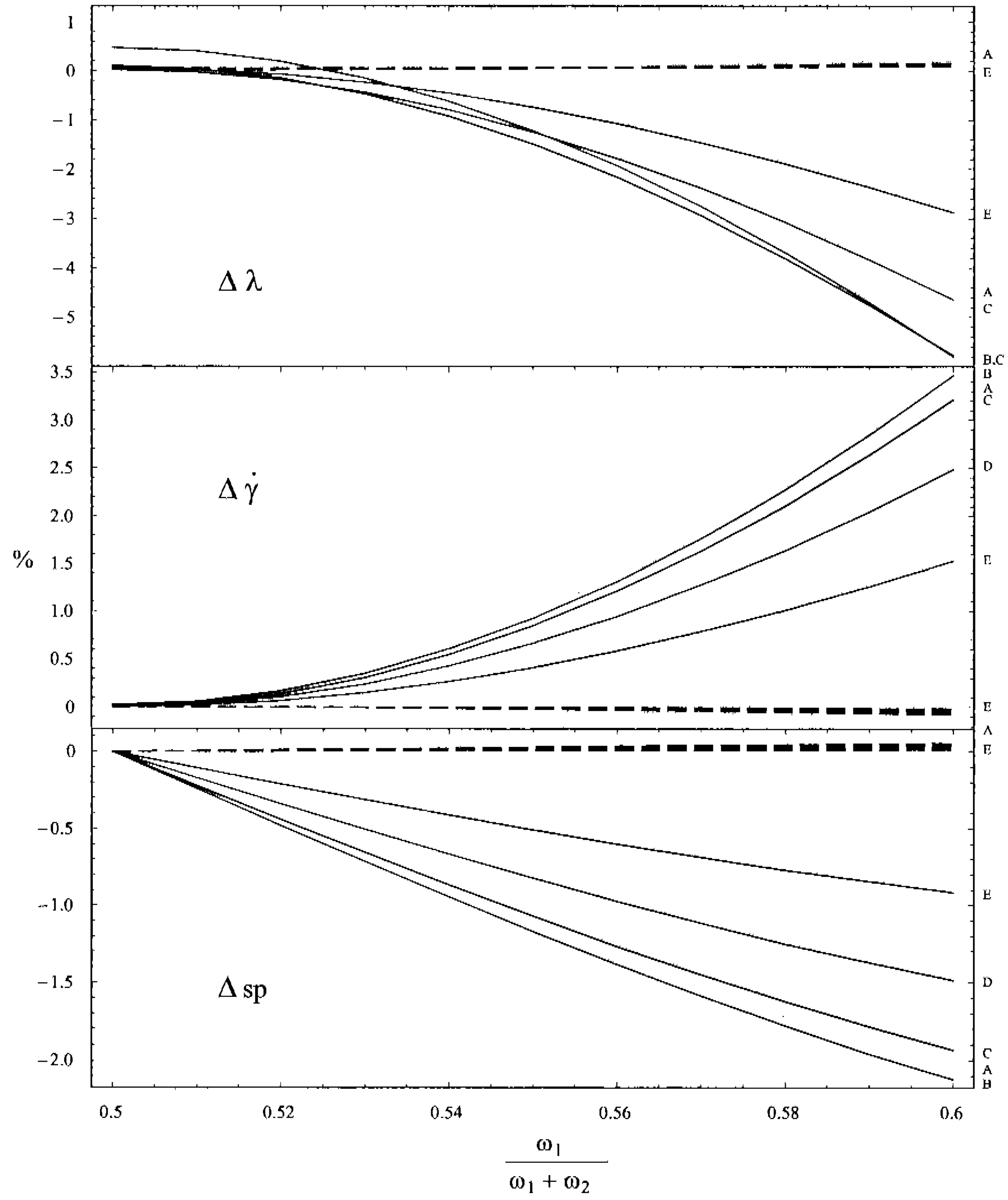

FIGURE 2.9. Graphs of the difference between the numerical data obtained from the TRM–B geometry and its respective TRM -Unbounded geometry, with respect to the analytical solution as function of the angular velocity variation. Graphs are for the flow-type parameter, $\Delta\lambda$; shear rate, $\Delta\dot{\gamma}$; and the position of the stagnation point, Δsp. Continuous lines corresponds to the bounded geometries, whereas dashed lines correspond to the unbounded cases.

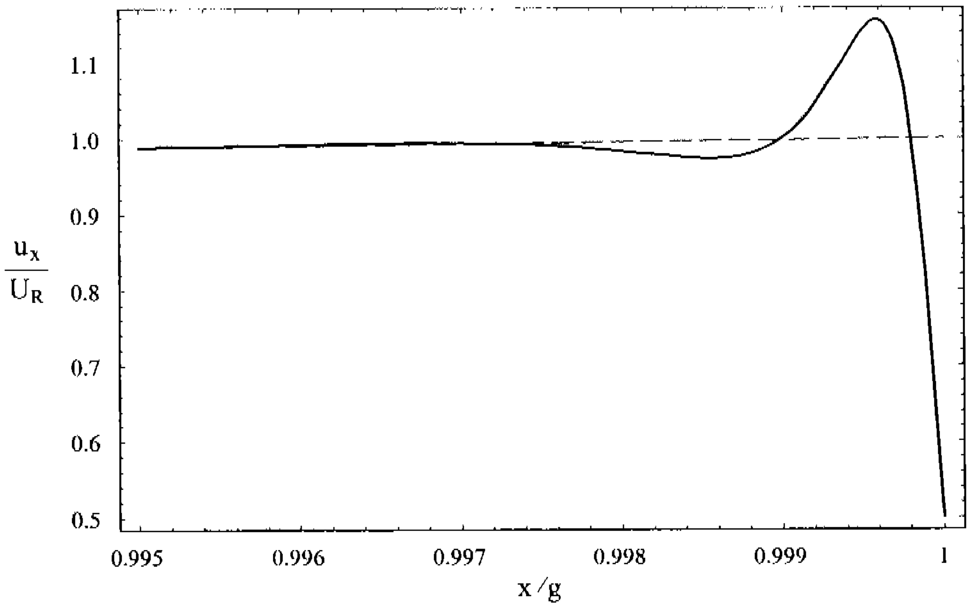

FIGURE 2.10. Velocity oscilations in the vicinity of a cylinder's boundary. Continuous line is the velocity numerically obtained, whereas dashed line is the actual value. The velocity is normalized with respect to the velocity at the cylinder, and the position with respect to the gap.

are produced due mainly - besides numerical noise in the velocity field - to derivatives of this field that are calculated by the method of centered differences, and which require values of the velocity at virtual positions inside the cylinders (or outside of the external boundary) without any physical meaning.

Chapter 3

Experimental flow cells for studies of drop dynamics

For experimental studies of the dynamics of breakup and coalescence of drops it is desirable to be able to modify on demand the external flow field parameters causing the drop deformation. For example, G. I. Taylor [31, 32] manipulated each of the cylinders of a Four-Roll Mill to position a drop precisely at the stagnation point. Once the drop was in place, Taylor was able for a short time to track changes that occur on the drop shape as a function of the imposed flow, until the drop was ejected from the saddle-point unstable stagnation point. Bentley and Leal [7] have shown that it is possible to control the position of drops indefinitely within the flow field of a Four-Roll Mill by adjusting *in real-time* the speed of rotation of each cylinder, and maintaining simultaneously constant values for the elongational flow field parameters. In these experiments, a video camera monitors the position of the drop within the flow field and a computer calculates the position of the drops relative to the stagnation point. The computer algorithm is capable of: (1) maintaining a flow history with prescribed values for all flow parameters and, (2) maintaining a drop at the stagnation point for very long periods by simply adjusting the relative rotational speeds of the cylinders. The control of the drop position is based upon an approximate solution for the non-steady flow, assuming hyperbolic (purely elongational flow) streamlines.

In this Chapter the main characteristics of a Two-Roll Mill flow cell suitable for experimental studies are presented. This device was designed specifically for studies of the dynamics of drops embedded in a viscous external fluid that imposes an extensional flow condition similar to a Four-Roll Mill, although with significantly more vorticity. The device is fitted with the necessary optics for the detection of the drop characteristics, such as deformation and orientation on two perpendicular planes, and is capable of maintaining a drop under prescribed flow conditions for extended periods of time. Given the extensional nature of the flow field, the drop dynamics amenable to study covers a range from small deformations to the mechanisms by which drops break up into smaller droplets. In the second part of this Chapter emphasis is given to the presentation of the control algorithm used to position and hold a drop at the stagnation point of the flow field. This control scheme is different from that used by Leal and collaborators due to the fact that with a Four-Roll Mill there are two extra degrees of freedom available to adjust the drop position in comparison to a Two-Roll Mill. However, it is shown that the advantages of flow fields by TRMs presented in Chapters 1 and 2 are maintained and that a reliable control mechanism for the position of the drop is also at our disposal with this configuration.

3.1 Two-Roll Mills for experimental studies of drop dynamics

Four-Roll Mills have been used for decades to study the dynamics of drops in strong linear flows. Flows generated with Four-Roll Mills have an irrotational character and are capable of causing large deformations or of bursting immersed drops. Studies with these devices assume that a 2-D linear flow exists about the center of the device where the main stagnation point is located. In order to control a drop at such point, the experimentalist carries out a calibration of the mill that allows for adjustments of flow parameter in the central region by correcting the rotational speed on the four cylinders in an independent manner.

The Two-Roll Mill apparatus proposed here presents several features not available for flow cells of the simple shear or the purely irrotational type of flow. As shown in Chapter 1 and 2, the TRM geometry generates flows for which an analytical solution exists. These features will be used firstly to define a deterministic environment for the embedded drop, and secondly to provide us with a control scheme suitable to maintaining a drop at the stagnation point even when there are only two cylinders to adjust the flow field. Furthermore, the flow configuration permits elongational flow with significant vorticity that can have a non negligible effect of the drop dynamics. These flows are an excellent complement of the kinematics accessible with the use of Four-Roll Mills such as those used by Taylor and Leal and collaborators. While the Four-Roll Mill is best for flows characterized by values of the flow-type parameter in the range $0.4 \leq \lambda \lesssim 1$, the Two-Roll Mill optimum range is $0 < \lambda \leq 0.3$.

Figure 3.1 presents a complete view of the proposed flow cell, optical lenses, motors, image acquisition CCDs, and support for the complete setup for studies of drop dynamics. The support accepts two geometries for the flow cells: TRM–A and TRM–B; their characteristics are presented in Chapters 1 and 2. With these mills the flow kinematics cover a range, on one end, very close to simple shear flows and, on the other, flows dominated by an elongational character.

Greco [33, 34] and Hu et al. [35, 36] have recently proposed that precise knowledge of the shape of a drop deformed by an external flow, regardless of its size, is sufficient for the determination of the most relevant physical characteristics of the fluids. As will be shown in Chapter 5, the hypothesis in this work is the determination of all properties of the two fluids. To accomplish this goal, besides accurate measurements of the drop dimensions, it is necessary to characterize the time evolution of the drop when a strong flow is suddenly started. These experimental observations are the basis for the design of the Two-Roll Mill, and emphasis will be given to an accurate prediction of the drop dimensions, to the generation of an elongational flow with high accuracy and to the control of the drop position for limitless time periods.

3.1.1 The optical train for processing of images of drops

Figure 3.1 shows also a large three-degrees translating stage supporting two imaging systems that are used to determine the drop properties. Using these two simultaneously, two views of drops immersed in the flow field are possible: (a) along the line perpendicular to the axes of the flow field -corresponds to the view from below, using a mirror at

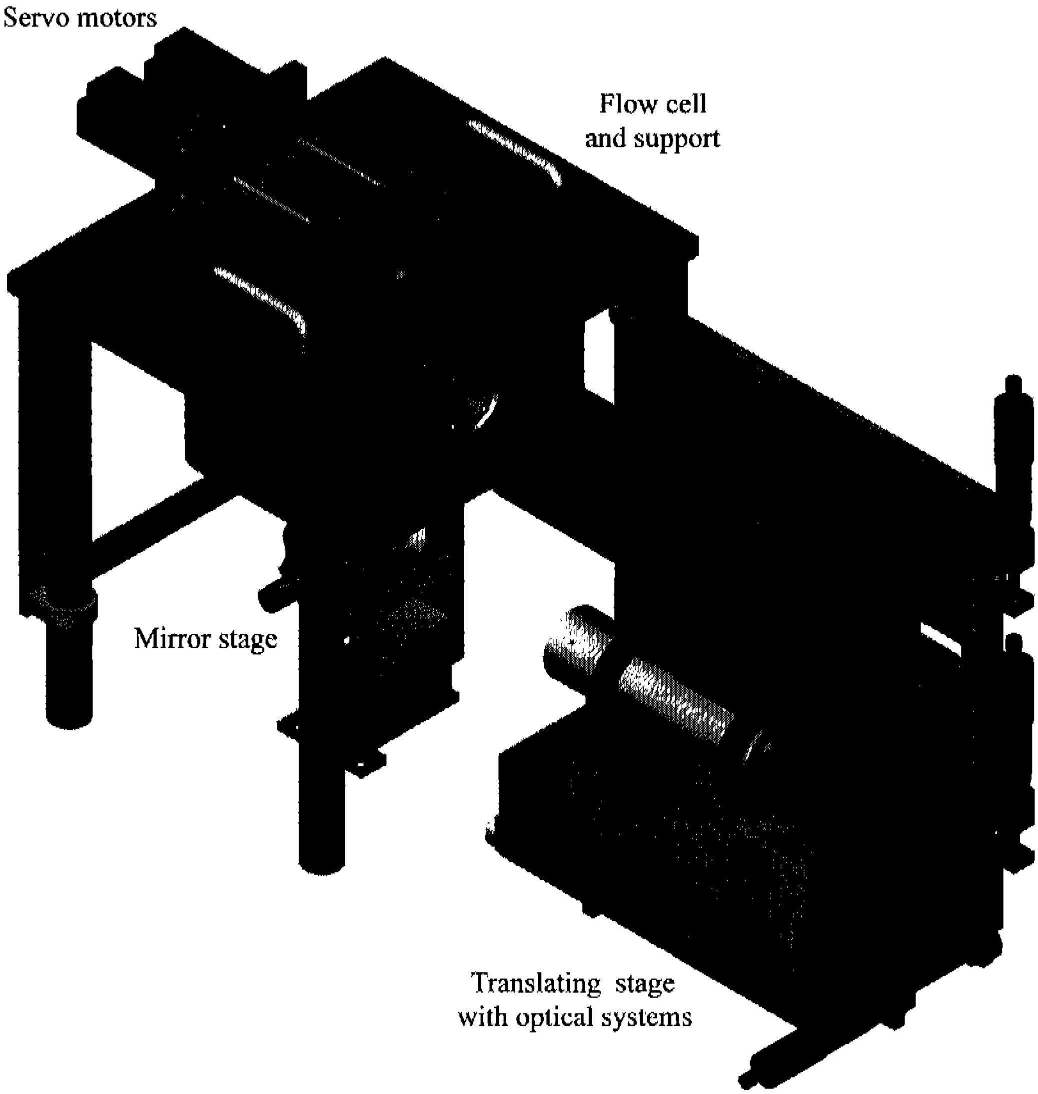

FIGURE 3.1. The complete setup for studies of the dynamics of drops subjected to strong flows. All drops can be observed from the side and from below with the use of the mirror –shown in gold. The setup has two imaging systems. These are mounted on an optical base of very high resolution, with load capacity above 100 kg, travel along three axes greater than 50 mm, with a precision better than a fraction of a micron. One optical system has 5 degrees of orientation and positioning; the second optical systems can be positioned with 3 degrees of freedom. Motors are controlled by a Sercos loop system.

45° orientation respect to the horizontal plane, and with the optical axis parallel to the cylinders axes; and (b) along a direction perpendicular to a normal plane defined by the directions of vorticity and the principal direction of the gradients axes. The complete set up was designed taking into consideration the need for studies of small drops. Hence, the cell has bottom and top windows, as well as two lateral windows, all made of the highest optically-flat glass commercially available, with a diameter of 1 in. The principal imaging system is a Navitar Telecentric 16X lens couple to a monochrome 1/2" CCD –model XCD-SX910 by Sony with 1.45 megapixels and a standard rate of 15 frames per second– along the perpendicular to the flow field. The second camera on the lateral view has a CCD with 6.1 megapixels and up to 3 frames per second; the complete system is by Nikon. Images are transfer to the main computer via FireWire links with a maximum capacity of 800 Mb s^{-1}.

The dual detection optics is used to carry out two functions: (a) before any data is actually processed about the drop shape and orientation, the first-in data is used to ensure that the drop is at the stagnation point, and (b) once the flow field parameters have the prescribed values, then the captured images can be used to determine the characteristics of the external and internal flow fields. The first set of images corresponds to views perpendicular to the plane of the flow. With these images, the relative position the drop with respect to the ideal external flow field can be monitored at all times. It is through this video system that images captured at a rate up to 30 frames per second are used to determine de drop position with respect to the center of the flow field. If the drop drifts away from the control volume, then a computer algorithm will establish the appropriate adjustment to the flow field such that the drop centroid is placed back at the stagnation point. The control volume can be much smaller than the drop size with just a couple of microns in size. This control scheme, compared with the Four-Roll Mill control, is based essentially on a fully deterministic process. Subsequently, these images are used to determine the geometrical characteristics of a deformed drop and its relative orientation with respect to the flow field in time. Post-processing algorithms are used to determine the correct drop form and all shape parameters.

Illumination is done from the top using dark or bright fields. By using fluorescence

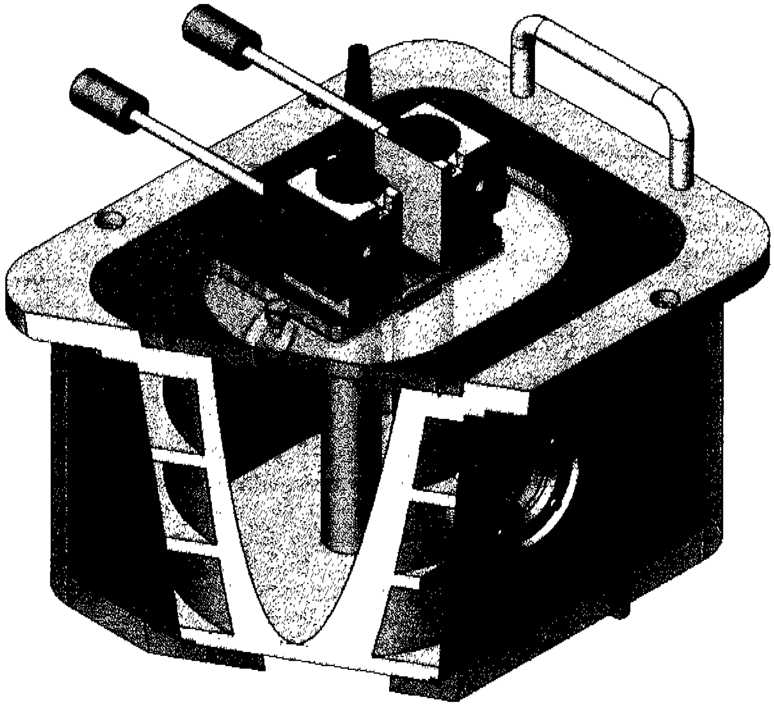

FIGURE 3.3. Section of the flow cell highlighting the channels of the cooling loop. The detachable top window is showed with more detail, as well as the lateral optical windows, the support for on one end of the gears and bearings and shaft of the motors, and on the other end of the cylinders of the TRM. The separation of the cylinder axes is 34 mm for TRM–A and 50 mm for TRM–B.

systems to generate the corresponding rate of rotation. This precision with servomotors is better than 0.2% as well.

The flow cell is mounted on a rigid base where the motors driving the cylinders are also attached. Especial care has been taken to guarantee that this support provides the highest rigidity with respect to the imaging systems base. As well the flow cell can be positioned with a good repeatability with respect to the optical systems mount. The flow device has a cooling loop around the vertical walls of the body designed to maintain the fluid within temperature variations of a couple of hundreds of a Kelvin. Figure 3.3 shows the channels and the connectors of the cooling loop, the top transparent cover for illumination, the housing for the gears, worms and top bearings, the loading ring for bearings, the lateral window housing, and the shafts coupling the Kollmorgen motors

3.1.3 The generation of a controlled flow field

The main tasks to be performed semi-autonomously by the experimental apparatus are the control and acquisition of drop images. These tasks are carried out by a dedicated computer that has direct interfaces to the imaging systems and to the motors driving each cylinder. The drop motion and deformation is captured using two video systems, while the latter is been illuminated with a dark field arrangement.

Images on the plane of the flow field are taken at a high rate, and are used for control and data acquisition purposes. With these images the computer calculates the position of the drop's centroid continuously. When the algorithm determines that an excessive drift of the centroid has occurred, then instructions are given to the motor drivers to adjust the flow field and to place the drop into a path for the return of the drop's centroid back to the position closest to the stagnation point. The analysis for this method is presented in the following Section.

The second lateral camera views the vertical drop position; it also has a dual purpose. First it is use to assure that the drop is near the middle of the flow device in the event that buoyancy effects are significant, and also it is used to measure the deformation normal to the flow of the drop. Once the flow conditions are those needed for the experiment, the processing of images is carried out to determine the geometrical characteristics of the embedded drop.

3.2 Control scheme for a drop in Two-Roll Mills

In order to obtain good results in drop deformation and eventually in drop breakup experiments, the drop's centroid must be placed and maintained at the stagnation point. The stagnation point is an unstable position for the drop's centroid (is a saddle point), where any disturbance in its position will cause it to drift along the outgoing streamline.

As already pointed out by Bentley and Leal [7], the only means to control the drop position is by changing the flow field by adjusting the cylinders' speed, with the constraint that these changes must be as small as possible to avoid significant modifications of the flow field. Then, the objective of the control scheme is to maintain the drop as close as possible to the stagnation point of the Two-Roll Mill for long times.

The control scheme proposed for Two-Roll Mills is based on the analytical solution for the flow device. The assumption used by Bentley and Leal is that the stagnation point can be displaced to any position within the flow field central region; however, this hypothesis can not be used with TRMs, because with the new geometry the only possible displacement of this point is along the line between the axes of the cylinders. The flow devices considered in this Thesis have cylinders of the same size and assumed to be spinning at equal angular velocities (that fixes the stagnation point at the center of the device), but is possible to mix the cylinders diameters and angular velocities to obtain other flow type parameter and shear rate values and different positions of the stagnation point.

The algorithm of the control system is based on the capability to move the stagnation point along the line between cylinder's axis, by changing the ratio between angular velocities of the cylinders. The control scheme applies the experimental conditions (the selected angular velocities) when the drop's centroid is inside a domain, and when the drop's centroid reach the boundaries of this range, the control system varies the angular velocities (applies a corrective flow field) in order to carry the drop's centroid back to the stagnation point of the flow field under study. From now on the instantaneous position of the stagnation point in the laboratory coordinates is the *experimental stagnation point* or *nominal stagnation point,* $\mathbf{x}_{Nom}$. The corrective flow field has its associated stagnation point, $\mathbf{x}_{ss}$, which its respective incoming and outgoing axes.

The control scheme described in this Section considers that the drop velocity is equivalent to that of a material point placed at its centroid in the nominal flow field conditions, and the effects of the drop on the local field are not taken into account, i. e., that the drop does not affect the position of the stagnation point. These assumptions are clearly a limitation as is shown in Chapter 5 of this Thesis. However, as a zero order approximation it is a valid working hypothesis.

For the control scheme algorithm, the following variables are used:

1. *Resolution area.* It is the area of "tolerance" for the position of the drop's centroid. The minimum value is related to the optical resolution of the system and its maximum value with the biggest variation allowed for the flow type parameter and shear rate. The optical resolution is the precision by which the centroid position can be evaluated.

2. *Offset.* It is the distance along the vertical limit of the resolution between the outgoing axis of the nominal stagnation point, and the incoming axis of the stagnation point of the perturbed flow field. The offset can be given as a factor of the resolution length.

3. mr. It is a fraction of the slope of the incoming axis of the nominal stagnation point, whose slope is $\sqrt{\lambda_{Nom}}$.

4. *TimeStep.* It is the time between measurements of the position of the drop's centroid. It is related to the velocity of the camera (fps) and the processing time of the drop's centroid.

5. $F(\dot{\gamma})$. In order to reduce one degree of freedom on the angular velocities for both cylinders, the following relation is used:

$$|\omega_1 R_1| + |\omega_2 R_2| = F(\dot{\gamma}), \tag{3.1}$$

   where $F(\dot{\gamma})$ is an adjustable variable selected according to the magnitude of the shear rate at the stagnation point.

Figure 3.4 shows the resolution area and the offset parameter. The streamlines of the nominal flow field are shown as dashed lines, and the streamlines of the corrective flow field are shown as continuous lines. For small variation of the cylinders rotations, both flow fields have the same characteristics with quasi-identical streamlines. The slope of the incoming (and outgoing) axis is related to the flow-type parameter at the stagnation point.

The *resolution area* is showed as a rectangle placed symmetrically around the nominal stagnation point. The resolution area has associated a *resolution length* or simply a *resolution* that is taken as half of the maximum side length. The length of the vertical side of the resolution area is given by the intersection of the incoming and outgoing axis with the horizontal length of the resolution.

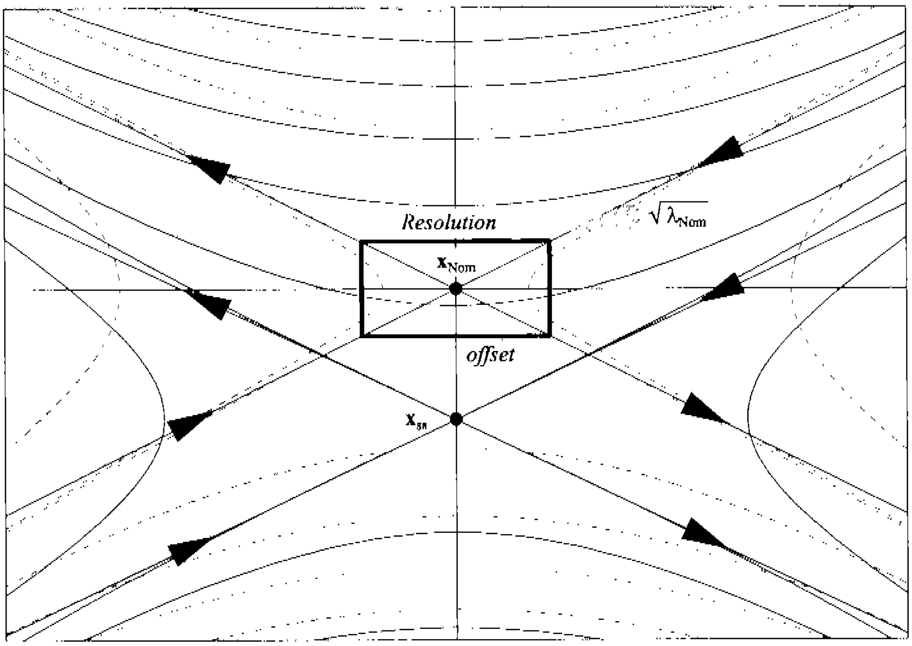

FIGURE 3.4. *Resolution area* and *offset* parameter of the control scheme for the TRM. $\mathbf{x}_{esp}$ is the experimental stagnation point and $\mathbf{x}_{ss}$ is the stagnation point of the corrective flow field. The *resolution* is the area where the drop's centroid is allowed to stay under the experimental flow conditions; *offset* is the distance between the outgoing axis of $\mathbf{x}_{esp}$ and the incoming axis of $\mathbf{x}_{ss}$.

Drops are convected away along the *outflow axes* of $\mathbf{x}_{Nom}$. The role played by the offset parameter is to give the off-center drop a new path based on the corrective flow field that assures that the centroid displaces towards the *incoming axis* of $\mathbf{x}_{Nom}$. The offset parameter must be greater than zero; otherwise, the drop's centroid would be on the incoming axis of $\mathbf{x}_{ss}$, and then the drop's centroid moves to the corrective flow field stagnation point with a velocity that decreases exponentially, and after some time always take a direction within the domain of the outgoing axis of $\mathbf{x}_{ss}$.

In order to carry out the control scheme, the flow field is divided in three regions with respect to the position of the incoming axis of the hyperbolic flow, and the x axis, as Fig. 3.5 shows. These zones are defined as:

Region 1 delimited by

$$\left[\left(y < \sqrt{\lambda_{Nom}}\,x\right) \cap (y > 0)\right] \cup \left[\left(y > \sqrt{\lambda_{Nom}}\,x\right) \cap (y < 0)\right], \tag{3.2}$$

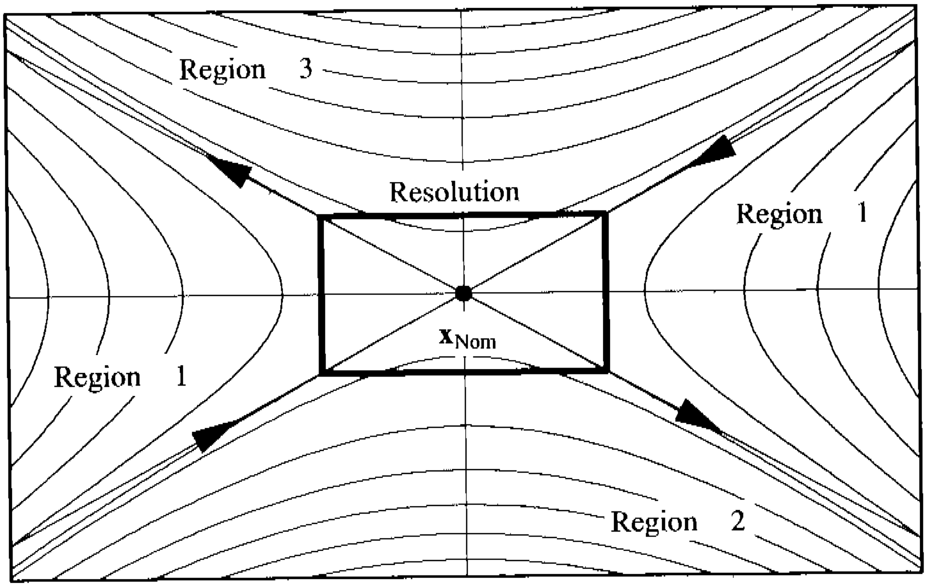

FIGURE 3.5. Streamlines and different Regions around the stagnation point. The control scheme for drops within each Region are described in detail. The rectangle delimits the *resolution area*, and the arrows are the direction of the incoming and outgoing streamlines from the stagnation point, $\mathbf{x}_{Nom}$.

where $\sqrt{\lambda} = \tan\theta$, and θ is the angle between the incoming (or outgoing) axis and the x axis.

Region 2 delimited by

$$\left(y \leq \sqrt{\lambda_{Nom}}\, x\right) \cap (y \leq 0)\,. \tag{3.3}$$

Region 3 delimited by

$$\left(y \geq \sqrt{\lambda_{Nom}}\, x\right) \cap (y \geq 0)\,. \tag{3.4}$$

When the drop's centroid is in Region 1, near but out of the resolution area, the control generates a corrective flow field by which the drop's centroid is placed in a trajectory directly towards $\mathbf{x}_{Nom}$. In order to calculate the required angular velocities on the cylinders to generate this transitory flow field, the value of the streamline that passes by the drop's centroid position is equated with that leading to $\mathbf{x}_{Nom}$ at the corrective flow field conditions, i. e.

$$\psi_{\omega_1^d,\omega_2^d}(\mathbf{x}_c) = \psi_{\omega_1^d,\omega_2^d}(\mathbf{x}_{Nom}), \tag{3.5}$$

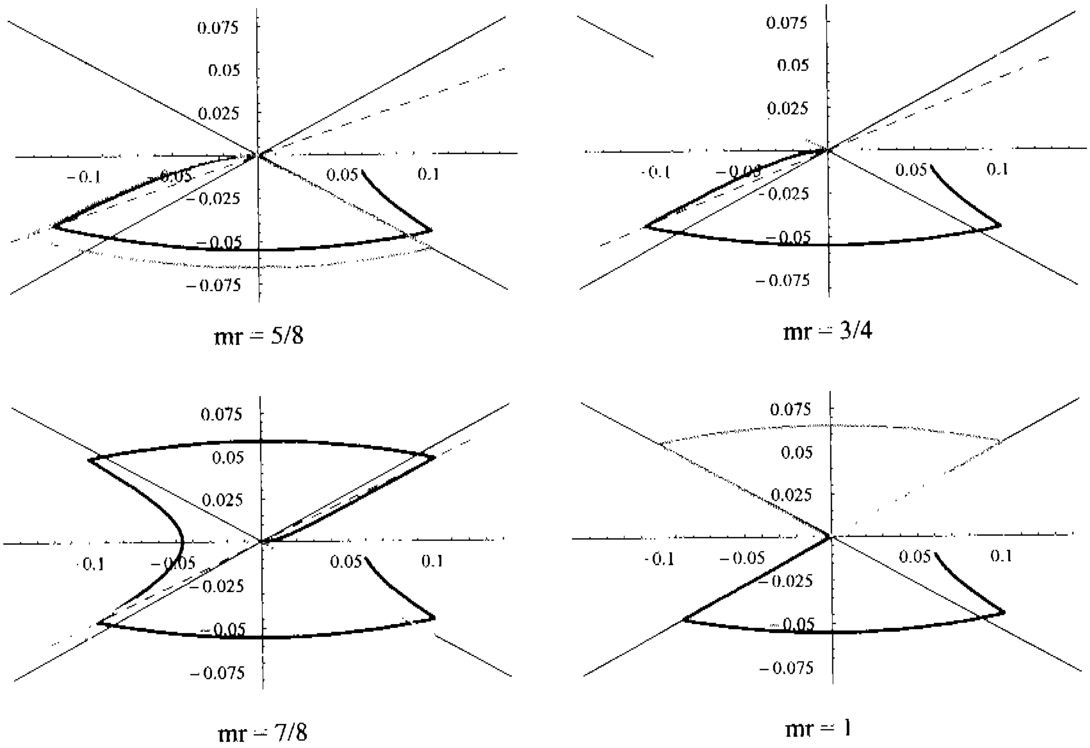

mr = 5/8

mr = 3/4

mr = 7/8

mr = 1

FIGURE 3.6. Paths obtained from the variation of the *mr* parameter in a TRM with $\lambda_{Nom} = 0.3$ and the *offset = resolution length*. Continuous lines are the incoming and outgoing axes of the nominal stagnation point, dashed lines are the axes defined by the *mr* parameter, and the gray rectangle is the resolution area. Gradient in the gray level of the path lines indicates the time evolution.

stagnation point of the transitory flow field is below the material point, along the $y-$ axis; this is the Stage 1 of the corrective cycle. Then, when the material point reaches the new position on the radial line, the flow field is again adjusted to now displace the material point towards $\mathbf{x}_{Nom}$; during this last condition, the stagnation point is located above the material point and corresponds to Stage 2. The graphs in Fig. 3.6 show that for smaller values of the *mr* parameter, the path followed by the material point moves away from the central region of the resolution area.

The graphs for $mr = 7/8$ and $mr = 1$ of Fig. 3.6 show that after Stage 1 of the corrective cycle is applied, the material point arrives to a point inside the resolution area. For these cases, the flow is under nominal flow field conditions, until the material point

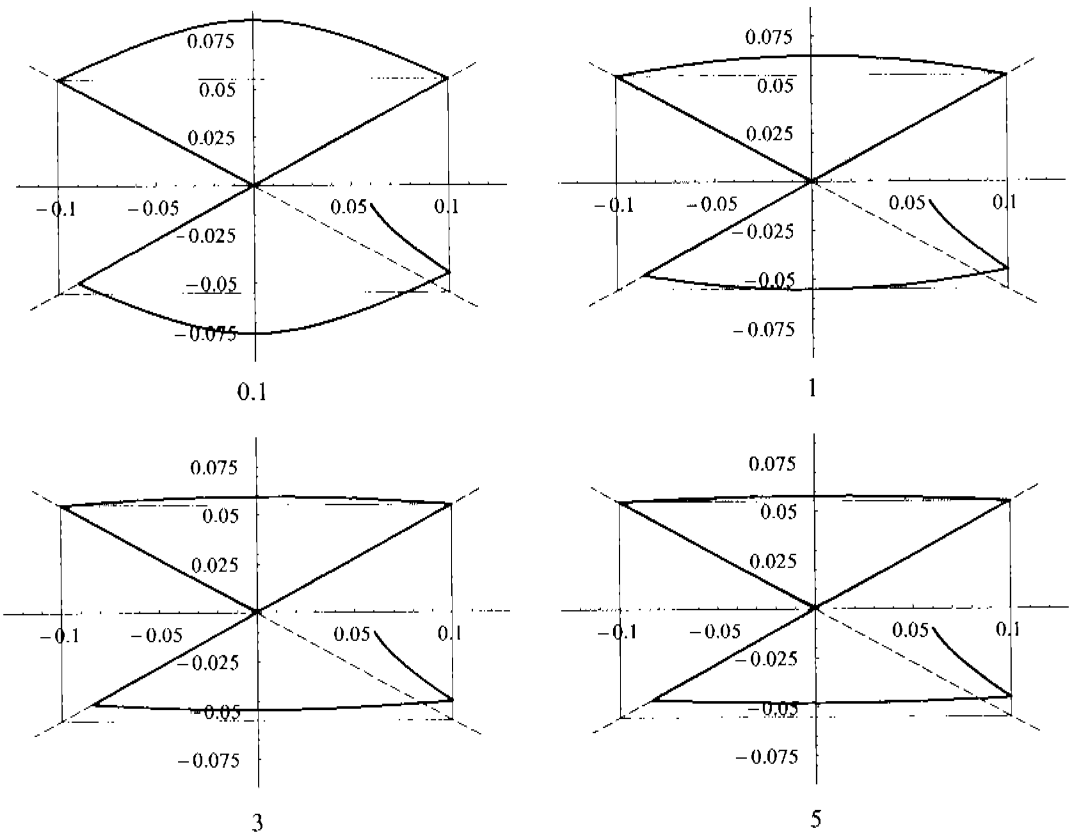

FIGURE 3.7. Paths obtained from the variation of the *offset* parameter in a TRM with $\lambda_{Nom} = 0.3$ ($\theta = 28.71\,^{\circ}$) using $mr = 1$. The labels in the graphs indicate the factor of the *offset* parameter that multiplies the resolution length.

reaches once more the boundary of the resolution area. For the case $mr = 1$, the control scheme does not apply corrective algorithm for Region 1, because the material point always arrive inside the resolution area.

Figure 3.7 shows the influence of the *offset* parameter for the geometry with $R_1 = R_2 = 10.00\,\text{mm}$, $g = 14.00\,\text{mm}$, $\lambda_{Nom} = 0.3$ ($\theta = 28.71\,^{\circ}$), and with $mr = 1$. In this plots, the *offset* parameter is varied as a factor of the *resolution length*, showing material paths for cases of 0.1, 1, 3 and 5 times the resolution length. In these plots, the initial position of the material point is again at $(0.06, -0.01)$. The path followed by the material point when the corrective flow field is applied has different curvatures due to the distance $\|\mathbf{x}_{Nom} - \mathbf{x}_{ss}\|$.

Stage 1 is slightly greater when the mr parameter is smaller. This is due to a path that is a slightly longer, see Fig. 3.6. The time needed for Stage 2 is greater when the mr parameter is bigger. For this Stage, the control scheme calculates a flow field where a streamline drags the material point away from its original position to $\mathbf{x}_{Nom}$, and because to this streamline is very close to the stagnation point of the corrective flow field, the transit time along this path becomes significantly longer because the velocity towards the stagnation point tends to zero. For this Stage, the closer mr is to 1 the closer to the nominal flow field the corrective flow becomes.

The path of material points during Stage 3 always occurs under nominal flow conditions (last column, in blue). Thus, the associated time is a highly dependent function of the computational precision of the control algorithm. For trajectories during Stage 2 that place any material point very close to the exact location of $\mathbf{x}_{Nom}$ –which is also a precision machine dependent probability– the transit time for Stage 3 can become immense; that is, Columns for Stage 3 can show a large variation of its height and depend on the effectiveness of the path for Stage 2 to position the material point precisely at the nominal stagnation point. If a material point is placed exactly on the stagnation point (or on its entrance streamline), the time needed for that the particle to leave (or to arrive to) the stagnation point becomes infinite. In practice, the transit time is bounded by the characteristic time of the diffusivity of the immersed object, because it will drift away towards streamlines with non-zero values of their velocities, and subsequently be pulled away from the stagnation point. The case of $mr = 1$ shows that time for Stage 3 is the shortest. This behavior is the result of an approximate value for the slope of the incoming axis to the stagnation point in the control algorithm, and the flow field near the stagnation point shows that it is very sensitive to the actual position of the material point.

The Graph for the difference of the flow-type parameter in Fig. 3.8 shows that changes of λ are small, and such differences may occur whenever the trajectory passes far away from the resolution area, which can be seen in the paths of Fig. 3.6. Then, how can be selected the parameter mr with the objective of increasing the time that the material point spends under nominal flow field conditions. An experimentally feasible condition exists for the mr parameter close to 1. In this situation, the time spent in Stage 2 is very long, having simultaneously a corrective flow field condition very close to that of the nominal flow.

In the Graph of the time per stage of Fig. 3.9, the first --red-- bar corresponds to the time spent by the translation of the material point from the intersection of the limit of the *resolution area* with the outgoing axis to the intersection of the limit of the *resolution area* with the incoming axis. This path occurs under the corrective flow field conditions given by the algorithms for Region 2 or Region 3 (during Stage 1). The second -blue- bar corresponds to the time spent by the transit of the material point from the intersection of the limit of the *resolution area* with the incoming axis towards $\mathbf{x}_{Nom}$ and continuing up to the limit of the *resolution area* along the outgoing axis; during all this time subjected to nominal flow conditions.

The time spent in Stage 1, when the corrective flow field is applied, is longer for those cases with smaller *offset* values; but the variations of λ behaves in the opposite way. The variation of the time of Stage 1 is due to the proximity of the corrective stagnation point, $\mathbf{x}_{ss}$, to the path of the material point, whereas the variation in λ increases with $\|\mathbf{x}_{Nom} - \mathbf{x}_{ss}\|$, i. e. the corrective flow field is more dissimilar to the nominal flow field conditions.

The variation of λ with the *offset* is more significant than for cases of *mr* variations. This fact becomes critical to the *offset* parameter, and to maintain a small variation in the nominal flow-type parameter. A value of the *offset* near one is acceptable, because it has a good ratio between the time of the nominal flow field conditions and the corrective flow field conditions, and a small percentage of the difference of λ.

Figure 3.10 shows the main features of the control scheme with optimized values of the parameters ($mr \approx 1$, $offset = 1$). The Graph to the left is the path with initial coordinates $\left(0.1,\ 0.1\sqrt{\lambda_{Nom}}\right)$. The inserted Graph is a close-up about the region containing the nominal stagnation point $\mathbf{x}_{Nom}$, as well as the corrective stagnation point $\mathbf{x}_{ss}$ location during Stage 2. The middle Graph shows the time needed in each stage of the control algorithm. The Graph to the right shows the percentages of the differences of the flow-type parameter, the variation of the angular velocity of one of the cylinders, and the maximum displacement of the stagnation point respect to the resolution length.

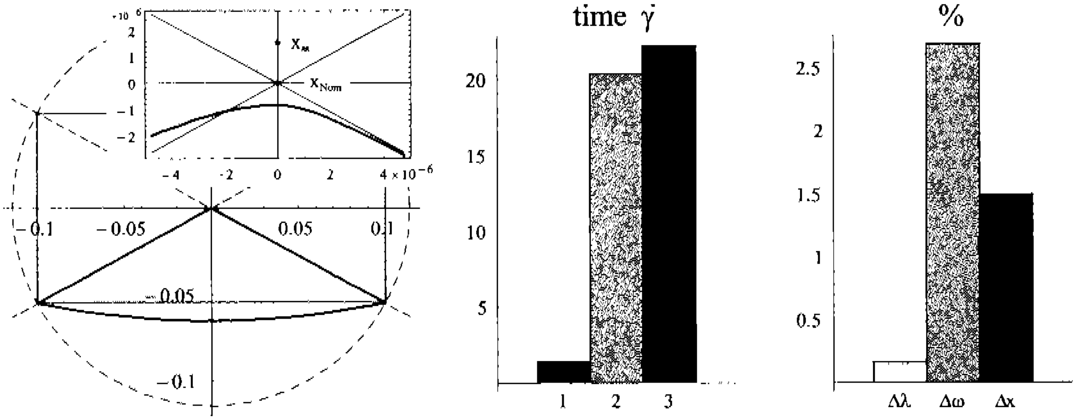

FIGURE 3.10. Properties of the control system with optimized parameters $(mr \approx 1,$ *offset* $= 1)$. The graph at the left is the path of a material point with initial coordinates $\left(0.1,\ 0.1\sqrt{\lambda_{Nom}}\right)$, and the inserted graph is a close-up of the nominal stagnation point, $\mathbf{x}_{Nom}$, and the corrective stagnation point $\mathbf{x}_{ss}$ for the Stage 2. The middle graph shows the time needed in each Stage of the control. The graph at the right shows the percentages of the differences of the flow-type parameter, the angular velocity at one of the cylinders, and the maximum displacement of the stagnation point.

Figure 3.10 shows that for these selected parameters, the material point is always inside the resolution area. The time for Stage 1 is short; the time for Stage 2 is nearly equal to the time of Stage 3. The Bar to the left of the Graph of percentages shows that the maximum variation of the flow-type parameter observed by the material point is small. This perturbation depends essentially on the distance from $\mathbf{x}_{Nom}$. The middle Bar (in green) shows the most significant variation of percentage that corresponds to the cylinders angular velocities. This is an acceptable environment for drops located near the stagnation point, which should not be affected significantly by the cylinders shear. As can be seen in the Bar to the right, the maximum displacement of the stagnation point is also within an acceptable range. The parameters of the flow field for Stage 2 have almost equal values to the nominal flow field conditions; therefore, the material point is most of the time under the desired flow. This accuracy depends of the size of the resolution area.

The control scheme as presented can drag a material point from any position within the central region towards the nominal stagnation point. This scheme is as well useful for placement of the drop at the stagnation point before an experiment for the deformation of drops is initialized.

3.2.1 Time delay in the control scheme

The scheme described in the previous Section is valid for fluids with high viscosity, dominated by a high speed of propagation of the perturbation generated by the corrective flow. Hence, under these conditions the control algorithm assumes that the flow field changes in a quasi instantaneous manner. Furthermore, this previous scheme provides insight about those factors that must be included in any operational control scheme. A refinement to this ideal control system must consider a delay in the response time of the flow field to changes of the angular velocities of the cylinders. Given that there is no analytical solution of the *temporal Stokes' flow* for a TRM, some approximations are proposed to carry out the control scheme. The usefulness of such approximation will become obvious whenever the external fluid has a significantly lower viscosity than the internal fluid of an immersed object such as the studies proposed more extensively in Chapter 5. As well in many industrial applications, e. g., emulsions and dispersions, it is assumed an external fluid of lower viscosity provides a deformation environment for an embedded object of larger viscosity.

To develop a control scheme that incorporates a delay time, a first approximation is the linearization of the flow field around the stagnation point. With the stagnation point placed at the origin, the velocity $\mathbf{u}$ at a point $\mathbf{x}$ can be approximated by the equation:

$$\mathbf{u} = \frac{d\mathbf{x}}{dt} = \nabla\mathbf{u}\cdot\mathbf{x}, \tag{3.12}$$

where

$$\nabla\mathbf{u} = -\dot{\gamma}\begin{bmatrix} 0 & 1 \\ \lambda & 0 \end{bmatrix}. \tag{3.13}$$

the minus sign is due to the sense of the rotation of the cylinders. When the stagnation point is displaced from the origin, the above equation becomes

$$\frac{d\mathbf{x}}{dt} = \nabla\mathbf{u}\cdot(\mathbf{x}-\mathbf{x}_s), \tag{3.14}$$

where $\mathbf{x}_s$ is the *instantaneous* position of the stagnation point under a new –let's say corrective– flow environment, which for the TRM geometry can only be displaced along

$y^c_{ss}(t)$ or $y_{ss}(t)$ when $t - t_0 \gg \tau$, and t_0 is the instant when the material point reaches the boundary of the Resolution domain.

After the displacement of the stagnation point to *Amp* the centroid path is set towards the incoming axis of the nominal flow. In this Stage, displacing the position of the nominal stagnation point to the final stagnation set point can be performed in several ways, such as a step function, a ramp or a sinusoidal form at different velocities (or accelerations) of displacement. In this work, the change of the position of the stagnation set point (and therefore of the cylinder's angular velocities) is performed in a ramp shape form, taking into account that this is a simple shape which is easily programmed with current technology for the electronic control of the driving motors. As a trade-off, transitory behavior in the flow due to the associated transient response of the motors may be the least severe. The slope of the ramp is given by the acceleration range allowed to the cylinders, which in the flow field is related with the velocity of displacement of the stagnation set point.

Figure 3.11 shows several paths of a material point when τ is varied with the *offset* fixed at 0.1. In this Figure, the region about the outgoing axis and the edge of the resolution domain is magnified: The outgoing axis corresponds to the continuous blue line with a negative slope, labeled with (1), near the top of the map, and the trajectories of the material object are in black; the material point is been ejected practically along the outgoing axis. The further right-end of the Resolution area is the gray rectangle. The dashed red line (2), with a positive slope, corresponds to the incoming axis of the corrective flow field, assuming a position for the stagnation point along the negative $y-$axis at a *Amp* position below the material point.

In this Figure, the trajectories with $\tau = 0$ correspond to an external fluid that responds to the corrective flow field in an instantaneous manner. For $\tau > 0$, the material points is subjected to the corrective flow in a time delay manner, with the possibility of particles being drag away from the Resolution area, as shown paths corresponding to $\tau = 1$ and 2. For fluids with lower viscosities, the solution is to increase the distance between the nominal and corrective stagnation point position by increasing the offset; that is, displacing to a lower position the incoming axis of instantaneous flow field.

This Figure shows that the offset parameter must be selected so that two criteria

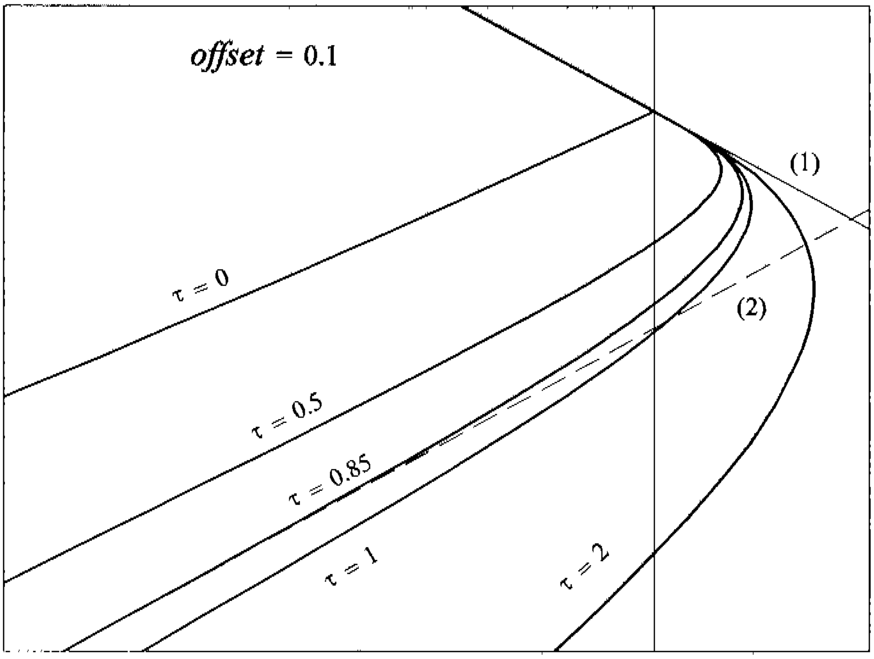

FIGURE 3.11. Paths of a material point with variations time of response τ with the *offset* parameter fixed at 0.1. The line labeled (1) is the outgoing axis of the nominal flow field, the line (2) is the incoming axis of the corrective flow field, the gray area is a part of the resolution area, the curves are the path of a material point for different values of the time of response. For the *offset* value illustrated, for $\tau > 0.85$, the control algorithm do not work.

are fulfilled. Firstly, the path of the material point should be close to the incoming axis of the corrective flow, in such a way that the centroid will be dragged to the incoming axis of the nominal flow field. The second criterion requires that the centroid's path must be sufficiently separated and above the incoming axis of the corrective flow, otherwise the time spent during transit (Stage 1) becomes very large, because a centroid place at the incoming axis eventually ends up in an infinite time at $\mathbf{x}_{ss}$.

Figure 3.12 presents the material trajectories assuming a fix time delay of $\tau = 0.5$ and traces for various offset values. For increasing value of the offset, the corrected stagnation point location is further away from the origin. The onset t_0 for application of the corrective flow is determined by the material point crossing out of the Resolution domain delimited by the vertical line. For every offset value, shown with a different dashed line, the corresponding path of the material point is a curve with the same dashed signature.

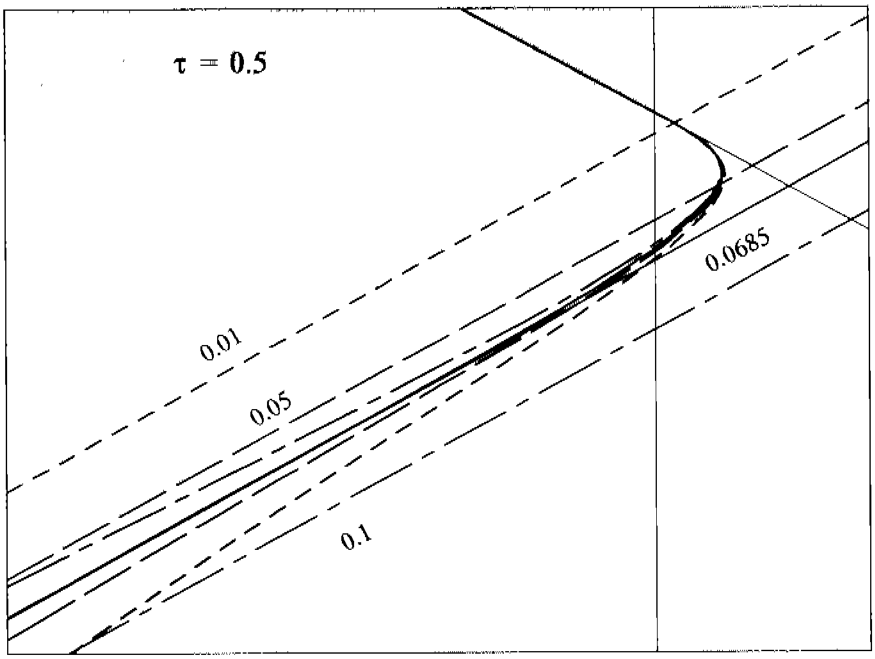

FIGURE 3.12. Paths of a material point with variations of the *offset* parameter with a time of response τ fixed at 0.5. The line with negative slope is the outgoing axis of the nominal flow field. The dashed lines with positive slope are the incoming axis of the corrective flow fields for several values of the *offset* parameter; the curves with the same dash-type of the those are the correspondingly paths of the material point.

The time evolution is essentially the same at the onset, but the transit evolution during the midsection of Stage 1 is strongly dependent on the offset. Too little offset and the particle will drift away from the nominal stagnation point; the control failed. A greater offset set a path that is characterized with a short transit time for Stage 1. For offsets greater than 0.0685, the path will always place the material point at the nominal incoming flow axis at the end of Stage 1.

In the control scheme described in the previous Section, whether the drop centroid arrives to the incoming axis of $\mathbf{x}_{ss}$ –or near to it– depends on the value of the mr parameter of the nominal flow field. After Stage 1 for values of $mr \neq 1$, the control changes the flow field once again (either for an evolution as suggested in Stages 2 or 3). The role of mr is to provide a path towards the nominal stagnation point with a finite time during such stage. In the present control scheme, the time delay of the angular velocities of the cylinders, alters

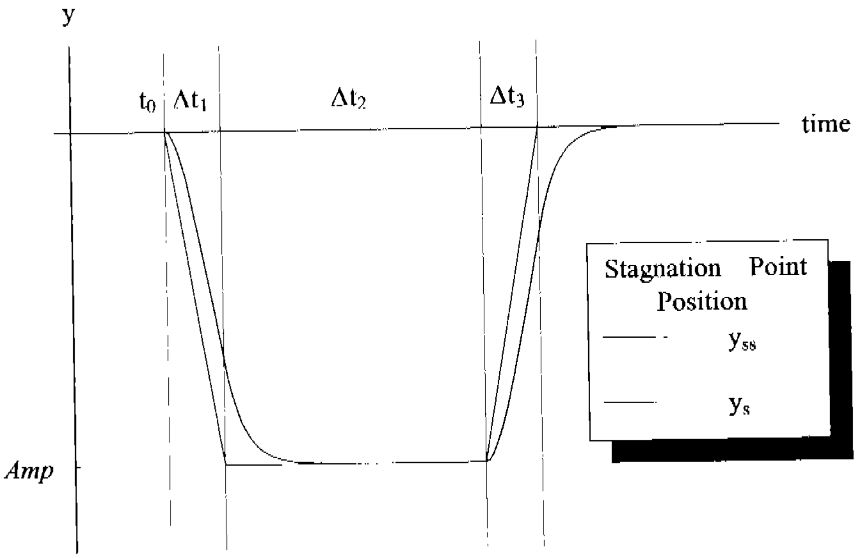

FIGURE 3.13. Time delay for the position of the instantaneous stagnation point y_s with respect to the position of the stagnation point set point y_{ss}.

the physical meaning of the *mr* parameter; in this case the flow fields are characterized by equivalent *mr* values always greater than one.

The function $y_{ss}(t)$ used in the simulations of the control is now explained. When the drop centroid reaches the limit of the resolution area at the time t_0, the stagnation set point evolves towards the *Amp* position. This evolution occurs in a finite time interval: Δt_1. After $y_{ss} = Amp$, the corrective flow is maintained for a time period of Δt_2; afterwards y_{ss} is returned to the position of the nominal stagnation point during a time interval of Δt_3. Figure 3.13 presents the time evolution for $y_{ss}(t - t_0)$ and $y_s(t - t_0)$.

Therefore, $y_{ss}(t)$ is given by

$$y^c_{ss}(t) = sign[y_c] \begin{cases} m_1(t - t_0) & t_0 < t < t_{0,1} \\ Amp & t_{0,1} \leq t \leq t_{0,2} \\ -m_2(t - t_{0,2}) & t_{0,2} \leq t \leq t_{0,3} \end{cases}, \tag{3.22}$$

where $sign[y_c]$ is the sign of y_c, t_0 is the instant when the corrective flow field is applied,

Part II

Hydrodynamics of viscous drops in flows generated by Two-Roll Mills

Introduction to Part II

Many processes in industry such as preparation of emulsions, preparation of inks for printing, in advanced materials such as nanoparticles prepared from solutions or from suspensions, production of polymer composites with enhanced optical, mechanical or texture appearance, mixing of multiphase viscous systems, immiscible displacement of crude oil in reservoirs are among many other applications with the same underlying physical phenomena. These applications require a good understanding of the fluid mechanics phenomena observed in fluid drops immersed in a second supporting fluid. More recently, studies in fluidics, nano-biomaterials [37] and suspensions of nanoparticles require a good understanding of the fluid mechanics but in very small systems: fluid droplets of a few picoliters of volume immersed in a second suspending fluid, while flowing in a channel a few microns wide; in all of which surface phenomena are dominant force fields.

Based on the latter applications, the basic problem addressed here is how a liquid drop may be deformed and may break up due to the stress field generated by a flow; or how two liquid drops may or may not coalesce under similar flow conditions. The occurrence of such phenomena is determined by the fluids properties as well as the density (concentration) of particles, interfacial tension, etc. The presence of surfactants also has an important effect on the end result for a two-phase fluids flow. Once a two-phase system is generated by the flow, how long does it remain in a stable condition is as well an important property of many systems. The stability of the suspension is also determined to a great extend by the same physical parameters [38].

Despite our current lack of knowledge in this field, understanding the fluid dynamics of embedded drops has been an important topic of research for the last 150 years.

Very early on, G. I. Taylor [31, 32], Mason [39], Grace [38], among others, realized that a detailed analysis of the rheological properties of a single droplet immersed in a secondary fluid represented a solid starting point for understanding more concentrated systems and more complex environments. Cox [40] and Rallison [41] have extended Taylor's theoretical understanding of the "two-liquid" problem, and there is now a complete theory available (valid up to second order) for the deformation of drops in simple shear flow and hyperbolic flow. These theories assume a slow flow condition, which can be analyzed theoretically via solutions of the Stokes equation. More recently, Greco and coworkers [42, 43, 33] have been able to measure with excellent accuracy all fluids properties, based on the theoretical understanding of small deformation induced on drops by simple flows. Hu and collaborators [44, 35, 36] have carried out imaging techniques with the purpose of determining values of the physical characteristics of the fluids, in particular viscosity of fluids using 2-D elongational flows.

However, most of the present knowledge is related to macroscopic drops several millimeters in diameter and for dynamics characteristic of idealized flow conditions: Slow simple shear flows and pure elongational flows. Three excellent reviews exist for this field: by Acrivos [4], Rallison [2], and Stone [3]. However, there still is a significant lack of information when the drop dynamics is strongly affected by the presence of large surface forces and whenever the flow parameters are similar to those of simple shear flow but still of an elongational nature. Furthermore, complex surface tension effects are not clearly understood for a large set of conditions, hence limiting severely the realm of technological applications.

In Chapter 4 an introduction to free-boundary problems is given. In this Chapter the Boundary Integral Equations for free-boundary problems are described and are applied to the case where a drop is subjected to external unbounded flows and where a drop is subjected to flows generated by nearby solid boundaries. Also, the method used to track the temporal evolution of the drop interface is described.

In Chapter 5 studies of the drop dynamics are carried out using Boundary Element Method (BEM), but giving emphasis to a class of flows not included in most of the previous studies. The relevant effects addressed here are due to the kinematics of simple shearing flows, of purely 2-D elongational (irrotational) flows and of what can be considered a new type of flow field capable of bridging all available information about drop dynamics in the first two environments. The first flow field corresponds to the upper limit of weak flows, because it contains significant vorticity, and with it only a feeble deformation of a drop is generally possible. On the contrary, irrotational flows are considered the most capable for deforming an embedded drop –or bursting it– mainly because there in no vorticity present but a dominant rate of deformation as its name implies.

The third flow field is less known and is here studied in detail. It corresponds to those flows generated by Two-Roll Mills (TRMs), which are also 2-dimensional flows but with a full spectrum of possible flow kinematics: Starting at one end with those similar to simple shear flows and sweeping smoothly towards the other end, where significant levels of elongation are present and capable of providing a flow environment similar to pure irrotational flows. Here, emphasis is given to understand the transition on the behavior of the drop dynamics from a flow field dominated by vorticity to another dominated by the rate of deformation of the velocity gradient. Thus, of special relevance are studies that can be performed with flow cells of the Two-Roll Mill (TRM) type.

A second relevant aspect of the dynamics of drops relates to the known and established relations for small deformations models in simple shear flows and irrotational flows; especially comparisons among the observed experimental behavior, and theoretical and numerical predictions. In particular, in this work emphasis will be given to the small deformation dynamics. Thanks to Cox [40], Rallison [41] and Greco [33], this is a well understood field of fluid dynamics and at the present time it also represents a significant (and unavoidable) benchmark to evaluate a new and large set of ideas and research paradigms that can be foreseen as a result of introducing the TRM flow cells. However, despite small deformation dynamics being an excellent benchmark, there exists several discrepancies that may require a better understanding of the theoretical expansions used for predictions of small deformations, especially a clear failure to predict the correct shape of drops; e. g., see Guido, Greco and Villone [42]. From the applications perspective, qualitative and quantitative models are required, both of an experimental as well as a theoretical kind. Chapter 5 presents the richness of behavior that is available to studies of drops in TRMs as well as some of the current difficulties to understand in depth the currently available results.

Given that a theoretical and numerical general solution exist for flows of TRMs [16, 17, 45], this is a significant advantage to be exploited in these studies. In Chapter 5 numerical techniques –based on boundary integral element methods or boundary element methods [28, 46] are applied to better understand the observed phenomena in drops subjected to very large deformations in flows other that simple shear or purely elongational. Hence, the use of TRMs will address physical problems of deformation, orientation, rupture and coalescence of drops under well characterized flow kinematics not yet studied, which may be important cornerstones for studies of naturally occurring two-phase flow fields. In particular, results about spheroidal drops will be used to address small deformation theories to experimental results for a large class of linear 2-D flow fields.

Chapter 4

BEM simulations for deformation of viscous drops in strong flow fields

Many fluid mechanics problems of interest to scientists and engineers involve the motion of two (or more) contiguous fluids that are immiscible and separated by an interface. These problems exhibit many complex phenomena and are especially difficult to solve because the position and shape of the interface is not known *a priori* and may change in response to the motion of the two fluids. Thus, although the Navier-Stokes equations can describe the motion of the fluids (each being Newtonian with its own viscosity and density), boundary conditions must be applied at the interface, and the shape of this interface cannot be specified ahead to time. Such problems are known as *free-boundary problems.*

Free-boundary problems of viscous drops in flows have received much attention due to its practical as well as its purely academic importance. Many papers in the scientific literature analyze shear flows and pure elongational flows (see Stone [3] and Briscoe et al. [5]), but a few consider effects of vorticity, although under limited conditions. The work of Bentley and Leal [12] is perhaps a notable exception addressing a 2-D unbounded elongational flow with significant vorticity. However, most of the previous experimental studies do not address yet wall effects. Among other effects that have been significantly less studied are Marangoni effects in complex flows, because many studies have been done with axisymmetric buoyancy driven drops, where concentration gradients of surfactants have a relative simple relationship [47]. But for other flow types, the parameters that affect the interfacial tension gradient are different. These ideas represent some of the most important motivation for doing studies in drops, where effects of walls can be measured or calculated.

To describe the flow field generated by the presence of an interface, the flow on each side of the interface must be considered separately, and then require for the velocity and the surface forces proper matching conditions. In the next Subsections, the governing equations for the interface's conditions are considered.

For drops or particles of small dimensions and immersed in a highly viscous fluid, inertial effects may be neglected and a slow flow solution is used to study its orientation, deformation or breakup dynamics. In this case, i. e., in the low Reynolds number limit, the incompressible fluid motion is governed by Stokes and continuity equations.

4.1 Boundary conditions at a fluid interface

For the behavior of a flow, the significance of an interface is two-fold. From a kinematical standpoint, the interface marks the permanent boundary between two adjacent regions of the flow with distinct physical constants. From a dynamical standpoint, the interface is a singular surface of concentrated forces; i. e., in general, the surface forces acting on the two sides of an interface have different values, termed the discontinuity in the surface force $\mathbf{\Delta f}$, which depends upon the physical properties of the fluids, on the structure or shape and on the thermodynamic properties of the interface. This dependence can be expressed in terms of a constitutive relationship that may involve a number of physical constants, including the densities of the fluids, surface tension, surface viscosity, surface elasticity, and surface modules of bending and dilatation. An interface is *active* when $\mathbf{\Delta f}$ is finite, and *inactive* or *passive* when $\mathbf{\Delta f} = \mathbf{0}$. An active interface plays a leading role in determining the dynamics of the flow, whereas a passive interface is simply advected by the flow [48].

Consider a closed interface S in either an unbounded fluid or a fluid that is bounded by a solid surface S_B. The Fluids 1 and 2 are characterized by the viscosities μ_1 and μ_2, and the densities ρ_1 and ρ_2. Furthermore, the Navier-Stokes equations are valid on both fluids.

4.1.1 Continuity of the velocity

The continuity of the velocity at the interface S corresponds to the *no-slip* boundary condition that has the form

$$\mathbf{u} = \hat{\mathbf{u}} \quad \text{on} \quad S, \tag{4.1}$$

where the velocity in the Fluid 1 is $\mathbf{u}$, and the velocity in the Fluid 2 is $\hat{\mathbf{u}}$.

4.1.2 Kinematic condition

The kinematic condition is based upon the assumption that the interface is neither a source nor a sink of mass. Accordingly, the normal component of the velocity at S in both fluid must be equal to the normal velocity of the surface itself. As the surface S may translate and deform into new shapes as a function of time, the kinematic condition can be expressed in the form of a relationship between $\mathbf{u} \cdot \mathbf{n}$ or $\hat{\mathbf{u}} \cdot \mathbf{n}$ (where $\mathbf{n}$ is the unit normal vector to S) and the time rate of change of the interface shape. To express this relationship in mathematical form, consider a function $F(\mathbf{x}, t)$ to represent the interface shape as the set of points $\mathbf{x}$ where $F(\mathbf{x}, t) \equiv 0$. Then, the unit normal vector $\mathbf{n}$ to S can be defined in terms of $F(\mathbf{x}, t)$ as

$$\mathbf{n} = \pm \frac{\boldsymbol{\nabla} F}{\|\boldsymbol{\nabla} F\|}, \tag{4.2}$$

where the sign is chosen by convention so that $\mathbf{n}$ is a positive unit vector when it points from S into the exterior Fluid 1. Now, since F is a scalar function which is always equal to zero at any point on the fluid interface, its time derivative following any material point on the interface is equal to zero, that is

$$\frac{\partial F}{\partial t} + \mathbf{u} \cdot \boldsymbol{\nabla} F = 0 \quad \text{for any point on} \quad S. \tag{4.3}$$

Replacing Eq. 4.2 into Eq. 4.3, the kinematic condition is given as

$$\frac{1}{\|\boldsymbol{\nabla} F\|} \frac{\partial F}{\partial t} + \mathbf{u} \cdot \mathbf{n} = 0 \quad \text{on} \quad S. \tag{4.4}$$

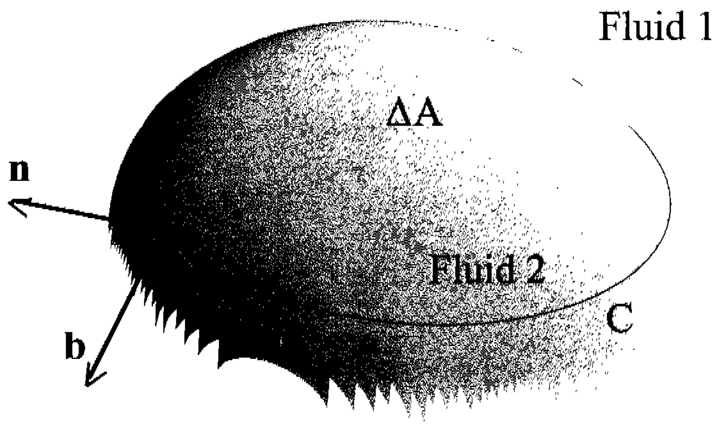

FIGURE 4.1. Schematic illustration of a section of a three-dimensional interface between two fluids.

4.1.3 Stress conditions

Stress conditions are necessary to determine completely the velocity field and the shape of the interface. A clean interface that does not contain impurities or surfactants is characterized by isotropic surface tension γ, acting in the plane of the interface. To obtain a relation between γ and $\Delta\mathbf{f}$, consider an element surface area at the interface ΔA that is enclosed by the contour C, then the force balance has the form

$$\iint_{\Delta A} (\boldsymbol{\sigma} - \hat{\boldsymbol{\sigma}}) \cdot \mathbf{n} \, dS \; + \oint_C \gamma \, \mathbf{b} \, dl = \mathbf{0}, \tag{4.5}$$

where the unit vector $\mathbf{b}$ lies on the plane tangent to the interface and is normal to C, see Fig. 4.1. Using the identity $\mathbf{b} = \mathbf{t} \times \mathbf{n}$, Eq. 4.5 can be rewritten in the equivalent form:

$$\iint_{\Delta A} (\boldsymbol{\sigma} - \hat{\boldsymbol{\sigma}}) \cdot \mathbf{n} \, dS \; = \oint_C \gamma \, \mathbf{n} \times \mathbf{t} \, dl \tag{4.6}$$

where $\mathbf{n}$ and $\mathbf{t}$ are unit vectors normal to the interface and tangential to C, respectively. To convert the contour integral of Eq. 4.6 into an area integral, a variation of the Stokes' theorem can be used; thus

$$\oint_C \mathbf{F} \times \mathbf{t}\, dl = \iint_{\Delta A} (\mathbf{n}\, \boldsymbol{\nabla} \cdot \mathbf{F} - \boldsymbol{\nabla}\mathbf{F} \cdot \mathbf{n})\, dS, \tag{4.7}$$

where $\mathbf{F}$ is a differentiable function defined over the whole space. Extending the domain of definition of the normal vector $\mathbf{n}$ and of the surface tension γ away from the interface into the whole space, setting $\mathbf{F} = \gamma\, \mathbf{n}$, and using Eq. 4.7, the following equation is obtained

$$\oint_C \gamma\, \mathbf{n} \times \mathbf{t}\, dl = \iint_{\Delta A} (\mathbf{n}\, \boldsymbol{\nabla} \cdot (\gamma\, \mathbf{n}) - \boldsymbol{\nabla}(\gamma\, \mathbf{n}) \cdot \mathbf{n})\, dS. \tag{4.8}$$

Substituting Eq. 4.8 into Eq. 4.6, and noting that $\boldsymbol{\nabla}\mathbf{n} \cdot \mathbf{n} = \frac{1}{2}\boldsymbol{\nabla}(\mathbf{n} \cdot \mathbf{n}) = \mathbf{0}$, thus

$$\begin{aligned} &\iint_{\Delta A} \Big[\ (\boldsymbol{\sigma} - \hat{\boldsymbol{\sigma}}) \cdot \mathbf{n} - \mathbf{n}\, \boldsymbol{\nabla} \cdot (\gamma\, \mathbf{n}) + \boldsymbol{\nabla}(\gamma\, \mathbf{n}) \cdot \mathbf{n}\ \Big]\, dS \\ &\qquad = \iint_{\Delta A} \Big[\ (\boldsymbol{\sigma} - \hat{\boldsymbol{\sigma}}) \cdot \mathbf{n} - \gamma\, \mathbf{n}\, \boldsymbol{\nabla} \cdot \mathbf{n} + (\mathbf{I} - \mathbf{n}\mathbf{n}) \cdot \boldsymbol{\nabla}\gamma\ \Big]\, dS. \end{aligned} \tag{4.9}$$

Given that the last equation is true for any arbitrary element of surface ΔA, then

$$(\boldsymbol{\sigma} - \hat{\boldsymbol{\sigma}}) \cdot \mathbf{n} = \gamma\, \mathbf{n} \boldsymbol{\nabla} \cdot \mathbf{n} - (\mathbf{I} - \mathbf{n}\mathbf{n}) \cdot \boldsymbol{\nabla}\gamma \tag{4.10}$$

where $\mathbf{I} - \mathbf{n}\mathbf{n}$ extracts the tangential component of the gradient of the surface tension, and $\mathbf{n}\mathbf{n}$ is the dyadic product. The first and the second term on the right hand side of Eq. 4.10 express, respectively, discontinuities in the normal and tangential directions. When the surface tension is uniform, the tangential component vanishes, and the jump in the interfacial traction points to the normal direction.

The divergence of the normal vector on the right-hand side of Eq. 4.10 is equal to twice the mean curvature of the interface, denoted by κ_m,

$$\boldsymbol{\nabla} \cdot \mathbf{n} = 2\, \kappa_m. \tag{4.11}$$

Other constitutive equations for the discontinuity in the interfacial traction, $\Delta\mathbf{f} = (\boldsymbol{\sigma} - \hat{\boldsymbol{\sigma}}) \cdot \mathbf{n}$, are described by Aris (Chapter 10 [49]), and Pozrikidis (Section 5.5 [28]). The effects of surfactants and other interfacial rheological effects such as surface shear and dilatational viscosities have been studied by Edwards et al. [50].

4.2 Parameters used in studies of drop deformation

From the dimensionless form of the stress boundary condition, two dimensionless numbers are obtained: the capillary and the Bond numbers. These numbers together with the following parameters govern drop deformation and breakup [2]: ratio of drop viscosity to that of the suspending fluid λ_μ, tensorial character of $\nabla \mathbf{u}$, history of the flow and initial drop shape.

The Capillary number Ca represents the ratio of flow forces to surface tension, it is given by

$$Ca = \frac{a\,\dot{\gamma}\,\mu_1}{\gamma}. \tag{4.12}$$

The Bond number B represents hydrostatic pressure variations relative to interfacial tension stresses;

$$B = \frac{\Delta p\, g\, a^2}{\gamma}. \tag{4.13}$$

The tensorial character of $\nabla \mathbf{u}$ gives the flow-type parameter λ. For a given elongational flow with vorticity, as it is shown in previous Chapters, λ values close to 1 imply an elongation dominated flow, while values close to zero imply a flow with strong vorticity; that is λ is a measure of the strength of the flow causing drops to deform, while the vorticity present in the flow induces a rotation of drops and can inhibit drop breakup. The history of the flow and the initial drop shape completely characterize the drop dynamics, determining whether or not transient effects eventually lead to breakup.

A dimensionless measure of the magnitude of the drop deformation is needed. This parameter is the *Taylor deformation parameter* D_T, defined in terms of the longest and shortest semi-axes of the ellipsoidal drop cross-section, i. e.

$$D_T = \frac{r_{\max} - r_{\min}}{r_{\max} + r_{\min}}. \tag{4.14}$$

The orientation angle of the drop is the angle between the longest axis of the drop and the x–axis (also the major principal axis of the deformation rate tensor can be taken, which, for the Two-Roll Mill geometry, is always at 45 ° from the x–axis).

4.3 Fluid-fluid interface in an external flow

Consider now the case of a drop of viscosity μ_2 immersed in a second immiscible fluid of viscosity μ_1 with an *externally-imposed velocity field* $\mathbf{u}^{\infty}(\mathbf{x})$. The boundary conditions at the fluid-fluid interface S_{int} require a continuous velocity and a balance between the net surface traction and interfacial tension forces, then,

$$\mathbf{u}_1(\mathbf{x}) \rightarrow \mathbf{u}^{\infty}(\mathbf{x}) \text{ as } \|\mathbf{x}\| \rightarrow \infty, \; \mathbf{u}_1(\mathbf{x}) = \mathbf{u}_2(\mathbf{x}) \text{ for } \mathbf{x} = \mathbf{x}_S \in S_{int}. \qquad (4.15)$$

The stress jump $\|\mathbf{n} \cdot \boldsymbol{\sigma}\|$, accounting for a surface energy difference and densities across the interface, is given by (the normal $\mathbf{n}$ points into Fluid 1)

$$\|\mathbf{n} \cdot \boldsymbol{\sigma}\| = \mathbf{n} \cdot \boldsymbol{\sigma}_1 - \mathbf{n} \cdot \boldsymbol{\sigma}_2 = \gamma\, \mathbf{n} \boldsymbol{\nabla} \cdot \mathbf{n} - (\mathbf{I} - \mathbf{n}\mathbf{n}) \cdot \boldsymbol{\nabla}\gamma + \Delta\rho(\mathbf{b} \cdot \mathbf{x})\mathbf{n} \quad \text{for} \quad \mathbf{x}_S \in S_{int}. \; (4.16)$$

Here γ, denotes the interfacial tension, $\Delta\rho$ is the density difference, and $\mathbf{x}_S$, denotes a point on the interface. The stress balance (Eq. 4.16) includes both a normal stress jump, $\gamma\, \mathbf{n}\boldsymbol{\nabla} \cdot \mathbf{n}$, proportional to the product of interfacial tension and the local curvature, and a tangential stress jump, $-(\mathbf{I} - \mathbf{n}\mathbf{n}) \cdot \boldsymbol{\nabla}\gamma$, owing to variations in interfacial tension along the surface. These variations may result from either temperature gradients or the presence of surfactants in the fluid. In such instances, additional field equations determine the temperature profile or the distribution of surfactant along the interface. Other stresses may be included in the stress jump boundary condition.

Although Stokes solution does not consider explicitly the time-dependence of a flow field, it is certainly appropriate for studies of time-dependent interface distortions. Under the conditions prevalent during the deformation of a drop, a kinematic constraint relates changes in the interface position to the local velocity. For example, the interface evolution may be described with a Lagrangian representation $dx/dt = \mathbf{u}(\mathbf{x}_s)$. This quasi-static assumption requires that $l^2/\nu \ll \tau$ where ν is the kinematic viscosity, and τ is a typical time for a change of the flow or geometry. Generally, $\tau = \min[O(\frac{l}{u^{\infty}}), O(\frac{l\mu}{\sigma})]$, where the former is a time scale for an externally-driven flow, and the latter is the time scale of an interfacial-tension-driven motion [51]. In most situations, the larger of the two fluid viscosities should be used for these estimates. Physically, the quasi-static approximation means that the fluid immediately adjusts to changes in the boundary location owing to the rapid vorticity diffusion.

4.3.1 Integral equation for a fluid-fluid interface in an external flow

Integral equation formulations are a natural choice for certain classes of Stokes flow problems. These methods may be applied to flows involving only rigid boundaries (e.g., a suspension of rigid particles [52]) or free-boundary problems. The principal difficulty when solving free-boundary problems is that the position of the interface is unknown a priori and must be determined as part of the solution. Thus, the problem of determining the time-dependent interface shape is inherently non-linear.

In order to describe a flow field in the presence of an interface, the flow on each side of the interface and the proper matching conditions for the velocities and surface forces must be considered. Typically, the continuity of velocity across the interface is required, as well as a constitutive relation for the discontinuity in the interfacial surface force. To construct a boundary integral representation, two boundary integral equations are necessary (for each flow field on either side of the interface) involving the interfacial velocity, and the interfacial surface force. Once the interfacial boundary conditions are established, a system of integral equations is obtained for the unknown interfacial functions.

Consider the case of a fluid drop represented by V_2 in an external fluid denoted by V_1, where the velocity vanishes at infinity, as shown in Fig. 4.1. For small droplets, the flow field is essentially linear and elongational in character, such as those considered by Bentley and Leal [12] and others. However, principal difference introduced here is the fact that experimentally there is no data published under flow conditions such as presented in this Chapter. Furthermore, theoretical analyses for flow conditions such as those proposed here are also very few, the exception been the work of Blawzdziewicz et. al. [53]. Most of previous studies emphasize the elongational character of the flow, as the main mechanism for bursting drops; while here, emphasis is given to the presence of vorticity in greater amounts, up to the case of kinematics typical of viscometric flows, and as the dominant class of environments prevalent in many applications and most relevant to technology. More recently, Leal and collaborators have studied the dynamics of drop coalescence under conditions that assume very small rotation of droplets while approaching each other; see for example: Park [54] and Baldessari [55].

The viscosity ratio is denoted by $\lambda_\mu = \mu_2/\mu_1$. Eq. 2.13 holds for $\mathbf{u}$ in both fluids and only the fluid-fluid interface S_{int} needs to be considered. Therefore, remembering that $\mathbf{n}$ is directed from Fluid 2 to Fluid 1, and using $\mathbf{f} = \mathbf{n} \cdot \boldsymbol{\sigma}$, the two equations can be written as

$$\begin{aligned}
&-\frac{1}{C_D \pi \mu_1} \int_S \mathbf{f}_1(\mathbf{x}) \cdot \mathbf{G}\left(\mathbf{x}, \mathbf{x}_0\right) \, dS(\mathbf{x}) \\
&\qquad + \frac{1}{C_D \pi} \int_S \mathbf{u}_1(\mathbf{x}) \cdot \mathbf{T}(\mathbf{x}, \mathbf{x}_0) \cdot \mathbf{n}(\mathbf{x}) \, dS(\mathbf{x}) = \begin{cases} \mathbf{u}_1(\mathbf{x}_0) & \mathbf{x}_0 \in V_1 \notin V_2 \\ \frac{1}{2}\mathbf{u}_1(\mathbf{x}_0) & \mathbf{x}_0 \in S \\ \mathbf{0} & \mathbf{x}_0 \in V_2 \notin V_1 \end{cases}, \qquad (4.17)
\end{aligned}$$

and

$$\begin{aligned}
&\frac{1}{C_D \pi \mu_2} \int_S \mathbf{f}_2(\mathbf{x}) \cdot \mathbf{G}\left(\mathbf{x}, \mathbf{x}_0\right) \, dS(\mathbf{x}) \\
&\qquad - \frac{1}{C_D \pi} \int_S \mathbf{u}_2(\mathbf{x}) \cdot \mathbf{T}(\mathbf{x}, \mathbf{x}_0) \cdot \mathbf{n}(\mathbf{x}) \, dS(\mathbf{x}) = \begin{cases} \mathbf{0} & \mathbf{x}_0 \in V_1 \\ \frac{1}{2}\mathbf{u}_2(\mathbf{x}_0) & \mathbf{x}_0 \in S \\ \mathbf{u}_2(\mathbf{x}_0) & \mathbf{x}_0 \in V_2 \notin V_1 \end{cases}. \qquad (4.18)
\end{aligned}$$

Multiplying Eq. 4.18 by λ_μ, and adding it to Eq. 4.17 yields

$$\begin{aligned}
&-\frac{1}{C_D \pi \mu_1} \int_S \Delta\mathbf{f}(\mathbf{x}) \cdot \mathbf{G}\left(\mathbf{x}, \mathbf{x}_0\right) \, dS(\mathbf{x}) \\
&\qquad + \frac{1-\lambda_\mu}{C_D \pi} \int_S \mathbf{u}_1(\mathbf{x}) \cdot \mathbf{T}(\mathbf{x}, \mathbf{x}_0) \cdot \mathbf{n}(\mathbf{x}) \, dS(\mathbf{x}) = \begin{cases} \mathbf{u}_1(\mathbf{x}_0) & \mathbf{x}_0 \in V_1 & \text{(a)} \\ \dfrac{1+\lambda_\mu}{2}\mathbf{u}_1(\mathbf{x}_0) & \mathbf{x}_0 \in S & \text{(b)} \\ \lambda_\mu \mathbf{u}_2(\mathbf{x}_0) & \mathbf{x}_0 \in V_2 & \text{(c)} \end{cases}, \qquad (4.19)
\end{aligned}$$

where the disturbance stress jump $\Delta\mathbf{f} = \mathbf{f}_1 - \mathbf{f}_2 = \mathbf{n} \cdot (\boldsymbol{\sigma}_1 - \boldsymbol{\sigma}_2)$. Alternatively, for problems with externally-imposed flows, it is more common to recast Eq. 4.19 in terms of the actual interfacial velocity and $\mathbf{u}^\infty(\mathbf{x})$. Using the identity [51]

$$\int_{V_1} \nabla \cdot \left(\boldsymbol{\sigma}^\infty \cdot \mathbf{G} + \mathbf{T} \cdot \mathbf{u}^\infty\right) dV = \mathbf{0}, \qquad (4.20)$$

the following integral equation is obtained:

$$\mathbf{u}^{\infty}(\mathbf{x}_0) - \frac{1}{C_D \pi \mu_1} \int_S \mathbf{\Delta f}(\mathbf{x}) \cdot \mathbf{G}(\mathbf{x}, \mathbf{x}_0)\, dS(\mathbf{x})$$
$$+ \frac{1-\lambda_\mu}{C_D \pi} \int_S \mathbf{u}_1(\mathbf{x}) \cdot \mathbf{T}(\mathbf{x}, \mathbf{x}_0) \cdot \mathbf{n}(\mathbf{x})\, dS(\mathbf{x}) = \begin{cases} \mathbf{u}_1(\mathbf{x}_0) & \mathbf{x}_0 \in V_1 \quad (\mathrm{a}) \\ \frac{1+\lambda_\mu}{2} \mathbf{u}_1(\mathbf{x}_0) & \mathbf{x}_0 \in S \quad (\mathrm{b}) \\ \lambda_\mu \mathbf{u}_2(\mathbf{x}_0) & \mathbf{x}_0 \in V_2 \quad (\mathrm{c}) \end{cases} . \quad (4.21)$$

To proceed with the numerical integration it is necessary to discretize Eq. 4.21b; that is, these integrals are calculated using Gauss-Legendre quadrature methods, given by the following equation

$$\sum_{l=1}^{N} \left[\frac{1}{C_D \pi \mu_1} \sum_{n=1}^{N} \Delta f_i^n \left(q^n \sum_{m=1}^{M+1} w_m G_{ij}\left(\mathbf{x}^m, \mathbf{x}_0^l\right) \right) - u_j^{\infty}\left(\mathbf{x}_0^l\right) + \right.$$
$$\left. \frac{1+\lambda_\mu}{2} u_j\left(\mathbf{x}_0^l\right) - \frac{1-\lambda_\mu}{C_D \pi} \sum_{n=1}^{N} \left(u_i^n q^n \sum_{m=1}^{M+1} w_m T_{ijk}\left(\mathbf{x}^m, \mathbf{x}_0^l\right) n_k^m \right) \right] = 0, \quad (4.22)$$

where M is the degree of the Gauss-Legendre quadrature, q^n is the resultant factor obtained from the transformation of the limits of integration to a canonical form for the segment n, w_m is the weight for the $\mathbf{x}^m$–th base point, N is the number of collocation points, and $\mathbf{G}(\mathbf{x}^m, \mathbf{x}_0)$, $\mathbf{T}(\mathbf{x}^m, \mathbf{x}_0)$ and $\mathbf{n}^m = \mathbf{n}(\mathbf{x}^m)$ are evaluated at the $\mathbf{x}^m$–th base point.

For a given external flow and a known interface shape S, Eq. 4.19b or Eq. 4.21b are a Fredholm integral equations of the second kind for the unknown interfacial velocity $\mathbf{u}(\mathbf{x}_S)$ (or the actual velocity $\mathbf{u}(\mathbf{x}_S)$), which depends on the stress jump $\mathbf{\Delta f}$ across the deformable surface. The stress jump is a function of the interface shape, dependent on position, the normal vector and local curvature, as given by Eq. 4.16. The above equations are the starting point for numerical investigation of numerous free-boundary problems. In addition, for a known interfacial velocity and interface shape, Eqs. 4.19a and 4.19c or Eqs. 4.21a and 4.21c determine the velocity field (and pressure field) at points off the surface and thus are useful for obtaining a detailed picture of the entire flow field.

The advantage of using this formulation is two fold: (1) The domain of integration of the integral equation extends only over S and is therefore finite, rather than over an infinite domain, as in the original problem; and (2) the dimensionality of the problem is reduced by one.

4.4 Fluid-fluid interface near solid boundaries

Hydrodynamic interactions of a particle with the surrounding walls will depend, besides their proximity, on the particle shape, orientation, and position, as well as the geometry of the containing walls. These conditions affect the motion and the general dynamic behavior of drops and bubbles. The primary effect due to the presence of a solid wall near a fluid particle is to increase the drag force on the particle. This phenomenon arises mainly because of the greater shear stress necessary to sustain a velocity difference between the particle and the container. There are other effects such as droplet deformation, and even drop breakup. The size of the drop and its initial position relative to the nearby wall are particularly important, and these factors determine the relative dominance of shear and elongational effects from the suspending fluid on the drop deformation.

Wall effects in viscous drops are divided in two cases depending on the diameter ratio $r_d = d_e/D$, where d_e is the diameter of the stationary drop (spherical) and D is the characteristic length of the container. One case is when r_d is less than about 0.6 [56]. At low r_d, the walls cause little deformation beyond that may be present for the fluid particle in an infinite medium. When the particle is located far away from a boundary, the effect of the boundary may be estimated by means of an asymptotic analysis of the boundary integral equations. The other case is when $r_d > 0.6$, that is the case of slug flow (or Taylor bubbles), where the container walls have a dominant effect on the shape of the bubble or drop.

While extensive work has been devoted to the modeling and simulation of drops deforming in an infinite fluid medium, relatively little work has been done in the case of a drop deforming in a confined domain. Some studies have been carried out with solid particles of very simple geometry, as those of Happel and Brenner (Chapter 7 [1]), and Kim and Karrila (Chapter 12 [52]). The motion of a drop in the vicinity of a plane wall was studied by Pozrikidis [57], by Ascoli et al. [58] and by Power [59], and in the vicinity of a deformable interface by Yiantsios and Davis [60]. The deformation of drops in confined flows was analyzed inside a circular straight tube by Martinez and Udell [61] and by Pozrikidis [62], and in a tube with a constriction by Tsai and Miksis [63]; however, these studies examined only axisymmetric motion [6]. Heat and mass transfer studies are treated in the book of Sadhal [64]. More recently, a series of works by Khayat et al. [65, 66, 67, 68, 6] studied numerically the planar deformation of a drop in confined flows.

For flow fields generated with TRMs, there exists the possibility of evaluating the effects of near walls on the dynamics of the droplet deformation. This point may be considered a significant advantage when compare with other flow fields such as those generated with Four-Roll Mills. For the latter, the underlying assumption of a linear 2-D flow field requires that droplets to be small compared to the gap between the cylinders. With Two-Roll Mills, it is possible to include a dimensionless length scale that relates the drop characteristic dimension independently of the characteristic size of the gap between the cylinders. In this manner drops of size of the order of the cylinders gap are studied and the results of the simulation are presented in Section 5.2.

4.4.1 Integral equation for a fluid-fluid interface near solid boundaries

Considering boundary conditions that explicitly take into account both surfaces of the cylinders could be a useful technique for evaluation wall effects in an elongational flow. Thus, the governing equation for a *large fluid drop* of volume V_2, in a flow field generated by the solid boundaries $S_{rigid,\ 1}$ and $S_{rigid,\ 2}$ on the Fluid 1, with volume V_1, as shown in Fig. 4.2 are necessary. Now, $S_{rigid,\ 1}$ and $S_{rigid,\ 2}$ correspond to each of the cylindrical inner surfaces, that can have different diameters, and may rotate at different speeds. For this particular flow field, the TRM is capable of generating a very rich class of flows, characterized by complex fields for the shear rate and the flow-type parameter values. As has been shown in Chapters 1-3, these general boundary conditions at $S_{rigid,\ 1}$ and $S_{rigid,\ 2}$ determine the stagnation point position within the flow field. Now, all points along the line between the cylinders axes are valid positions for a stagnation point. But as a result of these latter conditions, there may exist nonzero components of the gradients of the shear rate and the flow-type parameters along the line between the cylinders. These flow environments applied to the deformation of droplets do not exist in the scientific literature, albeit its usefulness in many industrial applications.

Here again the viscosity ratio is denoted by $\lambda_\mu = \mu_2/\mu_1$. Eq. 2.13 holds for $\mathbf{u}$ in both fluids and at the fluid-fluid interface S_{int}, and the solid boundary S_{rigid}. Therefore, remembering that $\mathbf{n}$ is directed from Fluid 2 to Fluid 1 and from the solid boundary into the Fluid 1, and using $\mathbf{f} = \mathbf{n} \cdot \boldsymbol{\sigma}$, the two equations can be written as

$$\begin{aligned}
&-\frac{1}{C_D\,\pi\mu_1}\int_S \mathbf{f}_1(\mathbf{x})\cdot\mathbf{G}(\mathbf{x},\mathbf{x}_0)\ dS(\mathbf{x}) \\
&\qquad +\frac{1}{C_D\,\pi}\int_S \mathbf{u}_1(\mathbf{x})\cdot\mathbf{T}(\mathbf{x},\mathbf{x}_0)\cdot\mathbf{n}(\mathbf{x})\ dS(\mathbf{x}) = \begin{cases} \frac{1}{2}\mathbf{u}_1(\mathbf{x}_0) & \mathbf{x}_0\in S_{rigid}, \\ \mathbf{u}_1(\mathbf{x}_0) & \mathbf{x}_0\in V_1 \\ \frac{1}{2}\mathbf{u}_1(\mathbf{x}_0) & \mathbf{x}_0\in S_{int}, \\ \mathbf{0} & \mathbf{x}_0\in V_2 \end{cases}, \qquad (4.23)
\end{aligned}$$

where $S = S_{rigid} \cup S_{int}$, and

$$\begin{aligned}
&\frac{1}{C_D\,\pi\mu_2}\int_{S_{int}} \mathbf{f}_2(\mathbf{x})\cdot\mathbf{G}(\mathbf{x},\mathbf{x}_0)\ dS(\mathbf{x}) \\
&\qquad -\frac{1}{C_D\,\pi}\int_{S_{int}} \mathbf{u}_2(\mathbf{x})\cdot\mathbf{T}(\mathbf{x},\mathbf{x}_0)\cdot\mathbf{n}(\mathbf{x})\ dS(\mathbf{x}) = \begin{cases} \mathbf{0} & \mathbf{x}_0\in V_1 \\ \frac{1}{2}\mathbf{u}_2(\mathbf{x}_0) & \mathbf{x}_0\in S_{int} \\ \mathbf{u}_2(\mathbf{x}_0) & \mathbf{x}_0\in V_2 \end{cases} \qquad (4.24)
\end{aligned}$$

Multiplying Eq. 4.24 by λ_μ, and adding to Eq. 4.23 yields

$$\begin{aligned}
&-\frac{1}{C_D\,\pi\,\mu_1}\int_{S_{rigid}} \mathbf{f}_1(\mathbf{x})\cdot\mathbf{G}(\mathbf{x},\mathbf{x}_0)\ dS(\mathbf{x}) \\
&\qquad +\frac{1}{C_D\,\pi}\int_{S_{rigid}} \mathbf{u}_1(\mathbf{x})\cdot\mathbf{T}(\mathbf{x},\mathbf{x}_0)\cdot\mathbf{n}(\mathbf{x})\ dS(\mathbf{x}) \\
&\qquad\qquad -\frac{1}{C_D\,\pi\,\mu_1}\int_{S_{int}} \Delta\mathbf{f}(\mathbf{x})\cdot\mathbf{G}(\mathbf{x},\mathbf{x}_0)\ dS(\mathbf{x}) \\
&\qquad\qquad\qquad +\frac{1-\lambda_\mu}{C_D\,\pi}\int_{S_{int}} \mathbf{u}_1(\mathbf{x})\cdot\mathbf{T}(\mathbf{x},\mathbf{x}_0)\cdot\mathbf{n}(\mathbf{x})\, dS(\mathbf{x}) = \\
&\qquad\qquad\qquad = \begin{cases} \mathbf{u}_1(\mathbf{x}_0) & \mathbf{x}_0\in V_1 & \text{(a)} \\ \dfrac{1+\lambda_\mu}{2}\mathbf{u}_1(\mathbf{x}_0) & \mathbf{x}_0\in S_{int} & \text{(b)} \\ \lambda_\mu\,\mathbf{u}_2(\mathbf{x}_0) & \mathbf{x}_0\in V_2 & \text{(c)} \\ \frac{1}{2}\mathbf{u}_1(\mathbf{x}_0) & \mathbf{x}_0\in S_{rigid}, & \text{(d)} \end{cases}. \qquad (4.25)
\end{aligned}$$

For the case of cylinders rotating at different speeds, $1/2\,\mathbf{u}_1(\mathbf{x}_0)$ for $\mathbf{x}_0 \in S_{rigid}$ requires establishing the appropriate speeds at $S_{rigid,\ 1}$ and $S_{rigid,\ 2}$ of Fluid 1, as shown in

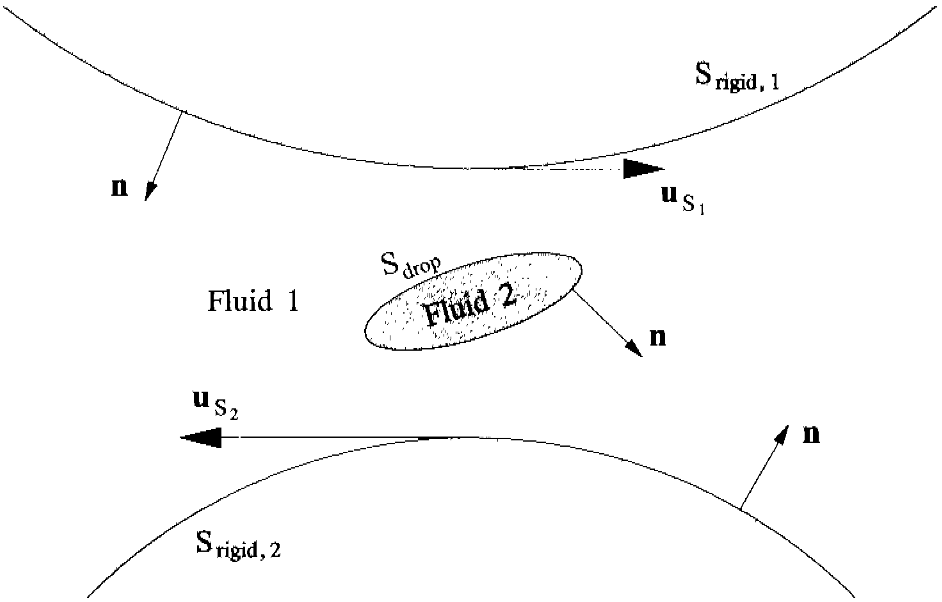

FIGURE 4.2. Fluid interface deformed by the flow field generated by solid boundaries

Fig. 4.2. The flow field characteristics in the absence of Fluid 2 are discussed in Chapters 1 to 3. For small drops at the gap between cylinders, predictions of the deformation dynamics by Eq. 4.25 will match those of Eq. 4.19.

A discretized representation of the integral equation for a fluid-fluid interface near solid boundaries (i. e., discretization of Eqs. 4.25b and 4.25d) is given by

$$
\begin{aligned}
&-\frac{1}{C_D\,\pi\,\mu_1}\sum_{n=1}^{N_{rigid}} f_i^n\left(q^n\sum_{m=1}^{M+1} w_m\,G_{ij}\left(\mathbf{x}^m,\mathbf{x}_0\right)\right)\\
&+\frac{1}{C_D\,\pi}\sum_{n=1}^{N_{rigid}} u_i^n\left(q^n\sum_{m=1}^{M+1} w_m\,T_{ijk}\left(\mathbf{x}^m,\mathbf{x}_0\right)\,n_k^m\right)\\
&-\frac{1}{C_D\,\pi\,\mu_1}\sum_{n=1}^{N_{int}} \Delta f_i^n\left(q^n\sum_{m=1}^{M+1} w_m\,G_{ij}\left(\mathbf{x}^m,\mathbf{x}_0\right)\right)\\
&+\frac{1-\lambda_\mu}{C_D\,\pi}\sum_{n=1}^{N_{int}} u_i^n\left(q^n\sum_{m=1}^{M+1} w_m\,T_{ijk}\left(\mathbf{x}^m,\mathbf{x}_0\right)\,n_k^m\right)\ -g\left(\mathbf{x}_0\right)\,u_j\left(\mathbf{x}_0\right)=0, \quad (4.26)
\end{aligned}
$$

where

$$g\left(\mathbf{x}_0\right)=\begin{cases}\frac{1+\lambda_\mu}{2} & \mathbf{x}_0\in S_{int}\\ \frac{1}{2} & \mathbf{x}_0\in S_{rigid},\end{cases}, \tag{4.27}$$

where M is the degree of the Gauss-Legendre quadrature, q^n is the resultant factor obtained from the transformation of the limits of integration to a canonical form for the segment n, w_m is the weight for the $\mathbf{x}^m$–th base point, N_{rigid} is the number of elements at the rigid surface, N_{int} is the number of elements at the fluid-fluid interface, and $\mathbf{G}\left(\mathbf{x}^m,\mathbf{x}_0\right)$, $\mathbf{T}\left(\mathbf{x}^m,\mathbf{x}_0\right)$ and $\mathbf{n}^m=\mathbf{n}\left(\mathbf{x}^m\right)$ are evaluated at the $\mathbf{x}^m$–th base point.

Now, Eq. 4.26 applies for each of the collocation points, thus

$$\begin{aligned}\sum_{l=1}^{N_{\mathrm{col}}}\Bigg[&-\frac{1}{C_D\,\pi\,\mu_1}\sum_{n=1}^{N_{rigid}} f_i^n\left(q^n\sum_{m=1}^{M+1} w_m\,G_{ij}\left(\mathbf{x}^m,\mathbf{x}_0^l\right)\right)\\ &+\frac{1}{C_D\,\pi}\sum_{n=1}^{N_{rigid}} u_i^n\left(q^n\sum_{m=1}^{M+1} w_m\,T_{ijk}\left(\mathbf{x}^m,\mathbf{x}_0^l\right)\,n_k^m\right)\\ &-\frac{1}{C_D\,\pi\,\mu_1}\sum_{n=1}^{N_{int}}\Delta f_i^n\left(q^n\sum_{m=1}^{M+1} w_m\,G_{ij}\left(\mathbf{x}^m,\mathbf{x}_0^l\right)\right)\\ &+\frac{1-\lambda_\mu}{C_D\,\pi}\sum_{n=1}^{N_{int}} u_i^n\left(q^n\sum_{m=1}^{M+1} w_m\,T_{ijk}\left(\mathbf{x}^m,\mathbf{x}_0^l\right)\,n_k^m\right)-g\left(\mathbf{x}_0^l\right)\,u_j\left(\mathbf{x}_0^l\right)\Bigg]=0,\end{aligned} \tag{4.28}$$

where N_{col} is the number of collocation points and $N_{\mathrm{col}}=N_{rigid}+N_{int}$. Therefore, a $D\ N_{\mathrm{col}}\times D\ N_{\mathrm{col}}$ system of linear equations is obtained, where D is the dimensionality of the problem. This system of linear equations is for the components $(i,j=1,...,D)$ of the surface force or traction $\mathbf{f}$ at each collocation point on the rigid surface and the components of the velocity $\mathbf{u}$ at each collocation point on the fluid-fluid interface. Once again, this system is dense and non-symmetric, and a general-purpose numerical method must be used for solving it, such as the Gauss elimination method or by an iterative method as Jacobi's method.

4.5 Numerical solution of the Boundary Integral Equations for a viscous drop in a strong flow

This Section summarizes standard numerical solution procedures for treating the free-boundary problem of the deformation of a single interface. An integrated numerical procedure for the simulation of an evolving interface using a boundary-integral method requires carrying out three main tasks: (a) the parametric representation of the interface; (b) the evaluation of an integral representation or solution of an integral equation for the interfacial velocities or for the density of a hydrodynamic potential; and (c) the time integration of the equations governing the motion of interfacial marker points and possibly the evolution of dynamically relevant surface functions. In the case of temperature- or surfactant-concentration-dependent surface tension, dynamically relevant surface functions include the temperature and the concentration of surfactant. For the case of an interface consisting of an elastic membrane, dynamically relevant surface functions include the coordinates and the curvature of the interface at the position of marker points in a reference configuration. The overall numerical method is described as the method of *interfacial dynamics for Stokes flow* [69].

Carrying out the aforementioned tasks is facilitated considerably by the use of piecewise numerical interpolation underlying the formalism of boundary-element methods. For the case of two-dimensional or axisymmetric flows, the interface is represented as a collection of planar elements in the form of straight segments, circular arcs, parabolic, cubic, cubic-spline, or higher order elements, all defined by consecutive interfacial nodes. The cubic-spline elements are described in parametric form by means of cubic-spline interpolation for the node coordinates, where the interpolation is done with respect to the polygonal or curved arc length. The geometrical properties of the interface including the normal vector and the curvature follow readily from its local representation. For a three-dimensional flow, interfaces are typically represented by an unstructured grid of three-dimensional elements defined by groups of interfacial nodes. Compared to a structured grid defined in global curvilinear coordinates, the unstructured grid has two advantages: the local curvilinear coordinates over each element are nonsingular, whereas the structured grid may have singular points; and the shape and size of elements may be readily controlled to enhance the spatial resolution at selected regions. The unstructured discretization is amenable to the meritorious finite-volume and finite-element formulations for solving integral and differential equations over evolving domains. Flat and curved triangular elements are particularly attractive because of their ease of implementation. A closed grid of triangles may be readily generated by successively subdividing a regular octahedron or icosahedron into four descendant elements, and subsequently deforming all elements to obtain the desired shape.

4.5.1 Computation of the Normal Vector and Mean Curvature

The unit normal vector and mean curvature of a two-dimensional or axisymmetric interface follow readily from the parametric representation using standard formulae of differential geometry. A simple method for computing the unit normal vector and mean curvature of a three-dimensional interface is by evaluating a contour integral. Consider an interfacial patch ΔA enclosed by the contour C and containing the point $\mathbf{x}_0$. Now, introduce the unit vector $\mathbf{b}$ tangent to the patch and lies on the plane that is normal to C at a point, as shown in Fig. 4.1. If $\mathbf{t}$ is the unit vector tangent to C, and $\mathbf{n}$ is the unit vector normal to the interface, then $\mathbf{b} = \mathbf{t} \times \mathbf{n}$. In the limit as the contour C shrinks to the point $\mathbf{x}_0$, the reduced vectorial line integral

$$\mathbf{a}(\mathbf{x}_0) = \frac{1}{\Delta A} \int_C \mathbf{b}(\mathbf{x}) \; dl(\mathbf{x}) \tag{4.29}$$

tends to the vector $2\,\kappa_m(\mathbf{x}_0)\;\mathbf{n}(\mathbf{x}_0)$, where κ_m is the mean curvature of the interface at the point $\mathbf{x}_0$, and ΔA is the surface. The unit normal vector $\mathbf{n}(\mathbf{x}_0)$ follows by normalizing the vector $\mathbf{a}(\mathbf{x}_0)$, possibly switching its direction to ensure that has the desired orientation. The mean curvature follows from the inner product $\mathbf{a}(\mathbf{x}_0) \cdot \mathbf{n}(\mathbf{x}_0) \equiv 2\,\kappa_m(\mathbf{x}_0)$. In practice, the contour C is identified either with jointed sections of surface curvilinear coordinates defining a surface element, or with groups of selected edges of boundary elements in the vicinity of a point.

4.5.2 Computation of the Singular Single-Layer Potential

Two distinct but somewhat related issues arise in the computation of the single-layer potential: (a) the accurate evaluation of the jump in interfacial traction $\mathbf{\Delta f}$, and (b) the accurate evaluation of the singular integral. The two issues are related in the sense that specialized methods for computing the single-layer potential may be devised for particular expressions for $\mathbf{\Delta f}$.

For the case of two-dimensional or axisymmetric flows, the kernel of the single-layer potential exhibits a logarithmic singularity which may be integrated by several methods, including the use of a Gaussian quadrature for a log-singular term. For three-dimensional flows, the kernel of the single-layer potential exhibits a weak singularity that behaves as $1/r$. In this section, selected strategies pertinent to the integral equations of Stokes flow are discussed.

Isolating the jump in traction

Let us consider the single-layer potential over an interfacial patch ΔA that is enclosed by the closed contour C, and introduce the single-layer potential

$$I_j^S(\mathbf{x}_0) \equiv \int_{\Delta A} G_{ij}(\mathbf{x},\mathbf{x}_0)\ \Delta f_i(\mathbf{x}_0)\ dS(\mathbf{x}). \tag{4.30}$$

A trapezoidal-like approximation can be used to decouple the product of the two functions in the integrand, thus, $I_j^S(\mathbf{x}_0)$ can be rewritten as

$$I_j^S(\mathbf{x}_0) \simeq \frac{1}{\Delta A}\int_{\Delta A} \Delta f_i(\mathbf{x}_0)\ dS(\mathbf{x}) \times \int_{\Delta A} G_{ij}(\mathbf{x},\mathbf{x}_0)\ dS(\mathbf{x}), \tag{4.31}$$

where ΔA is the surface area. Performing a force balance over the patch and assuming that the interface develops in-plane and transverse shear tensions, it is found that the first integral on the right-hand side of the Eq. 4.31 is equal to

$$\int_{\Delta A} \mathbf{\Delta f}(\mathbf{x}_0)\ dS(\mathbf{x}) = -\int_{\Delta A} \mathbf{b}(\mathbf{x})\cdot[\boldsymbol{\tau}(\mathbf{x}) + \mathbf{q}(\mathbf{x})\ \mathbf{n}(\mathbf{x})]\ dl(\mathbf{x}). \tag{4.32}$$

For example, if the interface exhibits uniform isotropic tension γ, $\boldsymbol{\tau} = \gamma\ \mathbf{P}$ and $\mathbf{q} = \mathbf{0}$, where $\mathbf{P} = \mathbf{I} - \mathbf{nn}$ is the tangential projection operator; in this case, $\mathbf{b}\cdot\boldsymbol{\tau} = \gamma\mathbf{b}$.

The computation of the right-hand side of the Eq. 4.32 requires the evaluation of the in-plane surface tension tensor $\boldsymbol{\tau}$ and transverse shear tension vector $\mathbf{q}$ along the contour C. In contrast, the computation of $\boldsymbol{\Delta}\mathbf{f}$ in the integrand on the left-hand side of Eq. 4.32 requires the evaluation of the surface divergence or gradient of $\boldsymbol{\tau}$ and $\mathbf{q}$ over ΔA, which can be a serious source of numerical error.

Direct numerical computation of the single-layer integral

In a typical boundary element numerical method, an interface is discretized into a collection of boundary elements, and the single-layer potential is computed over the individual elements. When the evaluation point $\mathbf{x}_0$ lies in the interior, along the edges, or at the vertices of a boundary element, then as the integration point $\mathbf{x}$ approaches $\mathbf{x}_0$, the integrand exhibits a singularity, and the element is classified as "singular". To compute the single-layer potential over a singular element E, the following equation is used

$$I_j^S(\mathbf{x}_0) = \int_{\Delta A} G_{ij}(\mathbf{x},\mathbf{x}_0)\ \left[\Delta f_i(\mathbf{x}) - \Delta f_i(\mathbf{x}_0)\right]\ dS(\mathbf{x}) + \Delta f_i(\mathbf{x}_0) \int_{\Delta A} G_{ij}(\mathbf{x},\mathbf{x}_0)\ dS(\mathbf{x})\,. \tag{4.33}$$

As the integration point $\mathbf{x}$ approaches the evaluation point $\mathbf{x}_0$, the integrand of the first integral on the right-hand side of Eq. 4.33 tends to a finite value that depends on the orientation of the vector $\mathbf{x}-\mathbf{x}_0$, and the integral may be computed with adequate accuracy using a standard quadrature method.

4.5.3 Computation of the Principal-Value Integral of the Double-Layer Potential

For two-dimensional or axisymmetric flows, the integrand of the principal-value integral of the double-layer potential is nonsingular and may be computed using a standard numerical method. For three-dimensional flows, the $1/\left|\mathbf{x}-\mathbf{x}_0\right|$ singularity of the principal value integral over a closed surface can be removed using a vector identity, then

$$\begin{aligned} I_j^D(\mathbf{x}_0) &\equiv \int_{\Delta A}^{PV} q_i(\mathbf{x})\, T_{ijk}(\mathbf{x},\mathbf{x}_0)\ n_k(\mathbf{x})\ dS(\mathbf{x}) \\ &= \int_{\Delta A} \left[q_i(\mathbf{x}) - q_i(\mathbf{x}_0)\right] T_{ijk}(\mathbf{x},\mathbf{x}_0)\ n_k(\mathbf{x})\ dS(\mathbf{x}) - 4\pi q_j(\mathbf{x}_0)\,, \end{aligned} \tag{4.34}$$

where $\mathbf{q}$ is the density of the double-layer potential (e.g., [28]). As the integration point $\mathbf{x}$ approaches the evaluation point $\mathbf{x}_0$, the integrand on the right-hand side of the Eq. 4.34 tends to a finite value that depends on the orientation of the vector $\mathbf{x} - \mathbf{x}_0$; the integral may be computed with adequate accuracy using a standard quadrature.

4.6 Interface description and evolution

The integral equations are linear equations for the interfacial velocity $\mathbf{u}(\mathbf{x}_S)$, but are non-linear when the shape is unknown. The interface evolves according to $dx_S/dt = \mathbf{u}(\mathbf{x}_S)$. Representing the interface at N discrete points $\mathbf{x}_S^i$, the numerical problem is to determine the evolution of $\mathbf{x}_S^i$ according to the system of equations

$$\frac{d\mathbf{x}_S^i(t)}{dt} = \mathbf{u}(\mathbf{x}_S^i) = \mathfrak{F}\left\{\mathbf{x}_S^i, \frac{d\mathbf{x}_S^i(t)}{dt}\right\}, \quad i = 1, ..., N \tag{4.35}$$

where the non-linear functional $\mathfrak{F}$ (e.g., Eq. 4.19b) depends on the unknown interface shape (hence involves knowledge of the surface normal vector and curvature) and the unknown interfacial velocities. Almost all solution techniques linearize Eq. 4.35 by relaxing the kinematic condition, so that the calculation of the velocity field decouples from the determination of the unknown shape [51].

One way to track the motion of an evolving interface is to mark it using a set of marker points and by computing the trajectories of these points describe its evolution [28]. It is convenient to identify the marker points using two Lagrangian marker variables ζ and η, and to consider the velocity $\mathbf{v}$ of a marker point as a function of ζ, η, and *time*

$$\frac{\partial \mathbf{x}}{\partial t}(\zeta, \eta, t) = \mathbf{v}(\zeta, \eta, t). \tag{4.36}$$

The velocity of the interface will be dependent upon the velocity of the fluid. Interpreting the interface simply as the boundary between two fluids requires that marker points should be allowed to slip along the interface, but are required to move normally to the interface at a velocity equal to that of the fluid element. Thus,

$$\mathbf{v} = [\mathbf{u}(\mathbf{x}, t) \cdot \mathbf{n}]\,\mathbf{n} + \delta\mathbf{t} \tag{4.37}$$

where $\mathbf{u}$ is the velocity of the fluid over the interface, $\mathbf{t}$ is an arbitrary tangent vector, and δ may be chosen arbitrarily and individually for each marker point. By setting $\delta\mathbf{t} = \mathbf{u} \cdot (\mathbf{I} - \mathbf{nn})$, the velocity of the marker points is equal to the velocity of the fluid element. Combining Eq. 4.36 and Eq. 4.37, and noting that the velocity $\mathbf{u}$ depends on the current configuration of the interface, a system of non-linear ordinary differential equations is obtained, which describes the trajectories of the marker points, given by

$$\frac{\partial \mathbf{x}}{\partial t}(\zeta, \eta, t) = [\mathbf{u}(\mathbf{x}, t) \cdot \mathbf{n}]\, \mathbf{n} + \delta\mathbf{t}. \tag{4.38}$$

The steady deformation is attained when the normal component of the velocity at the drop surface is zero, i. e.

$$\mathbf{u}(\mathbf{x}, t) \cdot \mathbf{n} = 0. \tag{4.39}$$

This condition is a highly nonlinear function of the shear rate, $\dot{\gamma}$ [2].

Free boundary problems, which involve interfacial tension, require accurate determination of positions, normal vectors and local curvatures of the interface. Thus, the deforming interface shape should have ideally a twice continuously differentiable representation. Axisymmetric or two-dimensional interface shapes have been studied extensively, representing the overall surface as a set of N discrete nodal points. The position, normal vector and curvature may be evaluated either directly at the nodes using a finite difference scheme, or at inter-nodal locations using interpolation. Investigations of three-dimensional surface deformation are still in their early stages and only modest distortions have been computed, primarily in the context of drop deformation in simple shear flow or pure extensional flow [69]. For the free-surface description there are several methods to carry out this, each one with advantages and disadvantages [70, 71].

Given a description of the interface, the integral equation in 4.19 or in Eq. 4.21 is reduced to a system of linear algebraic equations for the interfacial velocities $\mathbf{u}(\mathbf{x}_S^i)$, and for which several possible numerical techniques are available. The solution of the system of equations gives the interfacial marker-point velocities [28, 69].

For the case of a time evolving system, then its simulation requires computation of the motion of the finite collection of marker points defining the vertices of the boundary elements. The interface shape is updated using the kinematic condition given in Eq. 4.38.

For example, each marker point may be marched forward in time using the actual surface local velocity (a Lagrangian representation). This procedure tends to sweep points tangent to the surface even if only small shape changes actually occur. Consequently, frequent redistribution of marker points is necessary. However, it is straightforward problem to perform a multi-step integrator providing the time evolution of the interface.

Alternatively, an Eulerian view point can also be applied. In practice, points on the interface are moved in a direction normal to the interface using the normal projection of the surface velocity, $d\mathbf{x}_S/dt = (\mathbf{n} \cdot \mathbf{u}(\mathbf{x}_S))\ \mathbf{n}$. This has the advantage that marker points tend to remain evenly distributed. In this work, a second order Runge-Kutta method is used to track the interface shape, and when the drop deformation is small (the marker points remain evenly spaced), fourth order Adams-Bashforth-Moulton Multipoint Method is used [30]. The numerical error for the second order Runge-Kutta method is Δt^3, and for the fourth order Adams-Bashforth-Moulton method is Δt^5. The use of higher order methods is not practical, because there are necessary more CPU time consuming exploratory steps.

In most studies of the drop dynamics, the constant volume of the drop is not an imposed constraint, but rather volume changes are used as a measure of the accuracy of the numerical method. For $\lambda_\mu = 1$, the volume changes typically are insignificant. However, most researchers report noticeable volume changes for low viscosity ratios, $\lambda_\mu \lesssim 0.1$, and may resort to a shape rescaling in order to continue the simulations for long times [51].

The Boundary Element Method used in this work was programmed in Mathematica, in order to benefit from its optimized algorithms.

A problem that we had with the implementation of the BEM for drops was the interpolation of the drop interface, because of the undulations that arise with common interpolation methods. The method that works satisfactorily is the Akima method [72, 73]. This method tries to give the interpolation a more "natural" appearance, i. e., a shape that would be obtained by a hand interpolation method.

Chapter 5

The flow field dynamics of a droplet in a strong flow

All flows generated with Two-Roll Mills have a specific signature. For example, the field of values for the flow-type parameter λ, shear rate $\dot{\gamma}$, etc., are defined by the mill's geometry and the cylinders rotational speeds. Also, in Two-Roll Mill flows there exists a stagnation point where it is possible to position a droplet, and it should remain there for a much extended period of time. This quasi-stationary position together with a dynamic control scheme (see Chapter 3) allows long observation times that are appropriate for studies of deformation dynamics of a droplet. This is possibly the most important characteristic of Four-Roll that was initially exploited by Taylor in 1932 [31], which can also be used with Two-Roll Mills flow fields.

In this Chapter the dynamics of drops embedded in a strong-type of flow with significant vorticity are presented, especially the main features of the internal and external flow fields. These results are based on numerical BEM techniques that provide a powerful algorithms for the determination of the shape and orientation of a drop immersed in an external field. As well, these techniques are useful to calculate the time evolution of the drop, emphasizing those effects due to a significant vorticity in the elongational flows and effects due to different values of the Capillary number. Given that theoretical and experimental results have been published for the time evolution of a drop subjected to a simple shear flow, in this Chapter a comparison is given with these latter results and the numerical simulations of this work. Finally, assuming that for most applications the closeness of solid boundaries is a relevant physical condition, which may have a non-negligible effect on the external and internal flows, the BEM technique is applied for drops in strong flows in bounded domains.

5.1 Drop dynamics in an external strong flow

The equations discussed in Section 4.3 are now applied to conditions kinematically similar to those present at the stagnation point of symmetric TRMs. From Reyes and Geffroy [16], the two-dimensional velocity field at the stagnation point is given by

$$\begin{bmatrix} u_x \\ u_y \end{bmatrix} = \dot{\gamma} \begin{bmatrix} 0 & 1 \\ \lambda & 0 \end{bmatrix} \begin{bmatrix} x \\ y \end{bmatrix} . \tag{5.1}$$

This field is linear. In the Eq. 4.22, $\mathbf{u}^{\infty}$ is replaced by 5.1.

For the study of the drop dynamics in an external strong-type of flow, the values for the parameters used in this work' simulations corresponds to those of the System no. 12 of the Table 2 of Bentley and Leal [12], are $\lambda_{\mu} = 25.8$ ($\mu_1 = 1.193$ and $\mu_2 = 30.8$ Pa s), $\gamma = 5.19 \times 10^{-3}\,\mathrm{N/m}$. The radius of the initial spherical drop shape is $a = 1\,\mathrm{mm}$, and the shear rate is varied to achieve several values of the Capillary number.

The number of collocation points used to describe the drop interface are $N = 72$ and $N = 120$, with the degree of the Gauss-Legendre quadrature set at $M = 20$. The Stresslets and Stokeslets were placed at the collocation points. The evolution of the interface shape is calculated using a second order Runge-Kutta method to solve Eq. 4.38, and setting $\delta \mathbf{t} = \mathbf{0}$. The segments on the drop interface are building using the following method: (1) An interpolation function is made with the marker points and their angles using the Akima interpolation algorithm, the shape of the drop is parametrized using the coordinates of each collocation point or marker point (x, y), and its angle with respect to the origin $\left(\arctan \frac{y}{x}\right)$; (2) The half angles between marker points are obtained and these values are used to set the coordinates of the end points of each segment. In order to carry out the numerical integration, all segments are modeled as arc segments. The method proposed has some disadvantages, as is the fact that the collocation point can not actually in the middle of each segment. When two or more marker points on the drop have the same angle the method fails. Also, when a large deformation occurs the method generates a few very large segments, although this problem is minimized with the use of algorithms for generating a new finer grid. Finally, the time step used for the evolution for the interface are $0.1/\dot{\gamma}$ and $0.2/\dot{\gamma}$, depending on the magnitude of the shear rate and Capillary numbers.

5.1.1 The steady state flow field and deformation

Following Taylor [31, 32] and Bentley and Leal [7], nowadays it is a simple matter to place a drop at the stagnation point of an elongational dominated flow field such as a Four-Roll Mill or a Two-Roll Mill. However, the presence of a drop at the stagnation point modifies simultaneously both the external and the internal –inside the drop– flow fields. As a result, the values of the parameters at the stagnation point in a Two-Roll Mill are considered now the *nominal* flow-type parameter λ_{Nom} and shear rate $\dot{\gamma}_{Nom}$ because the introduction of a drop will modify these values. Thus, assuming a flow generated with a Two-Roll Mill with a droplet at the stagnation point, some of the basic questions addressed here are: (a) what are the characteristics of the modified external flow for a steady state flow condition; (b) how is the drop deformed and what are the main characteristics of the steady internal flow field; and (c) when the stresses of the external flow are not significant, what are the main dimensions of the final steady-state drop deformation, that is, what are the small deformation dimensions, and how these compare with respect to the results say of Greco [33].

Stationary shapes of a drop in an external velocity field may be produced by two stabilizing mechanisms which represent two branches of the solution; i.e., a bifurcation. One branch is dominated by drop rotation due to the vorticity of the external flow, and the second branch by drop relaxation due to capillary stresses [74]. Rotation is especially important for high-viscosity drops, because the time scale for drop rotation is independent of the ratio of viscosities λ_μ, unlike the time scales for capillary relaxation and drop convection by the straining components of the flow, both of which increase with $\lambda_\mu \gg 1$. The bifurcation occurs in the regime where the effects of drop deformation by the straining component of the

Nominal **Stag. Point**	λ_{Int}	$\dot{\gamma}_{Int}$	λ_{Ext}	$\dot{\gamma}_{Ext}$	$\dot{\gamma}\sqrt{\lambda_{Nom}}$	$\dot{\gamma}\sqrt{\lambda_{Ext}}$	r_{stp}
$\lambda_{Nom} = 0.0$	-0.770	0.364	0.071	0.655	–	0.177	2.16
$\lambda_{Nom} = 0.1$	-0.710	0.305	0.771	0.554	0.316	0.486	1.51
$\lambda_{Nom} = 0.2$	-0.597	0.212	0.188	0.938	0.447	0.407	1.34
$\lambda_{Nom} = 0.3$	-0.475	0.153	0.074	1.188	0.548	0.323	1.25

TABLE 5.1. Flow-type parameter and shear rate values at the stagnation points in the flow field around a stationary drop shape. The data for the stagnation point placed at the drop centroid are labeled with the *Int* subscript, data for the stagnation points in the suspending fluid are labeled with the *Ext* subscript, and r_{stp} is the ratio between the position of the stagnation point at the x-axis and the initial drop radius.

flow, drop rotation, and capillary relaxation are comparable. For an intermediate regime, the competing effects will generate an elongation and orientation of the droplet that will depend in time, and with an asymptotic behavior that may depend explicitly on the history of the flow field.

For a steady droplet form, determined mainly by the drop's rotation regime, the effects of the flow-type parameter of the external fluid are shown in Figs. 5.1 to 5.4. These Figures show the flow around a droplet for $Ca = 0.23$, $\lambda_{\mu} = 25$, and nominal flow-type parameter values of 0, 0.1, 0.2 and 0.3; the black lines are streamlines, the dots are stagnation points, and the colors show the magnitude of the velocity field; dark blue for the higher velocities, and dark red for more feeble speeds.. In this set of Figures, the internal flow field is a simple vortex with a flow-type parameter value λ_{Int} close to -1. Table 5.1 lists the maximum values of λ_{Int} for the corresponding TRMs characterized by a *nominal* external flow-type parameter λ_{Nom}. In fact, the value of λ_{Int} depends on the nominal external flow-type parameter λ_{Nom}, and may depend on $\dot{\gamma}_{Nom}$, the size of the droplet, as well as the asymmetry of the flow field when cylinders have different diameters. As can be observed in Fig. 5.1 at the position corresponding to the center of the flow field, λ_{Int} is very close to a value of -1 for the external simple shear flow with a value of $\lambda_{Nom} = 0$. The vortex has a nonzero rate of deformation, which can be evaluated by the eccentricity of the ellipses. As shown by the homogeneous hue of the inner fluid, mappings for λ_{Int} values are also quite even for all TRM geometries.

Two stagnation points exists around the drop when the droplet achieves its final

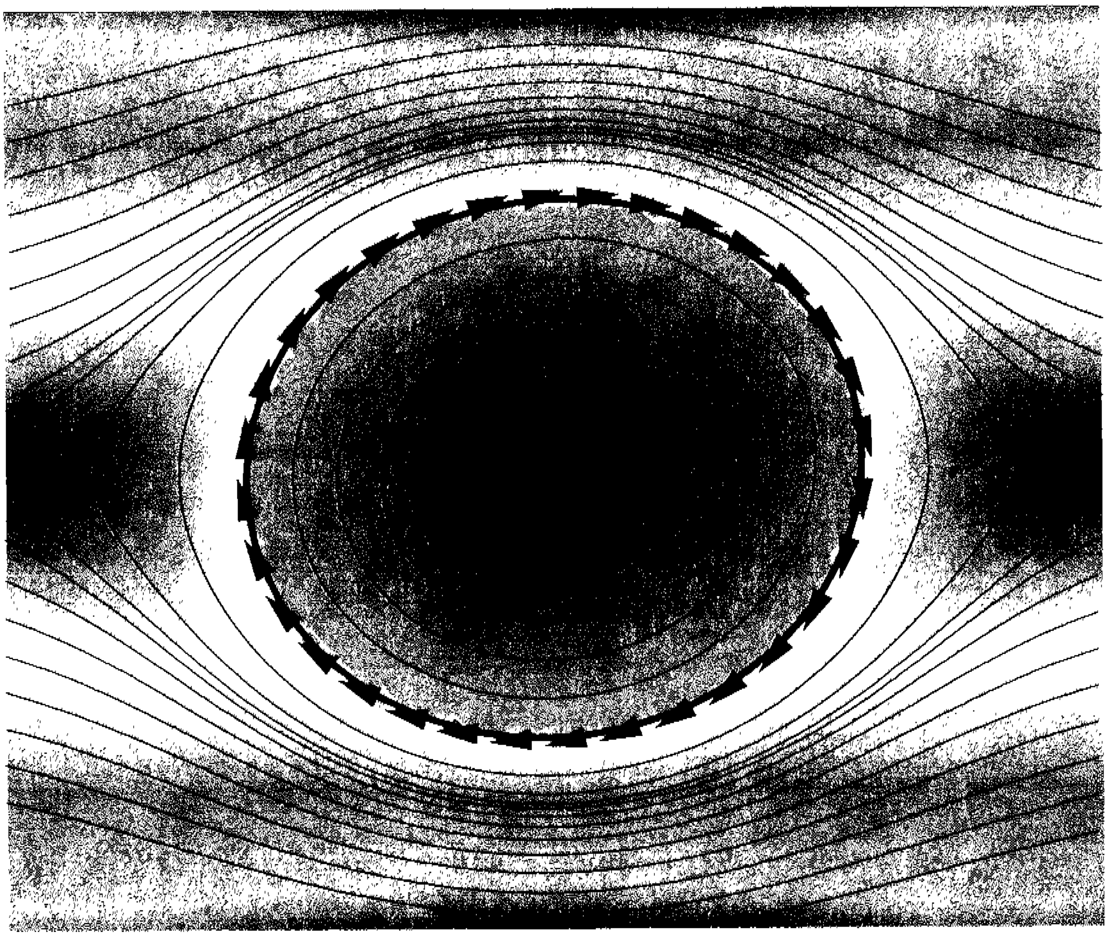

FIGURE 5.1. Flow around a droplet at steady flow conditions for simple shear flow ($\lambda_{Nom} = 0$), $Ca = 0.23$, $\lambda_{\mu} = 25.8$. The black lines are streamlines and the dot is the stagnation point. The close path of the streamlines inside the drop means that there is a vortex region in which the flow-type parameter is negative and close to -1.

stationary shape under steady external flow conditions, and the stabilizing mechanism is drop rotation due to the vorticity of the external flow. As shown in Fig. 5.1, to each side of the droplet, there are two regions –darker red– where values of $\lambda_{Ext} > \lambda_{Nom} = 0$. The arrows on the interface represent the tangential speeds, implying a droplet that rotates about its center, with the *nominal stagnation point region* -characterized with a positive value of λ- replaced now by an almost purely vortex region with very small deformation. This flow condition may have a significant implication for experimental studies: the stabilization and control of the drop's position in the external flow field is quite different from that prevalent when $\lambda_{Nom} > 0$ -the latter control scheme is presented in Chapter 3-. The control scheme presented in the Chapter 3 is based on the translation of the stagnation point of the unperturbed flow field, but the results obtained from the later simulations show that the problem of maintaining a drop at the stagnation point might be more complicated that previously considered. However, the experimental work of Bentley and Leal has shown that the basic assumption of a flow field not significantly affected by the presence of the drop is operationally correct, and is reasonable to assume that the same hypothesis applies for flow cells based on TRM devices. Despite the foreseen scenario, under flow field conditions very close to simple shear flow, the proposed control scheme for the drop position is possibly quite precarious, with a nonzero probability of migrating sideways that requires its position to be corrected at all times.

All calculated values shown in Table 5.1 correspond to nominal TRM flows with a shear rate at the stagnation point location of $\dot{\gamma}_{Nom} = 1$. The patterns for the flow fields listed in this Table are shown in Figs. 5.1-5.4. Two striking characteristics show up in this Table. First, the maximum value for λ_{Ext} at the external stagnation points can be significantly larger that λ_{Nom}. In particular, for $\lambda_{Nom} = 0.1$, $\lambda_{Ext} = 0.771$. This can be easily visualized from Fig. 5.2; the streamlines depicting the incoming and outgoing flow directions are quasi perpendicular to each other, implying almost pure irrotational kinematics.

The second striking characteristic of the modified flow field are the observed values of the shear rates. Because the inner fluid viscosity is 25 times higher than that of the external fluid in these simulations, then the prevalent values for the magnitude of the

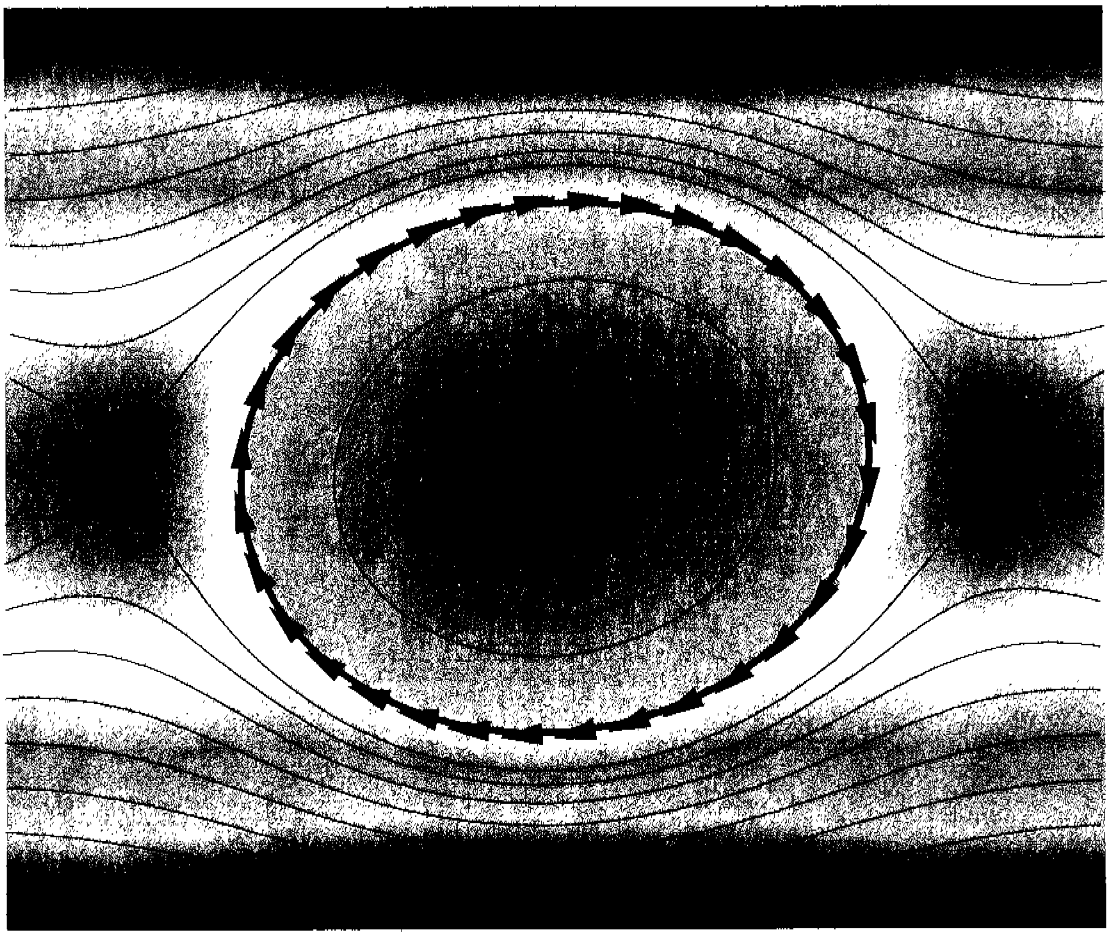

FIGURE 5.2. Flow around a droplet at steady flow conditions for $\lambda_{Nom} = 0.1$, $Ca = 0.23$, $\lambda_\mu = 25.8$. The black lines are streamlines and the dots are the stagnation points.

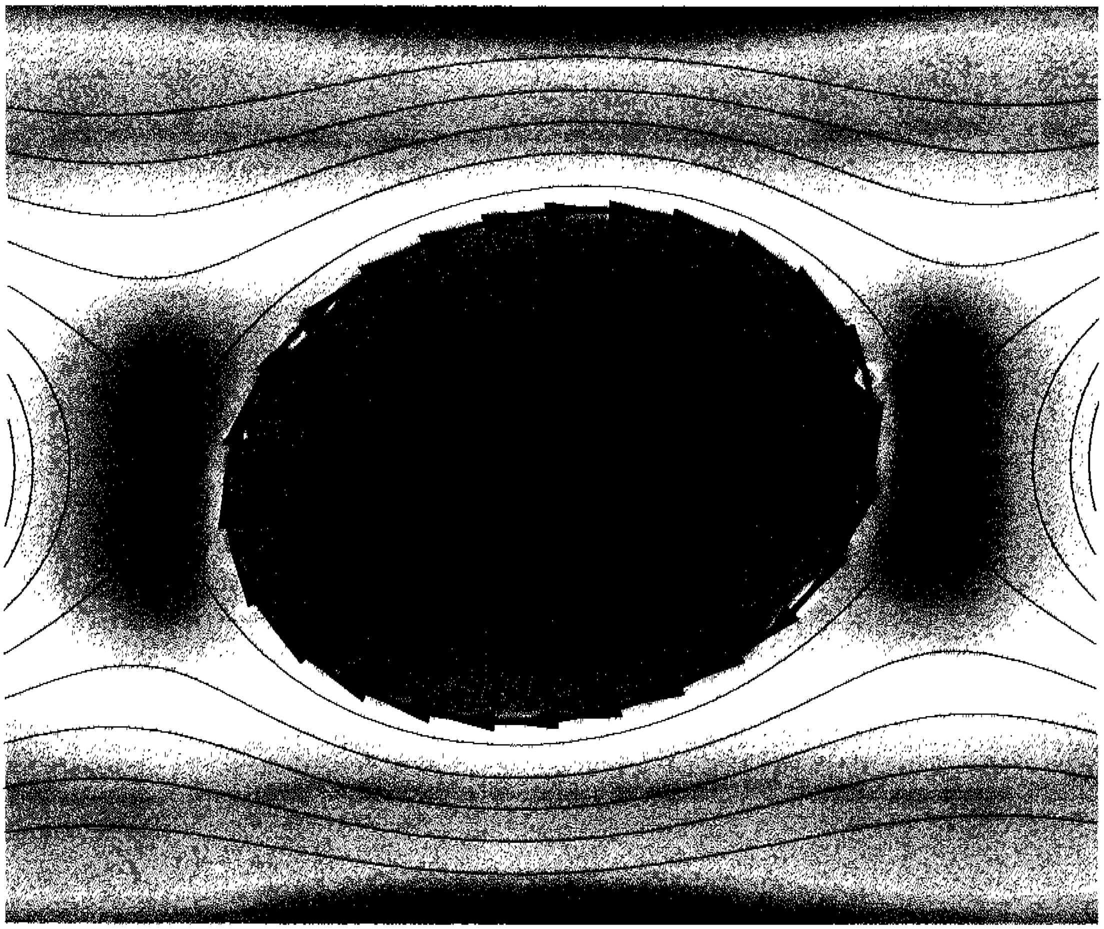

FIGURE 5.3. Flow around a droplet at steady flow conditions for $\lambda_{Nom} = 0.2$, $Ca = 0.23$, $\lambda_\mu = 25.8$. The black lines are streamlines and the dots are the stagnation points.

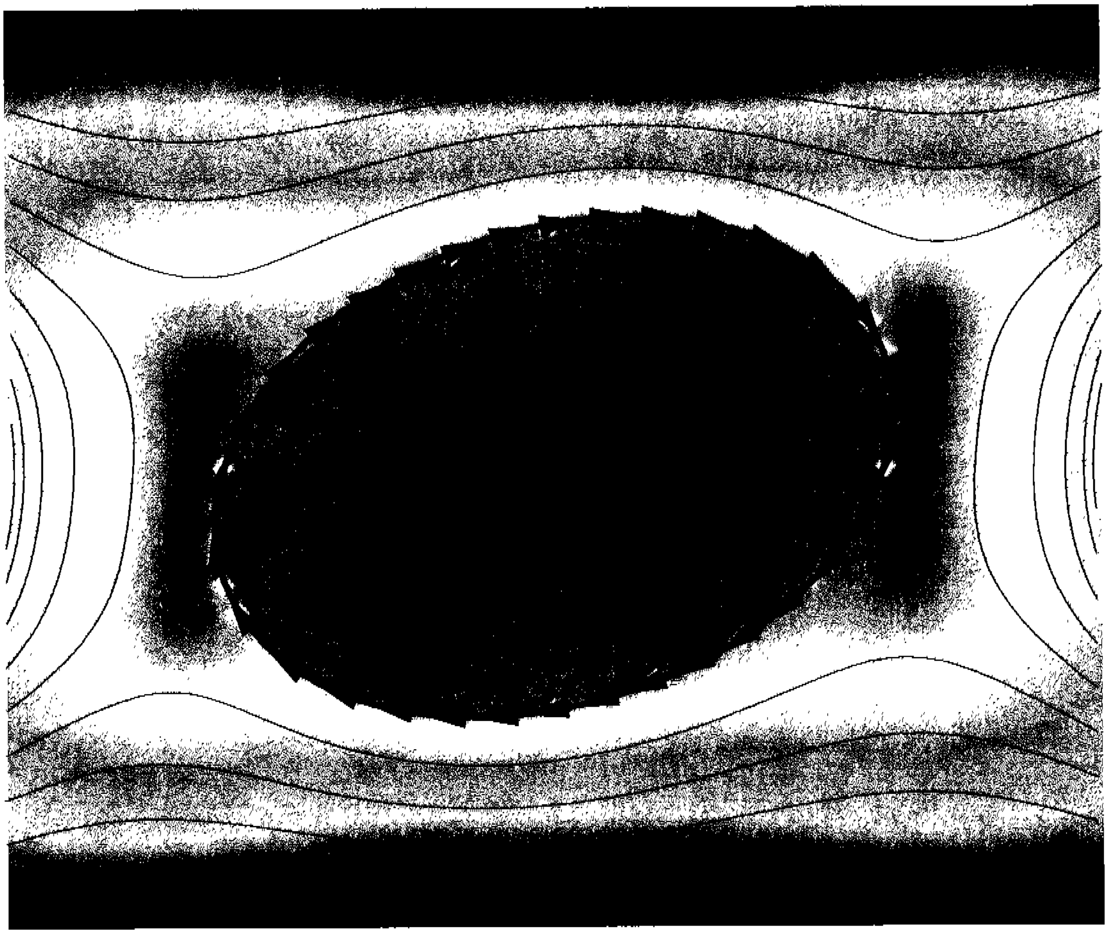

FIGURE 5.4. Flow around a droplet at steady flow conditions for $\lambda_{Nom} = 0.3$, $Ca = 0.23$, $\lambda_{\mu} = 25.8$. The black lines are streamlines and the dots are the stagnation points.

velocities inside the droplet should be significantly reduced; i. e., for a large inner flow with slow speeds, then $\dot{\gamma}_{Nom} > \dot{\gamma}_{Int}$ for all Two-Roll Mill geometries. However, for the larger values of λ_{Nom}, the reduction of the inner shear rate is most significant, possible due to the fact that a flow with a more elongational character allows for a weaker rate of rotation; hence, the deformed drop spins at a lower rate.

As can be observed in Fig. 5.4, the position of the external stagnation points is significantly closer to the surface of the droplet than, for example, that observed in Fig 5.2. In Table 5.1, r_{stp} corresponds to the ratio between the distance measured from the center of the flow field to the position of the stagnation point normalized by the drop's spherical radius. That is, the elongational character of the external flow, characterized by λ_{Nom}, pushes towards the droplet the external stagnation points; i. e., for the larger λ_{Nom} these results show that both stagnation points approach the surface of the drop at high values of $\dot{\gamma}_{Nom}$. Given that the steady flow equilibrium deformation of the droplet is dependent upon $\dot{\gamma}_{Nom}$, then r_{stp} will depend, besides of λ_{Nom}, on the initial drop volume and $\dot{\gamma}_{Nom}$. For larger values of λ_{Nom} the domain of the external elongational flow region increases in length (vertically) relative to the size of the droplet, and allows for a stagnation point to appear closer to the interface that is strongly influenced by the shearing flow on the boundary; thus, attaining a λ_{Ext} value closer to that of simple shear flow. For the flow field shown in Fig. 5.4 the external stagnation point is so close to the droplet interface (where a small but finite tangential velocity exists) that the values for the local shear rates $\dot{\gamma}_{Ext}$ can be actually greater than the nominal shear rate of 1 and shown in Table 5.1. This situation is perfectly reasonable if one evaluates the magnitude for the eigenvalues of the velocity gradient $\dot{\gamma}\sqrt{\lambda}$, which can be associated to the strength of the flow to induce a given rate of deformation [14, 75]. For the nominal flow field, $\dot{\gamma}\sqrt{\lambda}_{Nom}$ augments as the elongational character of the flow field becomes dominant. However, the predicted values for $\dot{\gamma}\sqrt{\lambda}_{Ext}$ are smaller than those of $\dot{\gamma}\sqrt{\lambda}_{Nom}$ for the external stagnation points. For the more elongational flow fields, the magnitude of the tangential velocities on the interface are also weaker as a result of closer external stagnation points; this conditions is consistent with the reduction of the shear rate for the internal fluid presented in Table 5.1.

Also, the region of the external stagnation points is closer to the interface but as well significantly more elongated than that observed at lower values of λ_{Nom}, as shown in Figs. 5.2 and 5.4. The maximum values for λ_{Ext} at the external stagnation points and the trend for the shape of these domains for higher λ_{Nom} flows imply that at sufficiently high nominal flow-type parameter –close to purely irrotational 2-D flows– each stagnation regions will develop two regions with maximum values of λ; a total of four points. Two are symmetrically placed very close to the drop surface near the elongated end of the droplet along each outflow axes , and the remaining two, along the incoming flow axes, more separated from the interface although at about the same distance from the center.

5.1.2 The transient flow history for a spheroidal drop in a strong flow

As a continuation of Taylor's work, Grace [38] and Mason and collaborators [76] carried out a series of experiments studying the time evolutions of the drop deformation that is induced by simple shear flows. Subsequently, Rallison presented results for a theoretical model based on small deformation of drops that qualitatively agrees with those earlier experiments [41]. In this work, the numerical predictions are compared with these earlier works for simple shear flows. But the results include as well a full set of elongational flows with vorticity which can be generated with Two-Roll Mills.

In the following Figures, emphasis is given to the time evolution for the parameters that characterized the induced deformation and orientation of a drop. The deformation parameter D_T (Eq. 4.14) and the orientation angle ϕ are used. The orientation angle of the drop, ϕ, is the angle between the longest axis of the drop and the x–axis (Torza et al. [76], measured ϕ with respect to the major principal axis of the deformation rate tensor, which for the Two-Roll Mill geometry, is always at 45 ° from the x–axis).

Before we continue with a discussion of the main characteristics of the drop shape induced by flow, it is perhaps necessary to provide a cautionary note about the limitation of the numerical method used to generate these results. When implementing BEM techniques to describe the transient dynamics of drops great care must be exercised, because numerical errors may increase causing a failure in the simulation. Two sources of errors have been detected that influence the results presented here. Firstly, spurious results are obtained easily during the interface interpolation step of the numerical method as a result of undulations on the interpolated interface. In this case, the numerical method that provides the most satisfactory interface description and that is used for these simulations is Akima's method [72, 73]. This method attempts to provide a smoother interface with a "natural" appearance; as if the form of the surface has been done by hand. Secondly, as will be apparent in the following Figures, when the shear rate value is high, then the parameters plotted show a significant level of numerical noise during the evolution of the drop. This condition is especially noticeable for Graphs of the orientation angle ϕ, and is most significant for the highest absolute values of the orientation angle. Under high shear rate conditions the duration of the time step for the evolution of the interface must be established as a function of the shear rate value in order to have accurate results. In particular, such noise is quite noticeable in curves of Fig. 5.5b which is discussed subsequently. Hence, the solution of this numerical problem requires a time dependent size for the time-step. One way to minimize this adverse effect is to use an adaptive step-size that decreases to a small enough value for those periods of the drop evolution so as to achieve the desire level of accuracy, and that increases again when a stable evolution of the drop is prevalent.

Figure 5.6 shows the deformation parameter D_T vs. the orientation angle ϕ for the cases shown in Fig. 5.5. Here all D_T vs. ϕ traces –corresponding the different shear rates– collapse onto each other except for the trace with the highest level of numerical noise. But even for this latter trace, the time evolution continues qualitatively on the same path as the rest. It is also obvious, that for the present fluids and this flow field, the number of cycles before a stationary deformation and orientation are reached is large and will not depend on $\dot{\gamma}_{Nom}$.

Mason and collaborators [76] carried out many experiments to study the time evolution of the deformation of drops in simple shear flows: Years later Rallison presented a detailed model for analytical predictions of the evolution of a drop deformation. This theoretical model is based on an expansion valid for small deformations of drops. Although Mason and collaborators [76] and Rallison [41] address mainly simple shear flows, those published results are good benchmarks for this numerical work. In general, all agree qualitatively and the time evolution for the shape and orientation with $\dot{\gamma}$ for the three kinds of experiments is similar to those in Fig. 5.5. The points of agreement as well as the

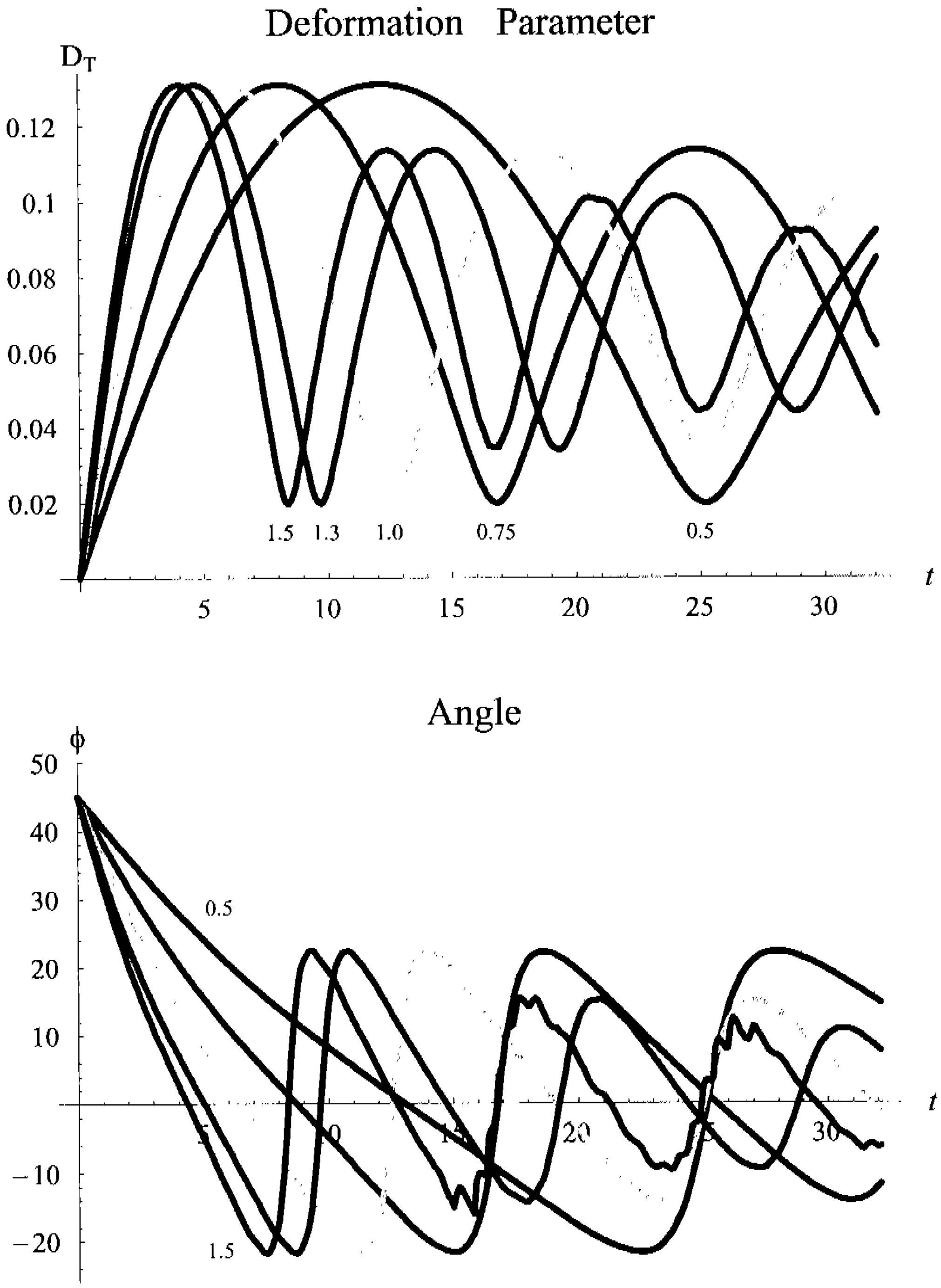

FIGURE 5.5. Deformation parameter D_T and orientation ϕ curves for $Ca = 1.5$ and $\lambda_\mu = 25$ for simple shear flow and different values of the shear rate. The black curves correspond to $\dot{\gamma} = 0.50$; red to $\dot{\gamma} = 0.75$; cyan to $\dot{\gamma} = 1.00$; blue to $\dot{\gamma} = 1.30$; and purple to $\dot{\gamma} = 1.50$.

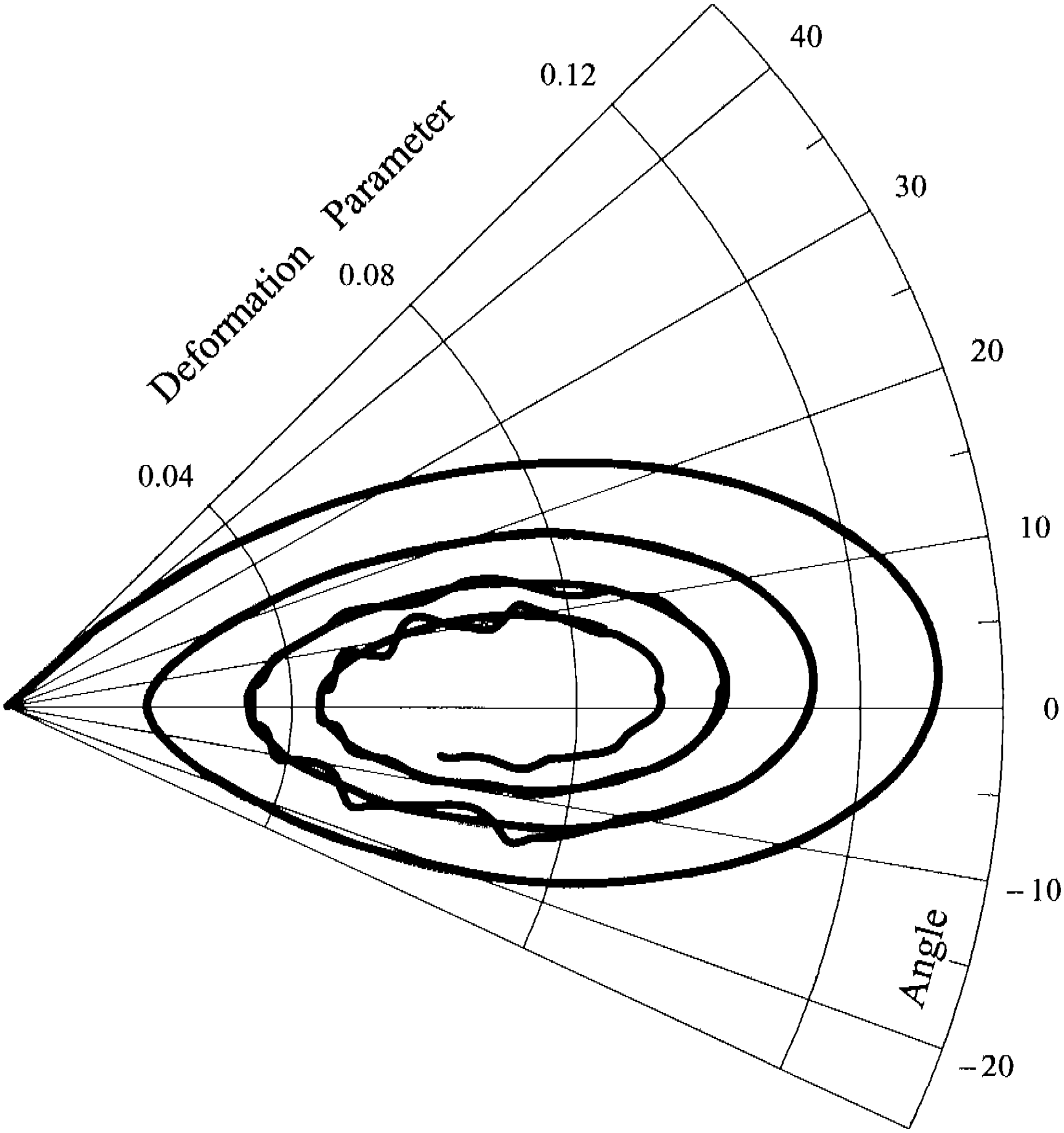

FIGURE 5.6. Polar plot of Deformation Parameter D_T vs. Orientation Angle ϕ for $Ca = 1.5$ and $\lambda_\mu = 25$ for simple shear flow and different values of the shear rate. The black curves correspond to $\dot{\gamma} = 0.50$; red to $\dot{\gamma} = 0.75$; cyan to $\dot{\gamma} = 1.00$; blue to $\dot{\gamma} = 1.30$; and purple to $\dot{\gamma} = 1.50$.

general trends predicted are now presented.

Figure 5.5 shows the time-dependent evolution of the Taylor's deformation parameter and the orientation of a drop ϕ –for the Capillary number $Ca = a\dot{\gamma}\,\mu_1/\gamma = 1.5$ and $\lambda_\mu = 25$– subjected to simple shear flow and considering different values of the shear rate $\dot{\gamma}$. For all cases the surface tension value is adjusted to set always the Capillary number to the value of 1.5. The general results predicted numerically agree well with the weakest of the strong flows as well as with the irrotational flow conditions studied by Leal and collaborators [12, 44]. In particular, elongated drops can spin about its centroid several times before a stationary condition is reached; that is, the orientation of the droplet undershooting significantly below the outflow axis, $\phi < 0$. It is also a general trend that the amplitude of the deformation parameter at each cycle does not seems to depend strongly on $\dot{\gamma}_{Nom}$. As well, the time spend during rotation with decreasing negative angles for the principal axis of the drop is significantly longer that the time required by the drop to return the principal axis orientation to a positive angle, as can be observed for all curves of Fig. 5.5b. Finally, as observed by Grace [38] and predicted by Rallison [41], the time evolution of the deformation parameter decays slowly to a steady state deformation. However, the relaxation rate predicted by these simulations appears significantly faster than that observed by Mason [76] or theoretically predicted by Rallison [41].

Now the effects due to the elongational character of the external flow are analyzed. Mainly, the deformation of a drop that is initially spherical, and suddenly the external flow is started with a constant shear rate. This time-dependent evolution of D_T and ϕ is evaluated as a result of different values of λ and Ca. The selected flow-type parameter values are those that can be generated with a Two-Roll Mills (that is, simple shear rate: $\lambda = 0$; $\lambda = 0.03$; $\lambda = 0.10$, $\lambda = 0.15$; $\lambda = 0.20$ and $\lambda = 0.30$). These selected values will be used in the near future in this laboratory and the predicted behavior is shown in Figures 5.7, 5.9, 5.11 and 5.13. The simulated Capillary numbers are 0.23, 0.5, 1 and 2, respectively. In all these cases, the viscosity ratio is $\lambda_\mu = 25.8$.

The general trend for the time dependent shape of drops is characterized by an initial deformation that starts from the spherical shape –a zero value for the deformation parameter–, with a limiting orientation aligned with the principal axis of deformation at

$\phi = +45^\circ$ with respect to the $x-$axis. With larger values of $\dot{\gamma}_{Nom}$ and λ_{Nom}, the drop shape becomes more elongated in time and become more aligned to the outflow axis.

Following Cox's polar plots [40], in Figures 5.8, 5.10, 5.12 and 5.14 the deformation parameter D_T vs. the orientation angle ϕ for the same cases are shown. This parametric time evolution shows clearly the deformation and orientation of a drop at its final stationary state, or when the deformation history occurs above a *critical value* of the Capillary number with breakup of the drop expected. As the Capillary number increases, the oscillatory behavior described by Rallison becomes more noticeable for all weak elongational flows. In particular, such situation becomes dominant for Capillary numbers greater than 0.5. For those cases that attain a stationary finite deformation under an external flow field, the final state may require more than one cycle in these plots. After a few cycles, all oscillatory deformations tend to the steady elongation of the drop D_T^{SS}, which is characterized with a positive value for the orientation. A more elongated form and a higher orientation angle should occur with higher values of λ_{Nom}. The amplitude of oscillations measured in terms of the deformation parameter or the orientation of the principal axis are significantly larger even when normalized by their stationary values. A departure from the described behavior is observed in all cases dominated by break up conditions; now drops evolve as if progressing towards a stationary deformation but before a half cycle is completed it will align back towards the principal axis of the rate of deformation and increase unconstrained its deformation thereafter.

At small Capillary number $Ca = 0.23$, Figs. 5.7 and 5.8 present the deformation and orientation of a drop. For start up of flow conditions, a rather fast evolution towards the stationary deformation is predicted. Only a weak oscillatory behavior is clearly observed for flows with $\lambda_{Nom} \leq 0.15$. Otherwise, the drop dynamics shows a monotonic evolution towards the stationary deformation that varies from $D_T = 0.065$ –for simple shear flow– to about 0.19 for the more elongational flow field; see Fig. 5.8. For all cases, rotation of the principal axis of the drop is weak, approaching the outflow axis but never crossing towards negative values for ϕ. Accordingly, a critical value for the stable deformation of a drop $D_{T,Max} \lesssim 0.2$ is shown to exist for all flow conditions.

At a Capillary number of $Ca = 0.5$ –see Fig. 5.9– a significant transition in

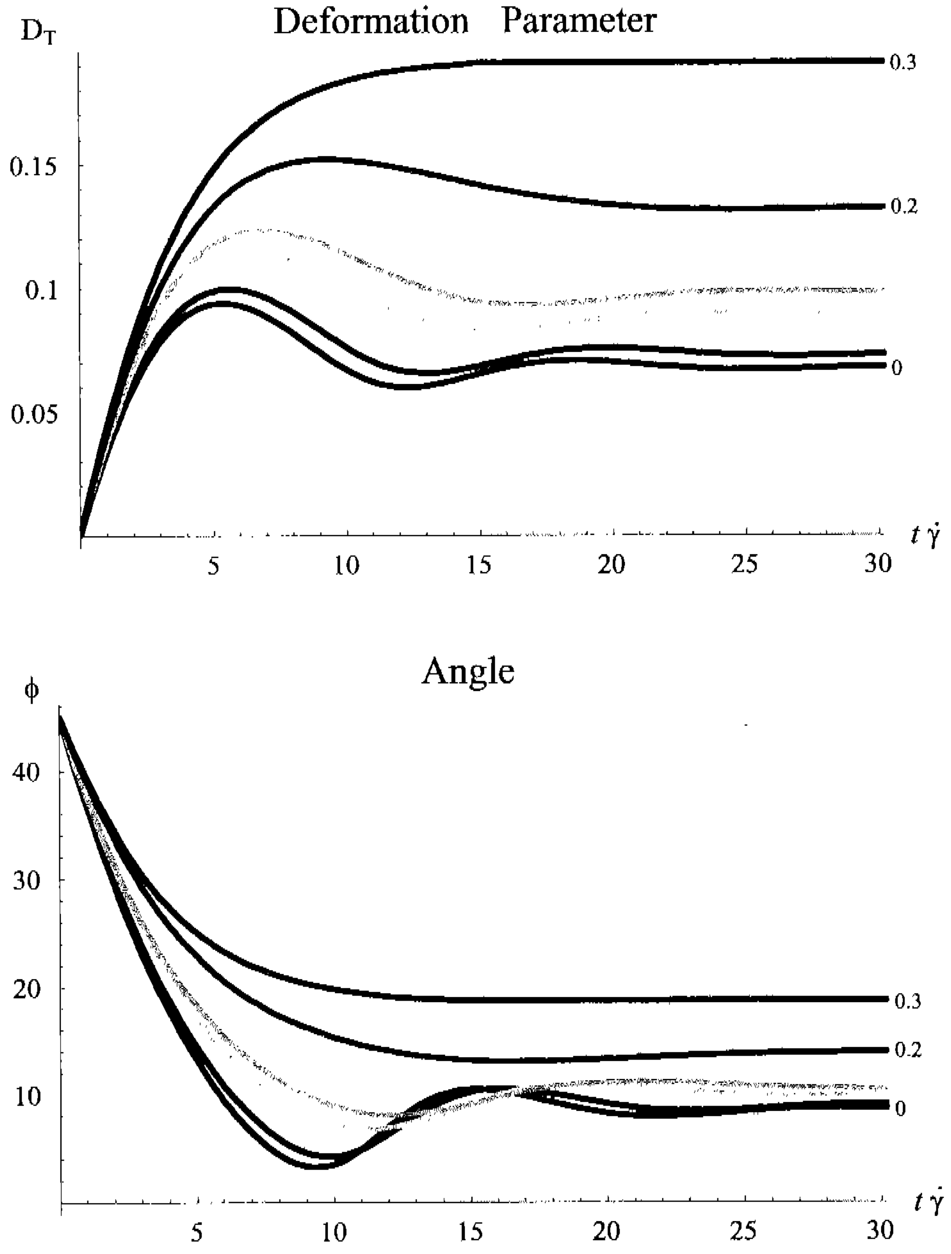

FIGURE 5.7. Deformation parameter D_T and orientation ϕ curves for $Ca = 0.23$, $\lambda_\mu = 25.8$, for several flow-type parameter values. The black curves correspond to simple shear flow, $\lambda = 0$; red to $\lambda = 0.03$; cyan to $\lambda = 0.1$; green to $\lambda = 0.15$; blue to $\lambda = 0.2$; and purple to $\lambda = 0.3$. At small Ca the drops rapidly reach a stationary shape that is more elongated for flows with less vorticity. The alignment attains a steady orientation with $\phi > 0$ for all values of the flow-type parameter.

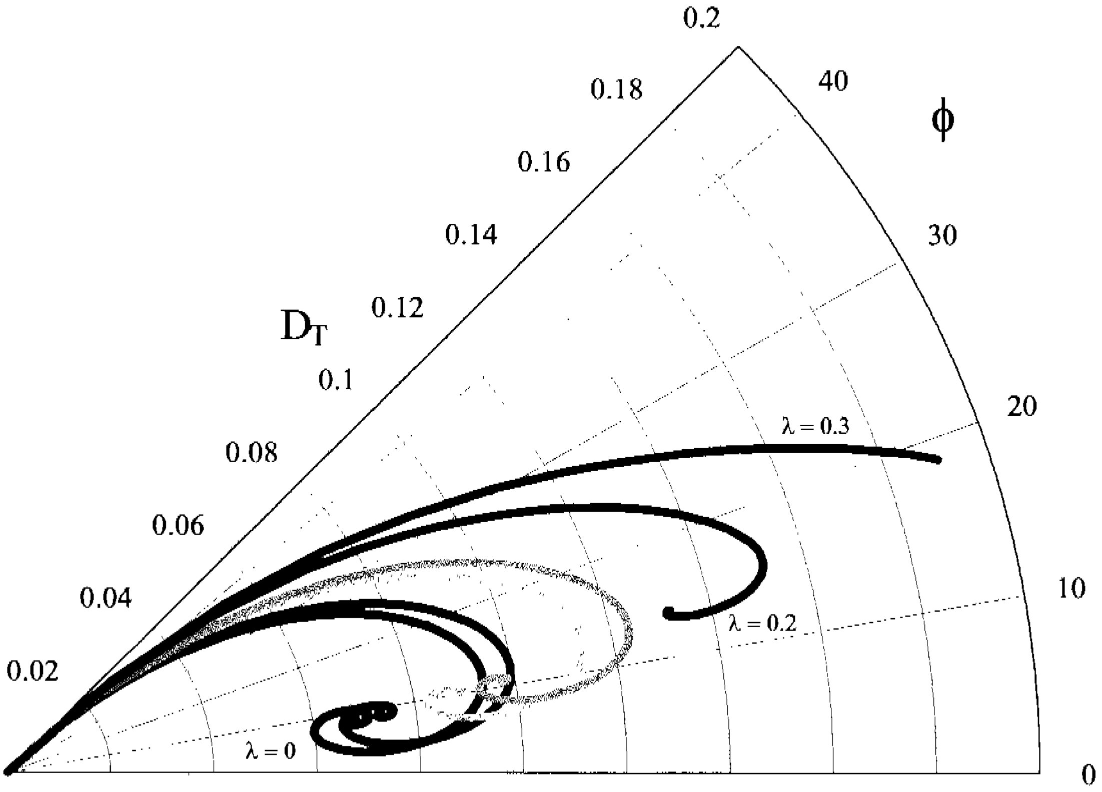

FIGURE 5.8. Polar plot of deformation parameter D_T vs. orientation angle ϕ for $Ca = 0.23$, $\lambda_\mu = 25.8$ and several flow-type parameter values. Curve nomenclature is the same as show in Fig. 5.7. The orientation angle ϕ_{SS} remains near 10 ° up to $\lambda_{Nom} \leq 0.1$. For $\lambda_{Nom} > 0.2$ the flow history becomes different, but still reaches a final stationary shape.

response of the drop deformation occurs that can be observed for $\lambda_{Nom} > 0.2$. Here drops do not seem to attain a stationary deformation. Thus, a critical Capillary number appears predicting the break up of drops for $\lambda_{Nom} > 0.2$, and a finite elongation at long times for $\lambda_{Nom} \leq 0.2$. For these simulations, whether the drops orientation ϕ undershoots below the outflow axis depends on the elongational character of the external flow. For $\lambda_{Nom} \geq 0.2$ the drops orientation is always positive, and eventually a burst of the drop will occur. The number of cycles required to attain the long term stationary deformation also appears to depend on Ca. Indeed, for a Capillary number greater than 0.5, more than 2.5 cycles may be required to attain a stationary deformation. Up to $Ca = 0.5$, the stationary deformation D_T^{SS} appears to be limited to values less than 0.2. Certainly, a general trend is predicted: for all flow fields characterized with a Capillary number of $Ca \geq 0.5$ and up to a critical value of $\lambda_{C,Nom}$ drops will present its principal axis with an orientation that undershoots significantly the $x-$axis. It is only the most elongational flow fields that at sufficiently large Capillary numbers will align drops mainly towards the principal eigenvector of the rate of deformation tensor: i. e., the outflow axis.

These results show that in flows where vorticity is small, as $\lambda > 0.1$, the drop deforms monotonically to the final stationary shape, and the deformation becomes large after a finite time. If the vorticity is significant, then an oscillatory deformation takes place in the drop shape that is damped by surface tension. As far as we are aware, the transition from the damped periodic oscillatory behavior to a monotonically deformation behavior has not been reported; therefore, the Two-Roll Mill is an excellent device to study experimentally this transition, because the flow-type parameter range accessible to this device matches the "transition interval", that the simple shear flow cells and the four-roll mill do not reach in a systematic manner.

For Capillary numbers larger than 1, the oscillatory behavior predicted by models of slightly deformed drops becomes dominant such as those shown in Figs. 5.11–5.14. In particular, the amplitude of those oscillations increases with the drop spinning many cycles before the final stationary state is reached. As well, large negative values of the orientation angle are attained, and these values are largest for flows with the larger vorticities, and increase with Ca. However, the damping rate for oscillations seems to have a rather

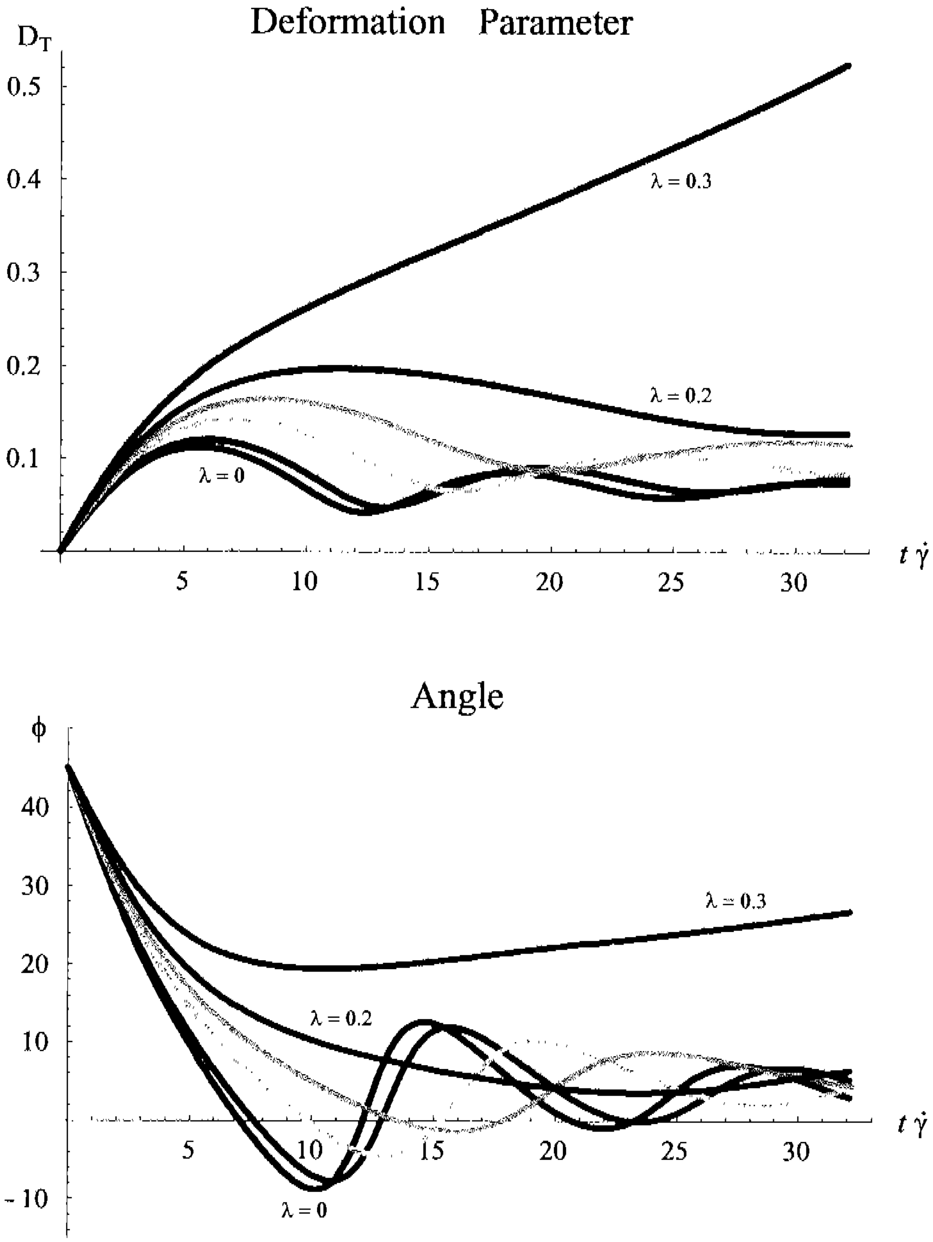

FIGURE 5.9. Time dependent deformation parameter D_T and orientation ϕ curves for $Ca = 0.5$, $\lambda_\mu = 25.8$, for several flow-type parameter values. For $\lambda \geq 0.3$, the deformation of the drop increases unbounded in time; its orientation becomes just slightly less than that corresponding to the principal axis of the rate of deformation tensor, for this case, $Ca > Ca_c$. Black curves correspond to simple shear flow, $\lambda = 0$; red to $\lambda = 0.03$; cyan to $\lambda = 0.1$; green to $\lambda = 0.15$; blue to $\lambda = 0.2$; and purple to $\lambda = 0.3$.

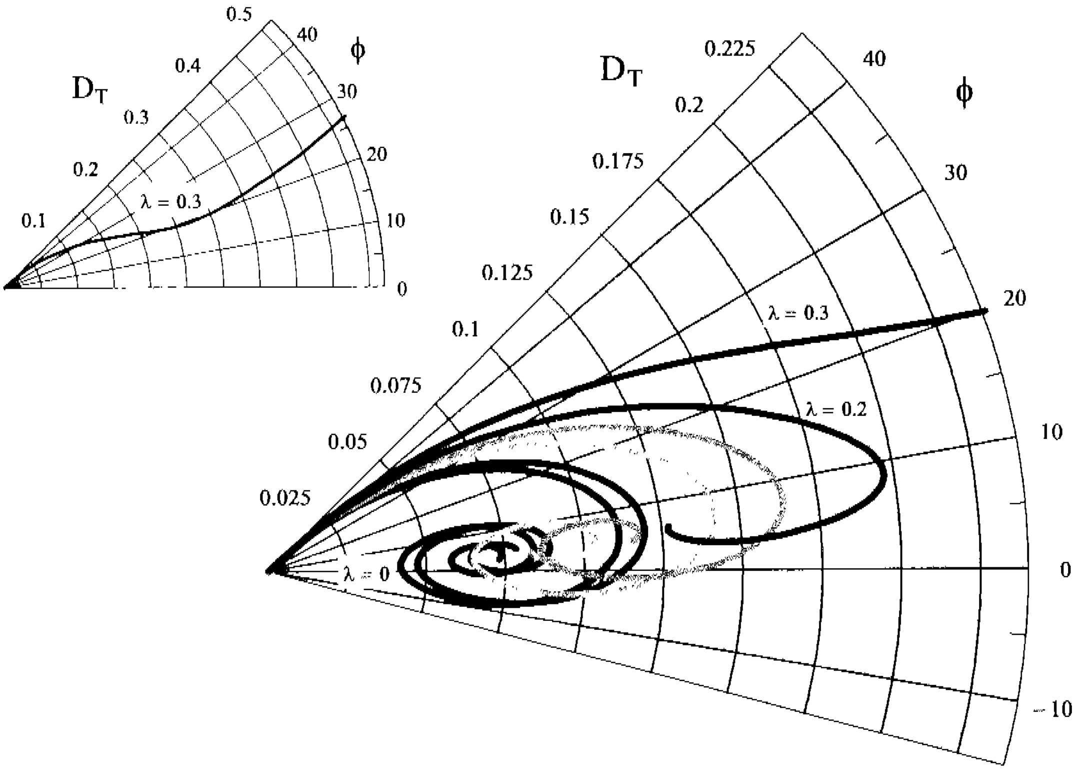

FIGURE 5.10. Polar plot of deformation parameter D_T vs. orientation angle ϕ for $Ca = 0.5$, $\lambda_\mu = 25.8$ and several flow-type parameter values. For the most elongational flow, $Ca > Ca_c$. Color code as the previous Figures. A stationary shape exists with a deformation history that presents at least a full cycle (for $\lambda_{Norm} \leq 0.2$).

constant value, at least for strong flows with significant vorticity.

For Capillary numbers closer to 1, the restoring force on the surface is reduced. For these cases one expects that non-stationary deformation of drops may occur, or that bursts of a drop are attained, etc. These results show the same qualitative behavior for simple shear flow as theoretically and experimentally observed; see Rallison [41]. There are some discrepancies between the results for small deformation of Rallison and those presented here, the latter being not limited to a second order approximation of the deformation of the drop as it is the case of the former. However, these results show that the numerical characteristic time-scale is about twice as long as that showed by Rallison [41]

The algorithms used are very sensitive to the step time, as can be observed in the noise of the curves of Figs. 5.13 and 5.14; therefore, a careful selection of this parameter is needed for accurate simulations. In should be pointed out that the numerical noise is especially noticeable in Cox plots, but it can not be associated to the magnitude of the velocity gradient, for traces for several values of $\dot{\gamma}_{Nom}$ coincide onto one. It appears that the noisy behavior is more prevalent when the drop is approaching its maximum or minimum orientation, with the rate de elongation changing at the fastest pace. That is, it appears that noise is significant when the stresses due to flow kinematics and those of surface tension work in phase to reduce the drop elongation in the second and fourth quadrants of the (x, y) = (flow direction, gradient of flow) plane such as that shown in Fig. 5.5. A possible solution to this problem is the use of an adaptive step-size control, that decreases the time step to a small enough value so as to achieve a desired level of accuracy; and that it increases again when times of numerical instability have passed.

However, the onset of the instability has not been established, and a second possible source for the observed noise may be the fact that under the prescribe flow conditions, the drop position is intrinsically unstable and the drop centroid may accumulate a sufficiently large offset from the center of the flow field –located at $(x, y) = (0, 0)$– that a steady drift can be predicted. The numerical algorithms presented here make extensive use of the symmetry properties of the drop shape and the flow field with the purpose of reducing the computational time for each experiment. If the centroid drifts significantly, the current version of the algorithm appears not to be sufficiently robust. However, the present un-

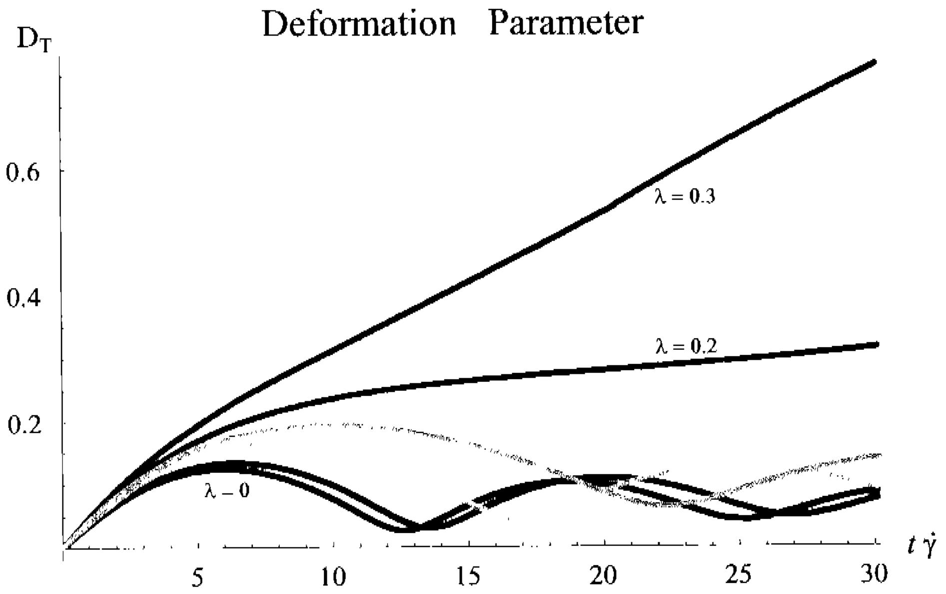

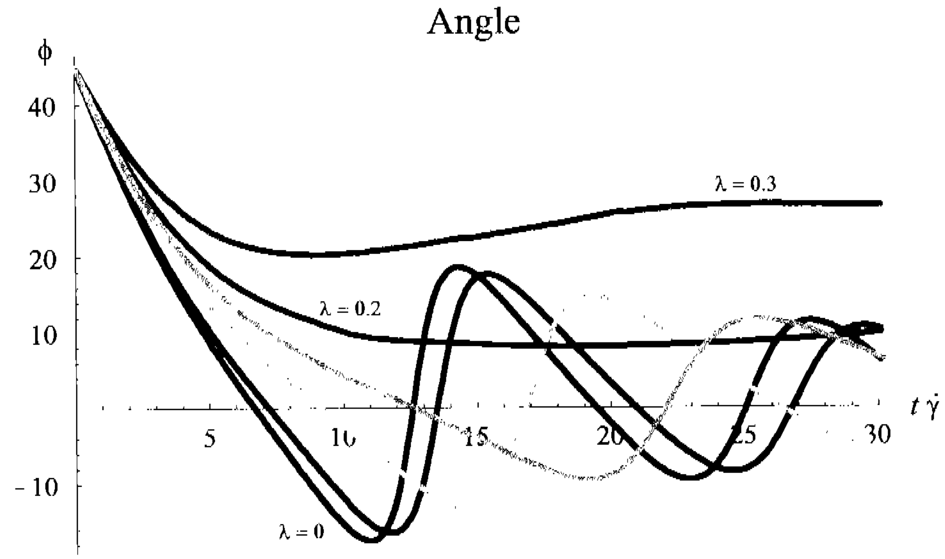

FIGURE 5.11. Time dependent deformation parameter D_T and orientation angle ϕ curves for $Ca = 1$ and same viscosity ratio as before. For flows with $\lambda \gtrsim 0.2$, the drop deformation is unbounded: $Ca > Ca_c$. Even for $\lambda \simeq 0.15$, the deformation attained is very close to the maximum value predicting a stationary shape. The color code used for the several flow-type parameter values is the same as in previous Figures.

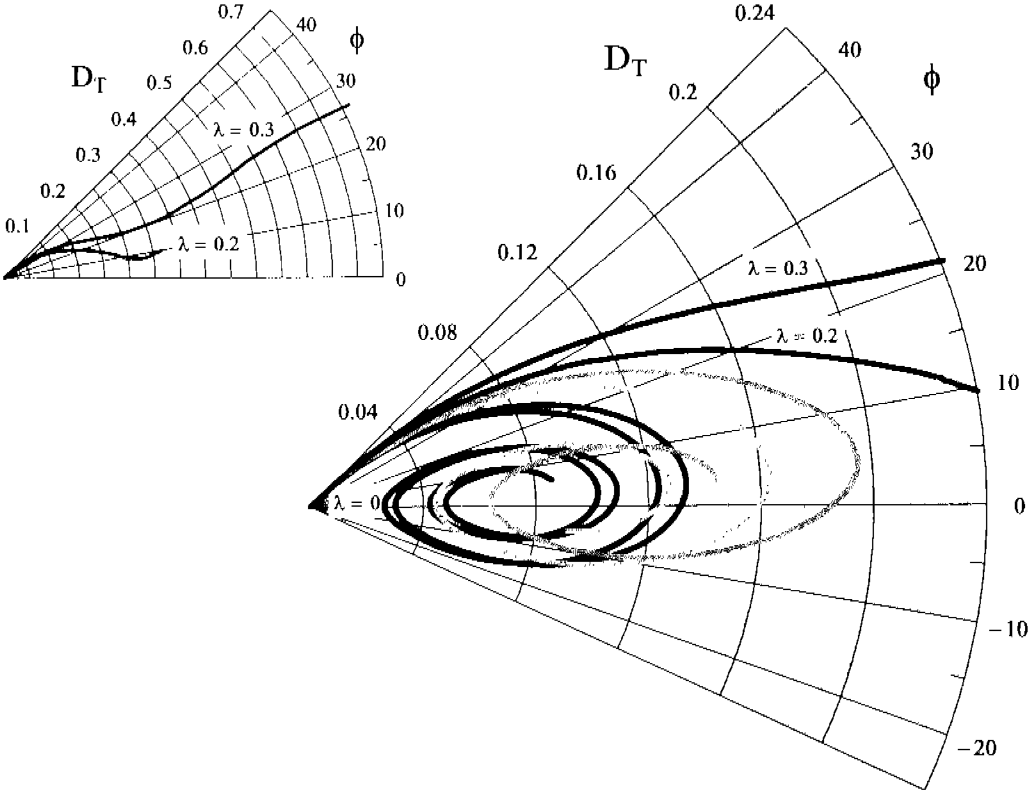

FIGURE 5.12. Polar plot of deformation parameter D_T vs. orientation angle ϕ for $Ca = 1$, $\lambda_\mu = 25.8$ and several flow-type parameter values. Left side insert shows the polar plots for long times, with break up of drops predicted for $\lambda \geq 0.2$. The color code used for the several flow-type parameter values is the same as in previous Figures.

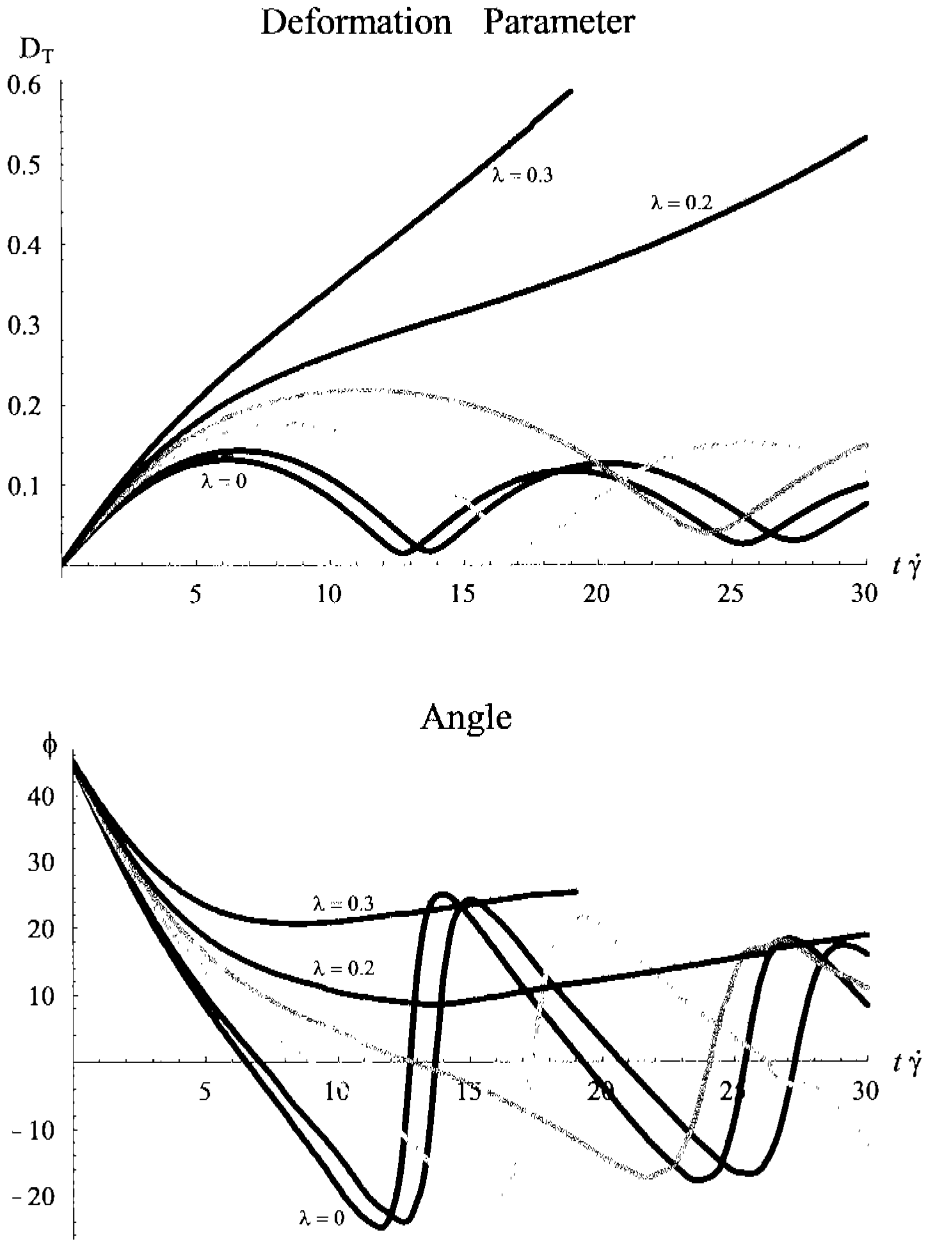

FIGURE 5.13. Time dependent deformation parameter D_T and orientation angle ϕ curves for several flow-type parameter values. Highest Capillary number simulated: $Ca = 2$; and same viscosity ratio. For flows with $\lambda \gtrsim 0.15$ the drop deformation increases unbounded. Even for $\lambda \simeq 0.15$ the deformation attained during the first cycle is very close to the maximum critical value of 0.22 for stationary deformations. The color code used for the several flow-type parameter values is the same as in previous Figures.

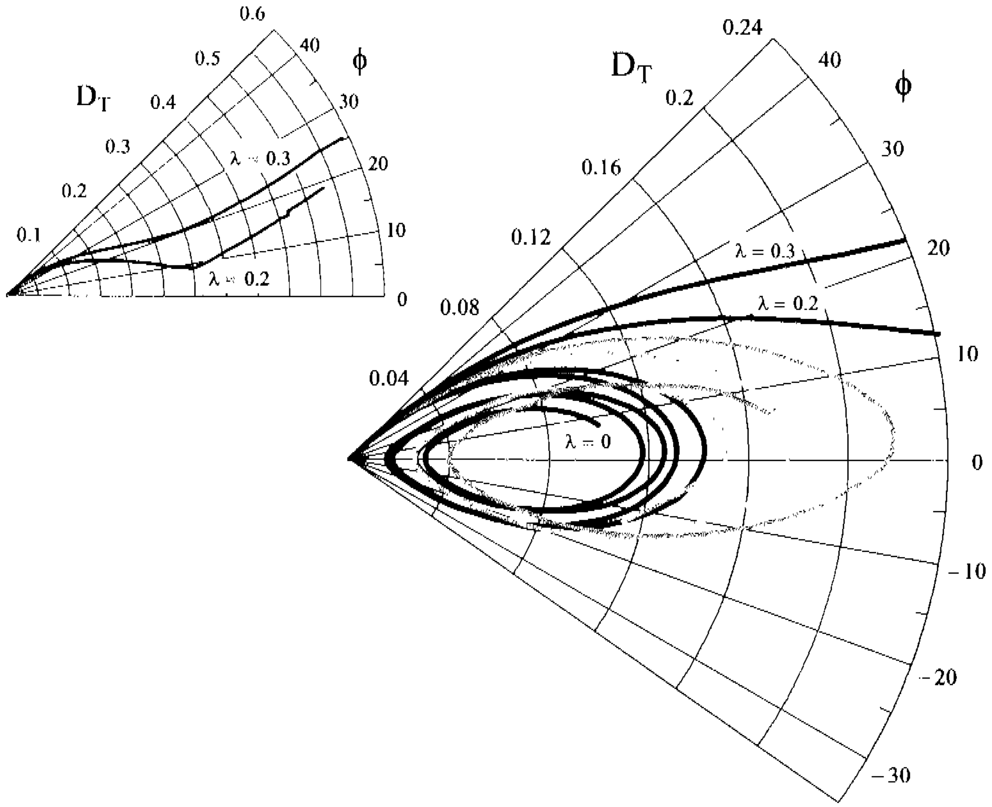

FIGURE 5.14. Polar plot of deformation parameter D_T vs. orientation angle ϕ for several flow-type parameter values; $Ca = 2$ and $\lambda_\mu = 25.8$. A higher value for Ca appears to stabilize the oscillatory behavior to a slightly greater value of λ. A drop immersed in a flow with $\lambda = 0.2$ is clearly aligned with the outflow axis at long times as shown in the left side insert. The color code used for the several flow-type parameter values is the same as in previous Figures.

derstanding of these simulations does not allow us to determine specifically the source of such noise; in fact the main source of noise may be another than those mentioned earlier. Currently, it is under investigation and should be addressed in a future publication.

Figure 5.15 shows the time evolution of the magnitude of the dimensionless velocity field and the streamlines for a drop subjected to flow conditions of $Ca = 0.5$, $\lambda_\mu = 25$, and $\lambda_{Nom} = 0.3$. Under these conditions the drop eventually breaks, because the Capillary number is above the critical value. The streamlines in each graph show how the flow field changes inside the drop as well as the driving external elongational flow. However, this graph deserves a note of caution: for $t > 28\,\mathrm{s}$, the streamlines do not depict with sufficiently high resolution the patterns of the flow field in those regions close to the interface; these artifacts are essentially the results of the numerical grids.

During the initial stages, the drop rotates and deforms and the flow inside the drop is a vortex. With time, the rotation ceases and the flow inside the drop changes to one that resembles simple shear flow. Then, the flow inside the drop continues evolving until developing into a strong flow type, characterized with positive values for the local λ's, alike that observed for the external flow. After this instant, the drop increases its deformation monotonically until its eventual breakup.

At $t\dot{\gamma} = 1$ in Fig. 5.15, the flow field presents clearly the incoming and outgoing flow axes, with two extensional dominated flow regions located to the right and left of the drop. These regions evolve in time to the point that each original stagnation point, characterized with positive values of λ_{Ext}, splits into two stagnation points, the latter approaching the drop interface later in time. Two of the new stagnation points are easily visible along the incoming flow direction, and the other two are located near the ends of the drop, in the region of the outflow axis.

The tangential velocities at the interface are highest for the initial part of the deformation, with the end-regions having also the highest accelerations. For later times, at about $t\dot{\gamma} = 34$, tangential velocities on the interface region between the nearest pair of stagnation points decrease significantly, and may actually change direction. After this point, the drop reduces (by pure compression) its volume in the central section while simultaneously having a purely elongational deformation for the external 2/3 of the drop's volume.

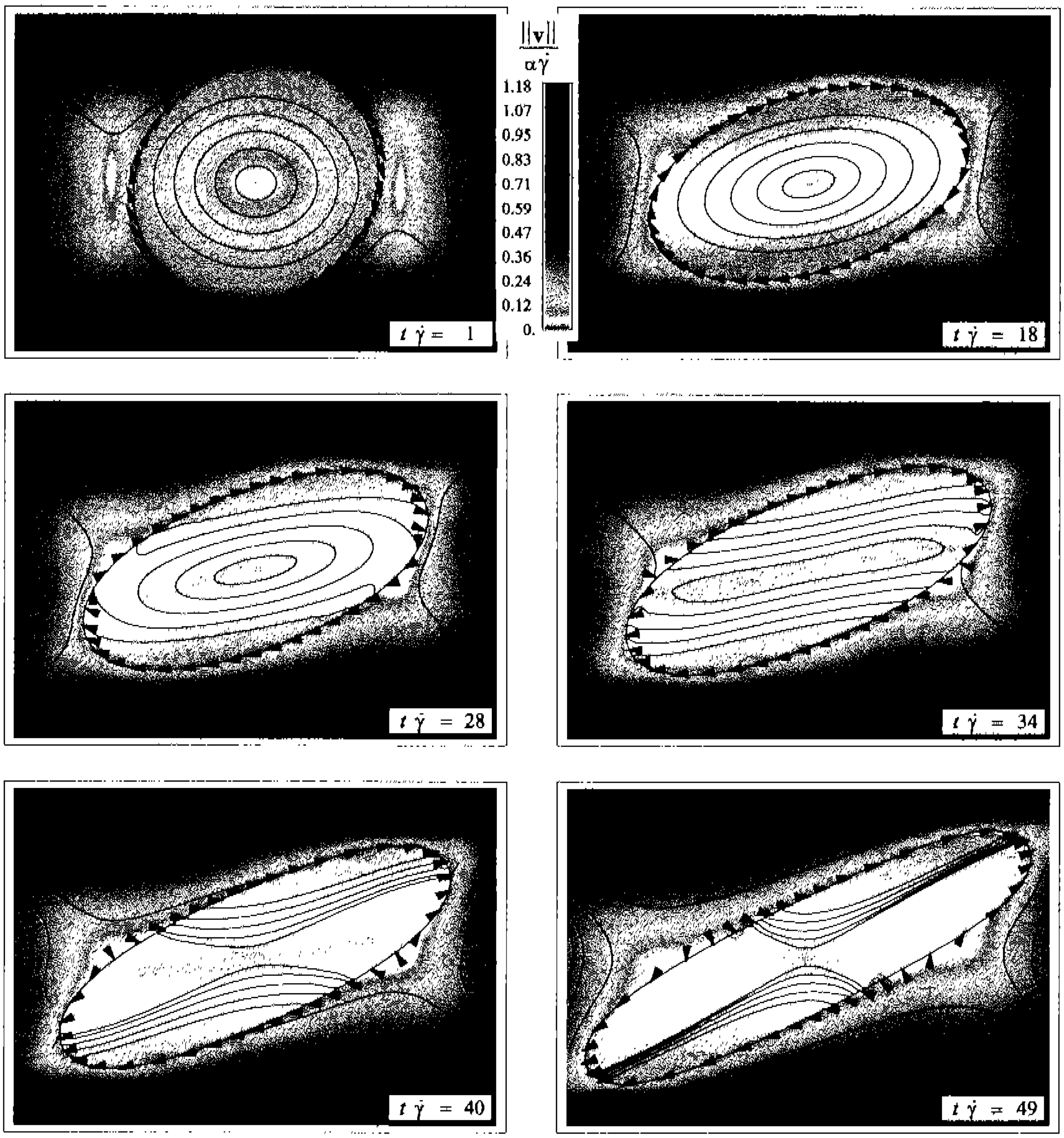

FIGURE 5.15. Magnitude of dimensionless velocity field for different dimensionless times, for $Ca = 0.5$, $\lambda_\mu = 25$, and $\lambda_{Nom} = 0.3$. At these conditions, the drop do not reach a stationary shape form, and this eventually breaks.

In general after this instant, all velocities are significantly weaker than those characteristic of the more spherical drop. Also, the flow field evolution changes quite drastically at about the same time, with the central vortex having now a significant elongation; subsequently at about $t\dot{\gamma} = 40$ the internal flow field shows a value for the flow-type parameter at the center that is no longer a vortex but clearly a strong flow with a complex flow pattern.

Figure 5.16 presents the experimental and theoretical works previously reported by Torza *et al.* [76] and Rallison [41]. All traces are high resolution digital scanning of Figure 1 in [41]. As can be observed in the polar plots, both theoretical as well as the experimental parametric path are significantly distorted in comparison with the numerical results previously presented. Hence, it is reasonable to say that only in a *qualitative manner* the results of simulations presented here match the theoretical approximate solution of Rallison and the experimental work by Torza *et al.* However, from a *quantitative point of view* it is possible to address several discrepancies, some of which have already been noticed. But it is now clear that the experimental polar trace is undetermined due to large uncertainties, to the point of showing many bifurcation points that more than likely are an artifact of the experiment.

Despite the uncertainty in the experimental data shown in polar plots, there are several noteworthy features. There is a significant discrepancy in the relaxation time for the oscillatory behavior, with the experimental results decaying very slowly, the theoretical results decaying slightly faster, and the numerical results decaying at a significantly higher rate even when having the largest initial deformation. A second discrepancy is the period for each cycle during the rotational regime. The shortest period corresponds to that of the small deformation approximation, and the longest to the numerical simulation with the lesser number of points –Trace S1– for the description of the interface. Surprisingly, this simulation also shows a significantly larger deformation of the drop, and compared to the simulation with the greater number of point onto the interface –Trace S2–, the latter becomes quite unstable for times longer than 20 dimensionless time-units.

Another way to look for a consistent correlation among the experimental, theoretical and numerical plots is to adjust the values of the flow and fluid parameters in the last two models. However, values that are needed for a better match with the experimental

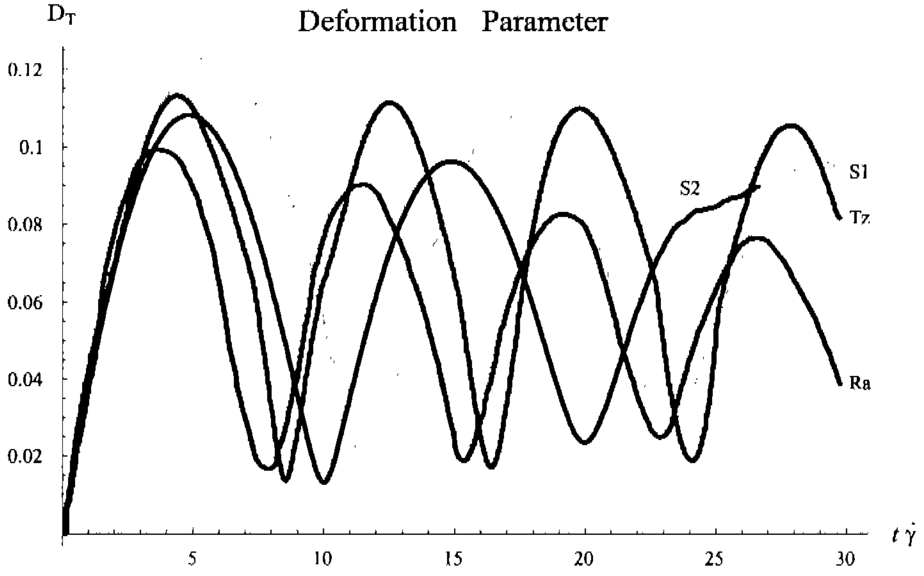

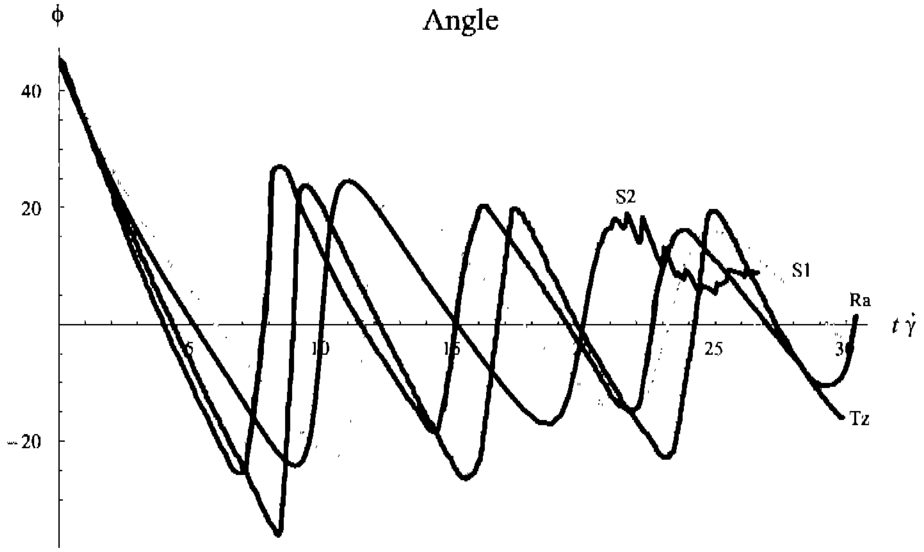

FIGURE 5.16. Time dependent deformation parameter D_T and orientation ϕ curves for $Ca = 1.5$, $\lambda_\mu = 25$, $\dot{\gamma} = 7.44\,\mathrm{s}^{-1}$, $a = 0.75\,\mathrm{mm}$ and $\lambda = 0$ for experimental, analytical and numerical data. The label Ra is for the Rallison theory, Tz is for the experimental data from Torza et al. [76], S1 is for the simulation with $N = 128$ and time step $t_s = 0.01\,\mathrm{s}$, and S2 is for the simulation with $N = 192$ and time step $t_s = 0.01\,\mathrm{s}$.

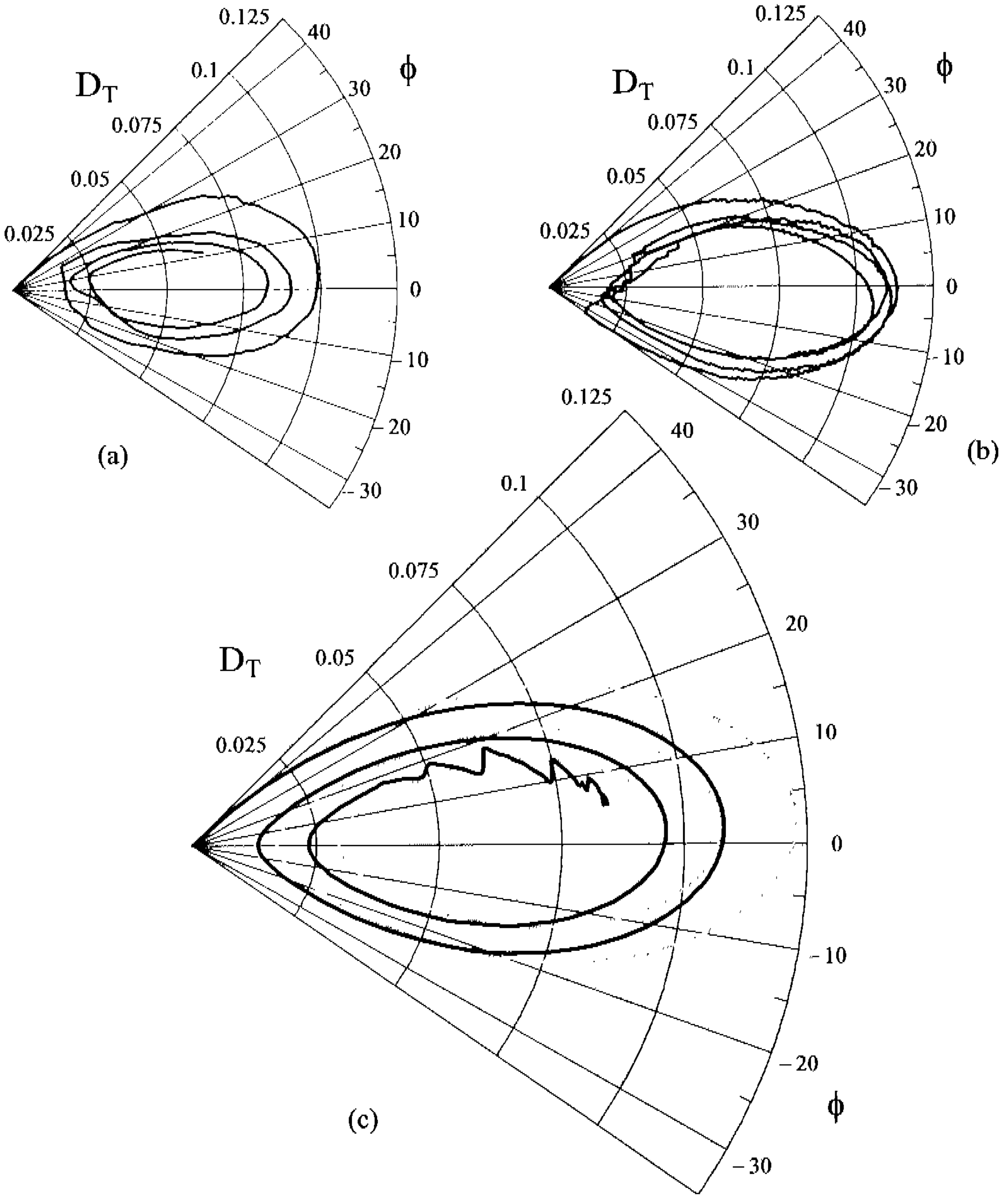

FIGURE 5.17. Polar plot of deformation parameter D_T vs. orientation angle ϕ for $Ca = 1.5$, $\lambda_\mu = 25$, $\dot{\gamma} = 7.44\,\mathrm{s}^{-1}$ and $a = 0.075\,\mathrm{cm}$ for simple shear flow and different values of the shear rate. (a) Rallison theory, (b) experimental data from Torza et al. [76], (c) Dashed line is for the simulation with $N = 128$ and time step $t_s = 0.01\,\mathrm{s}$, and solid line is for the simulation with $N = 192$ and time step $t_s = 0.01\,\mathrm{s}$.

traces are significantly different from those reported in the work by Torza et al.

5.2 Effects of solid boundaries on the deformation of a drop

The velocity field generated by a Two-Roll Mill in the vicinity of the stagnation point can be linearized with Eq. 3.12. When the drop size is small, this approximation is valid and can be used to carry out numerical simulations, but when the drop size increases, this approximation may no longer be useful; the flow field changes towards kinematics closer to simple shear near the cylinders surfaces. As a consequence of this finite flow domain, drops sizes, comparable to the characteristic gap size, are subjected to many other complexities of this flow field, such as nonhomogeneous values of the relevant flow parameters. In particular, λ_{Nom} and $\dot{\gamma}_{Nom}$ are now clearly position dependent. From the information obtained with the analytical and the numerical solutions for TRM geometry flows, the shear rate increases around the rollers' surfaces, while the flow-type parameter diminishes down to zero at the cylinders. Hence, simulation of drop dynamics under flow conditions that include the walls may explain the discrepancies observed when comparing them with the experimental results. Table 5.2 presents the characteristic length scales used for simulations of the drop dynamics for a set various drop radii in a nonhomogeneous strong flow. The radius of the drop is fixed at 0.1 mm as well as the flow-type parameter $\lambda_{Nom} = 0.1$. The simulations correspond to the same flow but with different widths of the gap. The nearest walls of the cylinders are taken explicitly, but there is no containment for the cylinders in the far field: it corresponds to an unbounded TRM geometry presented in Chapters 2 and 3. In these simulations, the drop size varies from a very small drop –30 times smaller than the gap– up to a drop size that is a significant fraction the channel width –length ratio of 1:2. With this objective, the BEM technique used in one that takes into account the closeness of the walls; see Sec. 1.3. The main disadvantage for these simulations is that a much greater time of computation is required, mainly because a greater number of points is needed to properly include nearby walls.

Figure 5.18 shows the deformation parameter and orientation curves for the set of ratios used and for $\lambda = 0.1$, $Ca = 0.23$, $\lambda_{\mu} = 25.8$ and $\dot{\gamma} = 1$ at the stagnation point for an

R	g	d_d/g
14.00	6.00	0.033
4.67	2.00	0.100
1.86	0.80	0.250
0.93	0.40	0.500

TABLE 5.2. Data used for calculate the effects of the boundaries on the deformation parameter and orientation angle in a drop. R is the radii of the cylinders, g is the gap between cylinders surfaces and d_d/g is the ratio of the drop diameter between the gap.

unperturbed flow field (without drop). For the largest two drops, the spatial dependence of the flow parameters should be a significant contribution to the drop behavior.

Figure 5.18 shows the history of the deformation parameter for four drop sizes. For the smallest drop, the one for which the boundaries ought to have a negligible effect, already presents several differences with respect to the same data but for the unbounded flow field. In particular as can be observed in Fig. 5.7, for the evolution of the deformation under flows with $\lambda = 0.1$, the maximum deformation is slightly greater than under the influence of walls, and the undershoot for the minimum deformation during the first cycle occurs significantly earlier in the deformation evolution. When comparing the ideal flow field with the bounded flow for the smallest drop dynamics under polar plots –see Figs. 5.8 and 5.19– deformations are clearly greater for the unbounded result, while the orientation of the principal axis of the drop is about the same for both cases. A possible explanation may be a reduction of the capacity of the external flow field to generate a deformation in the immersed object. The dominant value for this capacity is $\dot{\gamma}\sqrt{\lambda}$, but it may be significantly reduced away from the stagnation point by the mere existence of the walls.

For the larger drops, the flow field effects are quite noticeable and a more prolonged imposition of the flow is needed to reach stationary drop deformations. In particular, the trace in polar plots appears similar to that for the same Capillary number but for a flow with $\lambda = 0.3$ -see Fig. 5.8. This condition appears to a first consideration unsupported, but the presence of the walls does precisely that: generates a flow field with significant more vorticity that otherwise presumed. However, assuming this to be the proper scenario, the stationary drop shape is reached much earlier in time for the unbounded flow field, as if the closeness of boundaries retards the drop evolution. The stationary orientation of

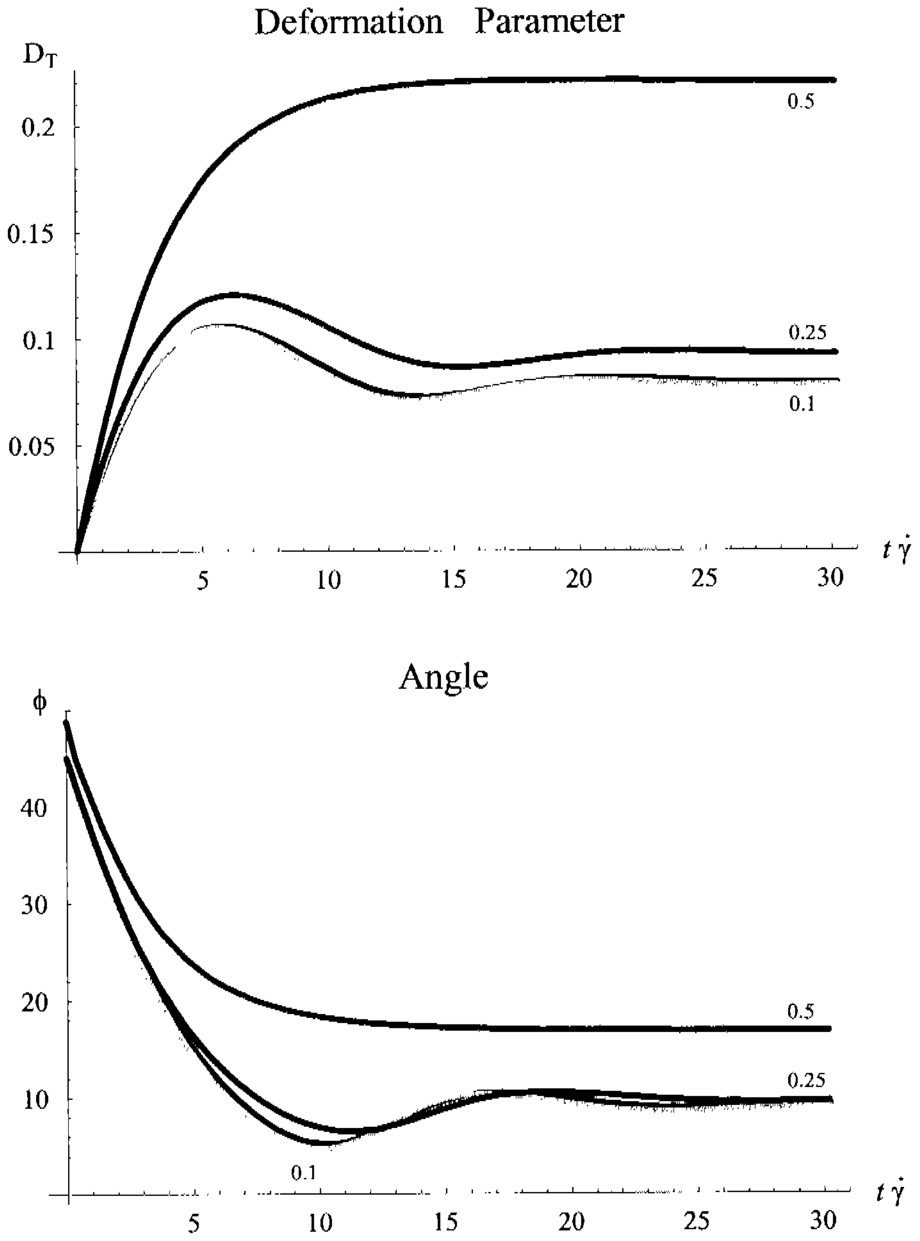

FIGURE 5.18. Time dependent deformation parameter D_T and orientation ϕ curves for several ratios of diameter of the drop between gap in unbounded TRM with $\lambda_{Nom} = 0.1$, $Ca = 0.23$ and $\lambda_\mu = 25.8$. The red curves correspond to $d_d/g = 0.033$; cyan to 0.1; blue to 0.25; and purple to 0.5.

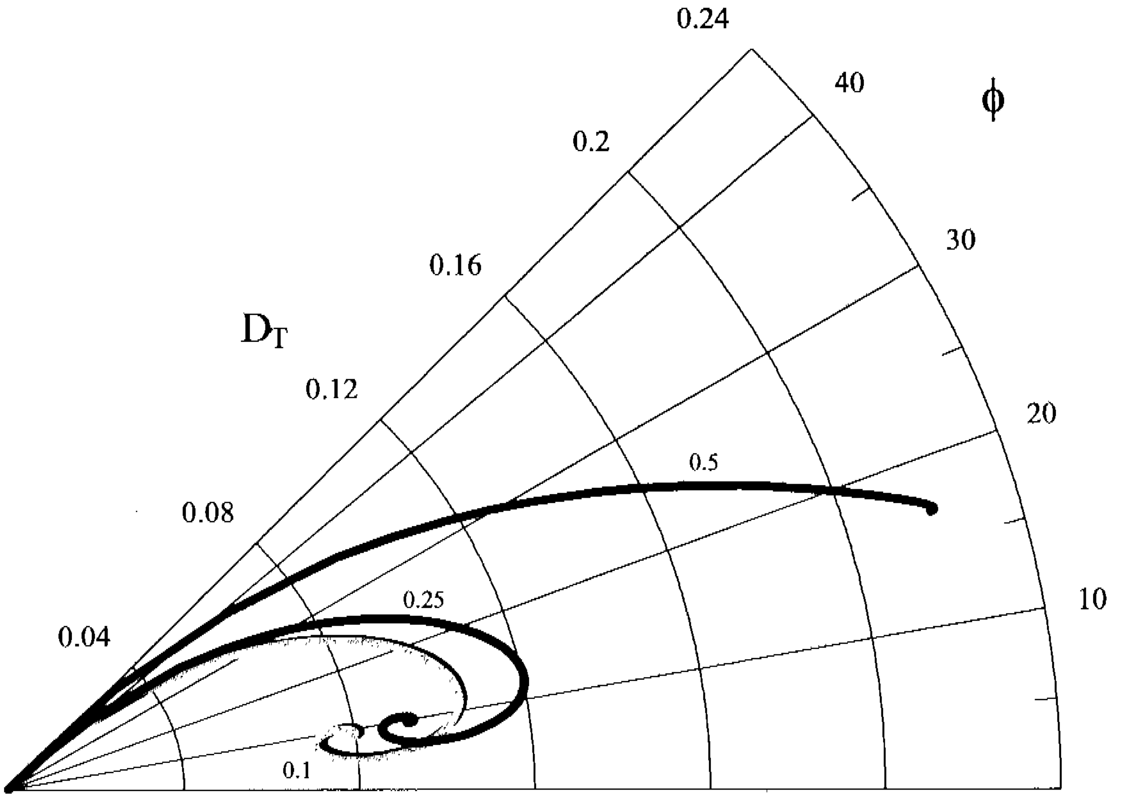

FIGURE 5.19. Polar plot of deformation parameter D_T vs. orientation angle ϕ for several ratios of diameter of the drop between gap in unbounded TRM for $\lambda_{Nom} = 0.1$, $Ca = 0.23$, $\lambda_\mu = 25.8$. All deformation histories attain a stationary deformation. For the highest values of the length ratio, the polar trajectory does not present an oscillatory behavior. Same color code as previous plot.

the largest drop at about 17.5 degrees matches the expected outflow axis orientation for $\lambda = 0.1$.

A full characterization of the effects of nearby boundaries still requires many more simulations in order to have a better understanding of the drop dynamics; this phenomenon has been until now much less explored and with a limited basis for the dominant mechanisms or characteristics of the drop deformation [6].

5.3 Conclusions

In this Chapter the dynamics of viscous drops immersed in creeping flows generated by TRMs is studied numerically by boundary element methods (BEM). These studies are carried out in unbounded linear strong flow fields and flow fields where the effects of walls are taken explicitly into account. The later conditions are amenable to experimental studies and Chapter 3 presents the basic ideas for its implementation in the laboratory. The drop dynamics has been studied considering as the two principal characteristics the flow-type parameter and the Capillary numbers. The flow-type parameter values used are 0 (simple shear flow), 0.03, 0.1, 0.2 and 0.3, and the simulated Capillary number values are 0.23, 0.5, 1 and 2. Under these conditions, the dominant effects of vorticity, elasticity of the drop interface and the rate of deformation of the flow field are sampled.

The simulations using BEM techniques show that the external and internal flow fields present a significant richness of features when the parameter space for the flow-type parameter and the Capillary number are investigated. Some of these characteristics are presented for the stationary –long time– flow solutions, as well as for the transient evolution of the drop dynamics. For the stationary drop shapes, the transition of behavior and critical values for the Capillary number, for the flow-type or for the drop deformation are presented and discussed. As well results are presented for the topology for the dominant stagnation points in the central region of the flow where the drop has been studied. For the transient states starting from the initial drop shape evolving towards the stationary shape, these studies show that, in the interval of λ's selected, the main transition of the drop response to the external flow occurs. This transition covers an interesting range of behaviors: from a damped periodic oscillatory behavior, until a final shape is obtained, to a monotonically deforming drop that continues elongating until the drop breaks up. This transition is observed in the interval $0.15 < \lambda < 0.2$ within the Capillary numbers selected.

The algorithms used are very sensible to the number of collocation points and to the length of the time step. Therefore, for simulations that require a higher degree of accuracy a possible solution is to increase the number of collocation points above 150 points and to use time steps smaller than $0.01/\dot{\gamma}$; however, we have noticed also that with finer simulations the method used for interpolating the interface can present higher noise levels, due likely to undulations of the spline interpolation at each segment.

Given that there are published results on drop shapes and orientations as a function of time, as well as theoretical models appropriate for small deformations, in this work a comparison among the three kinds of experiments is put forward. However, given the actual quality of the available data the comparison turned to be quite fruitless; uncertainties obscure the main features of the digitized theoretical and experimental data. Despite this unforeseen situation, there are several discrepancies as well as agreements. Finally, assuming that the numerical experiment does not include the effects of walls always present in the laboratory, a last attempt to match the experimental and the numerical data was made simulating flow conditions that include wall effects. The results appear to point towards the opposite direction, and although these seems quite relevant on their on right, matching this work data to the dynamics of drops observed experimentally and as reported some 30 years ago represents an open challenge.

Despite the difficulties encountered with these three kinds of experiments, as shown in Figs. 5.18 and 5.19, recent theoretical work by Guido [42, 43, 77], as well as the latest experimental developments by Leal and collaborators [55, 54], and others [35, 36, 77], all point towards a scenario where the theoretical, numerical and experimental techniques are now significantly mature for this particular creeping flow problem. It is now possible to carry out systematic attempts to understand those features of the drop dynamics presented earlier, but emphasizing its quantitative nature in the not so distant future. A future line of work will be to carry out detailed polar plots of the models by Rallison and by Greco [33] for the full range of 2-D Two-Roll Mill flows, carry out new experiments with the flow cells proposed here, and refine the numerical techniques possibly into a 3-D scenario. The designs for experimental TRM devices carried out during these years as a graduate student are presented in Chapter 3. These may offer some insight in the near future along this line. I believe that a unique opportunity for experimental studies exists, besides the current techniques developed for For-Roll Mills and microchannels [78], together with the understanding that Two-Roll Mill flow cells may provide.

Other very relevant questions that are not addressed here are those of a purely nonlinear character. The nonlinear character of drop dynamics in Stokes flow results from the nonlinear dependence of the flow field on the drop shape. Nonlinear effects include the existence of stable and unstable branches for the stationary shapes. These branches merge and disappear at critical values of the capillary number (dimensionless flow strength). Despite the nonlinear character of the system, the possibility of multiple stable branches of stationary shapes has not been explored [74]. All possible bifurcations occur under the regime where the effects of drop deformation by the straining component of the flow, drop rotation, and capillary relaxation are comparable in magnitude.

Chapter 6

Hydrodynamics of deformable objects in creeping flows: Summary of results and conclusions

In the First Part of this Thesis we carried out theoretical investigations of the characteristics of two-dimensional creeping flow fields generated by Two-Roll Mills (TRMs), and in the Second Part, we performed numerical simulations of the hydrodynamics of drops immersed in these flows. The aim of this work was to build a framework for future experiments in the laboratory to provide a useful starting point for understanding of more realistic multi-particle systems such as those found in two-phase fluids. The use of TRMs permit to address the physical problems of deformation, orientation, rupture and coalescence of drops under well characterized flow kinematics not yet studied, which may be important cornerstones for studies of naturally occurring two-phase flow fields.

In the First Part, the flows generated by co-rotating Two-Roll Mill is studied in detail analytically and numerically, with especial emphasis to the shear rate and the ratio of deformation to vorticity (flow-type parameter, λ). In these flows there is a stagnation point with properties of a strong flow (elongational flows with vorticity where $\lambda > 0$), which is appropriate for studies of drops placed in it. The range of values of the flow-type parameter that can be generated at the stagnation point is in a domain outside of the interval accessible with in Four-Roll Mills; therefore, studies carried out with these geometries are complementary.

In Chapter 1, the analytical solution for unbounded Two-Roll Mills is presented. The mathematical model is useful for the determination of all properties of the flows. Also, this solution shows that it is possible to generate flows which include gradients of the flow-type parameter as well as gradients of the shear rate at the stagnation point, by means of changes of the geometric features of the flow cell and the angular velocity of the cylinders. When ratios of angular velocities for cylinders are different than one, and the geometry is asymmetric, the flow field is significantly more complex that previously reported for strong flows generated in Four-Roll Mills. Concurrently to the strong flow conditions, other asymmetries appear, in particular, asymmetries in the flow-type and shear rate parameters. In turn, this asymmetric solution presents a rather complex scenario for studies of droplets at the stagnation point that has not been addressed. These asymmetries may represent a controlled scenario for studies of drop deformations of a more complex nature. An advantage provided by the analytical solution of TRMs geometries is a better predictive capacity of the applied flow dynamics. In this manner, drop phenomena analyzed with this experimental setup are similar kinematically, from the point of view of the applicable boundary conditions, as well as dynamically to the hydrodynamics of two-phase flows through pores and fractures. In Chapter 2, the flows generated by two bounded TRMs are studied numerically with a Boundary Element Method. In the same manner that for the analytical solution, all flow field parameters are studied and analyzed with the numerical solution, giving especial attention to the effects on the flow field by the presence of the flow cell boundaries.

An aim to study in detail flows in TRMs is to know the extent of the linear velocity field zone around the stagnation point. With this information, it is possible to determine when a drop in the stagnation point is only subjected to the linear velocity field and when it is not. This knowledge is an important reference, because it can be able to perform experiments on drop dynamics with more complex flow fields, but well characterized. With this setup, drop deformations can be studied under varied and well characterized kinematic conditions.

In Chapter 3, the design of the flow cells studied and a control algorithm for the position of a point particle at the stagnation point with values of the flow field parameters determined at all times are presented. The flow cells are capable of providing detailed experimental information about drop dynamics under conditions that include the effects of elongation with significant vorticity, nearby walls, and eventually, by the presence of surfactants or other polymeric additives, in addition to the study of time-dependent flow field histories. The flow cells are designed so that guarantee a minimum quality of the flow fields generated. The control scheme provides the necessary information required to adjust the flow field in order to subject the liquid drop to an evolving trajectory that places it back at the stagnation point within a finite amount of time.

In the Second Part, the dynamics of two-dimensional viscous drops immersed in unbounded linear strong flows and bounded flow fields generated in TRMs is studied numerically by Boundary Element Methods (BEM), which give emphasis to the class of flows that are not included in the most of previous studies. The simulations are performed for several flow-type parameter values and some Capillary numbers. The transient evolution from the initial spherical drop shape to the stationary shape is also studied. The simulations show that the external and internal flow fields present a significant richness of features when the parameter space for the flow-type parameter and the Capillary number are investigated. Some of these characteristics are presented for the stationary –long time– flow solutions, as well as for the transient evolution of the drop dynamics.

For the stationary drop shapes, the transition of behavior and critical values for the Capillary number, for the flow-type or for the drop deformation are presented and discussed. As well results are presented for the topology for the dominant stagnation points in the central region of the flow where the drop has been studied. For the transient states starting from the initial drop shape evolving towards the stationary shape, these studies show that, in the interval of flow-type parameter values selected, the main transition of the drop response to the external flow occurs. This transition covers an interesting range of behaviors: from a damped periodic oscillatory behavior, until a final shape is obtained, to a monotonically deforming drop that continues elongating until the drop breaks up. This transition is clearly observed in the interval $0.15 < \lambda < 0.2$ within the Capillary numbers selected. In the transient evolution of the drop dynamics, emphasis is given to understand the transition in the internal flow field of the drop from a flow dominated by vorticity to another dominated by the deformation.

The drop dynamic simulations performed in this Thesis were two-dimensional, therefore, the information obtained from those is useful in problems with low Capillary number, where the deformation in the normal axis to the plane of the external flow field is small, in order to use the results of the simulation to predict an experiment, but the simulations for medium Capillary numbers show interesting information that can be sought in experiments. We believe that a unique opportunity for experimental studies exists, besides the current techniques developed for For-Roll Mills and microchannels, together with the understanding that Two-Roll Mill flow cells may provide.

Other very relevant questions that are not addressed here are those of a purely nonlinear character. The nonlinear character of drop dynamics in Stokes flow results from the nonlinear dependence of the flow field on the drop shape. Nonlinear effects include the existence of stable and unstable branches for the stationary shapes. These branches merge and disappear at critical values of the capillary number (dimensionless flow strength). Despite the nonlinear character of the system, the possibility of multiple stable branches of stationary shapes has not been explored. All possible bifurcations occur under the regime where the effects of drop deformation by the straining component of the flow, drop rotation, and capillary relaxation are comparable in magnitude.

Appendix A

Bipolar coordinates system

Two-Roll Mill geometrics consists of two cylinders of which axis are parallel. The cylindrical bipolar coordinates system is the most appropriate for the geometry of the unbounded two-dimensional two roll mill, where the boundary cylinders are represented by values of coordinate α constants.

In the bipolar coordinates system, the coordinates are $x^1 = \alpha$, $x^2 = \beta$ and $x^3 = z$, defined by its relationships with the Cartesian coordinates as [79]

$$x = \frac{a \sin\beta}{\cosh\alpha - \cos\beta}, \tag{A.1}$$

$$y = \frac{a \sinh\alpha}{\cosh\alpha - \cos\beta}, \tag{A.2}$$

or

$$\alpha + i\beta = \ln\left(\frac{x + i\,(y + a)}{x + i\,(y - a)}\right). \tag{A.3}$$

In an extended form

$$\begin{aligned} \alpha &= \frac{1}{2}\ln\left(\frac{x^2 + (y + a)^2}{x^2 + (y - a)^2}\right), && \text{(A.4)} \\ \beta &= \arctan\left(\frac{2ax}{x^2 + y^2 - a^2}\right). && \text{(A.5)} \end{aligned}$$

The basis vectors of the bipolar coordinate system with respect to the Cartesian coordinates are

$$\mathbf{p} = \frac{a \sin\beta}{\cosh\alpha - \cos\beta}\mathbf{i}_1 + \frac{a \sinh\alpha}{\cosh\alpha - \cos\beta}\mathbf{i}_2 + z\,\mathbf{i}_3, \tag{A.6}$$

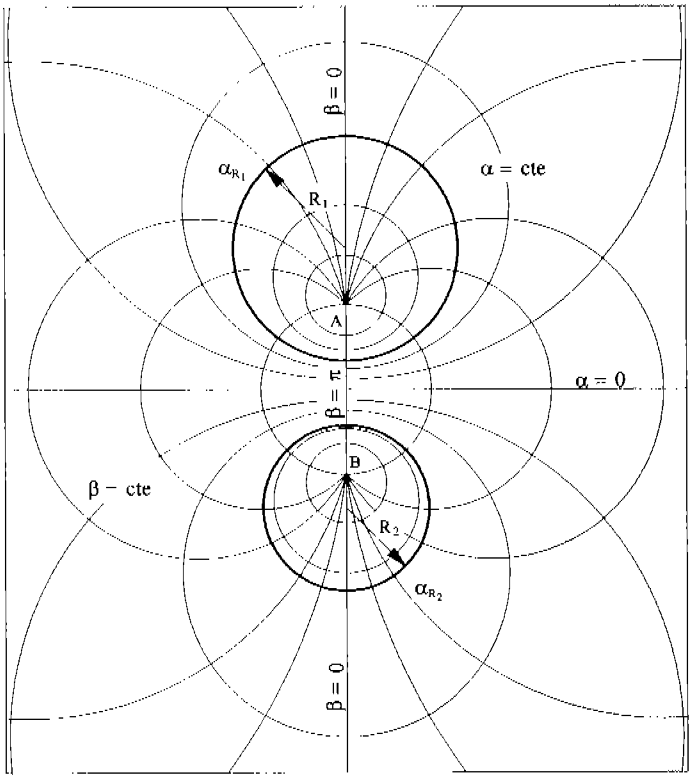

FIGURE A.1. Bipolar coordinates system. This picture show the lines where the coordinates α and β are constants. The points **A** and **B** are at the same distance a from the origin $(\alpha = 0, \beta = \pi)$.

$$\mathbf{g}_1 = \frac{\partial \mathbf{p}}{\partial \alpha} = -\frac{a \sinh \alpha \sin \beta}{(\cosh \alpha - \cos \beta)^2}\mathbf{i}_1 + \frac{a\,(1 - \cosh \alpha \cos \beta)}{(\cosh \alpha - \cos \beta)^2}\mathbf{i}_2, \tag{A.7}$$

$$\mathbf{g}_2 = \frac{\partial \mathbf{p}}{\partial \beta} = \frac{a\,(\cosh \alpha \cos \beta - 1)}{(\cosh \alpha - \cos \beta)^2}\mathbf{i}_1 - \frac{a \sinh \alpha \sin \beta}{(\cosh \alpha - \cos \beta)^2}\mathbf{i}_2, \tag{A.8}$$

$$\mathbf{g}_3 = \frac{\partial \mathbf{p}}{\partial z} = \mathbf{i}_3. \tag{A.9}$$

With the expressions for $\mathbf{g}_k$, the metric tensor is obtained

$$(g_{kl}) = \begin{pmatrix} \frac{a^2}{(\cosh \alpha - \cos \beta)^2} & 0 & 0 \\ 0 & \frac{a^2}{(\cosh \alpha - \cos \beta)^2} & 0 \\ 0 & 0 & 1 \end{pmatrix}, \tag{A.10}$$

where the metric factor is

$$g_{11} = g_{22} = h_{11}^2 = h_{22}^2 = h^2 \tag{A.11}$$

For a two-dimensional vectorial field expressed in its physical components

$$\mathbf{v} = v_\alpha \mathbf{e}_1 + v_\beta \mathbf{e}_2 + 0\mathbf{e}_3,$$

the gradient of this field gives a second-order tensor,

$$\nabla \mathbf{v} = \mathbf{g}^k \frac{\partial \mathbf{v}}{\partial x^k} = v_{n;k}\, \mathbf{g}^k \mathbf{g}^n \tag{A.12}$$

where the tensor component is

$$v_k = \sqrt{g_{kk}}\, v_{(k)} = h_k\, v_{(k)} \tag{A.13}$$

and the covariant partial derivative is

$$v_{n;k} = v_{n,k} - v_m \begin{Bmatrix} m \\ k \;\; n \end{Bmatrix} = \frac{\partial v_n}{\partial x^k} - v_m \begin{Bmatrix} m \\ k \;\; n \end{Bmatrix} \tag{A.14}$$

where $\left\{ {}_{k}{}^{m}{}_{n} \right\} = \frac{\partial x^m}{\partial z^l} \frac{\partial^2 z^l}{\partial x^k \partial x^m}$ are the *Christoffel symbols of the second kind.* The Christoffel symbols represent partial derivatives of basis vectors of a curvilinear coordinate system with respect to coordinate variables (For a full explanation of tensor calculus see Narasimham [80]). In bipolar coordinates the Christoffel symbols of the second kind are

$$\begin{array}{ll} \left\{ {}_{1}{}^{1}{}_{1} \right\} = -\dfrac{\sinh\alpha}{\cosh\alpha - \cos\beta}, & \left\{ {}_{1}{}^{2}{}_{1} \right\} = \dfrac{\sin\beta}{\cosh\alpha - \cos\beta}, \\ \left\{ {}_{2}{}^{1}{}_{2} \right\} = \dfrac{\sinh\alpha}{\cosh\alpha - \cos\beta}, & \left\{ {}_{2}{}^{2}{}_{2} \right\} = -\dfrac{\sin\beta}{\cosh\alpha - \cos\beta}, \\ \left\{ {}_{1}{}^{1}{}_{2} \right\} = \left\{ {}_{2}{}^{1}{}_{1} \right\} = -\dfrac{\sin\beta}{\cosh\alpha - \cos\beta}, & \left\{ {}_{1}{}^{2}{}_{2} \right\} = \left\{ {}_{2}{}^{2}{}_{1} \right\} = -\dfrac{\sinh\alpha}{\cosh\alpha - \cos\beta}; \end{array} \tag{A.15}$$

and all other $\left\{ {}_{k}{}^{m}{}_{n} \right\} = 0$.

Appendix B

Local Reynolds number

In order to determine the range of validity of the creeping motion approximation for the cases where there is not a closed analytical solution for the Two-Roll Mill geometry, it is necessary to know an estimate of the local magnitudes of the inertial and viscous forces terms of the motion equation [48].

The global Reynolds number for a co-rotating Two-Roll Mill with cylinders of the same size at the same angular velocity is

$$\mathrm{Re} = \frac{R\,(de - 2R)\,\omega}{2\,\nu} = \frac{R\,g\,\omega}{2\,\nu}, \tag{B.1}$$

where R is the radii of the cylinders, de is the distance between the cylinders' axes, ω is the angular velocity, g is the gap between the cylinders' surfaces, and ν is the kinematic viscosity. For a general co-rotating Two-Roll Mill (with cylinders of different radii and angular velocity), the global Reynolds number is proposed to have the following form

$$\mathrm{Re}_{global} = \frac{(R_i\,\omega_i)_{m\acute{a}x}\,D}{\nu}, \tag{B.2}$$

where $(R_i\,\omega_i)_{m\acute{a}x}$ is the larger tangential velocity, and D is given by

$$D = \frac{(R_i\,\omega_i)_{m\acute{a}x}\,g}{(R_1\,\omega_1 + R_2\,\omega_2)}. \tag{B.3}$$

As the Reynolds number, the ratio of the inertial forces term $(\mathbf{u}\cdot\boldsymbol{\nabla}\mathbf{u})$ and the viscous forces term $\left(\nu\,\boldsymbol{\nabla}^2\mathbf{u}\right)$ is used with the purpose to obtain an idea of the relationship between these terms in the flow. The inertial term is expressed in the next equation (See Appendix A)

$$
\begin{aligned}
\mathbf{u}\cdot\boldsymbol{\nabla}\mathbf{u} \;=\;& u_i\,\mathbf{g}^i\cdot u_{j;k}\,\mathbf{g}^k\,\mathbf{g}^j = u_i\,u_{j;k}\,g^{ik}\,\mathbf{g}^j = u_i\,u_{j;k}\,g^{ik}\,h\,\mathbf{e}^j = \qquad\qquad \text{(B.4)}\\
& \begin{bmatrix} \dfrac{1}{h}\left(u_\alpha\left(\dfrac{\partial u_\alpha}{\partial\alpha}-\dfrac{h}{a}\sin\beta\;u_\beta\right)+u_\beta\left(\dfrac{\partial u_\alpha}{\partial\beta}+\dfrac{h}{a}\sinh\alpha\;u_\beta\right)\right)\\ \dfrac{1}{h}\left(u_\alpha\left(\dfrac{\partial u_\beta}{\partial\alpha}+\dfrac{h}{a}\sin\beta\;u_\alpha\right)+u_\beta\left(\dfrac{\partial u_\beta}{\partial\beta}-\dfrac{h}{a}\sinh\alpha\;u_\alpha\right)\right)\end{bmatrix}, \qquad \text{(B.5)}
\end{aligned}
$$

with magnitude

$$
\begin{aligned}
\|\mathbf{u}\cdot\boldsymbol{\nabla}\mathbf{u}\| = \frac{1}{\sqrt{h^2}}\Bigg[&\left(u_\alpha\left(\frac{\partial u_\alpha}{\partial\alpha}-\frac{h}{a}\sin\beta\;u_\beta\right)+u_\beta\left(\frac{\partial u_\alpha}{\partial\beta}+\frac{h}{a}\sinh\alpha\;u_\beta\right)\right)^2+\\
&\left(u_\alpha\left(\frac{\partial u_\beta}{\partial\alpha}+\frac{h}{a}\sin\beta\;u_\alpha\right)+u_\beta\left(\frac{\partial u_\beta}{\partial\beta}-\frac{h}{a}\sinh\alpha\;u_\alpha\right)\right)^2\Bigg]^{\frac{1}{2}} \qquad \text{(B.6)}
\end{aligned}
$$

The Laplacian of the velocity (viscous term) is

$$
\begin{aligned}
\boldsymbol{\nabla}^2\mathbf{u} = \boldsymbol{\nabla}\cdot\boldsymbol{\nabla}\mathbf{u} = \mathbf{g}^i\frac{\partial}{\partial x^i}\cdot u_{j;k}\mathbf{g}^k\mathbf{g}^j &= \left(u_{j;k}\right)_{;i}\;g^{ik}\;\mathbf{g}^j\\
&= h\;\left(u_{j;k}\right)_{;i}\;g^{ik}\;\mathbf{e}^j = h\,u_{j;ki}\;g^{ik}\;\mathbf{e}^j \qquad \text{(B.7)}
\end{aligned}
$$

where

$$
u_{j;ki} = u_{j,ki} - u_{n,i}\begin{Bmatrix} n \\ j\quad i\end{Bmatrix} - u_n\begin{Bmatrix} n \\ j\quad i\end{Bmatrix}_{,i} - u_{n;k}\begin{Bmatrix} n \\ j\quad i\end{Bmatrix} - u_{j;n}\begin{Bmatrix} n \\ k\quad i\end{Bmatrix},
$$

then,

$$
\boldsymbol{\nabla}^2\mathbf{u} = \begin{bmatrix} \dfrac{1}{a\,h}\left(\dfrac{a}{h}\left(\dfrac{\partial^2 u_\alpha}{\partial\alpha^2}+\dfrac{\partial^2 u_\alpha}{\partial\beta^2}\right)-(\cosh\alpha+\cos\beta)\;u_\alpha+\right.\\ \qquad\qquad\left. 2\sinh\alpha\dfrac{\partial u_\beta}{\partial\beta}-2\sin\beta\dfrac{\partial u_\beta}{\partial\alpha}\right)\\ \dfrac{1}{a\,h}\left(\dfrac{a}{h}\left(\dfrac{\partial^2 u_\beta}{\partial\alpha^2}+\dfrac{\partial^2 u_\beta}{\partial\beta^2}\right)-(\cosh\alpha+\cos\beta)\;u_\beta-\right.\\ \qquad\qquad\left. 2\sinh\alpha\dfrac{\partial u_\alpha}{\partial\beta}+2\sin\beta\dfrac{\partial u_\alpha}{\partial\alpha}\right)\end{bmatrix},
$$

and the magnitude of the viscous term is

$$\nu \left\|\nabla^2 \mathbf{u}\right\| = \frac{\nu}{a\sqrt{h^2}} \left[\left(\frac{a}{h} \left(\frac{\partial^2 u_\alpha}{\partial \alpha^2} + \frac{\partial^2 u_\alpha}{\partial \beta^2} \right) - (\cosh\alpha + \cos\beta)\, u_\alpha + \right. \right.$$
$$\left. 2\sinh\alpha \frac{\partial u_\beta}{\partial \beta} - 2\sin\beta \frac{\partial u_\beta}{\partial \alpha} \right)^2 +$$
$$\left(\frac{a}{h} \left(\frac{\partial^2 u_\beta}{\partial \alpha^2} + \frac{\partial^2 u_\beta}{\partial \beta^2} \right) - (\cosh\alpha + \cos\beta)\, u_\beta - \right.$$
$$\left. \left. 2\sinh\alpha \frac{\partial u_\alpha}{\partial \beta} + 2\sin\beta \frac{\partial u_\alpha}{\partial \alpha} \right)^2 \right]^{\frac{1}{2}}. \quad \text{(B.8)}$$

Then, the "local" normalized Reynolds number is given by the equation

$$\mathrm{Re}_{local} = \frac{1}{\mathrm{Re}_{global}} \frac{\left\|\mathbf{u} \cdot \nabla \mathbf{u}\right\|}{\nu \left\|\nabla^2 \mathbf{u}\right\|}. \quad \text{(B.9)}$$

Notes: When more than a single characteristic dimension enters into a given problem, the Reynolds number may be significantly greater than unity without inertial effects being appreciable (Happel [1], pp. 42).

But since no actual flow can occur at a Reynolds number which is identically zero, inertial effects must exist to some extent in all real systems (Happel [1], pp. 45).

When the geometric configuration has the same cylinders' radii, the stagnation point in the closed solution coincides with the point where the inertial and the viscosity terms vanish, but the limit of the local Reynolds number is defined. In other case, there is a singular point where the Reynolds number is not defined. Outside of the interval where the red line is showed (where the viscosity term is equal to zero), the local Reynolds number is splitting off to both sides of the line $\beta = \pi$.

When the geometric configuration has different cylinders' radii, the stagnation point in the closed solution does not coincide with the point where the viscosity term is zero, and there is a point where the local Reynolds numbers is not defined. In the case where the inertial term and the viscosity term coincide in the same point, the limit of the Reynolds number is defined too.

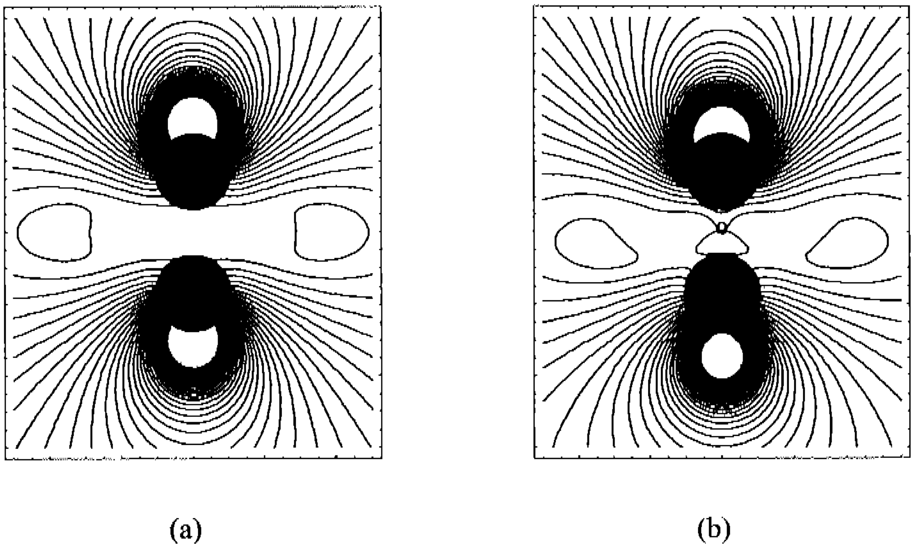

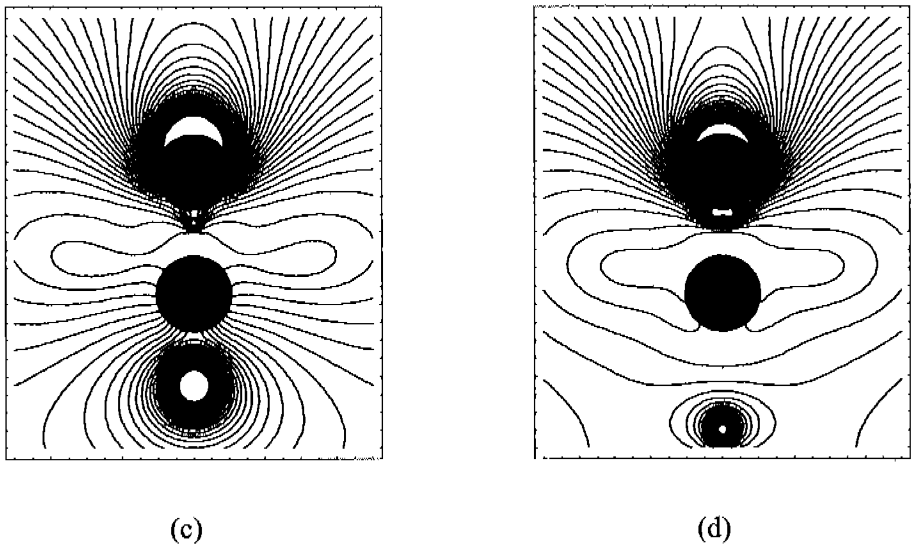

FIGURE B.1. Variation of the local Reynolds number in a TRM with $g/de = 0.3588$ for different ratios of the angular velocities of the cylinders. The angular velocity ratios are: (a) $\omega_{R_2}/\omega_{R_1} = 1$, (b) $\omega_{R_2}/\omega_{R_1} = 0.75$, (c) $\omega_{R_2}/\omega_{R_1} = 0.5$ and (d) $\omega_{R_2}/\omega_{R_1} = 0.25$. In these plots, the regions where the local Reynolds number is high have a high density of lines.

Appendix C

The expansion of the term $(\cosh\alpha - \cos\beta)\ln(\cosh\alpha - \cos\beta)$

In order to find the values of the coefficients of the stream function, Eq. 1.12, is convenient to expand the logarithmic term of ψ in Fourier's series. Starting from the following equation [1]

$$\ln\left(1 - 2x\cos\phi + x^2\right) = -2\sum_{n=1}^{\infty}\frac{\cos n\phi}{n}x^n \tag{C.1}$$

and using the equivalence

$$\ln\left(x + \sqrt{1+x^2}\right) = \sinh^{-1}x; \quad x^2 \leq 1 \quad \text{and} \quad x\cos\phi \neq 1, \tag{C.2}$$

then, the Eq. C.1 can be expressed as

$$\ln\left(\frac{1+x^2}{2x} - \cos\phi\right) = -\ln(2x) - 2\sum_{n=1}^{\infty}\frac{\cos n\phi}{n}x^n. \tag{C.3}$$

From the above equation, the logarithmic term can be obtained using the change of variables $\phi = \beta$ and $\frac{1+x^2}{2x} = \cosh\alpha = \varrho$. Now, the next step is obtain x as function of α. Then, frm $\frac{1+x^2}{2x} = \varrho$, the following equation is obtained

$$1 - 2x\varrho + x^2 = 0, \tag{C.4}$$

---

[1] Obtained from Ryzhik and Gradshteyn [81], Eq. 1.514.

which solutions are

$$
\begin{aligned}
x &= \frac{-(-2\varrho) \pm \sqrt{4\varrho^2 - 4}}{2} = \varrho \pm \sqrt{\varrho^2 - 1}, && \text{(C.5)}\\
x &= \cosh\alpha \pm \sqrt{\cosh^2\alpha - 1} = \cosh\alpha \pm \sinh\alpha, && \text{(C.6)}\\
x &= \frac{(\mathrm{e}^{\alpha} + \mathrm{e}^{-\alpha}) \pm (\mathrm{e}^{\alpha} - \mathrm{e}^{-\alpha})}{2} = \frac{(1 \pm 1)\,\mathrm{e}^{\alpha} + (1 \mp 1)\,\mathrm{e}^{-\alpha}}{2} && \text{(C.7)}
\end{aligned}
$$

and finally

$$x = \mathrm{e}^{\pm\alpha}\,. \qquad \text{(C.8)}$$

For $\alpha > 0$ and $x^2 \leq 1$, only the root with negative exponent is valid. Therefore, applying the change of variables to the Eq. C.3 with the relation for x,

$$
\begin{aligned}
\ln(\cosh\alpha - \cos\beta) &= -\ln\left(2\,\mathrm{e}^{-\alpha}\right) - 2\sum_{n=1}^{\infty} \frac{\mathrm{e}^{-n\alpha}}{n}\cos n\beta \\
&= \alpha - \ln 2 - 2\sum_{n=1}^{\infty} \frac{\mathrm{e}^{-n\alpha}}{n}\cos n\beta \\
&= \mathrm{a}_0 + \sum_{n=1}^{\infty} \mathrm{a}_n \cos n\beta && \text{(C.9)}
\end{aligned}
$$

where

$$
\begin{aligned}
\mathrm{a}_0 &= \alpha - \ln 2, && \text{(C.10)}\\
\mathrm{a}_n &= -2\frac{\mathrm{e}^{-n\alpha}}{n}. && \text{(C.11)}
\end{aligned}
$$

Generalizing the above relations for all values of α,

$$
\begin{aligned}
\mathrm{a}_0 &= \sqrt{\alpha^2} - \ln 2, && \text{(C.12)}\\
\mathrm{a}_n &= -2\frac{\mathrm{e}^{-n\sqrt{\alpha^2}}}{n}. && \text{(C.13)}
\end{aligned}
$$

The left side of logarithmic term in the stream function is multiplied by the $(\cosh\alpha - \cos\beta)$ term. In order to expand this product, first expand the term multiplied by $\cos\beta$

$$
\begin{aligned}
\cos\beta\,\ln(\cosh\alpha - \cos\beta) &= \left(\mathrm{a}_0 + \sum_{n=1}^{\infty} \mathrm{a}_n \cos n\beta\right)\cos\beta \\
&= \mathrm{a}_0\cos\beta + \sum_{n=1}^{\infty} \mathrm{a}_n \cos\beta\cos n\beta. && \text{(C.14)}
\end{aligned}
$$

Using the identity $\cos\beta\cos n\beta = \frac{1}{2}\cos(n+1)\beta + \frac{1}{2}\cos(n-1)\beta$, the latter equation can be expressed as

$$\begin{aligned}\sum_{n=1}^{\infty} \mathrm{a}_n \cos\beta\cos n\beta &= \sum_{n=1}^{\infty} \mathrm{a}_n \left(\tfrac{1}{2}\cos(n+1)\beta + \tfrac{1}{2}\cos(n-1)\beta\right) \\ &= \frac{\mathrm{a}_1}{2}\cos 2\beta + \frac{\mathrm{a}_1}{2} + \frac{\mathrm{a}_2}{2}\cos 3\beta + \frac{\mathrm{a}_2}{2}\cos\beta \\ &\quad + \sum_{n=3}^{\infty} \mathrm{a}_n \left(\tfrac{1}{2}\cos(n+1)\beta + \tfrac{1}{2}\cos(n-1)\beta\right) \qquad \text{(C.15)}\end{aligned}$$

and with further simplifications

$$\sum_{n=1}^{\infty} \mathrm{a}_n \cos\beta\cos n\beta = \frac{\mathrm{a}_1}{2} + \frac{\mathrm{a}_2}{2}\cos\beta + \sum_{n=2}^{\infty}\left(\frac{\mathrm{a}_{n+1}}{2} + \frac{\mathrm{a}_{n-1}}{2}\right)\cos n\beta. \qquad \text{(C.16)}$$

Finally, the Eq. C.14 is written as

$$\begin{aligned}\cos\beta\,\ln(\cosh\alpha - \cos\beta) &= \mathrm{a}_0\cos\beta + \frac{\mathrm{a}_1}{2} + \frac{\mathrm{a}_2}{2}\cos\beta + \sum_{n=2}^{\infty}\left(\frac{\mathrm{a}_{n+1}}{2} + \frac{\mathrm{a}_{n-1}}{2}\right)\cos n\beta \\ &= \frac{\mathrm{a}_1}{2} + \left(\mathrm{a}_0 + \frac{\mathrm{a}_2}{2}\right)\cos\beta + \sum_{n=2}^{\infty}\left(\frac{\mathrm{a}_{n+1}}{2} + \frac{\mathrm{a}_{n-1}}{2}\right)\cos n\beta. \qquad \text{(C.17)}\end{aligned}$$

Proceeding with the term multiplied by $\cosh\alpha$

$$\begin{aligned}\cosh\alpha\,\ln(\cosh\alpha - \cos\beta) &= \mathrm{a}_0\cosh\alpha + \sum_{n=1}^{\infty} \mathrm{a}_n\cosh\alpha\cos n\beta \\ &= \mathrm{a}_0\cosh\alpha + \mathrm{a}_1\cosh\alpha\cos\beta \\ &\quad + \sum_{n=2}^{\infty} \mathrm{a}_n\cosh\alpha\cos n\beta. \qquad \text{(C.18)}\end{aligned}$$

Thus, the product $(\cosh\alpha - \cos\beta)\ln(\cosh\alpha - \cos\beta)$ is expressed as

$$\begin{aligned}&(\cosh\alpha - \cos\beta)\ln(\cosh\alpha - \cos\beta) = \\ &\quad = \cosh\alpha\,\ln(\cosh\alpha - \cos\beta) - \cos\beta\,\ln(\cosh\alpha - \cos\beta) \\ &\quad = \mathrm{a}_0\cosh\alpha + \mathrm{a}_1\cosh\alpha\cos\beta + \sum_{n=2}^{\infty} \mathrm{a}_n\cosh\alpha\cos n\beta \\ &\qquad - \frac{\mathrm{a}_1}{2} - \left(\mathrm{a}_0 + \frac{\mathrm{a}_2}{2}\right)\cos\beta - \sum_{n=2}^{\infty}\left(\frac{\mathrm{a}_{n+1}}{2} + \frac{\mathrm{a}_{n-1}}{2}\right)\cos n\beta, \qquad \text{(C.19)}\end{aligned}$$

and grouping the above equation in terms of $\cos n\beta$,

$$\begin{aligned}(\cosh\alpha - \cos\beta)\ln(\cosh\alpha - \cos\beta) &= \\ &= \left(a_0\cosh\alpha - \frac{a_1}{2}\right) + \left(a_1\cosh\alpha - a_0 - \frac{a_2}{2}\right)\cos\beta \\ &\quad + \sum_{n=2}^{\infty}\left(a_n\cosh\alpha - \frac{a_{n+1}}{2} - \frac{a_{n-1}}{2}\right)\cos n\beta. \qquad \text{(C.20)}\end{aligned}$$

And using the following relations

$$b_0 = a_0\cosh\alpha - \frac{a_1}{2}, \qquad \text{(C.21)}$$

$$b_1 = a_1\cosh\alpha - a_0 - \frac{a_2}{2}, \qquad \text{(C.22)}$$

$$b_n = a_n\cosh\alpha - \frac{a_{n+1}}{2} - \frac{a_{n-1}}{2} \qquad \text{(C.23)}$$

finally

$$(\cosh\alpha - \cos\beta)\ln(\cosh\alpha - \cos\beta) = b_0 + b_1\cos\beta + \sum_{n=2}^{\infty} b_n\cos n\beta. \qquad \text{(C.24)}$$

Appendix D

Eulerian to Lagrangian transformation

In order to tracking the path of a point in a flow field, is necessary to integrate the motion equations. The analytical solution expressed the flow field in an Eulerian form, therefore is necessary to have it in a Lagrangian form.

The velocity field can be expressed as

$$\mathbf{v} = \frac{d\mathbf{x}}{dt} = \frac{\partial \mathbf{x}}{\partial a}\,\frac{\partial a}{\partial t} + \frac{\partial \mathbf{x}}{\partial \beta}\,\frac{\partial \beta}{\partial t}, \tag{D.1}$$

or in terms of its components

$$v^{(k)} = \frac{\partial x^{(k)}}{\partial t}, \tag{D.2}$$

where the Cartesian vector of position $\mathbf{x}$ is function of the bipolar coordinates

$$\mathbf{x} = \frac{a\ \sin\beta}{\cosh\alpha - \cos\beta}\mathbf{i}_1 + \frac{a\ \sinh\alpha}{\cosh\alpha - \cos\beta}\mathbf{i}_2. \tag{D.3}$$

Then, replacing the Eq. D.3 into Eq. D.1, the following equations are obtained

$$\frac{dx^{(1)}}{dt} = -\frac{h^2}{a}\sinh\alpha\ \sin\beta\,\frac{d\alpha}{dt} + \left(h\ \cos\beta - \frac{h^2}{a}\sin^2\beta\right)\,\frac{d\beta}{dt} \tag{D.4}$$

and

$$\frac{dx^{(2)}}{dt} = \left(h\ \cosh\alpha - \frac{h^2}{a}\sinh^2\alpha\right)\,\frac{d\alpha}{dt} - \frac{h^2}{a}\sinh\alpha\ \sin\beta\,\frac{d\beta}{dt}, \tag{D.5}$$

where $h = \frac{a}{\cosh\alpha - \cos\beta}$ is the metric factor. The Cartesian components of the velocity in terms of the Bipolar components are

$$\mathbf{v} = \frac{h}{a}\begin{pmatrix} -\sinh\alpha\ \sin\beta\ u_\alpha + (\cosh\alpha\ \cos\beta - 1)\ u_\beta \\ (1-\cosh\alpha\ \cos\beta)\ u_\alpha - \sinh\alpha\ \sin\beta\ u_\beta \end{pmatrix}, \tag{D.6}$$

where

$$u_\alpha = \frac{1}{h}\,\frac{\partial\psi}{\partial\beta} \text{ and } u_\beta = -\,\frac{1}{h}\,\frac{\partial\psi}{\partial\alpha}. \tag{D.7}$$

Therefore, replacing into the Eq. D.2, the Eqs. D.6, D.4 and D.5, the following equations are obtained

$$\begin{aligned} -\sinh\alpha\ \sin\beta\ \frac{\partial\psi}{\partial\beta} - (\cosh\alpha\ \cos\beta - 1)\ \frac{\partial\psi}{\partial\alpha} &= \\ = -\ h^2\sinh\alpha\ \sin\beta\ \frac{d\alpha}{dt} &+ \left(a\ h\ \cos\beta - h^2\ \sin^2\beta\right)\ \frac{d\beta}{dt} \\ = -\ h^2\sinh\alpha\ \sin\beta\ \frac{d\alpha}{dt} &+ h^2\ (\cosh\alpha\ \cos\beta - 1)\ \frac{d\beta}{dt}, \end{aligned} \tag{D.8}$$

and

$$\begin{aligned} (1-\cosh\alpha\cos\beta)\ \frac{\partial\psi}{\partial\beta} + \sinh\alpha\ \sin\beta\ \frac{\partial\psi}{\partial\alpha} &= \\ = \left(a\ h\ \cosh\alpha - h^2\sinh^2\alpha\right)\ \frac{d\alpha}{dt} &- h^2\sinh\alpha\ \sin\beta\ \frac{d\beta}{dt} \\ = -\ h^2\ (\cosh\alpha\ \cos\beta - 1)\ \frac{d\alpha}{dt} &- h^2\sinh\alpha\ \sin\beta\ \frac{d\beta}{dt}. \end{aligned} \tag{D.9}$$

Solving these equations for $\frac{d\alpha}{dt}$ and $\frac{d\beta}{dt}$,

$$\frac{d\alpha}{dt} = \frac{1}{h^2}\ \frac{\partial\psi}{\partial\beta}, \tag{D.10a}$$

$$\frac{d\beta}{dt} = -\ \frac{1}{h^2}\ \frac{\partial\psi}{\partial\alpha}. \tag{D.10b}$$

Using the above Equations and the initial conditions

$$\alpha(t_0) = \alpha_0, \text{ and } \beta(t_0) = \beta_0, \tag{D.11}$$

a system of differential equations is obtained, that can be solved (numerically) for any *material point* $\mathbf{X} = (\alpha_0,\ \beta_0)$.

Appendix E

Articles

This Appendix contains the following articles:

Marco A. H. Reyes and Enrique Geffroy, "Study of low Reynolds number hydrodynamics generated by symmetric corotating two-roll mills," *Revista Mexicana de Física*, **46**(2), 135-147 (2000).

Marco A. H. Reyes and Enrique Geffroy, "A corotating two-roll mill for studies of two-dimensional elongational flows with vorticity," *Physics of Fluids*, **12**(10), 2372-2376 (2000).

INVESTIGACIÓN REVISTA MEXICANA DE FÍSICA 46 (2) 135–147 ABRIL 2000

Study of low Reynolds number hydrodynamics generated by symmetric corotating two-roll mills

Marco A.H. Reyes and Enrique Geffroy
Instituto de Investigaciones en Materiales, Universidad Nacional Autónoma de México
Cd. Universitaria, 04510 México, D.F., Mexico

Recibido el 4 de mayo de 1999; aceptado el 3 de diciembre de 1999

A Closed-form analytical solution for the creeping flow equations in bipolar cylindrical coordinates is presented and used to study the flow generated by a corotating symmetric two-roll mill. The flow field has a stagnation point where elongational flow conditions exist. The geometric characteristics of the mill define the ratio of vorticity to rate of deformation that exists at the stagnation point. The solution is based upon Jeffery's solution of the biharmonic equation obtained for the stresses on a plate [*Proc. Roy. Soc. London A* **101** (1922) 169]. The streamlines, the velocity field, the magnitude of the velocity gradient and other properties of the flow are obtained for the complete flow domain. For the region around the stagnation point, the calculated results show good agreement with the numerical predictions of Singh and Leal [*J. Rheology* **38** (1994) 485] and the experimental measurements of Wang *et al.* [*Phys. Fluids* **6** (1994) 3519]. This solution should be useful for investigations of the dynamics of drops, elastic capsules, or studies of chaotic advection, where exact solutions are necessary benchmarks.

Keywords: Elongational flows; two-roll mills; stokes flow

Se presenta una solución analítica cerrada para el flujo de Stokes generado por un molino de dos rodillos. El flujo generado tiene un punto de estancamiento en el centro del molino en donde existen condiciones de flujo elongacional. Las características geométricas del molino determinan la razón de vorticidad entre la rapidez de deformación que existe en el punto de estancamiento. La solución se basa en la solución de Jeffery de la ecuación biharmónica obtenida para los esfuerzos sobre una placa [*Proc. Roy. Soc. London A* **101** (1922) 169]. Las líneas de corriente, el campo de velocidades, la magnitud del gradiente de velocidades y otras propiedades del dominio completo del flujo también se dan. Para la región alrededor del punto de estancamiento, los resultados calculados tienen buena concordancia con las predicciones numéricas del Singh & Leal [*J. Rheology* **38** (1994) 485] y los resultados experimentales de Wang *et al.* [*Phys. Fluids* **6** (1994) 3519]. La solución será de utilidad para investigaciones en la dinámica de gotas, cápsulas elásticas o para estudios de advección caótica, en donde las soluciones exactas son patrones de referencia indispensables.

Descriptores: Flujo elongacional; molino de dos rodillos; flujo de stokes

PACS: 47.55.Dz; 47.80.+v; 83.50.-v

1. Introduction

The two-roll mill consists of two cylinders of equal radii, with colinear axes, and separated by a small distance. The analytical solution assumes a steady, two-dimensional flow as if generated by rollers of infinite length and rotating with equal angular velocities. Inertial terms are considered negligible. For corotating two-roll mills, there exists a stagnation point on the line between the cylinders' axes, with local kinematic conditions characteristic of elongational flow with some vorticity. According to Chong *et al.* [1], the stagnation point corresponds to a two-dimensional critical point where all three velocity components are zero, and the slope of the streamline is indeterminate. Unlike many other critical points, in the case of the two-roll mill the kinematics is defined only by the angular velocity of the rollers, and by their geometric aspect, *i.e.*, the cylinders' diameter and the separation between them. When identical cylinders rotate at the same speed, the stagnation point is located at equal distances from the centers of rotation. In this case, the gap between the rollers and their radii also determine the ratio of the rate of deformation to vorticity that exists in the neighborhood around the stagnation point. Hence, one of the interesting features of the elongational flow field generated by these mills is the fact that the solution takes into account, firstly, the presence of the rollers at a finite distance, and secondly, that the flow parameters are defined only by the mill's geometry.

Given that bipolar cylindrical coordinates are the natural reference frame for systems composed of two cylinders, an important set of flow devices have already been theoretically and experimentally studied. In 1922, G.B. Jeffery [2] presented a solution for the Stokes flow generated *inside the annular region of eccentric cylinders*. The solution prescribes the boundary of the cylinders by constant values of one of the bipolar coordinates [3, 4] for a stream-function that satisfies the biharmonic equation. Jeffery [2] gave also a solution for a *counter-rotating* two-roll mill in an unbounded fluid. For this flow, fluid is drawn in in one direction and driven out in the opposite direction. In 1925, R.A. Frazer [6] used Stokes' "principle of successive reflections" [4, 7] to study flows generated by two rotating cylinders in a viscous fluid. In particular, a solution is given for (a) the induced flow in a quiescent fluid and *valid only for specific* **ratios** *of the rates of rotation of the cylinders*, and (b) the steady motion with the fluid quiescent at infinity when the two-roll mill revolves like *a planetary system* about a particular focus situated on their line of centers. To the authors knowledge, no new solutions have been published ever since analyzing the problem of Stokes flow for a corotating two-roll mill. Here, a general solution is presented for the Stokes flow induced by two cylinders of equal radii and corotating at the same angular speed in a quiescent fluid, and capable of fast, accurate predictions.

The lack of analytical solutions for some configuration of mills has not hampered the use of these devices for experimental studies. In particular, two- and four-roll mills have been frequently used in the laboratory to study the effects of two-dimensional elongational flow upon embedded objects. These flow geometries provide the means of generating a complete class of strong flows at the critical point located between the cylinders, with a variety of possible rates of deformation applicable to deformable bodies. Astarita [8], and Olbricht *et al.* [9] have classified two-dimensional steady flows as strong or weak flows. Strong flows are those that have locally a larger rate of deformation than its vorticity, with weak flows being those dominated by vorticity; simple shear flows correspond to the upper limit of weak flows and have a ratio of rate of deformation to vorticity equal to one. Hence strong flow can cause large deformations to an embedded deformable body in contrast with the small deformations achievable only with steady, weak flows. Furthermore, the residence time for an embedded object at the stagnation point can be extremely long, allowing studies of its dynamics under a large set of known conditions.

These latter characteristics make the two- and four-roll mills useful devices for many studies in low Reynolds number hydrodynamics. Indeed, these mills have been used to study the dynamics of drops, capsule, emulsions, etc., and more recently the dynamics of chaotic or mixing systems, with significant responses observed when using these strong flows as compared to simple shear or purely extensional flows. In 1932, G.I. Taylor [10, 11] performed some of the earliest experiments of a drop deformation due to a strong flow field generated by a four-roll mill. More recently, Leal and coworkers [12–15] have used a computer-controlled four-roll mill to study the dynamics of drops suspended in a viscous fluid. These studies have provided a clearer understanding of the effects of the viscosities of the fluids, surface tension, surfactant additives, etc. Rallison [16] and Stone [17] have recently summarized the theoretical, experimental and numerical studies of the dynamics of drops and bubbles in well-characterized flows with ratios of the rate of deformation to vorticity well in excess of the characteristic value for simple shear flow. Finally, Chang and Olbricht [18] have studied the dynamics of breakup of *elastic capsules* filled with a liquid under purely elongational and simple shear flow conditions. Ottino and coworkers [19] have recently studied Stokes flows generated by a *blinking* two-roll mill contained inside a third rotating cylinder. However and because of the intrinsic noise of numerical simulations, Ottino and collaborators [19] emphasize the need for analytical solutions of the flow field of complex Stokes flows: small changes in the numerical calculated velocity field can produce very different advection patterns. Finally, Leal and coworkers [20–22] have used a two- and four-roll mill configuration to study the flow field of non-Newtonian fluids subjected to elongational flows with vorticity. Among those studies, special emphasis has been given to studies of the dynamics of polymeric liquids [23] its optical properties and the evaluation of constitutive equations for fluids subjected to strong flows. Hence the spectrum of applications of the analytical solution of the Stokes flow of two-roll mills can provide useful insight for a large number of problems in fluid mechanics. Also these studies have relevance to a large number of industrial applications (*e.g.*, see Stone [17]).

Given the usefulness of two- and four-roll mills, for the study of a slow, strong flow, it is now important to emphasize the different options that these two systems offer to the experimentalist. For the four-roll mill, the rotational speed of the cylinders sets the shear rate, and the ratio of the speeds of next to each other rollers sets the ratio of vorticity to rate of deformation that exist at the stagnation point. However, in contrast with the two-roll mill, and on one hand, the four-roll mill requires an experimental determination of the proportionality constants that express the shear rate as a function of the speed of the cylinders. Furthermore, there is no analytical solution for the Stokes flow generated with a four-roll mill when the position and size of the cylinders needs to be taken into account. On the other hand, there is no need to vary the geometrical form of the device in order to vary the ratio of the rate of deformation to vorticity that exists at the stagnation point as needed with the two-roll mill set-up, a condition that has prompted an undue disregard for the two-roll mill hydrodynamics. This apparent drawback of the experimental studies reported until now is mainly due to the concomitant perturbations to the two-dimensionality of the flow as a result of presence of boundaries along the axes of rotation of the cylinders, which is dependent of the ratio of cylinders' length to the gap between them. These have been important limitations to experimental studies using strong flows with large vorticity such as those generated by a two-roll mill, because comparisons of experimental data against theoretical or numerical results are often difficult to correlate. However for many studies, the application of similar techniques to those used by Bentley and Leal [12] can reduce significantly the adverse effects of boundaries in two-roll mills. Finally, the four-roll mill only requires to change the relative speed of diagonally opposed rollers to modify the ratio of vorticity to rate of deformation. It generates a well defined flow when small vorticities are needed, but does not provide an adequate flow field when the ratio of speeds of next to each other cylinders is large; *i.e.*, when ratios of rate of deformation to vorticity have values close to one. Under these circumstances, the two-roll mill is a better device to generate 2-D strong flows.

The contents of this paper are as follows. In Sect. 2 the mathematical solution for the flow induced by a corotating two-roll mill is presented in cylindrical bipolar coordinates.

Jeffery's solution for the biharmonic equation together with the symmetry properties of the flow field are used to obtain the Fourier series expansion of the stream function. The series allows the calculation of the flow properties in closed-form to the required precision; the convergence of the truncated series is analyzed with respect to the accuracy of the prediction of flow parameters. Finally in Sect. 3, the flow field in the neighborhood of the stagnation point is studied, giving emphasis to the most relevant parameters for the study of embedded bodies. For the flow about the stagnation point, Stokes flow solution is compared with the solution of Dunlap [24] valid only locally. Furthermore, these analytical results are compared with numerical results [20] and experimental measurements of the principal components of the velocity gradient tensor [22].

2. The solution for creeping flows generated by two-roll mills

2.1. Geometry, and governing equations in cylindrical bipolar coordinates

The corotating two roll mill is best described using cylindrical bipolar coordinates. Figure 1 shows a two-roll mill with parallel cylinders of equal radii R, and separated by a gap g. In cylindrical bipolar coordinates a point on the plane $\mathrm{P}(x, y)$ is represented by two vectors $\mathbf{r}_A$ and $\mathbf{r}_B$, plus two angles θ_A, and θ_B respectively, drawn from two fixed points A and B which are symmetrically located from the origin at a distance d. In this manner the bipolar coordinates (α, β, z') are

$$\alpha = \ln\left(\frac{\|\mathbf{r}_B\|}{\|\mathbf{r}_A\|}\right) \quad \text{and} \quad \beta = \theta_A - \theta_B,$$

with the 3-dimensional space (x, y, z) described by

$$\mathbf{P} = \frac{d\sin\beta}{\cosh\alpha - \cos\beta}\mathbf{i}_1 + \frac{d\sinh\alpha}{\cosh\alpha - \cos\beta}\mathbf{i}_2 + z\,\mathbf{i}_3, \qquad (1)$$

where $\mathbf{P}$ is a point, and $\{\mathbf{i}_i\}$ is the Cartesian base. This is a *conjugate* cylindrical coordinate system, and hence it is an *orthogonal* curvilinear coordinate system perpendicular to the z-axis. The metric factor h can be expressed in terms of the metric coefficients $\mathbf{g}_k$

$$\mathbf{g}_1 = \frac{\partial\mathbf{P}}{\partial\alpha} = -\frac{d\sinh\alpha\sin\beta}{(\cosh\alpha - \cos\beta)^2}\mathbf{i}_1 + \frac{d(1 - \cosh\alpha\cos\beta)}{(\cosh\alpha - \cos\beta)^2}\mathbf{i}_2, \quad (2)$$

$$\mathbf{g}_2 = \frac{\partial\mathbf{P}}{\partial\beta} = \frac{d(\cosh\alpha\cos\beta - 1)}{(\cosh\alpha - \cos\beta)^2}\mathbf{i}_1 - \frac{d\sinh\alpha\sin\beta}{(\cosh\alpha - \cos\beta)^2}\mathbf{i}_2, \quad (3)$$

$$\mathbf{g}_3 = \frac{\partial\mathbf{P}}{\partial z'} = \mathbf{i}_3; \quad (4)$$

such that

$$\frac{\partial\mathbf{P}}{\partial q_k} = \frac{\partial x}{\partial q_k}\mathbf{i}_1 + \frac{\partial y}{\partial q_k}\mathbf{i}_2 + \frac{\partial z}{\partial q_k}\mathbf{i}_3, \quad (q_k = \alpha, \beta, \text{or } z'). \quad (5)$$

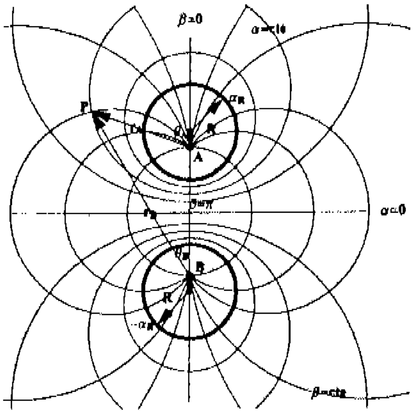

FIGURE 1. The configuration of the two-roll mill in cylindrical bipolar coordinates (α, β, z'). For α = constant, a family of eccentric circles above and below the x-axis is generated. For constant values of β a second family of circles is generated with centers on the x-axis. All circles (β = constant) intersect at the point d along the y-axis, which also corresponds to the limit of circles when α tends to ∞. Two cylinders of radii R are shown as $\alpha = \alpha_R$. The center of the xy coordinate system corresponds to $(\alpha = 0, \beta = \pi)$.

And the metric tensor is

$$(g_{kl}) = \begin{pmatrix} \dfrac{d^2}{(\cosh\alpha - \cos\beta)^2} & 0 & 0 \\ 0 & \dfrac{d^2}{(\cosh\alpha - \cos\beta)^2} & 0 \\ 0 & 0 & 1 \end{pmatrix}$$

so that

$$g_{11} = g_{22} = h_{11}^2 = h_{22}^2 = h^2. \qquad (6)$$

Furthermore, this coordinate system is characterized by the following relations

$$x^2 + y^2 - d^2 - 2dx\cot\beta = 0, \qquad (7)$$

and

$$(y - d\coth\alpha)^2 + x^2 = d^2\mathrm{csch}^2\alpha. \qquad (8)$$

Hence, for β = constant (with values between $0 \le \beta \le 2\pi$) a family of circles is generated with their centers located on the x-axis at $(d\cot\beta, 0)$, and with radii equal to $d\csc\alpha$. Each circle passes through the points A and B. For α = constant, a second set of circles is generated with their centers located on the y-axis at $(0, d\coth\alpha)$ and radii $d\,\mathrm{csch}\,\alpha$. In this manner, at every point $\mathbf{P}(x, y)$ a circle of each family intersect *orthogonally*, allowing its representation with a unique set (α, β). The point A corresponds to $\alpha = +\infty$ and B to $\alpha = -\infty$. $\beta = 0$ corresponds to vertical lines above A and below B, and $\beta = \pi$ generates the segment (A, B). The origin corresponds to $\alpha = 0$ and $\beta = \pi$, and a point at infinity is defined by $\alpha, \beta = 0$. A more detailed description of the bipolar coordinate system is given in Appendix A of Ref. 4.

The two-roll mill is described by selecting constant values of $\alpha = \pm\, \alpha_R$, with α playing the role of the tangential coordinate, and β being the normal coordinate to the cylinders. The geometric aspects of the two-roll mill are defined by

$$\frac{g}{2R} = \cosh \alpha_R - 1, \quad \text{and} \quad d = R \sinh \alpha_R. \tag{9}$$

Now, consider an isothermal, incompressible, Newtonian fluid, under laminar flow conditions generated by a two-roll mill. The fluid velocity $\mathbf{u}$ and the hydrodynamic pressure P are governed by the continuity and the Navier-Stokes equations

$$\nabla \cdot \mathbf{u} = 0, \qquad \frac{D\mathbf{u}}{Dt} = -\frac{1}{\rho}\nabla P + \nu \nabla^2 \mathbf{u},$$

where ρ is the density, and ν is the kinematic viscosity of the fluid. Let l_c and U_c be the characteristic length and velocity of the flow such that a characteristic Reynolds number is $\mathrm{Re} = \rho l_c U_c/\mu$. Then, the *dimensionless* governing equations for a quasi-steady, creeping flow are

$$\nabla^2 \mathbf{u} - \nabla p = 0, \tag{10}$$

$$\nabla \cdot \mathbf{u} = 0. \tag{11}$$

This equation is exactly valid for Reynolds number equal to zero, and is also a good approximation for small values of the Reynolds number. For a two-dimensional flow a simpler equation prescribes the creeping flow in terms of the stream function. That is, the velocity components u and v along the x and y directions can be expressed in terms of the stream function as

$$u = \frac{\partial \psi}{\partial y}, \quad v = -\frac{\partial \psi}{\partial x},$$

and the vorticity ω as

$$\omega = \frac{\partial v}{\partial x} - \frac{\partial u}{\partial y} = -\nabla^2 \psi.$$

With the above equations, the pressure can be eliminated from Eq. (10) and

$$\frac{1}{2}\mathrm{Re}\left(\frac{\partial \omega}{\partial t} + \frac{\partial \psi}{\partial y}\frac{\partial \omega}{\partial x} - \frac{\partial \psi}{\partial x}\frac{\partial \omega}{\partial y}\right) = \nabla^2 \omega,$$

and the solution of the flow field must satisfy the biharmonic equation

$$\nabla^4 \psi = 0. \tag{12}$$

2.2. Jeffery's Stream Function of a two-roll mill in bipolar coordinates

In 1920, Jeffery [5] presented a solution for the biharmonic equation in bipolar coordinates used to study the stresses generated on a flat plate with round holes. In 1922, Jeffery used this solution to study the internal flow field generated by two eccentric circular cylinders. The stream function proposed is given as a Fourier series expansion

$$\begin{aligned}\frac{\psi}{h} &= A_0 \cosh \alpha + B_0 \alpha (\cosh \alpha - \cos \beta) + C_0 \sinh \alpha \\ &\quad + D_0 \alpha \sinh \alpha + K (\cosh \alpha - \cos \beta) \ln (\cosh \alpha - \cos \beta) \\ &\quad + [A_1 \cosh (2\alpha) + B_1 + C_1 \sinh (2\alpha)] \cos \beta \\ &\quad + [A_1' \cosh (2\alpha) + C_1' \sinh (2\alpha)] \sin \beta \\ &\quad + \sum_{n=2}^{\infty} [\phi_n (\alpha) \cos (n\beta) + \phi_n' (\alpha) \sin (n\beta)],\end{aligned} \tag{13}$$

where the metric factor

$$h = \frac{d}{(\cosh \alpha - \cos \beta)}, \tag{14}$$

and the coefficient of the Fourier series are

$$\begin{aligned}\phi_n (\alpha) &= A_n \cosh (n+1)\, \alpha + B_n \cosh (n-1)\, \alpha \\ &\quad + C_n \sinh (n+1)\, \alpha + D_n \sinh (n-1)\, \alpha,\end{aligned} \tag{15}$$

and

$$\begin{aligned}\phi_n' (\alpha) &= A_n' \cosh (n+1)\, \alpha + B_n' \cosh (n-1)\, \alpha \\ &\quad + C_n' \sinh (n+1)\, \alpha + D_n' \sinh (n-1)\, \alpha.\end{aligned} \tag{16}$$

Given that the two-roll mill has equal cylinders rotating at equal speeds, the flow field must be anti-symmetric with respect to reflections upon the x- or y-axis as shown in Fig. 2. In order to take advantage of the simplification due to the symmetry properties, the velocity field in terms of the stream function is needed. Hence,

$$\mathbf{u} = \nabla \times \psi = \frac{1}{h^2}\begin{vmatrix} h\mathbf{e}_1 & h\mathbf{e}_2 & \mathbf{e}_3 \\ \dfrac{\partial}{\partial \alpha} & \dfrac{\partial}{\partial \beta} & \dfrac{\partial}{\partial z} \\ 0 & 0 & \psi \end{vmatrix} = h\frac{\partial \psi}{\partial \beta}\mathbf{e}_1 - \frac{1}{h}\frac{\partial \psi}{\partial \alpha}\mathbf{e}_2$$

The velocity component tangential to the surface of the cylinders is

$$u_\alpha = \frac{1}{h}\frac{\partial \psi}{\partial \beta} = \frac{\partial}{\partial \beta}\left(\frac{\psi}{h}\right) - \left(\frac{\psi}{h}\right)\frac{1}{h}\frac{\partial}{\partial \beta}\left(\frac{1}{h}\right); \tag{17}$$

that is,

$$\begin{aligned}u_\alpha &= B_0 \alpha \sin \beta + K[\ln(\cosh \alpha - \cos \beta) + 1] \sin \beta \\ &\quad - (A_1 \cosh 2\alpha + B_1 + C_1 \sinh 2\alpha) \sin \beta \\ &\quad + (A_1' \cosh 2\alpha + C_1' \sinh 2\alpha) \cos \beta \\ &\quad + \sum_{n=2}^{\infty} \{-n[A_n \cosh(n+1)\alpha + B_n \cosh(n-1)\alpha \\ &\quad + C_n \sinh(n+1)\alpha + D_n \sinh(n-1)\alpha] \sin n\beta \\ &\quad + n[A_n' \cosh(n+1)\alpha + B_n' \cosh(n-1)\alpha \\ &\quad + C_n' \sinh(n+1)\alpha + D_n' \sinh(n-1)\alpha] \cos n\beta\} \\ &\quad - \frac{\psi}{h}\frac{\sin \beta}{\cosh \alpha - \cos \beta}.\end{aligned} \tag{18}$$

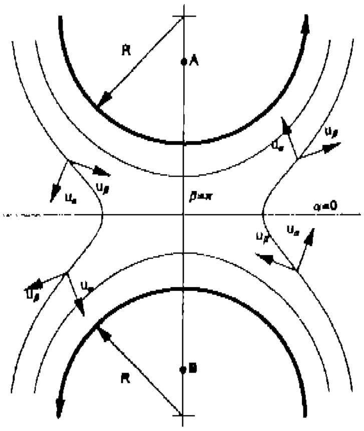

FIGURE 2. The velocity field and its velocity components u_α, and u_β in bipolar coordinates. The symmetry lines $\alpha = 0$, and $\beta = \pi$ are shown. The symmetry properties of the stream function are obtained using the symmetry properties of u_α, and u_β near the stagnation point where the components are parallel to the Cartesian coordinates.

The velocity component normal to the cylinders

$$u_\beta = -\frac{1}{h}\frac{\partial\psi}{\partial\alpha} = -\frac{\partial}{\partial\alpha}\left(\frac{\psi}{h}\right) + \left(\frac{\psi}{h}\right) h \frac{\partial}{\partial\alpha}\left(\frac{1}{h}\right), \tag{19}$$

and

$$\begin{aligned} u_\beta = {} & -A_0 \sinh\alpha - B_0\left[(\cosh\alpha - \cos\beta) + \alpha\sinh\alpha\right] \\ & - C_0\cosh\alpha - D_0(\alpha\cosh\alpha + \sinh\alpha) \\ & - K\sinh\alpha\,\left[1 + \ln(\cosh\alpha - \cos\beta)\right] \\ & - (2A_1\sinh 2\alpha + 2C_1\cosh 2\alpha)\cos\beta \\ & - (2A_1'\sinh 2\alpha + 2C_1'\cosh 2\alpha)\sin\beta \\ & - \sum_{n=2}^{\infty}\{[A_n(n+1)\sinh(n+1)\alpha \\ & + B_n(n-1)\sinh(n-1)\alpha \\ & + C_n(n+1)\cosh(n+1)\alpha \\ & + D_n(n-1)\cosh(n-1)\alpha]\cos n\beta \\ & + [A_n'(n+1)\sinh(n+1)\alpha \\ & + B_n'(n-1)\sinh(n-1)\alpha \\ & + C_n'(n+1)\cosh(n+1)\alpha \\ & + D_n'(n-1)\cosh(n-1)\alpha]\sin n\beta\} \\ & + \frac{\psi}{h}\frac{\sinh\alpha}{\cosh\alpha - \cos\beta}. \end{aligned} \tag{20}$$

In Fig. 2 the symmetry properties of the velocity field are shown; in particular for the components of the velocity field u_α, and u_β, which allow an initial reduction of the coefficients that must be determined. That is, at the center $(\alpha = 0, \beta = \pi)$ there is a stagnation point. This "stagnation point" exists along an axis parallel to the cylinders axes, and therefore should be strictly referred to as the *stagnation line* of the flow field. For simplicity it is referred here as the stagnation point, although it may refer to a line running along the flow and perpendicular to the curvilinear coordinate system. On the xy-plane and above the stagnation point, for a counter-clockwise rotation of cylinders, material points move to the left, while below it, all material points move towards the opposite direction with the same speeds as the one located at the same distance above the center. This flow pattern implies that for those points near the horizontal line $(\alpha \simeq 0)$ the velocity component u_α, when α tends to 0 from above, $u_\alpha(0^+)$, must have the same value and direction as when α tends to 0 from below $u_\alpha(0^-)$. Also, the velocity component u_β must have equal values but opposite sign when crossing the horizontal line. That is,

$$\forall\beta: \quad \left\{ \begin{array}{c} u_\alpha(\alpha \to 0^-) = u_\alpha(\alpha \to 0^+) \\ u_\beta(\alpha \to 0^-) = -u_\beta(\alpha \to 0^+) \end{array} \right\}.$$

A similar condition exists between the left and right side of the flow field: material points on the right side are displaced upwards on the right and downward on the left side. In the neighborhood around the line joining the centers of the cylinders (when $\beta \simeq \pi$), the velocity component u_α, when β tends to π from the right, $u_\alpha(\pi^+)$, must have the same value and but opposite direction as when β tends to π from the left $u_\alpha(\pi^-)$. Also, the velocity component parallel to the x-axis, u_β, must have the same value when β tends to π from the right and left. Hence,

$$\forall\alpha: \quad \left\{ \begin{array}{c} u_\alpha(\beta \to \pi^-) = -u_\alpha(\beta \to \pi^+) \\ u_\beta(\beta \to \pi^-) = u_\beta(\beta \to \pi^+) \end{array} \right\}.$$

Imposing these symmetry conditions upon the velocities implies that the coefficients $B_0, C_0, C_1, C_n, C_n', D_n$, and D_n' must all be equal to zero. Then, the stream function reduces to

$$\begin{aligned} \frac{\psi}{h} = {} & A_0\cosh\alpha + D_0\alpha\sinh\alpha \\ & + K(\cosh\alpha - \cos\beta)\ln(\cosh\alpha - \cos\beta) \\ & + \sum_{n=1}^{\infty}[A_n\cosh(n+1)\alpha + B_n\cosh(n-1)\alpha]\cos n\beta. \end{aligned} \tag{21}$$

Using Eq. (A.7), the logarithmic term can be expressed as a cosine series and the stream function is

$$\begin{aligned} \frac{\psi}{h} = {} & A_0\cosh\alpha + D_0\alpha\sinh\alpha \\ & + K\Big(b_0 + b_1\cos\beta + \sum_{n=2}^{\infty} b_n\cos n\beta\Big) \\ & + \sum_{n=1}^{\infty}[A_n\cosh(n+1)\alpha + B_n\cosh(n-1)\alpha]\cos n\beta, \end{aligned} \tag{22}$$

with coefficients $b_0 + b_1$ and b_n given by Eqs. (A.8).

2.3. Boundary conditions satisfied by the stream function

On the cylinder's walls, the boundary condition prescribing the impenetrability of the surface implies that the velocity component normal to the roller is zero; that is

$$u_\alpha\left(\alpha_R\right) = \left|\frac{1}{h}\frac{\partial\psi}{\partial\beta}\right|_{\alpha_R} = 0, \qquad (23)$$

where α_R is the cylinder radius given in bipolar coordinates. The dynamic no-slip boundary condition is

$$u_\beta\left(\alpha_R\right) = -\left|\frac{1}{h}\frac{\partial\psi}{\partial\alpha}\right|_{\alpha_R} = \omega R, \qquad (24)$$

with ω being the angular velocity in radians, and R is the cylinder radius. At infinity, the fluid must remain at rest and

$$\psi\left(\alpha \to 0, \beta \to 0\right) = 0 \qquad (25)$$

for the velocity to be $\mathbf{u}\left(\alpha \to 0, \beta \to 0\right) = 0$. That is, the stream function valued far from the cylinders implies that

$$A_0 + \sum_{n=1}^{\infty}\left(A_n + B_n\right) = 0. \qquad (26)$$

The condition of no-flow through the cylinder's walls is set by a constant value for the stream function, say M, so that

$$\begin{aligned}\frac{1}{h}\psi\left(\alpha_R, \beta\right) = \left(\frac{\cosh\alpha - \cos\beta}{d}\right)M \\ = A_0\cosh\alpha_R \\ + K\left[b_0 + b_1\cos\beta + \sum_{n=2}^{\infty} b_n\cos n\beta\right] \\ + D_0\alpha_R\sinh\alpha_R \\ + \sum_{n=1}^{\infty}\left[A_n\cosh(n+1)\alpha_R\right. \\ \left. + B_n\cosh(n-1)\alpha_R\right]\cos n\beta \qquad (27)\end{aligned}$$

Collecting those terms of same $\cos n\beta$ order the first system of $n+2$ equations is obtained

$$\left(A_0 - \frac{M}{d}\right)\cosh\alpha_R + D_0\,\alpha_R\sinh\alpha_R + K\,b_0 = 0, \qquad (28)$$

$$\frac{M}{d} + A_1\cosh 2\alpha_R + B_1 + Kb_1 = 0, \qquad (29)$$

and for $n \geq 2$,

$$A_n\cosh(n+1)\alpha_R + B_n\cosh(n-1)\alpha_R + Kb_n = 0. \qquad (30)$$

The no-slip boundary condition on the cylinders surface, $u_\beta\left(\alpha_R\right) = \omega R$, implies

$$\begin{aligned}\omega R = -A_0\sinh\alpha_n \\ - D_0\left(\alpha_R\cosh\alpha_R + \sinh\alpha_R\right) + \frac{M}{d}\sinh\alpha_R \\ - K\sinh\alpha_R\Big(1 + a_0 + \sum_{n=1}^{\infty} a_n\cos n\beta\Big) \\ - \sum_{n=1}^{\infty}\left[A_n(n+1)\sinh(n+1)\alpha_R\right. \\ \left. + B_n(n-1)\sinh(n-1)\alpha_R\right]\cos n\beta. \qquad (31)\end{aligned}$$

And collecting terms of equal $\cos n\beta$ order, a second system of $n+2$ equations is obtained,

$$\begin{aligned}A_0\sinh\alpha_R + D_0\left(\alpha_R\cosh\alpha_R + \sinh\alpha_R\right) \\ + K\sinh\alpha_R\left(1 + a_0\right) - \frac{M}{d}\sinh\alpha_n + \omega R = 0, \qquad (32)\end{aligned}$$

$$2A_1\sinh 2\alpha_R + Ka_1\sinh\alpha_R = 0, \qquad (33)$$

and for $n \geq 2$,

$$\begin{aligned}A_n(n+1)\sinh(n+1)\alpha_R \\ + B_n(n-1)\sinh(n-1)\alpha_R + Ka_n\sinh\alpha_R = 0. \qquad (34)\end{aligned}$$

There are $2n+4$ unknowns: A_0, A_1, A_n, B_1, B_n, D_0, K and M; but only $2n+3$ equations. Given that M corresponds to the value of the stream function ψ on the surface of the cylinders, set arbitrarily by the computation, any constant value can be used. Therefore, the solution consists of a system of $2n+3$ equations and unknowns. Equations (30) and (34) imply that

$$\frac{A_n}{K} = \frac{(n+1) - e^{-2n\alpha_R} - ne^{-2\alpha_R}}{n(n+1)\left[n\sinh 2\alpha_R + \sinh 2n\alpha_R\right]}, \qquad (35a)$$

$$\frac{B_n}{K} = \frac{(n-1) + e^{-2n\alpha_R} - ne^{2\alpha_R}}{n(n-1)\left[n\sinh 2\alpha_R + \sinh 2n\alpha_R\right]}, \qquad (35b)$$

The remaining coefficients are

$$A_0 = \frac{2R\omega\alpha_R\sinh\alpha_R - 2K\left[b_0\left(\sinh\alpha_R + \alpha_R\cosh\alpha_R\right) - \left(1 + a_0\right)\alpha_R\sinh^2\alpha_R\right]}{2\alpha_R + \sinh 2\alpha_R}, \qquad (36a)$$

$$A_1 = -\frac{Ka_1\operatorname{sech}\alpha_R}{4}, \qquad (36b)$$

$$B_1 = -Kb_1 + \frac{Ka_1\coth 2\alpha_R\sinh\alpha_R}{2}, \qquad (36c)$$

$$D_0 = -\frac{A_0\cosh\alpha_R + Kb_0}{\alpha_R\sinh\alpha_R}. \qquad (36d)$$

The last coefficient K can be expressed using Eqs. (27), (36), and (37) as follows:

$$A_0 = -\sum_{n=1}^{\infty}(A_n + B_n) = -A_1 - B_1 - \sum_{n=2}^{\infty} K\left(\frac{A_n}{K} + \frac{B_n}{K}\right) \quad (37)$$

and

$$A_0 + A_1 + B_1 = -K\sum_{n=2}^{\infty}\left(\frac{A_n}{K} + \frac{B_n}{K}\right) \equiv -KS, \quad (38)$$

where

$$S = \sum_{n=2}^{\infty} \frac{(-2n)e^{-2n\alpha_R} + \left(n-n^2\right)e^{-2\alpha_R} + \left(n+n^2\right)e^{2\alpha_R}}{n\,(n-1)(n+1)\,(n\sinh 2\alpha_R + \sinh 2n\alpha_R)}. \quad (39)$$

Consequently,

$$\begin{aligned} K = -4R\omega\alpha_R \sinh\alpha_R \Big[& 2S\,(2\alpha_R + \sinh 2\alpha_R) \\ & + 4\alpha_R\,(a_0+1)\sinh^2\alpha_R - 4b_0\,(\sinh\alpha_R + \alpha_R\cosh\alpha_R) \\ & - 2b_1\,(2\alpha_R + \sinh 2\alpha_R) \\ & + a_1\Big(2\alpha_R \coth 2\alpha_R \sinh\alpha_R - \alpha_R \operatorname{sech}\alpha_R \\ & - \frac{3}{2}\sinh\alpha_R + \frac{1}{2}\sinh 3\alpha_R\Big)\Big]^{-1}. \quad (40) \end{aligned}$$

Finally, the explicit form of the stream function for Stokes flow generated by the two-roll mill is given by Eqs. (23), (35), (36), and (40). Figure 3 shows the stream functions for two different geometries of the two-roll mill. The geometrical parameters for these mills corresponds to those given by Geffroy and Leal [25] where the distance between the cylinder axes is maintained fixed and the cylinder's radii changes. That is, the value for the parameter d takes a different value for every pair of rollers.

3. The Stokes flow about the stagnation point

The kinematic conditions at the stagnation point located between the cylinders is perhaps the region of the flow field most frequently used until now for studies of the dynamics of non-Newtonian fluids. For example, Dunlap [24] studied the dynamics of various dilute polymeric solutions under the flow conditions that exist in the neighborhood of the stagnation point assuming kinematics similar to those prevalent for Newtonian fluids. In particular, the correlation of polymer deformations induced by the flow and the rates of deformation applied by the flow is a critical parameter for those experiments. More recently, Wang *et al.* [22] have studied the flow field of polymeric liquids using the homodyne light scattering technique [26] (a method capable of measuring directly the most relevant flow parameters) in order to determine the flow conditions that affect the deformation of the polymeric structure. One of the most relevant aspect of these studies is the fact that the *flow-type parameter* and the *shear rate* of the flow at the stagnation point have been directly related to the rate of rotation of the rollers and the geometry of the two-roll mill.

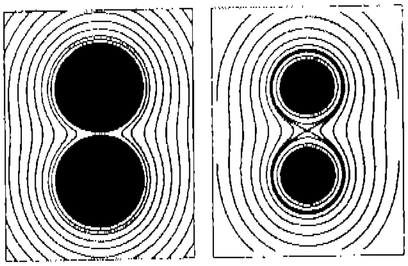

FIGURE 3. The streamlines for two different geometries of the two-roll mill. The distance from the center to the axes of the cylinders is 0.017 m for both devices. The cylinder's radii are 0.01665 m and 0.01075 m, for the left and right configuration respectively, which corresponds to rollers A and I of Table I.

3.1. Shear rate and value of the flow-type parameter at the stagnation point

With the equation for the stream function it is possible to obtain a simpler expression, valid in the neighborhood of the stagnation point, by using a Taylor series expansion about $\alpha = 0$ and $\beta = \pi$ and keeping only terms up to second order. That is, $y \cong d\alpha/2$ and $x \cong d\,(\pi - \beta)\,/2$, and Eq. (23) becomes

$$\begin{aligned} \left[\frac{2 - 2x^2 + 2y^2}{d}\right]\psi = {} & A_0\left(1+2y^2\right) + 4y^2 D_0 \\ & + K\left[4y^2\left(\frac{1 - x^2 - \ln 2}{8}\right) + 2\ln 2 - 2x^2\,(1+\ln 2)\right] \\ & + \sum_{n=1}^{\infty}(-1)^n\left(1 - 2n^2x^2\right)\left\{A_n\left[1 + 2y^2(n+1)^2\right]\right. \\ & \left. + B_n[1 + 2y^2(n-1)^2]\right\}. \quad (41) \end{aligned}$$

In this equality, the left term is proportional to $\left(1 - x^2 + y^2\right)$. Multiplying both sides by $\left(1 + x^2 - y^2\right)$, then the left side is $\left(1 - x^2 + y^2\right)\left(1 + x^2 - y^2\right) = 1 - x^4 + 2x^2y^2 - y^4 \approx 1$, valid up to quartic order. Therefore, Eq. (41) becomes

$$\begin{aligned} \frac{2}{d}\left(1 - x^2 + y^2\right)\left(1 + x^2 - y^2\right)\psi \approx \frac{2\psi}{d} \\ \approx A_0 + 2K\ln 2 + \sum_{n=1}^{\infty} i^{2n}\,(A_n + B_n) \\ + y^2\Big(A_0 + 4D_0 + 2K \\ + \sum_{n=1}^{\infty} i^{2n}\left\{2\left[A_n(n+1)^2 + B_n(n-1)^2\right] - [A_n + B_n]\right\}\Big) \\ + x^2\Big\{A_0 - 2K + \sum_{n=1}^{\infty} i^{2n}\left[(A_n + B_n) - 2n^2\,(A_n + B_n)\right]\Big\}. \end{aligned}$$

The stagnation point is characterized by a saddle point, which implies that the coefficients for the x^2 and y^2 have opposite signs. In this manner, the stream function can then be expressed as a 2-dimensional hyperbolic flow $y^2 - \lambda x^2 = c$, with

$$\lambda = -\frac{A_0 - 2K + \sum_{n=1}^{\infty} i^{2n}[(A_n + B_n) - 2n^2(A_n + B_n)]}{A_0 + 4D_0 + 2K + \sum_{n=1}^{\infty} i^{2n}\{2[A_n(n+1)^2 + B_n(n-1)^2] - (A_n + B_n)\}}, \tag{42}$$

and

$$\epsilon = \frac{(2/d)\psi - A_0 - 2K\ln 2 - \sum_{n=1}^{\infty} i^{2n}(A_n + B_n)}{A_0 + 4D_0 + 2K + \sum_{n=1}^{\infty} i^{2n}\{2[A_n(n+1)^2 + B_n(n-1)^2] - (A_n + B_n)\}}. \tag{43}$$

Furthermore, given the linear character of Stokes equations, the velocity field at the stagnation point can be expressed by

$$\mathbf{u} \cong \nabla\mathbf{u}^T \cdot \mathbf{x}, \tag{44}$$

where

$$\begin{bmatrix} u_x \\ u_y \end{bmatrix} \cong \dot\gamma \begin{bmatrix} 0 & 1 \\ \lambda & 0 \end{bmatrix} \begin{bmatrix} x \\ y \end{bmatrix},$$

and

$$\nabla\mathbf{u}\Big|_{(\alpha=0,\beta=\pi)} = \begin{bmatrix} 0 & \dfrac{2}{d}\dfrac{\partial u_\alpha}{\partial\beta} \\ \dfrac{2}{d}\dfrac{\partial u_\beta}{\partial\alpha} & 0 \end{bmatrix}$$

The expansion for u_α and u_β as a Taylor series up to quadratic terms and about $(\alpha = 0, \beta = \pi)$ is

$$u_\alpha = \frac{x}{d}\left\{ -A_0 + 2K + \sum_{n=1}^{\infty} i^{2n}[(2n^2 - 1)(A_n + B_n)]\right\},$$

and

$$u_\beta = \frac{-y}{d}\Big(A_0 + 4D_0 + 2K + \sum_{n=1}^{\infty} i^{2n}\Big\{2\Big[A_n(n+1)^2 + B_n(n-1)^2\Big] - (A_n + B_n)\Big\}\Big).$$

Since both the Cartesian and bipolar coordinate systems are orthogonal, then at the stagnation point $\mathbf{x}'$,

$$u_y \cong u_\alpha(\mathbf{x}'), \text{and} u_x \cong -u_\beta(\mathbf{x}').$$

Therefore, based upon Eq. (44) the velocity components can be recast as

$$\begin{bmatrix} u_x \\ u_y \end{bmatrix} = \begin{bmatrix} \dot\gamma y \\ \dot\gamma\lambda x \end{bmatrix},$$

where $\dot\gamma$ is the *magnitude of the velocity gradient or the shear rate* of the flow at the stagnation point and is given by

$$\dot\gamma = \frac{1}{d}\Big(A_0 + 4D_0 + 2K + \sum_{n=1}^{\infty} i^{2n}\Big\{2\Big[A_n(n+1)^2 + B_n(n-1)^2\Big] - (A_n + B_n)\Big\}\Big), \tag{45}$$

and the *flow-type parameter* or *degree of extensional flow*, λ, is given by Eq. (42). For the two-roll mill geometry, the flow-type attains values larger than zero (but smaller than one); a value of zero corresponds to the case of simple shear flow and can only be reached when the gap between the cylinders is infinitesimally small, *i.e.*, $\alpha_a \to 0$. Figure 4 presents the streamlines in the vicinity of the stagnation point for two different geometries.

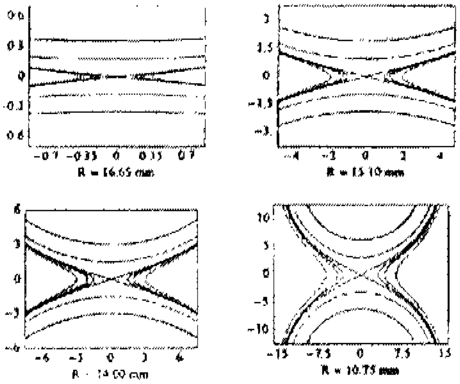

FIGURE 4. Streamlines in the vicinity of the stagnation point for different geometries of the two-roll mill. (a) R = 16.65 mm; (b) R = 15.10 mm; (c) R = 14.00 mm; (d) R = 10.75 mm. The angle sustained by the asymptotic streamlines at the stagnation point corresponds to 2θ, and are the most probable orientation for a highly deformed body embedded in the flow.

When analyzing the dynamics of polymeric liquids, changes of the fluid microstructure are easily measured by evaluating the flow-induced optical anisotropy. In these studies, the orientation of the polymer anisotropy occurs near the outgoing axes of the hyperbolic flow. The angle sustained by the asymptotic lines of the hyperbolic flow (when $\epsilon \to 0$) is defined by

$$2\theta_f = \arctan\left(\frac{y}{x}\right) = \arctan\left(\lambda^{\frac{1}{2}}\right), \tag{46}$$

with θ_f being the angle of an asymptote and the x-axis. θ_f corresponds to the orientation of the principal eigenvector of the velocity gradient tensor $\nabla\mathbf{u}$, and also corresponds to the most probable orientation of an immersed, deformed body, since the principal eigenvector of the rate of deformation tensor $\mathbf{D} = (\nabla\mathbf{u} + \nabla\mathbf{u}^T)$ is also aligned at this angle. Even for the simplified solution about the stagnation point, the orientation angle and the flow-type parameter depend only upon the geometrical characteristics of the two-roll mill. For a slightly deformed body or a fluid with microstructure, the alignment with respect to the flow must have an angle $\theta_f \leq \theta \leq \pi/4$. The upper limit corresponds to a two-dimensional *pure extensional* flow, and for flows close to simple shear the lowest value is near zero. The experimentally observed values for θ, smaller than θ_f, as reported for polymeric liquids are the result of a strong modification of the local kinematics of the flow field due to the nonlinear effects introduced by non-Newtonian constitutive equations (see, for example, Ref. 25).

Dunlap [24] obtained an expression for the stream function valid at the stagnation point:

$$\psi = \frac{d^2\omega}{\cosh\alpha - \cos\beta}\left(A_0\cosh\alpha + D_0\sinh\alpha\right), \tag{47}$$

where

$$A_0 = \frac{\alpha_R}{\alpha_R + \sinh\alpha_R\cosh\alpha_R},$$

$$D_0 = -\frac{\coth\alpha_R}{\alpha_R + \sinh\alpha_R\cosh\alpha_R}. \tag{48}$$

The flow-type parameter and the shear rate are, respectively,

$$\lambda = \left(\frac{4\coth\alpha_R}{\alpha_R} - 1\right)^{-1}, \tag{49}$$

and

$$\dot{\gamma} = \frac{A_0\omega}{\lambda}. \tag{50}$$

This solution has several disadvantages, but as will be shown subsequently, this simplified solution is remarkably accurate about the stagnation point, and in particular for flow-type values close to those of simple shear flow. Among its drawbacks are that it does not represent correctly the flow field far from the stagnation point, and it does not have the centers for the vorticity located at the axes of the cylinders. Instead they coincide with points A and B; that is, for $\alpha \to \infty$. As a result, the extent of the region about the stagnation point with kinematic conditions determined by the above values of $\dot{\gamma}$, λ, and θ is unknown in relation to the length-scales defined by the geometry of the mill.

3.2. Flow parameters for experimental two-roll mill configurations

Two-roll mill flow devices have been used in the past, especially to study the dynamics of polymeric fluids (see, for example, Refs. 20, 22, 24, and 25). The advantage of the use of the two-roll mill for these studies is the fact that the flow-type parameter is larger than zero, but corresponds to a extensional flow field with significant amounts of vorticity, in particular when the values achieved are compared to values accessible with a four-roll mill configuration. That is, when the conformation of the fluid structure can be altered significantly by the degree of extensional flow, then the use of two-roll mill is superior since the response of the fluid can be more easily differentiated due to the presence of vorticity causing a less drastic deformation of the microstructure.

TABLE I. Dimensions for the two-roll mill with different sizes of diameters for the cylinders. For all cases, the distance between roller-s's axes is fixed at 17.0 mm. d corresponds to the distance from the center of the flow cell (the stagnation point) to the position along the y-axis where $\alpha \to \infty$ and allows the representation of the rollers by α_R

Roller	Radii (mm)	gap (mm)	d (mm)
A	16.65	0.70	3.431836
B	16.35	1.30	4.655910
C	15.70	2.60	6.519969
D	15.10	3.80	7.809609
E	14.17	5.66	9.392076
F	14.00	6.00	9.643651
G	12.78	8.44	11.210334
H	11.69	10.62	12.342767
I	10.75	12.50	13.169567

3.2.1. *Geometrical parameters*

In studies reported by Geffroy and Leal [25], the two-roll mill geometry is such that the centers of the cylinders is maintained fixed at 0.0170 m, while eight different sets of rollers is used to vary the flow parameters. Table I lists the diameters of the cylinders and the gap existing between them. The calculated value for half the distance between points A and B (d), and which allows the representation of the cylinders' surface by a constant value of $\alpha = \alpha_R$, is also given and is always larger that the separation between cylinders.

3.2.2. *The flow type parameter*

Given the geometric characteristics of the flow devices it is now possible to compare the precision of the calculated values of the flow parameters. Table II presents the values of the flow-type parameter using the approximated expression (λ_{approx}) by Dunlap [24], Stokes solution [given by Eqs. (23), (35), (36), and (40)], the numerical value reported by Singh and Leal [20], and the experimental values by Wang *et al.* [22]. This Table considers three possible precisions for the summations implied by Eq. (39) and obtained by truncating the sum after $n = 5$, 25, and 125 terms. The entries without values in the numerical and experimental columns imply that these are not available.

It is clear that the flow-type values predicted for the complete range of flow devices is approximately the same when more than 25 terms of the summation are considered. In fact, the latter criteria is adequate for λ values greater than 0.04. The number of terms required at low values of λ increases and, surprisingly, provides values equivalent to those obtained with the simplified expression of Dunlap. Figure 5 presents the dependence of the calculated value of the flow-type parameter on the number of terms of the sum [Eq. (39)]. The plot corresponds to the two-roll mill configuration with

TABLE II. Calculated values of the flow type, λ, as a function of the flow device geometry and evaluated at the stagnation point. λ_{approx} corresponds to the predicted values using Dunlap's expression, and λ_n are those evaluated using Eq. (42) with n the number of summands considered. λ_{num} and λ_{exp} are the numerical and experimental results reported in Refs. 20, and 22, respectively.

Roller	λ_{Approx}	$\lambda\ (n=5)$	$\lambda\ (n=25)$	$\lambda\ (n=125)$	λ_{num}	λ_{exp}
A	0.0104379	0.115312	0.0105409	0.0104379	...	...
B	0.0196209	0.0988742	0.0196247	0.0196209	...	...
C	0.0403169	0.0810291	0.040316	0.040316	...	0.047
D	0.060474	0.081976	0.060461	0.060461	...	0.067
E	0.093974	0.102122	0.094123	0.094123	...	0.096
F	0.100424	0.107371	0.100692	0.100692	...	0.114
G	0.150133	0.154612	0.152789	0.152789	0.153	0.160
H	0.200548	0.207745	0.207191	0.207191	...	0.196
I	0.297712	0.259299	0.259108	0.259108	...	...

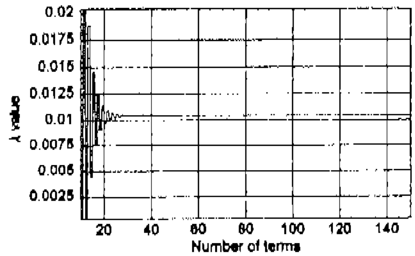

FIGURE 5. Convergence of calculated values for the flow-type parameter, λ, as a function of the number of terms before truncation of the analytic solution for the stream function.

the smallest gap (rollers A) since its computation presents the weakest convergence behavior. For this mill, whenever more that 40 terms in the summation are taken into account the value for λ hardly changes. For the results given here, the sums are truncated after 125 terms.

3.2.3. The magnitude of the velocity gradient tensor

The magnitude of the velocity gradient at the stagnation point is another important parameter for these flows. That is, given a fixed maximum angular velocity of rotation of the cylinders provided by a set of motors, the top shear rate that the mill can produce is a function of its geometry via the tangential speed and the gap between rollers. For the same two-roll mill geometries, Table III presents the values of the normalized shear rates (with respect to the angular speed of the cylinders) as calculated by the expression of Dunlap ($\dot{\gamma}_D/\omega$), the exact solution (considering 125 terms), and the experimental values obtained by Wang *et al.* ($[\dot{\gamma}/\omega]_{\text{exp}}$). However, in this table, the second and fourth left most columns are found using the full solutions as given by Eqs. (47) and (48) for Dunlap's expression, and Stokes solution based on Eqs. (23), (35), (36), and (40). The first and third columns are obtained using the expressions valid about the stagnation point.

TABLE III. Magnitude of the principal eigenvalue of the velocity gradient tensor, normalized with respect to the angular speed of the cylinders. $[\dot{\gamma}_D/\omega]_{\text{approx}}$ and $[\dot{\gamma}_D/\omega]$ are the predicted values based upon Dunlap's expression. $[\dot{\gamma}/\omega]_{\text{approx}}$ and $[\dot{\gamma}/\omega]$ are the predicted values for the locally and globally valid Stokes solution, respectively. $[\dot{\gamma}/\omega]_{\text{exp}}$ are the reported results of Wang *et al.* [22].

Roller	$\left[\frac{\dot{\gamma}_D}{\omega}\right]_{\text{approx}}$	$\frac{\dot{\gamma}_D}{\omega}$	$\left[\frac{\dot{\gamma}}{\omega}\right]_{\text{approx}}$	$\frac{\dot{\gamma}}{\omega}$	$\left[\frac{\dot{\gamma}}{\omega}\right]_{\text{exp}}$
A	47.237331	47.239904	47.237331	47.239904	...
B	24.819154	24.823931	24.819154	24.823931	24.1
C	11.741155	11.750694	11.741156	11.750694	11.7
D	7.610899	7.624803	7.610783	7.624681	7.84
E	4.670160	4.690736	4.669733	4.690372	4.83
F	4.329777	4.351555	4.329427	4.351319	4.44
G	2.692708	2.722886	2.695945	2.727231	2.80
H	1.868669	1.905877	1.87967	1.919587	1.84
I	1.391422	1.434168	1.41084	1.457431	...

Figure 6 presents a comparison of λ values calculated with the exact solution and Dunlap's expression. It is clear that for large gaps (small cylinders radii), the expression valid at the stagnation point overestimates the values of the flow-type parameter; in fact, λ can have unrealistic values larger than one. The series solution attains the expected limiting values of $\lambda = 0$ for the smallest gap, and $\lambda = 1$ when the rollers have a minimum diameter. As shown in Table II, both the approximate expression and the complete solution have discrepancies of less than one percent for $\lambda < 0.2$. For values $0.2 < \lambda < 0.4$, the calculated values differ, but the two-roll mill geometry has not been used for such large values although it appears to be a useful geometry for λ values as high as 0.8. However, for such large values, the four-roll mill may be a better alternative to generate elongational flows

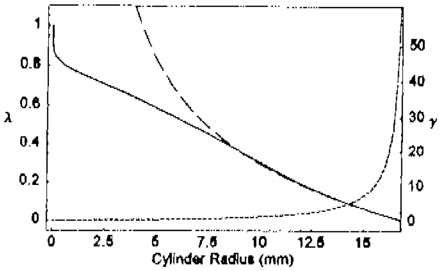

FIGURE 6. Calculated values for the flow-type parameter using the approximate expression of Dunlap [24] (the dotted line) and the series expansion given here (continuous line) with truncation after 125 terms. The separation between cylinders' axes is 0.034 m. Dunlap's expression predicts unrealistic values whenever the radii of the cylinders are less than 0.0043 m. The series solution predicts the correct values for the largest ($\lambda = 0$) and smallest radii ($\lambda = 1$).

with small amounts of vorticity since according to Table III it is obvious that the magnitude of the accessible shear rates can be extremely limited for two-roll mills with a large-λ-value configuration. The available range of shear rates with a four-roll mill is not as severely limited as is the case of the two-roll mill.

4. Discussion and conclusions

A solution valid for zero Reynolds number flows generated by two-roll mills is given. This solution can be a useful benchmark for a number of elongational creeping flows because its flow parameters evaluated at the stagnation point can be accurately known. Also, this solution could be useful as a first order approximation for studies of inertial effects (nonzero Reynolds numbers) or non-Newtonian constitutive equations, and to perform stability analyses of the full 3D-flow field. Inertial effects may disrupt the symmetric properties of the flow field; in particular, the streamlines for fluid parcels approaching the stagnation point will tend to curve faster, while those departing from the stagnation point will follow patterns close to the central line (x-axis). Furthermore, this solution could be useful to study a new class of nonsteady flows, or the Stokes paradox present far from the stagnation point [4]. When studying non-Newtonian constitutive equations, this flow field may present smaller values for the shear rates and flow type as a result of nonzero normal stresses. In the case of hydrodynamic instabilities, the two-dimensional character of the zero Reynolds number flow field could be modified.

Even for nonzero Reynolds numbers, the present solution can be useful as a benchmark for a number of experimental and numerical techniques used to study the flow field near the central stagnation point. As shown in Tables II and III, The available experimental values are slightly higher that the numerical and theoretical predictions for the flow-type as well as the shear rate, which may be a consequence of the fact that different models for the flow field were used. That is, the numerical simulation of Singh and Leal, and the experimental results of Wang *et al.*, have used a two-roll mill contained inside a third circular cylinder with flat ends that conform the flow cell while the analytical results assumes an unbounded fluid domain. Furthermore, the third cylinder is stationary which represents a significant departure from the kinematic conditions implied by the unbounded domain. Consequently, for the numerical and experimental data, the presence of boundaries on the $\alpha\beta$-plane at a finite distance may affect the observed values for the flow parameters. However, for the flow field near the stagnation point the discrepancy with the theoretical calculations appear clearly at odds with the experimental values and less with the numerical result. This is true for the calculated values for the flow-type and the shear rate as shown in Tables II and III, especially for the set of rollers from C to G. It is not clear why this is the case, but perhaps these theoretical and numerical results can provide some insight into the accuracy of the experimental technique or as a benchmark to "fine-tune" the precision of the experimental measurements.

The significant drop of the measured value for λ and $\dot{\gamma}$ for the largest set of rollers H may be a consequence of significant three-dimensionality effects present for that configuration. That is, for these devices, the rollers are about 0.0254 m long and the length-to-gap ratio is only about two to one. The flow cell encloses the cylinders with non-slip boundary conditions at the extreme of the cylinders, and perpendicular to the axes. The flow field on the layers next the flat covers must be similar to that of simple shear flow, which implies that the observed value of λ may be dependent upon the depth of the flow cell. Furthermore, the velocity field may also be weaker due to the proximity of the container walls and the shear rate is consequently smaller. Hence, boundary effects normal to the rollers axes and due to the existence of flat surfaces may reduced the net value of the flow-type parameter especially when the gap is relatively large and even when it is evaluated at the central position of the "stagnation line" as shown in Table II; these conditions can also reduced the measured shear rate as given in Table III. If this assertion is correct, then two-roll mill flow cells need to consider a design with a significantly larger value for the length to gap ratio for all rollers, or the means to reduced the friction at the walls, in order to determine a consistent flow-type parameter for geometries with large values of λ.

Acknowledgments

Technical help from Gerardo F. Guevara is duly acknowledged. M.A.H.R. was supported by a DGEP-UNAM Scholarship. E.G. acknowledges partial support for the present study from Grants 3451A9310 and G27837U of CONACyT, IN303093 of PAPITT-DGAPA, UNAM, and 0598 of FIES-IMP.

Appendix A

The solution of the stream function valid for the two-roll mill requires an equivalent expression for the logarithmic term that appears in Eq. (21). A simple Fourier series solution can be found when the following relation is used [27]:

$$\ln\left(1 - 2x\cos\phi + x^2\right) = -2\sum_{n=1}^{\infty}\frac{\cos n\phi}{n}x^n. \qquad \text{(A.1)}$$

Since

$$\ln\left(x + \sqrt{1+x^2}\right) = \sinh^{-1} x;$$

$$x^2 \leq 1 \quad \text{and} \quad x\cos\phi \neq 1,$$

Equation (52) can be cast as

$$\ln\left(\frac{1+x^2}{2x} - \cos\phi\right) = -\ln(2x) - 2\sum_{n=1}^{\infty}\frac{\cos n\phi}{n}x^n.$$

From the above equation, the logarithmic term can be easily obtained with the change of variables $\phi = \beta$, and $(1+x^2)/2x = \cosh\alpha = \varrho$, such that the following equality:

$$1 - 2x\varrho + x^2 = 0,$$

has solutions

$$x = \frac{-(-2\varrho) \pm \sqrt{4\varrho^2 - 4}}{2} = \varrho \pm \sqrt{\varrho^2 - 1}$$

$$= \cosh\alpha \pm \sqrt{\cosh^2\alpha - 1} = \cosh\alpha \pm \sinh\alpha$$

$$= \frac{(e^{\alpha} + e^{-\alpha}) \pm (e^{\alpha} - e^{-\alpha})}{2} = \frac{(1\pm 1)e^{\alpha} + (1\mp 1)e^{-\alpha}}{2}.$$

Hence,

$$x = e^{\pm\alpha}.$$

This last equation must have only one solution. For $\alpha > 0$, and $x^2 \leq 1$, only the negative root is valid. Therefore, applying the change of variables on the tabulated equality [Eq. (A.1)] with the relation for x imply that

$$\ln(\cosh\alpha - \cos\beta) = -\ln\left(2e^{-\alpha}\right) - 2\sum_{n=1}^{\infty}\frac{\cos n\beta}{n}e^{-n\alpha}$$

$$= \alpha - \ln 2 - 2\sum_{n=1}^{\infty}\frac{e^{-n\alpha}}{n}\cos n\beta$$

$$= a_0 + \sum_{n=1}^{\infty}a_n\cos n\beta, \qquad \text{(A.2)}$$

where

$$a_0 = \alpha - \ln 2 \text{ and } a_n = -2\frac{e^{-n\alpha}}{n}. \qquad \text{(A.3)}$$

The left side of expression for the stream function is multiplied by the $(\cosh\alpha - \cos\beta)$ term. Hence, from Eqs. (A.2) and (A.3) the right most term is the logarithmic summand is

$$\cos\beta\ln\left(\cosh\alpha - \cos\beta\right) = \left(a_0 + \sum_{n=1}^{\infty}a_n\cos n\beta\right)\cos\beta$$

$$= a_0\cos\beta + \sum_{n=1}^{\infty}a_n\cos\beta\cos n\beta.$$

Using the identity $\cos\beta\cos n\beta = \frac{1}{2}\cos(n+1)\beta + \frac{1}{2}\cos(n-1)\beta$, the sum of the latter equation can be written as

$$\sum_{n=1}^{\infty}a_n\cos\beta\cos n\beta =$$

$$\sum_{n=1}^{\infty}\frac{a_n}{2}\left[\cos(n+1)\beta + \cos(n-1)\beta\right]$$

$$= \frac{a_1}{2}\cos 2\beta + \frac{a_1}{2} + \frac{a_2}{2}\cos 3\beta + \frac{a_2}{2}\cos\beta$$

$$+ \sum_{n=3}^{\infty}\frac{a_n}{2}\left[\cos(n+1)\beta + \cos(n-1)\beta\right],$$

and with some further simplifications

$$\sum_{n=1}^{\infty}a_n\cos\beta\cos n\beta = \frac{a_1}{2} + \frac{a_2}{2}\cos\beta$$

$$+ \sum_{n=2}^{\infty}\left(\frac{a_{n+1}}{2} + \frac{a_{n-1}}{2}\right)\cos n\beta. \qquad \text{(A.4)}$$

In this manner,

$$\cos\beta\ln(\cosh\alpha - \cos\beta) = \frac{a_1}{2} + \left(a_0 + \frac{a_2}{2}\right)\cos\beta$$

$$+ \sum_{n=2}^{\infty}\left(\frac{a_{n+1}}{2} + \frac{a_{n-1}}{2}\right)\cos n\beta. \qquad \text{(A.5)}$$

The remaining term becomes

$$\cosh\alpha\ln(\cosh\alpha - \cos\beta) =$$

$$a_0\cosh\alpha + \sum_{n=1}^{\infty}a_n\cosh\alpha\cos n\beta$$

$$= a_0\cosh\alpha + a_1\cosh\alpha\cos\beta$$

$$+ \sum_{n=2}^{\infty}a_n\cosh\alpha\cos n\beta; \qquad \text{(A.6)}$$

Hence, the product $(\cosh\alpha - \cos\beta)\ln(\cosh\alpha - \cos\beta)$ can be obtained from Eqs. (A.5) and (A.6) so that

$$(\cosh\alpha - \cos\beta)\ln(\cosh\alpha - \cos\beta) =$$

$$\cosh\alpha\ln(\cosh\alpha - \cos\beta) - \cos\beta\ln(\cosh\alpha - \cos\beta)$$

$$= a_0\cosh\alpha + a_1\cosh\alpha\cos\beta + \sum_{n=2}^{\infty}a_n\cosh\alpha\cos n\beta$$

$$-\frac{a_1}{2} - \left(a_0 + \frac{a_2}{2}\right)\cos\beta - \sum_{n=2}^{\infty}\left(\frac{a_{n+1}}{2} + \frac{a_{n-1}}{2}\right)\cos n\beta,$$

or equivalently,

$$(\cosh\alpha - \cos\beta)\ln(\cosh\alpha - \cos\beta) = \left(a_0\cosh\alpha - \frac{a_1}{2}\right) + \left(a_1\cosh\alpha - a_0 - \frac{a_2}{2}\right)\cos\beta + \sum_{n=2}^{\infty}\left(a_n\cosh\alpha - \frac{a_{n+1}}{2} - \frac{a_{n-1}}{2}\right)\cos n\beta.$$

Finally,

$$(\cosh\alpha - \cos\beta)\ln(\cosh\alpha - \cos\beta) = b_0 + b_1\cos\beta + \sum_{n=2}^{\infty} b_n\cos n\beta, \tag{A.7}$$

with

$$b_0 = a_0\cosh\alpha - \frac{a_1}{2}, \tag{A.8a}$$

$$b_1 = a_1\cosh\alpha - a_0 - \frac{a_2}{2}, \tag{A.8b}$$

$$b_n = a_n\cosh\alpha - \frac{a_{n+1}}{2} - \frac{a_{n-1}}{2}. \tag{A.8c}$$

1. M.S. Chong, A.E. Perry, and B.J. Cantwell, *Physics Fluids A* **2** (1990) 765.
2. G.B. Jeffery, *Roy. Soc. Proc. A* **101** 169 (1922).
3. Sir H. Lamb, *Hydrodynamics*, 6th edition, (Cambridge UP, Cambridge, England, 1932) p. 68.
4. J. Happel and H. Brenner, *Low Reynolds number hydrodynamics*, (Kluwer Acad. Publ., Dordrecht, The Netherlands, 1991) p. 497.
5. G.B. Jeffery, *Philos. Trans. A* **221** (1920) 265.
6. R.A. Frazer, *Philos. Trans. A* **225** (1925) 93.
7. Sir G.G. Stokes, *Mathematical and physical papers*, (Cambridge UP, Cambridge, England, 1883).
8. G. Astarita, *J. Non-Newtonian Fluid Mech* **6** (1979) 69.
9. W.L. Olbricht, J.M. Rallison, and L.G. Leal, *J. Non-Newtonian Fluid Mech.* **10** (1982) 291.
10. G.I. Taylor, *Proc. R. Soc. London Ser. A* **138** (1932) 41.
11. G.I. Taylor, *Proc. R. Soc. London Ser. A* **146** (1934) 501.
12. B.J. Bentley and L.G. Leal, *J. Fluid Mech.* **167** (1986) 219.
13. B.J. Bentley and L.G. Leal, *J. Fluid Mech.* **167** (1986) 241.
14. H.A. Stone, B.J. Bentley, and L.G. Leal, *J. Fluid Mech.* **173** (1986) 131.
15. W.J. Milliken, H.A. Stone, and L.G. Leal, *Phys. Fluids A* **5** (1993) 69.
16. J.M. Rallison, *Ann. Rev. Fluid Mech.* **16** (1984) 45.
17. H.A. Stone, *Ann. Rev. Fluid Mech.* **26** (1994) 65.
18. K.S. Chang and W.L. Olbricht, *J. Fluid Mech.* **250** (1993) 609.
19. S.C. Jana, G. Metcalfe, and J.M. Ottino, *J. Fluid Mech.* **269** (1994) 199.
20. P. Singh and L.G. Leal, *J. Non-Newtonian Fluid Mech.* **67** (1996) 137.
21. J. Feng and L.G. Leal, *J. Non-Newtonian Fluid Mech.* **72** (1997) 187.
22. J.J. Wang, D. Yavich, and L.G. Leal, *Phys. Fluids* **6** (1994) 3519.
23. D. Yavich and L.G. Leal, *Rheol. Acta* **34** (1995) 360.
24. P.N. Dunlap, Ph. D. Thesis, California Institute of Technology, (1986).
25. E. Geffroy and L.G. Leal, *J. Polym. Sci.; Polym. Phys.* **30** (1992) 1329.
26. G.G. Fuller, J.M. Rallison, R.L. Schmidt, and L.G. Leal, *J. Fluid Mech.* **100** (1980) 555.
27. I.S. Gradshteyn and I.M. Ryzhik, *Table of integrals, Series and Products, Corrected and Enlarged Edition*, (Academic Press, San Diego, USA, 1981) Eq. 1.514.

PHYSICS OF FLUIDS VOLUME 12, NUMBER 10 OCTOBER 2000

A corotating two-roll mill for studies of two-dimensional elongational flows with vorticity

Marco A. H. Reyes and Enrique Geffroy[a)]
Instituto de Investigaciones en Materiales, Universidad Nacional Autónoma de México, Apdo. Postal 70-360, Cd. Universitaria, 04510 México, D. F., México

(Received 30 November 1999; accepted 13 June 2000)

A closed-form analytical solution for the Stokes flow generated by a corotating two-roll mill is used to generate two-dimensional elongational flows with well-defined amounts of vorticity. These flow devices can generate conditions found between simple shear and purely elongational flows, and are among the few systems that can take into account the presence of nearby boundaries. In the laboratory, these devices have been used for studies of the microstructural dynamics of complex fluids such as polymeric solutions, colloids, bubbles and drops, etc., and allow pointwise optical studies of the flow parameters. Hence, a comparison is presented of available experimental and numerical results for the stagnation point versus the analytical solution presented here. Based upon this solution, a new design for the two-roll mill is presented for the purpose of minimizing the disadvantages of current mills. © *2000 American Institute of Physics.* [S1070-6631(00)00510-9]

I. INTRODUCTION

For studies in fluid mechanics of non-Newtonian fluids,[1,2] chaotic advection,[3,4] drop and bubble dynamics,[5,6] and many industrial applications (see, e.g., Stone[6]), the use of laminar flows capable of inducing significant deformation on the fluid or the embedded objects are a necessary tool. In general, these flows are needed to study fluid systems that show a marked nonlinear, hysteretic behavior due to its *microstructure*. Simple viscometric flows and purely extensional flows (see, e.g., Ref. 7) are among the two most frequently used flow fields that are kinematically different. On the one hand, viscometric flows have significant amounts of vorticity, and are not expected to produce large deformations on an embedded object; thus, they are classified as *weak flows*. The observed behavior in viscometric steady flows is understood by parcels of fluid that at any given time separate linearly in time (at most, the separation can only grow algebraically); hence, these flows produce only a moderate change on the fluid structure. On the other hand, for steady extensional flows there is no vorticity and two neighboring elements of fluid separate in time *exponentially*; given enough time, the flow induces significant changes on the microstructure of the fluid regardless of its relaxation mechanisms; therefore, these are *strong flows*.[8,9]

The purpose of this paper is to present a flow device capable of significant modification of the microstructure of the fluid: the *two-roll mill*. First, the Fourier series expansion for the Stokes solution is presented, followed by the analytical results for the two most important flow parameters. Then, a comparison of the theoretical predictions of this model versus the experimental and numerical results, available for the region about the stagnation point, is given. Finally, the exact solution is used to propose and predict the behavior of a new configuration for experimental two-roll mills that should be useful for experimental studies of complex fluids.

II. STOKES' SOLUTION FOR THE TWO-ROLL MILL

The two-roll mill consists of two cylinders of equal radii, with collinear axes, and separated by a small distance. This flow cell is based on a new analytical solution that assumes a steady, two-dimensional flow as if generated by rollers of infinite length and rotating with equal angular velocities.[10] Inertial terms are considered negligible. For corotating two-roll mills, there exists a *stagnation point* on the line between the cylinders' axes, with local kinematic conditions characteristic of *elongational flow with some vorticity*.[1] Hence, some of the features of the elongational flow field generated by these mills are as follows.[10] (a) The flow parameters are defined only by the mill's geometry, with the shear rate and the ratio of magnitudes of the rate of deformation tensor to its vorticity prescribed independently. (b) Although these flows belong to the family of *strong flows*, simple shear flows can be approached as closely as needed, increasing monotonically the vorticity. (c) The analytical solution takes into account the presence of the cylinders' boundaries, in contrast with other strong flows used to study long-term effects in embedded objects, such as four-roll mills.[5]

Bipolar cylindrical coordinates (α,β) have been theoretically[11] and experimentally used to study other mills. In 1922, Jeffery[12] presented a solution for the Stokes flow inside the annular region of eccentric cylinders, where the stream function satisfies the biharmonic equation. Two-roll mills with identical cylinders are described by constant values of $\alpha = \pm\alpha_R$, with α being the tangential coordinate, and β being the normal coordinate to the cylinders. The geometric aspects are defined by

$$\frac{g}{2R} = \cosh\alpha_R - 1, \quad d = R\sinh\alpha_R, \tag{1}$$

[a)] Electronic mail: geffroy@servidor.unam.mx where g is the gap between rollers, R the cylinders' radii, and $2d$ the distance between points $\alpha=\pm\infty$. The stream function used here is the Fourier series expansion proposed by Jeffery[12] for a bounded domain, but supplemented with a logarithmic term so that the flow at infinity is stationary, and the vortices coincide with the center of the rollers.[13] For two-roll mills with equal cylinders rotating at equal speeds (and located over the y axis), the dynamic no-slip tangential velocity component on cylinders implies $u_\alpha(\pm\alpha_R)=\omega R$, and the normal velocity component being zero requires $u_\beta(\pm\alpha_R)=0$. At infinity the fluid must remain at rest and $\psi(\alpha\rightarrow 0,\beta\rightarrow 0)=0$. The number of unknowns is always greater by one than the number of equations; therefore, an arbitrary value for the stream function on the cylinders is set by the computation defining a relative value for the rollers' angular speed. A closed-form solution is obtained once the latter constraints are used (see Ref. 10).

The solution for this Stokes flow is given by

$$\frac{\psi}{h}=A_0\cosh\alpha+D_0\alpha\sinh\alpha+K\left(b_0+b_1\cos\beta+\sum_{n=2}^{\infty}b_n\cos n\beta\right)+\sum_{n=1}^{\infty}[A_n\cosh(n+1)\alpha+B_n\cosh(n-1)\alpha]\cos n\beta, \tag{2}$$

where

$$b_0=a_0\cosh\alpha-\frac{a_1}{2},\quad b_1=a_1\cosh\alpha-a_0-\frac{a_2}{2}, \tag{3a}$$

$$b_n=a_n\cosh\alpha-\frac{a_{n+1}}{2}-\frac{a_{n-1}}{2}, \tag{3b}$$

and

$$a_0=\alpha-\ln 2,\quad a_n=-2\exp(-n\alpha)/n. \tag{4}$$

The remaining coefficients A_0, A_1, B_1, D_0, A_n, and B_n are given, respectively, by

$$A_0=\frac{2R\omega\alpha_R\sinh\alpha_R-2K[b_0(\sinh\alpha_R+\alpha_R\cosh\alpha_R)-(1+a_0)\alpha_R\sinh^2\alpha_R]}{2\alpha_R+\sinh 2\alpha_R}, \tag{5a}$$

$$A_1=-\frac{Ka_1\operatorname{sech}\alpha_R}{4}, \tag{5b}$$

$$B_1=-Kb_1+\frac{Ka_1\coth 2\alpha_R\sinh\alpha_R}{2}, \tag{5c}$$

$$D_0=-\frac{A_0\cosh\alpha_R+Kb_0}{\alpha_R\sinh\alpha_R}, \tag{5d}$$

$$\frac{A_n}{K}=\frac{(n+1)-e^{-2n\alpha_R}-ne^{-2\alpha_R}}{n(n+1)[n\sinh 2\alpha_R+\sinh 2n\alpha_R]}, \tag{5e}$$

$$\frac{B_n}{K}=\frac{(n-1)+e^{-2n\alpha_R}-ne^{2\alpha_R}}{n(n-1)[n\sinh 2\alpha_R+\sinh 2n\alpha_R]}. \tag{5f}$$

And

$$\begin{aligned}K=&-4R\omega\alpha_R\sinh\alpha_R[2S(2\alpha_R+\sinh 2\alpha_R)\\&+4\alpha_R(a_0+1)\sinh^2\alpha_R-4b_0(\sinh\alpha_R+\alpha_R\cosh\alpha_R)\\&-2b_1(2\alpha_R+\sinh 2\alpha_R)+a_1(2\alpha_R\coth 2\alpha_R\sinh\alpha_R\\&-\alpha_R\operatorname{sech}\alpha_R-\tfrac{3}{2}\sinh\alpha_R+\tfrac{1}{2}\sinh 3\alpha_R)]^{-1},\end{aligned} \tag{6}$$

with all coefficients a_i, and b_i being evaluated at α_R; and

$$\begin{aligned}S&=-\frac{A_0+A_1+B_1}{K}\\&=\sum_{n=2}^{\infty}\frac{(-2n)e^{-2n\alpha_R}+(n-n^2)e^{-2\alpha_R}+(n+n^2)e^{2\alpha_R}}{n(n-1)(n+1)(n\sinh 2\alpha_R+\sinh 2n\alpha_R)}.\end{aligned} \tag{7}$$

The accuracy of the solution depends on the summation S, and implicitly on the numbers of terms considered, which guarantees a value of n for the desired level of precision on the stream function. Whenever α_R values are small—large cylinders' radii VS gap—the number of terms required for the summation [Eq. (7)] increases. All parameters presented here were obtained with 125 terms assuring good accuracy over the complete flow domain.

III. THE FIELD PARAMETER AND THE SHEAR RATE

Despite the flow field being linear, it is not homogeneous. Four-roll mills[5] show that purely hyperbolic stream lines at the stagnation point are possible only if four vortices are present at points along the cardinal directions. Consequently, for the two-roll mill with two vortices explicitly associated with the cylinders, the remaining nonassociated vortices are located along the x axis. In order to characterize those features, the two most important observables of the strong flow field are the flow-type parameter λ, and the shear rate $\dot{\gamma}$. In particular, these parameters are most useful for studies of polymeric solutions, embedded objects, etc., over the extended stagnation region, where a well-characterized elongational flow exists. For λ, it is necessary to evaluate the magnitude of the rate of deformation $\|\mathbf{D}\|=\sqrt{\mathrm{Tr}(\mathbf{D}\mathbf{D}^T)}$ and the vorticity $\|\mathbf{W}\|$ as a function of position, taking into consideration an objective measure of vorticity. For $\dot{\gamma}$, the magnitude of the velocity gradient is needed. The flow-type parameter is

$$\lambda=\frac{\|\mathbf{D}\|+\|\overline{\mathbf{W}}\|}{\|\mathbf{D}\|-\|\mathbf{W}\|}=\frac{|q|-|A|}{|q|+|A|}; \tag{8}$$

for $\alpha=0$ (the line between the cylinders),

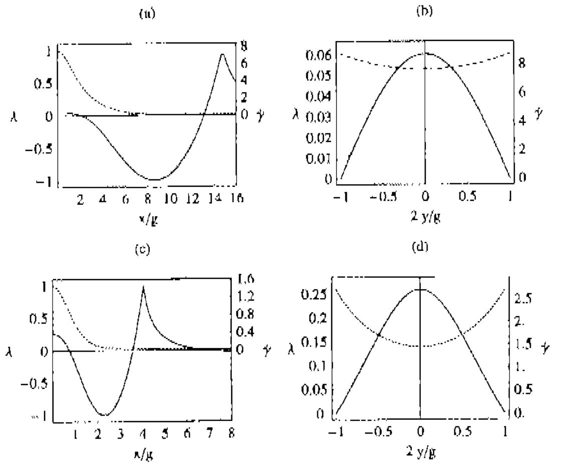

FIG. 1. Plots of flow-type parameter λ (solid lines) and the shear rate $\dot{\gamma}$ (dashed lines) along the x axis and the y axis normalized by half the gap distance. For rollers D (a) along the x axis and (c) for the y axis. For rollers I equivalent plots (b) and (d), respectively.

$$q=\frac{(B+C)}{h}+D,\quad B=\frac{\partial u_\alpha}{\partial\beta},\quad C=\frac{\partial u_\beta}{\partial\alpha},\quad D=\frac{\sin\beta}{d}u_\alpha, \tag{9a}$$

$$A=\frac{(B-C)}{h}+D-\frac{u_\alpha}{hq}\frac{\partial p}{\partial\alpha}, \tag{9b}$$

$$\frac{\partial p}{\partial\alpha}=\frac{1}{h}\left(\frac{\partial^2u_\alpha}{\partial\alpha^2}-\frac{\partial^2u_\beta}{\partial\alpha\partial\beta}\right)-\frac{\sin\beta}{d}C+\frac{u_\alpha}{d}; \tag{9c}$$

and for $\beta=\pi$—the line joining the axes of the cylinders—the coefficients are given by

$$q=\frac{(C+B)}{h}+D,\quad B=\frac{\partial u_\beta}{\partial\alpha},\quad C=\frac{\partial u_\alpha}{\partial\beta},\quad D=\frac{\sinh\alpha}{d}u_\beta, \tag{10a}$$

$$A=\frac{(C-B)}{h}-D-\frac{\mu_\beta}{hq}\frac{\partial p}{\partial\beta}, \tag{10b}$$

$$\frac{\partial p}{\partial\beta}=\frac{1}{h}\left(\frac{\partial^2u_\alpha}{\partial\alpha\partial\beta}-\frac{\partial^2u_\beta}{\partial\beta^2}\right)+\frac{\sinh\alpha}{d}C+\frac{u_\beta}{d}. \tag{10c}$$

The magnitude of the velocity gradient tensor, $\dot{\gamma}=\|\nabla\mathbf{u}\|$ is given by

$$\dot{\gamma}=\sqrt{\left(\frac{1}{h}B\right)^2+\left(\frac{1}{h}C+D\right)^2}. \tag{11}$$

Based on Eqs. (8) and (11), Fig. 1 shows $\dot{\gamma}$ and λ along the x and y axes normalized with respect to the gap, for two geometries that correspond to rollers D and I of Table I. The behavior is the same for all geometries, up to rollers with a λ value as high as 0.801. While $\dot{\gamma}$ (dashed lines) decays monotonically, λ (solid lines) has a positive value at the origin, decreases to a value close to −1 (due to a nonassociated vortex), sharply increases up to a value near one, followed by a slow monotonic decay to a value for $\lambda(x\to\infty)$ close to −1. In Fig. 1, the rotational speed of the cylinders is the same; consequently, the maximum shear rate depends on the gap width. Figures 1(b) and 1(d) present the typical spatial dependence along the line joining the centers of the cylinders ($\beta=\pi$). For λ the profile is almost parabolic. The values of $\dot{\gamma}$ across the gap have a flatter profile, especially for the smaller gaps.

For studies of complex fluids subjected to strong flows, the extent of the stagnation region can be defined up to the point where λ changes sign. The shear rate provides a second criterion for such a region based upon material points which separate at a constant rate. For smaller gaps the length of these regions is about 4.8 gap units regardless of the criteria, while for the largest gaps ($g=1.163R$) the extent of the region is smaller for a λ—than a $\dot{\gamma}$—criterion: 0.72 and 0.86 gap units, respectively.

Also, the impact of nonassociated vortices on the flow field depends on the geometry, being most relevant when the shear rate of the vortex is largest. Figures 1(a) and 1(c) show that the relative magnitude of $\dot{\gamma}$ at the vortices is higher for the largest λ values. Furthermore, the position along the x axis of the nonassociated vortices (where $\lambda=-1$) varies according to the λ value of the flow device. For the smallest gaps, the vortices are driven away to about twice the distance than that along the y axis to the center of rotation of the cylinder, and simultaneously their strength decreases. For the largest λ's available, the vortex position is about 5/3 the distance to the center of the cylinders; only for λ's close to 1 do the vortices' positions approach the distance to the cylinders axes.[14]

IV. EXPERIMENTAL, NUMERICAL, AND STOKES' SOLUTION RESULTS

Two-roll mill flow devices have been used in the past, especially to study polymeric fluids (e.g., Refs. 1, 2, and 15). In these studies, the centers of the cylinders are fixed 0.0170 m apart (on the y axis and measured from the center), and λ is varied using eight different sets of rollers. Columns 1–3 of Table I list the rollers' identification (from A to I), the cylinders' diameters, and the calculated value for d, associated with the origins of the radial vector of the bipolar coordinate system. Columns 4–6 of Table I present the values of λ, determined first by Eqs. (2)–(7), then the numerical value reported by Singh and Leal,[2] and finally the experimental values by Wang *et al.*[15] Entries without values in the numerical and experimental columns imply that these are not available. The magnitude of the velocity gradient at the stagnation point is also a function of its geometry via the tangential speed and the gap between rollers. Columns 7 and 8 provide information about $\dot{\gamma}/\omega$ by theoretical and experimental values ($[\dot{\gamma}/\omega]_{\mathrm{expt}}$).

The experimental values are slightly higher than the numerical and theoretical predictions for λ and $\dot{\gamma}$, because different models of the flow field were used. As shown in Fig. 2(a), the numerical and experimental results have used a two-roll mill contained inside a third stationary, circular cylinder; a distortion of the unbounded fluid domain. However for rollers C to G, the theoretical values for λ and $\dot{\gamma}$ appear at odds with the experimental values but less with the numeri-

TABLE I. Dimensions for the two-roll mill with different diameters for the cylinders and their associated flow parameters. The cylinders' radii and the corresponding d values for the calculation of the Fourier series expansions are given in columns 2 and 3. For all cases, the distance between rollers' axes is fixed at 17.0 mm. The values of λ, evaluated at the stagnation point, are carried out using Eq. (2) with $n=125$. λ_{num} and λ_{expt} are the corresponding numerical and experimental results reported in Refs. 2 and 15, respectively. The right-most columns present the magnitude of the principal eigenvalue of the velocity gradient tensor, normalized with respect to the angular speed of the cylinders. $[\dot{\gamma}/\omega]$ is the theoretical value for the shear rate; and $[\dot{\gamma}/\omega]_{\text{expt}}$ is the reported result of Wang *et al.* (Ref. 15).

Rollers	Radii (mm)	d (mm)	λ ($n=125$)	λ_{num}	λ_{expt}	$\frac{\dot{\gamma}}{\omega}$	$\left[\frac{\dot{\gamma}}{\omega}\right]_{\text{expt}}$
A	16.65	3.431 836	0.010 437	⋯	⋯	47.239 90	⋯
B	16.35	4.655 910	0.019 620	⋯	⋯	24.823 93	24.1
C	15.70	6.519 969	0.040 316	⋯	0.047	11.750 69	11.7
D	15.10	7.809 609	0.060 461	⋯	0.067	7.624 681	7.84
E	14.17	9.392 076	0.094 123	⋯	0.096	4.690 372	4.83
F	14.00	9.643 651	0.100 692	⋯	0.114	4.351 319	4.44
G	12.78	11.210 334	0.152 789	0.153	0.160	2.727 231	2.80
H	11.69	12.342 767	0.207 191	⋯	0.196	1.919 587	1.84
I	10.75	13.169 567	0.259 108	⋯	⋯	1.457 431	⋯

cal results. The source of the discrepancy is not clear, but perhaps these results can provide some insight into the accuracy of the experimental technique or can be used as a benchmark to "fine-tune" the experimental measurements.

For rollers H, the marked drop of the measured values may be the result of significant three-dimensionality flow effects due to a length-to-gap ratio of about two to one. Also, the flow field on the layers next to the flat covers must be similar to that of simple shear flow, which implies that the observed value of λ must depend upon the depth of the flow cell. Furthermore, the velocity field may also be weaker due to the proximity of the container walls generating a smaller shear rate. This three-dimensional effect may also have other consequences; in particular, at high $\dot{\gamma}$ the stability of the flow may be compromised.

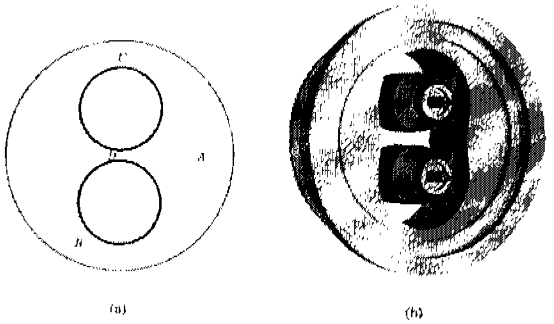

FIG. 2. Configuration of two-roll mills. (a) Mill reported in Refs. 1, 2, and 15: Region A represents a significant volume fraction of small relevance to the flow field. Region B presents a spurious elongational flow due to the existence of container walls. Region C can apply shear rates to the fluid microstructure as large as those generated in the central region. (b) The new container based on the streamlines calculated with the analytical solution. The flow cell also considers a cooling loop to maintain the temperature within 0.01 K. The top and bottom covers can be made of transparent crystal, allowing studies over the complete flow field. The rollers have conical ends to guarantee smaller shear rates for every fluid parcel than those applied at the stagnation point.

V. EXPERIMENTAL DEVICES FOR PLANAR, ELONGATIONAL FLOWS

Figure 2 shows a new flow cell based upon the calculated streamlines, and the typical two-roll mill configuration used to date with (1) region A representing a volume of fluid not used, (2) region B a secondary elongational flow domain since $\mathbf{u}\cdot\nabla\mathbf{u}\neq\mathbf{0}$, and (3) region C where shear rates can be of the same order as those that occur at the stagnation point, when the interior gap and that due to the presence of the walls have about the same width. Figure 2(b) shows the new flow cell exterior contour. Although the optimal location of the boundary on the $\alpha\beta$ plane may imply different effects on different flow properties, a general criterion is outlined which reduces the most important disadvantages mentioned above, and at the same time provide an estimate of the boundary's perturbation on the velocity field, λ, $\dot{\gamma}$, and the streamlines. The new contour for the container is based upon the calculated streamlines, assuming that the cylinders remain fixed as shown in Fig. 2(b). First, the range of geometries to be used defines the extreme variation on streamlines generated by a complete set of pairs of cylinders; see Fig. 3(a). The streamlines shown correspond to those of the largest and smallest diameters of cylinders in Table I. Second, the difference of areas—their absolute values along the streamline—delimited by these two streamlines is evaluated as a function of the distance away from the cylinders. For large radial distances away from a cylinder, the contours are very similar—at infinity, both streamlines are circles—but the length of the curve increases; closest to the cylinders, the area difference increases. Hence, there is a radial distance where the difference of the areas attains its minimum value. For a distance of 41.5 mm from a cylinder axis, the relative areal difference with respect to the total area contained within a closed streamline is less that 0.001. This curve will induce a small perturbation to all possible geometries of the two-roll mill and for the most relevant flow parameters.

Figures 3(b) and 3(c) present isopleths for the magnitude of the velocity field, $\|\mathbf{u}\|$, and $\dot{\gamma}$ for the overall domain with

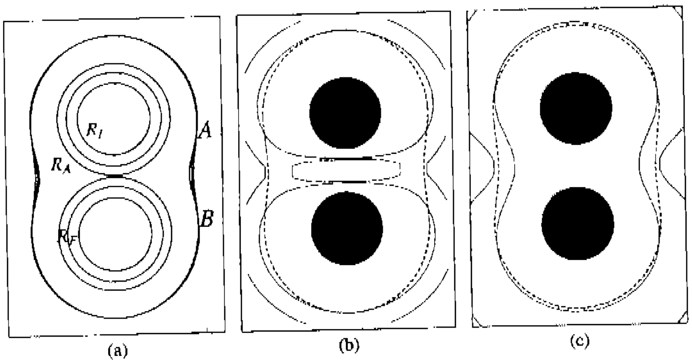

FIG. 3. The new container for two-roll mills is defined taking into account the distance at which the associated streamlines for the smallest and largest two-roll mills produce the minimum mismatch. (a) The optimum location minimizes the difference of the areas delimited by the streamlines associated to every mill. For rollers I, isopleths of the magnitude of the velocity field (b), and the velocity gradient (c) of the *unbounded* two-roll mill superposed by the contour—dashed line—of the flow cell.

the selected cell-contour superposed. For the magnitude of the fluid velocities, the most significant perturbation occurs on the portion of the flow furthest to the stagnation point (toward the exterior part of the cylinders), thus a minimal flow modification should be caused on parameters such as λ, the magnitude of the rate of deformation, and the objective vorticity. For isopleths of $\dot{\gamma}$, the strongest deviation occurs for the largest λ values near the $\alpha=0$ axis. However, these effects can be considered minimal because shear rates near the x axis and away from the stagnation point are already very small. Also for all those geometries, the rate of deformation is significantly larger at the stagnation point than far away. The variation of $\dot{\gamma}$ as a function of position along the selected streamline should increase most significantly opposite to the stagnation point behind the cylinders, where the relative modification can be at most 8% with respect to those generated at the stagnation point; furthermore, there should be a small change for the local values of λ. Finally, the machining of the walls with the prescribed streamline is possible if a sixth-order spline fit to the exterior wall is used. There are computer packages that generate the machining codes to the required precision.

VI. CONCLUSIONS

The use of the Fourier series solution for the Stokes flow generated by a two-roll mill can provide detailed information about a complete class of elongational flow with vorticity.[10] The solution presented here shows a good correlation among predicted values and the available experimental and numerical results for two of the most important flow parameters: the shear rate and the flow-type parameter. The solution is used to design and construct laboratory models of these flows that assure minimal perturbation to the desirable features of the flow. The elongational flows generated have characteristics defined exclusively by the geometry of the device and the rate of rotation of the cylinders. Furthermore, the analytical solution for these flows include the effects of inner boundaries. Because of the presence of the container's boundaries, a quantitative analysis of the perturbations is given for the velocity fields, the magnitude of the velocity gradient, the flow-type parameter, and the shear rate. These may be important advantages for studies of the microstructure of complex fluids, with analytical means to determine most of the effects due to creeping flows.

ACKNOWLEDGMENTS

Our special thanks to Gerardo F. Guevara and Jesús Camacho at the Materials Research Institute, UNAM. M.A.H.R. was supported by a DGEP-UNAM Scholarship. E.G. acknowledges partial support from Grants Nos. 3451A9310 and G27837U of CONACyT, IN303093 of PAPITT-DGAPA, UNAM, and 0598 of FIES-IMP.

[1] E. Geffroy and L. G. Leal, "Flow birefringence studies of a concentrated polystyrene solution in a two-roll mill. I. Steady flow and start-up of steady flow," J. Polym. Sci., Part B: Polym. Phys. **30**, 1329 (1992).
[2] P. Singh and L. G. Leal, "Computational studies of the FENE dumbbell model with conformation-dependent friction in a corotating two-roll mill," J. Non-Newtonian Fluid Mech. **67**, 137 (1996).
[3] S. C. Jana, G. Metcalfe, and J. M. Ottino, "Experimental and computational studies of mixing in complex Stokes: The vortex mixing flow and multicellular cavity flows," J. Fluid Mech. **269**, 199 (1994).
[4] T. Atobe, "Lagrangian chaos in the Stokes flow between two-eccentric rotating cylinders," Int. J. Bifurcation Chaos Appl. Sci. Eng. **7**, 1007 (1997).
[5] B. J. Bentley and L. G. Leal, "An experimental investigation of drop deformation and breakup in steady two-dimensional linear flows," J. Fluid Mech. **167**, 241 (1986).
[6] H. A. Stone, "Dynamics of drop deformation and breakup in viscous fluids," Annu. Rev. Fluid Mech. **26**, 65 (1994).
[7] R. R. Huilgol and N. Phan-Thien, *The Fluid Mechanics of Viscoelasticity* (Elsevier, Amsterdam, 1998).
[8] W. L. Olbricht, J. M. Rallison, and L. G. Leal, "Strong flow criteria based on microstructure deformation," J. Non-Newtonian Fluid Mech. **10**, 291 (1982).
[9] M. S. Chong, A. E. Perry, and B. J. Cantwell, "A general classification of three dimensional flow fields," Phys. Fluids A **2**, 765 (1990).
[10] M. A. H. Reyes and E. Geffroy, "Study of low Reynolds number hydrodynamics generated by symmetric corotating two-roll mills," Rev. Mex. Fis. **46**, 135 (2000).
[11] J. Happel and H. Brenner, *Low Reynolds Number Hydrodynamics* (Kluwer, Dordrecht, 1991), pp. 497–499.
[12] G. B. Jeffery, "The rotation of two-circular cylinders in a viscous fluid," Proc. R. Soc. London, Ser. A **101**, 169 (1922).
[13] C. Pozrikidis, *Theoretical and Numerical Fluid Mechanics* (Oxford University Press, Oxford, 1994).
[14] G. G. Fuller, J. M. Rallison, R. L. Schmidt, and L. G. Leal, "The measurement of velocity gradients in laminar flows by homodyne-light scattering spectroscopy," J. Fluid Mech. **100**, 555 (1980).
[15] J. J. Wang, D. Yavich, and L. G. Leal, "Time resolved velocity gradient and optical anisotropy in linear flows by photon correlation spectroscopy," Phys. Fluids **6**, 3519 (1994).

References

[1] J. Happel and H. Brenner. *Low Reynolds number hydrodynamics.* Kluwer Acad. Publ., Dordrecht, The Netherlands, 1991.

[2] J. M. Rallison. The deformation of small viscous drops and bubbles in shear flows. *Annual Review of Fluid Mechanics*, **16**:45, 1984.

[3] H. A. Stone. Dynamics of drop deformation and breakup in viscous fluids. *Annual Review of Fluid Mechanics*, **26**:65, 1994.

[4] A. Acrivos. The breakup of small drops and bubbles in shear flows. *Ann. NY Acad. Sci.*, **404**:1, 1983.

[5] B. J. Briscoe, C. J. Lawrence, and W. G. P. Mietus. A review of immiscible fluid mixing. *Advances in colloid and interface science*, **81**:1, 1999.

[6] R. E. Khayat, A. Luciani, L. A. Utracki, F. Godbille, and J. Picot. Influence of shear and elongation on drop deformation in convergent-divergent flows. *International Journal of Multiphase Flow*, **26**:17, 2000.

[7] B. J. Bentley and L. G. Leal. A computer-controlled four-roll mill for investigations of particle and drop dynamics in two-dimensional linear shear flows. *Journal of Fluid Mechanics*, **167**:219, 1986.

[8] Enrique Geffroy and L. G. Leal. Flow birefringence studies of a concentrated polystyrene solution in a two-roll mill. i. steady flow and start-up of steady flow. *J. Polym. Sci.; Polym. Phys.*, **30**:1329, 1992.

[9] P. Singh and L. G. Leal. Computational studies of the fene dumbbell model with conformation-dependent friction in a corotating two-roll mill. *Journal Non-Newtonian Fluid Mechanics*, **67**:137, 1996.

[10] S. C. Jana, G. Metcalfe, and J. M. Ottino. Experimental and computational studies of mixing in complex stokes flows: the vortex mixing flow and multi-cellular cavity flow. *Journal of Fluid Mechanics*, **269**:199, 1994.

[11] T. Atobe. Lagrangian chaos in the stokes flow between two-eccentric rotating cylinders. *Int. J. Bifurcation & Chaos*, **7**:1007, 1997.

[12] B. J. Bentley and L. G. Leal. An experimental investigation of drop deformation and breakup in steady two-dimensional linear flows. *Journal of Fluid Mechanics*, **167**:241, 1986.

[13] R. R. Huilgol and N. Phan-Thien. *The fluid mechanics of viscoelasticity.* Elsevier, The Netherlands, 1998.

[14] W. L. Olbricht, J. M. Rallison, and L. G. Leal. Strong flow criteria based on microstructure deformation. *Journal Non-Newtonian Fluid Mechanics*, **10**:291, 1982.

[15] M. S. Chong, A. E. Perry, and B. J. Cantwell. A general classification of three dimensional flow fields. *Phys. Fluids A*, **2**:765, 1990.

[16] Marco A. H. Reyes and Enrique Geffroy. Study of low reynolds number hydrodynamics generated by symmetric corotating two-roll mills. *Revista Mexicana de Física*, **46**(2):148, 2000.

[17] Marco A. H. Reyes and Enrique Geffroy. A corotating two-roll mill for studies of two-dimensional, elongational flows with vorticity. *Physics of Fluids*, **12**(10):2372, 2000.

[18] P. Singh and L. G. Leal. Computational studies of the fene dumbbell model in a co-rotating two-roll mill. *Journal of Rheology*, **38**:485, 1994.

[19] J. J. Wang, D. Yavich, and L. G. Leal. Time resolved velocity gradient and optical anisotropy in lineal flow by photon correlation spectroscopy. *Physics of Fluids*, **6**(11):3519, 1994.

[20] B. Y. Ballal and R. S. Rivlin. Flow of a newtonian fluid between eccentric rotating cylinders: Inertial effects. *Arch. Ration. Mech. Anal.*, **62**:237, 1975.

[21] G. B. Jeffery. The rotation of two circular cylinders in a viscous fluid. *Proc Royal Society*, **A 101**:169, 1922.

[22] H. Lamb. *Hydrodynamics*. Cambridge University Press, Cambridge, England, 6th edition, 1932.

[23] G. B. Jeffery. Plane stress and plane strain in bipolar coordinates. *Philos. Trans. Royal Society*, **A 221**:93, 1928.

[24] G. Astarita. Objective and generally applicable criteria for flow classification. *Journal Non-Newtonian Fluid Mechanics*, **6**:69, 1979.

[25] Y. Ueda, A. Sellier, T. Kida, and M. Nakanishi. On the low-reynolds-number flow about two rotating circular cylinders. *Journal of Fluid Mechanics*, **495**:255, 2003.

[26] O. A. Ladyzhenskaya. *The Mathematical Theory of Viscous Incompressible Flow*. Gordon and Breach, U. K., 1969.

[27] C. A. Brebbia. *The Boundary Element Method for Engineers*. Pentech Press, London, England, 1978.

[28] C. Pozrikidis. *Boundary Integral and Singularity Methods for Linearized Viscous Flow*. Cambridge University Press, USA, 1992.

[29] A. Iglesias and H. Power. Boundary elements with mathematica. In P. Mitic V. Keränen and A. Hietamäk, editors, *Innovation in Mathematics. Proceedings of the Second International Mathematica Symposium*, U.K., 1997. Computational Mechanics Publications.

[30] C. Pozrikidis. *Numerical Computation in Science and Engineering*. Oxford University Press, USA, 1998.

[31] G. I. Taylor. The viscosity of a fluid containing small drops of another fluid. *Proc. R. Soc. London, Ser. A*, **138**:41, 1932.

[32] G. I. Taylor. The formation of emulsions in definable fields of flow. *Proc. R. Soc. London, Ser. A*, **146**:501, 1934.

[33] Francesco Greco. Second order theory for the deformation of a newtonian fluids in a stationary flow field. *Physics of Fluids*, **14**(3):946, 2002.

[34] Francesco Greco. Drop deformation for non-newtonian fluids in slow flows. *Journal Non-Newtonian Fluid Mechanics*, **107**:111, 2002.

[35] Y. T. Hu and A. Lips. Determination of viscosity from drop deformation. *Journal of Rheology*, **45**(6):1453, 2001.

[36] Y. T. Hu and A. Lips. Transient and steady state three-dimensional drop shapes and dimensions under planar extensional flow. *Journal of Rheology*, **47**(2):349, 2003.

[37] Julio M. Ottino and Stephen Wiggins. Designing optimal micromixers. *Science*, **305**:485, 23 july 2004.

[38] Harold P. Grace. Dispersion phenomena in high viscosity immiscible fluid systems and applications of static mixers as dispersion devices in such systems. *Chem. Eng. Comm.*, **14**:225, 1982.

[39] F. D. Rumscheidt and S. G. Mason. Particle motions in sheared suspensions. XII. deformation and burst of fluid drops in shear and hyperbolic flow. *Journal of Colloid Science*, **16**:238, 1961.

[40] R. G. Cox. The deformation of a drop in a general time-dependent fluid flow. *Journal of Fluid Mechanics*, **37**(3):601, 1969.

[41] J. M. Rallison. Note on the time-dependent deformation of a viscous drop which is almost spherical. *Journal of Fluid Mechanics*, **98**(3):625, 1980.

[42] S. Guido, F. Greco, and M. Villone. Experimental determination of drop shape in slow steady shear flow. *Journal of Colloid and Interface Science*, **219**:298, 1999.

[43] Stefano Guido and Francesco Greco. Drop shape under slow steady shear flow and during relaxation. experimental results and comparison with theory. *Rheologica Acta*, **40**:176, 2001.

[44] Y. T. Hu, D. J. Pine, and L. Gary Leal. Drop deformation, breakup, and coalescence with compatibilizer. *Physics of Fluids*, **12**(3):484, 2000.

[45] Marco A. H. Reyes and Enrique Geffroy. Experimental flow cell for rupture and coalescence of drops in elongational flows. 1. analytical solution for the flow field. *Submitted to Physics of Fluids*, 2004.

[46] C. Pozrikidis. *A Practical Guide to Boundary Element Method with the Software Library BEMLIB.* Chapman-Hall/CRC Press, Boca Raton, USA, 2002.

[47] R. A. Johnson and A. Borhan. Stability of the shape of a surfactant-laden drop translating at low reynolds number. *Physics of Fluids*, **12**(4):773, 2000.

[48] Gary L. Leal. *Laminar Flow and Convective Transport Processes. Scaling Principles and Asymptotic Analysis.* Butterworth-Heinemann, Boston, USA, 1992.

[49] R. Aris. *Vectors, Tensors and the Basic Equations of Fluid Mechanics.* Dover, USA, 1989.

[50] D. A. Edwards, H. Brenner, and D. T. Wasan. *Interfacial Transport Processes and Rheology.* Butterworth-Heinemann, USA, 1991.

[51] J. Tanzosh, M. Manga, and H. A. Stone. Boundary integral methods for viscous free-boundary problems: Deformation of single and multiple fluid-fluid interface. In C. A. Brebbia and M. S. Ingber, editors, *Boundary Element Technology VII*, USA, 1992. Computational Mechanics Publications.

[52] S. Kim and S. J. Karrila. *Microhydrodynamics: Principles and Selected Applications.* Butterworth-Heinemann, USA, 1991.

[53] J. Blawzdziewicz, V. Cristini, and M. Loewenberg. Critical behavior of drops in linear flows. i. phenomenological theory for drop dynamics near critical stationary states. *Physics of Fluids*, **14**(8):2709, 2002.

[54] Chungsoo Charles Park. *Flow Induced Drop Coalescence.* PhD thesis, University of California, Santa Barbara, June 2002.

[55] Fabio Baldessari. *Flow-Induced Coalescence of Drops: Theory and Simulations.* PhD thesis, University of California, Santa Barbara, June 2004.

[56] R. Clift, J. R. Grace, and M. E. Weber. *Bubbles, Drops and Particles.* Academic Press, USA, 1978.

[57] C. Pozrikidis. The deformation of a liquid drop moving normal to a plane wall. *Journal of Fluid Mechanics*, **215**:331, 1990.

[58] E. P. Ascoli, D. S. Dandy, and L. G. Leal. Boundary-driven motion of a deformable drop toward a planar wall at low reynolds number. *Journal of Fluid Mechanics*, **213**:287, 1990.

[59] H. Power. The interaction of a deformable bubble with a rigid wall at small reynolds number: A general approach via integral equations. *Engineering Analysis with Boundary Elements*, **19**:291, 1997.

[60] S. G. Yiantsios and R. H. Davis. On the buoyancy-driven motion of a drop towards a rigid or deformable interface. *Journal of Fluid Mechanics*, **217**:547, 1990.

[61] M. J. Martinez and K. S. Udell. Axisymmetric creeping motion of drops through circular tubes. *Journal of Fluid Mechanics*, **210**:565, 1990.

[62] C. Pozrikidis. The buoyancy-driven motion of a train of viscous drops within a cylindrical tube. *Journal of Fluid Mechanics*, **237**:627, 1992.

[63] T. M. Tsai and M. J. Miksis. Dynamics of a drop in a constricted capillary tube. *Journal of Fluid Mechanics*, **274**:197, 1994.

[64] S. S. Sadhal, P. S. Ayyaswamy, and J. N. Chung. *Transport Phenomena with Drops and Bubbles.* Springer, USA, 1997.

[65] R. E. Khayat, A. Luciani, and L. A. Utracki. Boundary-element analysis of planar drop deformation in confined flow. part 1. newtonian fluids. *Engineering Analysis with Boundary Elements*, **19**:279, 1997.

[66] R. E. Khayat, M. A. Huneault, L. A. Utracki, and R. Duquette. A boundary element analysis of planar drop deformation in the screw channel of a mixing extruder. *Engineering Analysis with Boundary Elements*, **21**:155, 1998.

[67] R. E. Khayat. A three-dimensional boundary element approach to confined free-surface flow as applied to die casting. *Engineering Analysis with Boundary Elements*, **22**:83, 1998.

[68] R. E. Khayat. Boundary element analysis of planar drop deformation in confined flow. part II. viscoelastic fluids. *Engineering Analysis with Boundary Elements*, **22**:291, 1998.

[69] C. Pozrikidis. Interfacial dynamics for stokes flow. *Journal of Computational Physics*, **169**:250, 2001.

[70] J. Crank. *Free and Moving Boundary Problems.* Clarendon Press, Northern Ireland, 1984.

[71] R. Scardovelli and Stéphane Zaleski. Direct numerical simulation of free-surface and interfacial flow. *Annual Review of Fluid Mechanics*, **31**:567, 1999.

[72] Hiroshi Akima. A method of univariate interpolation that has the accuracy of a third-degree polynomial. *ACM Transactions on Mathematical Software*, **17**(3):341, 1991.

[73] Hiroshi Akima. ALGORITHM: 697. a method of univariate interpolation that has the accuracy of a third-degree polynomial. *ACM Transactions on Mathematical Software*, **17**(3):341, 1991.

[74] J. Blawzdziewicz, Vittorio Cristini, and Michael Loewenberg. Multiple stationary states for deformable drops in linear stokes flows. *Physics of Fluids*, **15**(5):37, 2003.

[75] G. Astarita and G. Marrucci. *Principles of Non-Newtonian Fluid Mechanics*. McGraw-Hill, Great Britain, 1974.

[76] S. Torza, R. G. Cox, and S. G. Mason. Particle motions in sheared suspensions. XXVII transient ans steady deformation and burst of liquid drops. *Journal of Colloid and Interface Science*, **38**(2):395, 1972.

[77] S. Guido, M. Simeone, and F. Greco. Deformation of a newtonian drop in a viscoelastic matrix under steady shear flow. experimental validation of slow flow theory. *Journal Non-Newtonian Fluid Mechanics*, **114**:65, 2003.

[78] Paula Gould. Microfluidics realizes potential. *Materials Today*, page 48, July/August 2004.

[79] G. Arfken. *Mathematical Methods for Physicists*. Academic Press, USA, 2nd. edition, 1971.

[80] M. N. L. Narasimham. *Principles of Continuum Mechanics*. John Wiley & Sons, USA, 1993.

[81] I. S. Gradshteyn and I. M. Ryzhik. *Tables of Integrals, Series and Products*. Academic Press, USA, corrected and enlarged edition, 1981.